

Controlling the excitonic response and the electronic ground state in two-dimensional semiconductors

Inauguraldissertation

zur

Erlangung der Würde eines Doktors der Philosophie
vorgelegt der
Philosophisch-Naturwissenschaftlichen Fakultät
der Universität Basel

von

Lukas Sponfeldner

2023

The original document is saved on the University of Basel document server

<http://edoc.unibas.ch>



This work is licensed under a Creative Commons
Attribution-NonCommercial-NoDerivatives 4.0 International License.

The complete text may be reviewed here:

<http://creativecommons.org/licenses/by-nc-nd/4.0/>

Genehmigt von der Philosophisch-Naturwissenschaftlichen Fakultät auf Antrag von

Erstbetreuer: Prof. Dr. Richard J. Warburton

Zweitbetreuerin: Prof. Dr. Ilaria Zardo

externer Experte: Prof. Dr. Alexander I. Tartakovskii

Basel, den 18. Oktober 2022

Prof. Dr. Marcel Mayor
Dekan

Abstract

The vast amount of different two-dimensional (2D) materials and the possibility of combining them into arbitrary heterostructures provide an exciting playground for studying and exploiting novel physical phenomena. Semiconducting transition metal dichalcogenides (TMDs) are particularly interesting as they host strongly bound excitons, which dominate their optical response. Embedding TMDs in high-quality optoelectronic devices provides full control of the electrostatic environment and enables a large tunability of their excitonic response and their electronic ground state.

In bilayer TMD systems, interlayer excitons (IX) can form, where the electron and hole are spatially separated in the adjacent layers. A finite twist angle between the two layers leads to moiré and atomic reconstruction effects that dominate the excitonic properties. Interlayer excitons are studied in a type-II MoSe₂/WSe₂ heterobilayer. Their real space origin in the moiré potential and their momentum space origin are determined using photoluminescence spectroscopy. While these IX are widely tunable by electric fields, their coupling to light is considerably weak. Overcoming this deficit, hybridised interlayer excitons (IE) in naturally stacked homobilayer MoS₂ are discovered that combine a large tunability of their energy with a big oscillator strength. The large tunability is used to bring the IE into resonance with the intralayer excitons revealing two different types of exciton-exciton couplings. A classical model of two coupled optical dipoles is developed that shows a good agreement with the experimentally measured couplings. The model reveals that the measured optical susceptibility determines both the magnitude and the phase of the coupling constants.

The electronic ground state in monolayer MoS₂ is explored using photoluminescence spectroscopy as a local spin- and valley-sensitive probe. In a large external magnetic field, the electrons in MoS₂ form a ferromagnetic phase at low charge carrier densities. Evidence is presented that it is also possible to stabilise the ferromagnetic phase at zero magnetic field by using a circularly polarised excitation laser. On injecting electrons into the monolayer, a first-order phase transition from the ferromagnetic phase to a paramagnetic phase is observed at a certain critical carrier density.

Contents

Abstract	iii
1. Introduction	1
2. Optical response of transition metal dichalcogenides	5
2.1. Crystal structure	6
2.2. Bandstructure and optical selection rules	6
2.3. Excitons	9
2.4. Charged excitons	11
2.5. Intralayer and interlayer excitons in bilayer TMDs	11
2.6. Moiré effects in twisted TMD heterobilayers	14
2.6.1. Optical selection rules in a moiré superlattice	15
2.6.2. Moiré potential	16
2.6.3. Moiré excitons	17
2.6.4. Atomic reconstruction of bilayers	19
2.7. Excitons in electric or magnetic fields	20
2.7.1. Electric field	20
2.7.2. Magnetic field	21
2.8. Optically probing correlated electronic states	25
3. Sample fabrication and experimental methods	27
3.1. Exfoliation and flake identification	27
3.2. Stacking van der Waals heterostructures	30
3.2.1. Polymer stamp	31
3.2.2. Stacking setup	31
3.2.3. Planning a heterostructure	33
3.2.4. Heterostructure stacking and contacting	34
3.3. Heterobilayer alignment using second harmonic generation	36
3.4. Heterostructure electrostatics	38
3.4.1. Single-gate device	40
3.4.2. Dual-gate device	40
3.5. Optical characterisation techniques	42
3.5.1. Absorption spectroscopy	43
3.5.2. Photoluminescence spectroscopy	46

3.6. Thin-film interference effects in heterostructures	46
3.7. Experimental setup	49
4. Interlayer exciton origin in a MoSe₂/WSe₂ heterobilayer	53
4.1. Introduction	54
4.2. Electrostatic device characterisation	55
4.3. Two interlayer exciton species	57
4.4. Momentum-indirect and momentum-direct interlayer exciton tunability	63
4.4.1. Crossover power	64
4.4.2. Excitonic density blueshift	65
4.4.3. Stark tuning of interlayer excitons	67
4.4.4. Energy difference of the two excitons	74
4.4.5. Excitonic response in a magnetic field	75
4.4.6. Tuning the charge carrier density	80
4.5. Conclusion and outlook	84
5. Giant Stark splitting of an exciton in bilayer MoS₂	87
5.1. Introduction	88
5.2. Energetic tunability of interlayer excitons	89
5.3. Excitonic Zeeman splitting in a magnetic field	92
5.4. Tuning interlayer and intralayer transitions into resonance	94
5.5. Theoretical calculation of the electric field effects	97
5.6. Interlayer excitons in MoS ₂ trilayers	100
5.7. Conclusion	102
6. Capacitively and inductively coupled excitons in bilayer MoS₂	103
6.1. Introduction	104
6.2. Optical response of homobilayer MoS ₂	104
6.3. Classical exciton-exciton coupling model	107
6.4. Modelling the absorption in homobilayer MoS ₂	110
6.5. Influence of the sign of the coupling strength on the excitonic absorption	112
6.6. Constructive and destructive interference	113
6.7. Microscopic origin of the two different exciton-exciton couplings	115
6.7.1. IE ₂ -B _{L2} coupling	115
6.7.2. IE ₁ -A _{L1} coupling	116
6.7.3. B _{L1} exciton	117
6.7.4. A _{L2} exciton	118
6.7.5. Applying coupled dipole model to GW+BSE results	118
6.8. Intravalley exchange coupling of A- and B-excitons	119
6.9. Conclusion and outlook	120

7. First-order magnetic phase transition of mobile electrons in monolayer MoS₂	123
7.1. Introduction	124
7.2. Photoluminescence emission of monolayer MoS ₂	125
7.3. First-order magnetic phase transition	127
7.4. Effective electron mass	130
7.5. Stabilising the ferromagnetic phase at zero magnetic field	130
7.5.1. Trion states in monolayer MoS ₂	131
7.5.2. Laser-induced spin polarisation	134
7.6. Conclusion and outlook	137
8. Conclusion and outlook	139
Appendices	143
A. Fabrication recipes	143
A.1. Electron-beam lithography for etching and contacts	143
A.2. Reactive ion etching	143
A.2.1. O ₂ plasma	143
A.2.2. Ar/O ₂ plasma	144
A.3. Fabrication of metal contacts	144
A.4. Drop-down PMMA coating of 2D materials	144
A.5. Making nano-holes in graphene	145
A.5.1. Etching	146
A.5.2. Focused ion beam milling	146
B. Van der Waals heterostructure device details	147
B.1. MoSe ₂ /WSe ₂ heterobilayer device	147
B.2. Homobilayer MoS ₂ devices	149
B.3. Monolayer MoS ₂ devices	150
C. Raman spectroscopy	153
D. Supplemental information to Chapter 5: “Giant Stark splitting of an exciton in bilayer MoS₂”	155
D.1. Experimental details	155
D.2. Beyond-DFT calculations	156
D.2.1. Computational details	156
D.2.2. Bandstructure modifications due to the electric field	157
D.2.3. Decomposition of the excitonic oscillator strength	158

E. Supplemental information to Chapter 6: “Capacitively and inductively coupled excitons in bilayer MoS₂”	161
E.1. Exciton-exciton coupling model	161
E.1.1. Equations of motion	161
E.1.2. Decoupling the equations of motion	162
E.1.3. Frequency response of the coupled masses	164
E.1.4. Calculation of the dissipated power	165
E.1.5. Linking the mechanical system to the optical response of coupled excitons	166
E.1.6. Complex coupling constant	168
E.1.7. Quadratic Stark shift of the A-exciton	169
E.1.8. Semi-classical frequency response and absorption of excitons in a semiconductor	169
E.1.9. Coupled RLC circuits	171
E.1.10. Zero coupling case	173
E.1.11. Experimental observability of interference effects	174
E.1.12. Equal absorption strength point	175
E.2. Measurement data processing	176
E.3. Computational details of the GW+BSE calculations	179
F. Supplemental information to Chapter 7: ‘First-order magnetic phase transition of mobile electrons in monolayer MoS₂’	181
F.1. Experimental details	181
F.2. Additional photoluminescence data	182
F.2.1. Photoluminescence without an applied magnetic field	183
F.2.2. Photoluminescence at elevated temperature	184
F.2.3. Absorption measurement	185
Bibliography	187
Acknowledgements	215
Curriculum Vitae	217
List of Publications	219

“A tiny blue dot set in a sunbeam.

Here it is.

That’s where we live.

That’s home.

We humans are one species and this is our world. It is our responsibility to cherish it. Of all the worlds in our solar system, the only one so far as we know, graced by life.”

Carl Sagan, Cosmos: A Personal Voyage (1990)

Chapter 1

Introduction

The dimensionality of a physical system is very important. Strong confinement of a particle in one dimension leads to a reduced dimensionality, which in turn can result in stronger interactions. In systems, where the energies associated with these interactions dominate over all other energy scales, strong coupling between particles and stable correlated states become experimentally accessible.

An ideal two-dimensional (2D) confinement in the solid state is an atomically thin sheet. Such a system was realised for the first time in 2004 by A. Geim and K. Novoselov, who isolated graphene, a single layer of carbon atoms [Nov04]. This discovery was awarded the Nobel Prize in physics in 2010 and laid the foundation of the entirely new and fast-growing field of 2D materials, the so-called van der Waals materials. These layered materials consist of truly 2D atomic sheets with strong in-plane bonds, while the neighbouring sheets only couple weakly through van der Waals forces. Using Scotch tape, individual layers can be removed from the bulk crystal to thin down the material to the monolayer limit. Among the vast zoo of 2D materials, semiconducting transition metal dichalcogenides (TMDs) are particularly interesting due to their optical and electronic properties. Another important property of these 2D materials is that due to the truly 2D nature of each layer, they have no dangling bonds. This is in stark contrast to the established III-V semiconducting materials (e.g. GaAs), which exhibit dangling bonds and consequently large electric fields at the surface, negatively affecting their properties [Man20, Naj21].

Different 2D material layers can be stacked on top of each other into van der Waals heterostructures with atomically flat interfaces (atomic Lego) to create novel materials, only limited by our imagination [Gei13]. Unlike stacking Lego blocks, stacking two single 2D layers offers an additional degree of freedom: the relative twist angle between the layers. Stacking two layers of graphene or TMDs at a certain twist angle can lead to strongly

correlated electronic states that arise due to the hybridisation of charge carriers between the layers (see Subsection 2.8). Another advantage of 2D materials over conventional 2D semiconductor systems is that the fabrication of heterostructures is rather cheap, flexible, and does not require complex growth methods such as molecular beam epitaxy. The easy accessibility of 2D materials (“only” bulk crystal and scotch tape needed) and a large number of possible combinations of a variety of 2D materials lead to rapid progresses in low-dimensional condensed matter physics.

In this thesis, the physical properties of different TMD monolayer and bilayer systems are studied using optical spectroscopy. The TMD layers are embedded in electrically contacted, high-quality van der Waals heterostructures, which allow full control of the electrostatic environment. The optical response of TMDs is dominated by elementary excitations at energies close to the bandgap, like an exciton, a bound electron-hole pair. The 2D nature of TMDs leads to strong Coulomb interactions between the charge carriers. As a consequence, correlated electronic states can form in a monolayer [Roc19, Smo21]. Furthermore, large exciton binding energies make excitons stable even at room temperature [Mak10, Spl10]. The ability to electrically and optically control the excitonic response and the electronic ground state is crucial for studying and exploiting novel physical phenomena in two dimensions.

Chapter 2 introduces the fundamental concepts of monolayer and bilayer TMDs, which are necessary for the understanding of this thesis. Based on the TMD crystal structure, the electronic bandstructure and the corresponding optical selection rules of the excitonic transitions are discussed. Next, the concepts of intralayer excitons and (hybridised) interlayer excitons are presented. Then, the optical and electronic properties of TMD heterobilayers, which are dominated by moiré and atomic reconstruction effects, are explained briefly. Following a discussion on the influence of external electric and magnetic fields on the excitonic response of TMDs, the means of probing the electronic ground state of TMD systems in optical experiments is presented.

Chapter 3 describes the device fabrication and gives insight into the most important experimental methods used in this thesis. First, the exfoliation of 2D materials and the identification of the desired layers are discussed. Then, a dry-transfer stacking procedure to combine several materials into a functional heterostructure is presented. For the stacking of a TMD heterobilayer, second harmonic generation is introduced as a tool for precise alignment of the monolayer crystals. Then, the electrostatic device designs are shown, followed by a brief introduction of the main optical techniques used for the study of the TMD systems: absorption and photoluminescence spectroscopy. Afterwards, the influence of thin-film interference effects on the optical properties of TMDs embedded in heterostructures is discussed. Lastly, the complete experimental setup is presented and explained.

Chapter 4 discusses the real and momentum space origin of interlayer excitons in a twisted $\text{MoSe}_2/\text{WSe}_2$ heterobilayer. A broad two-peak structure is observed over a wide range of experimental parameters. Using laser-power dependent and polarisation-resolved photoluminescence measurements, the interlayer exciton origins are proposed to be from a lower energy momentum-indirect transition and a larger energy momentum-direct transition. While the momentum space origin is different for each exciton, it is shown, that the real space origin of both excitons corresponds to the minimum of the moiré potential. Furthermore, using several experimental parameters as tuning parameters, the large tunability of both interlayer exciton species is discussed.

Chapter 5 presents the excitonic response in homobilayer MoS_2 using absorption spectroscopy. It is found that homobilayer MoS_2 hosts hybridised interlayer excitons (IE) with a large oscillator strength and a high tunability by external electric fields. On increasing the electric field, two interlayer resonances are found with opposite dipole moments, leading to a giant splitting of their energies.

Chapter 6 builds upon the findings of the previous chapter and shows that the large dipole moments can be used to tune the IE in homobilayer MoS_2 into resonance with the intralayer A- and B-excitons. In both cases, an avoided crossing is observed, indicating an exciton-exciton coupling. Using a classical model of two coupled optical dipoles, it is shown that the measured optical susceptibility reveals both the magnitude and the phase of the coupling constants. The IE-B coupling has a 0-phase (“capacitive” coupling, hole tunnelling) while the IE-A coupling has a π -phase (“inductive” coupling, electron-hole exchange). Using the IE as an energy-tunable sensor, the A-B intravalley exchange coupling is determined.

Chapter 7 shows studies of the electronic ground state in monolayer MoS_2 using photoluminescence spectroscopy as a local spin- and valley-sensitive probe. At low charge carrier densities, the electrons in MoS_2 form a ferromagnetic phase due to the strong Coulomb interaction and electron-electron exchange between the two valleys. Evidence is presented that, at a certain critical carrier density, the ferromagnetic state undergoes a first-order phase transition to a paramagnetic phase. Due to the symmetry of spin-up and spin-down states, the ferromagnetic phase is unstable at zero magnetic field. However, a careful study of the optical response enabled the observation of a laser-induced ferromagnetic phase even at zero magnetic field.

Chapter 8 summarises the results presented in this thesis and gives a short outlook on future experiments.

*“You know, I’m something of a scientist myself”
Willem Dafoe, Spiderman (2002)*

Chapter **2**

Optical response of transition metal dichalcogenides

The possibility to isolate a single layer of graphite, called graphene, kicked off the new field of two-dimensional (2D) materials [Nov04, Nov05a, Zha05]. They are also called van der Waals materials. A van der Waals material is a layered material that has strong in-plane bonds but the individual atomically thin layers are only weakly attached to each other. This makes it possible to cleave thin layers apart by using Scotch tape. Through mechanical exfoliation, a bulk crystal can be thinned down to a monolayer with properties encompassing insulators, (semi-)metals, superconductors, and semiconductors. Relevant to this thesis are the semiconducting transition metal dichalcogenides (TMDs) which form a direct bandgap in the monolayer limit [Mak10, Spl10]. Prominent features of the optical response of TMDs are elementary excitations at energies close to the bandgap, like an exciton, a bound electron-hole pair. The optical study of these states in monolayer and bilayer TMDs is the central part of this thesis.

This chapter gives an overview of the general properties of monolayer and bilayer TMDs focusing on their optical response. Section 2.1 introduces the crystal structure of TMDs. The resulting bandstructure and optical selection rules are explained in Section 2.2. The fundamentals of excitons, bound electron-hole pairs, are discussed in Section 2.3. In Section 2.4, the concept of charged excitons, a three-particle state, is briefly introduced. After the discussion of intralayer and (hybridised) interlayer excitons in bilayer TMDs in Section 2.5, moiré effects in twisted TMD heterobilayers are presented in Section 2.6. The discussed moiré effects include the adjusted optical selection rules, the moiré potential with the moiré excitons living in it, and atomic reconstruction of the bilayer system. The effect of external electric and magnetic fields on the excitonic properties is discussed in

Section 2.7. The chapter concludes in Section 2.8 with a brief overview of correlated electronic states in TMDs.

2.1 Crystal structure

Transition metal dichalcogenides (TMDs) are atomically-thin layered crystals. The atoms in each layer are covalently bonded together while each layer is only weakly bound to another layer by van der Waals interaction. Each layer consists of a central plane of transition metal atoms ($M = \text{Mo}, \text{W}$) sandwiched between two layers of chalcogen atoms ($X = \text{S}, \text{Se}, \text{Te}$). The chemical formula of TMDs is MX_2 . Figure 2.1a shows the side view of a TMD bilayer. For a bulk TMD, these two layers would be repeated over and over again. The layer spacing is roughly 0.6 nm. TMD bulk crystals mainly consist of 2H-stacked (hexagonal) layers where alternating layers are rotated by 180° with respect to each other. There exists another stable, albeit less frequent, stacking configuration where the layers are not rotated with respect to each other which is referred to as 3R-stacking or simply R-stacking (rhombohedral). Figure 2.1b shows the top view of a TMD monolayer with its hexagonal lattice of alternating M and X atoms. The hexagonal lattice has a threefold rotation symmetry. The primitive unit cell (red shaded area) is spanned by the lattice vectors \vec{a}_1 and \vec{a}_2 . For TMDs, the lattice constant $a_0 = |\vec{a}_{1,2}|$ is roughly 3 \AA (see Table 2.1 for detailed values). It can be seen in Figure 2.1a that a single layer lacks inversion symmetry but has a mirror symmetry around the transition metal plane.

The TMD crystal symmetry leads to a hexagonal first Brillouin zone as sketched in Figure 2.1c. The high-symmetry points Γ , K, K', and M are marked. The Q point is not a high symmetry point and lies in the middle of the line connecting the Γ and K points. The six corners of the Brillouin zone form two groups consisting of three K or K' points each. The three equal K (K') points can be related by the reciprocal lattice vectors \vec{b}_1 and \vec{b}_2 . K and K' cannot be transformed into each other by the reciprocal lattice vectors and are therefore inequivalent.

2.2 Bandstructure and optical selection rules

Bulk TMDs are indirect bandgap semiconductors with the valence band maximum located at the Γ point and the conduction band minimum located at the Q point [Yun12, Zha13]. At these points, the bands mainly contain atomic orbitals with an out-of-plane contribution. Therefore, the band energy at the Γ and Q points strongly depends on the layer number of TMDs. On the other hand, the atomic orbitals at the K/K' points are strongly confined to the transition metal layer. They consist of transition metal atom $d_{x^2-y^2} + d_{xy}$ (d_{z^2}) states in the valence (conduction) band slightly mixed with chalcogen atom $p_x + p_y$ states [Zhu11, Kor15]. Upon going from bulk TMDs to a single layer, the Γ -Q energy difference increases while the K-K energy difference is nearly unaffected [Spl10]. In the monolayer

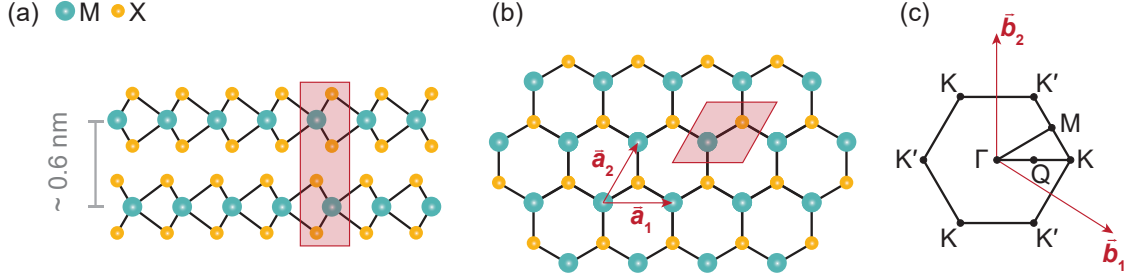


Figure 2.1. Crystal structure of TMDs. (a) Side view of a 2H-stacked TMD bilayer where the layers are rotated by 180° with respect to each other. The green balls represent the transition metal atoms (M) and the yellow balls are the chalcogen atoms (X). The distance between the layers is roughly 0.6 nm. The primitive unit cell is shown as the red shaded area. (b) Top view of a TMD monolayer. The lattice vectors \vec{a}_1 and \vec{a}_2 span the primitive unit cell (red shaded area). (c) Sketch of the first Brillouin zone defined by the reciprocal lattice vectors \vec{b}_1 and \vec{b}_2 . The inequivalent high-symmetry K and K' points are located at the corners of the Brillouin zone. In-between the K and Γ points lies the Q point.

limit, TMDs become a direct bandgap semiconductor with the minimum energy transition located at the K and K' points [Spl10, Mak10].

Figure 2.2 shows the parabolic electronic bands around the K and K' points for MoS₂ (MoSe₂), and WSe₂ monolayers. The heavy transition metal atoms lead to a strong spin-orbit interaction. The spin-orbit interaction lifts the degeneracy of the spin-states in the valence and conduction bands at the K/K' points. The valence band spin-splitting Δ_v is large (> 100 meV) [Zhu11, Che12, Xia12]; the conduction band spin-splitting Δ_c is much smaller [Liu13, Kos13]. Theoretically calculated values for the spin-splitting for MoS₂, MoSe₂, and WSe₂ monolayers are given in Table 2.1. Please note that the conduction band spin-splitting has an opposite sign for Mo- and W-based TMDs. The K and K' points are related by time-reversal symmetry which leads to an inverse spin-ordering in the two valleys. The two spin-allowed intravalley A (lower energy) and B (higher energy) transitions are a consequence of the large spin-orbit interaction.*

The inversion symmetry in TMD monolayers is broken which leads to valley-dependent optical selection rules and dictates an opposite sign of the orbital moment at K and K' [Yao08, Xia12, Cao12]. The origin of the selection rules is the phase winding of the Bloch electrons under rotational symmetry [Yao08, Liu15]. This winding influences the orbital magnetic moment of the electronic states at the K/K' points. The valence bands transform with an angular momentum of 0, while the conduction band states have an angular

*At even higher energies, there exists a third transition denoted as the C-transition [Qiu13]. The physical origin of C is quite different from A and B. The lowest conduction and highest valence bands between the Γ and Q point have approximately the same slope leading to a band nesting region [Wan17b]. The band nesting enhances the optical response and the resonant transition is called C.

	MoS ₂	MoSe ₂	WSe ₂
a_0 (Å)	3.185	3.319	3.316
Δ_v (meV)	148	184	462
Δ_c (meV)	-3	-20	37
m_h (m_0)	0.54	0.60	0.36
m_e (m_0)	0.47	0.58	0.29

Table 2.1. Calculated material parameters for the studied TMD monolayers. All numbers are extracted from Reference [Kor15]. a_0 is the lattice constant, $\Delta_{v,c}$ is the valence and conduction band splitting, and $m_{h,e}$ are the effective hole and electron masses.

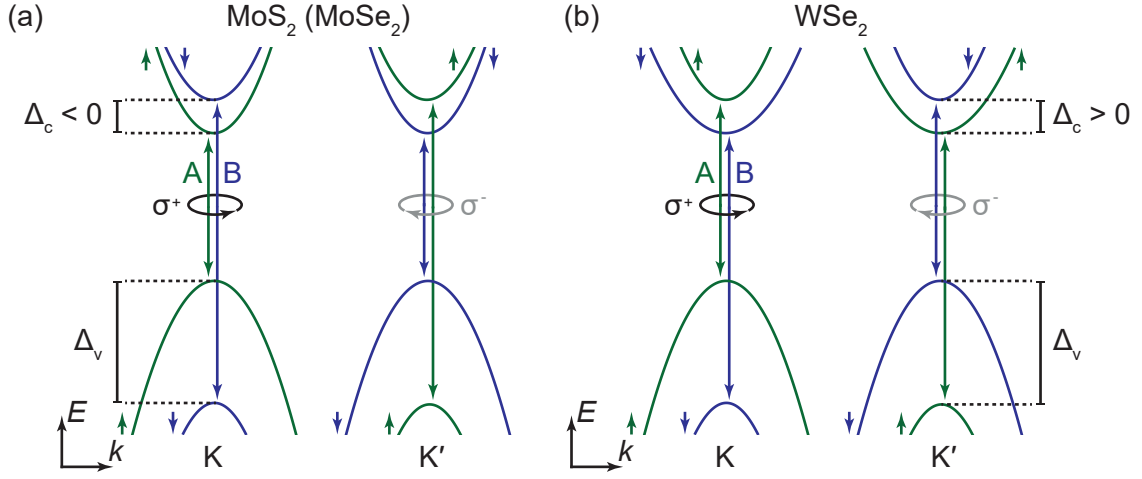


Figure 2.2. Bandstructure and optical selection rules in (a) monolayer MoS₂ (MoSe₂) and (b) monolayer WSe₂. In the monolayer limit, these materials have a direct bandgap at the K and K' points (also referred to as valleys) in the Brillouin zone [Mak10, Spl10]. Spin-orbit coupling splits the spin-↑ (green) and the spin-↓ (blue) bands. The K and K' points are linked by time-reversal symmetry which leads to opposite spin-ordering in the two valleys. The splitting in the valence band Δ_v is much larger than the splitting in the conduction band Δ_c (see Table 2.1). The sign of Δ_c depends on the metal atom (Mo or W). The lowest-energy spin-allowed transition is called the A-transition while the higher-energy one is called B-transition. The broken inversion symmetry in TMD monolayer crystals leads to valley-dependent optical selection rules [Yao08, Xia12, Cao12]. Transitions in the K (K') valley couple to σ^+ (σ^-) circularly polarised light.

momentum of ± 1 at K/K' [Cao12]. The angular momentum of a left/right circularly-polarised photon is ± 1 . Therefore, TMD monolayer K (K') transitions couple to σ^+ (σ^-) circularly polarised light (see Figure 2.2).

2.3 Excitons

An exciton is a Coulomb-bound electron-hole pair. In semiconductors, an electron can be excited from the valence band into the conduction band through the absorption of a photon with an energy above the bandgap. Simultaneously, this process creates a positively charged hole in the valence band. The opposite charge of electron and hole leads to an attractive Coulomb interaction binding them together. The resulting bound state is called an exciton. Typically, excitons are categorised into two limiting cases: Frenkel excitons and Wannier-Mott excitons. Frenkel excitons are strongly localised and tightly bound excitons with a size of roughly the lattice constant [Fre31]. The weakly bound Wannier-Mott excitons are highly mobile with a size much larger than the lattice constant [Wan37, Mot38]. Typically, Wannier-Mott excitons exist in semiconductors. In TMDs, the exciton radius is on the order of 1-2 nm [Gor19] which is larger than the lattice constant (see Table 2.1). Therefore, the excitons in TMDs can be described as Wannier-Mott excitons [Wan18a].

The bound nature of an exciton reduces its ground state energy as compared to the energy difference of a free electron and hole. The energy difference is known as the binding energy E_b . In other words, E_b is the energy needed for ionisation of the bound exciton state. The larger the binding energy is, the more stable the excitons are. The energy of an exciton with principal quantum number n and with a zero centre-of-mass in-plane wave vector ($\vec{K} = 0$) is given by [Gro14]

$$E_X^{(n)} = E_g - E_b^{(n)}, \quad (2.1)$$

with E_g being the renormalised free particle bandgap ($n = \infty$). Figure 2.3a shows the dispersion of the quantised bound states with principle number n . The energy dispersion as a function of \vec{K} is given by the kinetic energy of the exciton $\frac{\hbar^2 |\vec{K}|^2}{2(m_e + m_h)}$ [Kli12]. The optical absorption is sketched in Figure 2.3b. The strong Coulomb interaction leads to excitonic resonances below the bandgap. The exciton energy approaches the bandgap energy for increasing n . An important property of an excitonic state is how well it couples to an external light field. This interaction is described by a quantity called oscillator strength f which scales as $f \propto \left(n - \frac{1}{2}\right)^{-3}$ in two dimensions [Kli12].

A Wannier-Mott exciton is an analogue of the hydrogen atom with the hole replacing the proton and with the semiconducting crystal lattice acting as a dielectric background. Solving this problem for a 2D system, one can write the binding energy of the ground ($n = 1$) or excited ($n > 1$) bound states as [Kli12]

$$E_b^{(n)} = R_X \frac{1}{\left(n - \frac{1}{2}\right)^2}, \quad n = 1, 2, 3, \dots, \quad (2.2)$$

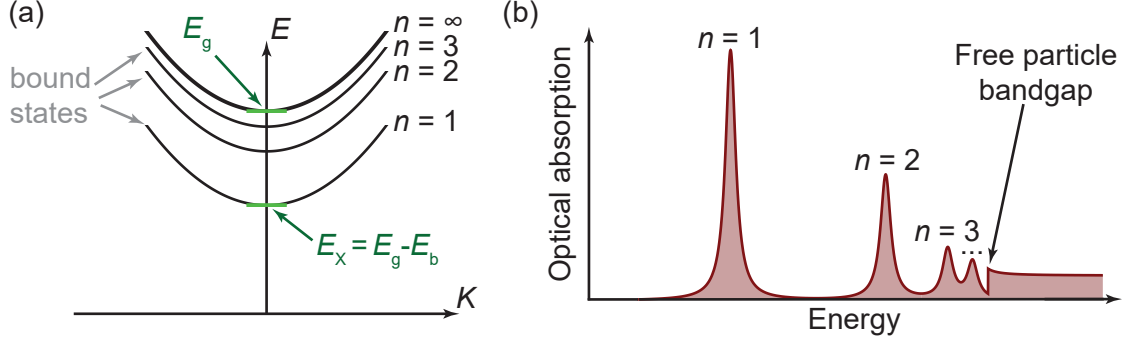


Figure 2.3. (a) Exciton dispersion of the quantised bound states with principal quantum number n . \vec{K} is the excitonic centre-of-mass wave vector. The exciton ground state energy E_X ($n = 1$) with $\vec{K} = 0$ is given by the renormalised bandgap energy E_g minus the excitonic binding energy E_b . (b) Sketch of the optical absorption in a 2D semiconductor. Excitonic states appear below the bandgap energy. The energy difference between the excitonic states decreases upon approaching the free particle bandgap. The figure is adapted from Reference [Wan18a].

with R_X being the excitonic Rydberg energy. For the calculation, a locally screened $\propto \frac{1}{r}$ Coulomb potential is assumed, where r is the distance between the charges. The term $n - \frac{1}{2}$ comes from the two-dimensionality of the confinement (in 3D: $E_b \propto \frac{1}{n^2}$). In analogy to the hydrogen Rydberg series, the bound exciton states are often labelled as 1s, 2s, etc. The excitonic Rydberg energy is given by

$$R_X = \frac{1}{2} \frac{e^2}{4\pi\epsilon_0\epsilon_r a_X}, \quad (2.3)$$

with the elementary charge e , the dielectric constant of the lattice ϵ_r , the vacuum permittivity ϵ_0 , and the excitonic Bohr radius a_X . The Bohr radius is defined as

$$a_X = \frac{4\pi\epsilon_0\epsilon_r\hbar^2}{\mu e^2}, \quad (2.4)$$

where $\mu = (\frac{1}{m_e} + \frac{1}{m_h})^{-1}$ is the reduced effective mass of the exciton. Using typical values for TMDs ($m_{e,h} = 0.5m_0$ and $\epsilon_r = 7$ [Lat18]), a Bohr radius of ≈ 1.5 nm and a binding energy of ≈ 280 meV can be estimated. Due to the large binding energy, the excitonic bound states are stable at room temperature and above ($\frac{E_b}{k_B} \approx 3000$ K). The small Bohr radius suggests that the Coulomb effects are very dominant in TMDs. Consequences of the strong interaction will be discussed in Chapter 7.

It is interesting to put the Bohr radius and binding energy of TMDs in perspective with the properties of a conventional semiconductor like GaAs. Typical values for excitons in GaAs are $R_X = 4.2$ meV and $a_X = 13$ nm [Fox10]. Excitons in TMDs are much stronger bound than excitons in GaAs. One reason is that the effective exciton mass is much smaller

in GaAs ($\mu = 0.06m_0$) [Fox10]. Another reason is that TMDs are typically surrounded by a dielectric material with a small permittivity (e.g. hBN $\epsilon_r = 3.76$ [Lat18]). This means a significant amount of the electric field between electron and hole is also confined to the surrounding dielectric which has a huge impact on E_b and E_g [Sti16b, Raj17]. As a consequence, the assumption of a simple $\frac{1}{r}$ Coulomb potential breaks down especially for low n [Che14]. The strong screening in the TMD layer and the weak screening in the dielectric is modelled by the Rytova-Keldysh potential [Ryt67, Kel67]. For a small electron-hole separation, the potential scales as $\log(r)$; at a large separation, it scales as $\frac{1}{r}$ [Che14].

2.4 Charged excitons

Excitons can interact with free charge carriers present in the semiconductor. A free electron or hole can bind to an exciton forming a three-particle bound state. In the few-particle picture, the resulting state is referred to as a negative or positive trion (X^- or X^+). Neutral excitons are denoted as X^0 . In TMD monolayers, the trion emission energy E_{X^-} is smaller than the free exciton emission energy E_{X^0} . In the limit of zero free charge carriers in the monolayer, the energy difference is given by [Mak13, Ros13]

$$E_{X^0} - E_{X^-} = E_T^0, \quad (2.5)$$

where E_T^0 is the trion binding energy. Typical values of E_T^0 in TMD monolayers are 20 – 30 meV [Mak13, Ros13]. Due to the Pauli exclusion principle, the additional charge carrier cannot have the same spin and valley state as the charge in the exciton. This results in different possible intra- and intervalley trion states in TMD monolayers [Sin16, Li18, Zhu20, Rob21, Grz21, Kle22]. Charged excitons can also be described in a many-body approach, the Fermi-polaron picture [Sur01, Efi17, Sid17, Roc19]. In this picture, the exciton is dressed by interactions with the Fermi sea of electrons. These interactions split the exciton into two resonances, the higher-energy repulsive polaron (exciton branch) and the lower-energy attractive polaron (charged exciton branch). For a small charge carrier density, the trion and polaron pictures yield identical results [Gla20]. However, the three-particle trion picture breaks down at higher charge densities. The charged exciton optical response in monolayer MoS₂ will be discussed in Chapter 7.

2.5 Intralayer and interlayer excitons in bilayer TMDs

So far, the discussion has been limited to excitons in TMD monolayers. Adding a second TMD monolayer to form a bilayer system creates new types of excitons with rather interesting properties as discussed below. Excitons in bilayer TMDs can be sorted into two categories: Intralayer and interlayer excitons. For intralayer excitons, the Coulomb-bound

electron-hole pair resides in the same layer while for interlayer excitons the electron and hole reside in different layers. The two exciton types are sketched in Figure 2.4. Sometimes these two exciton categories are also referred to as spatially direct and indirect excitons. Interlayer excitons are particularly interesting to study as they possess an out-of-plane electric dipole moment which enables a large energetic tunability (see Subsection 2.7.1).

Interlayer excitons can have very different properties depending on the TMD material of each layer and the twist angle between them. Generally, one can distinguish two types of interlayer excitons that depend on the electronic orbitals that constitute the electron-hole pair. A hybridised interlayer exciton (IE) has an electron or a hole state that is delocalised across both layers (see Figure 2.4a). In this case, an interlayer exciton is effectively mixed with an intralayer exciton which can lead to interesting exciton-exciton coupling effects (see Chapter 6). The other type is an interlayer exciton (IX) where the electron and hole are purely confined to the opposite single layer (see Figure 2.4c). Please note the different abbreviations for the two types of interlayer excitons (IE and IX) which will be used throughout this thesis.

The mixed excitonic states forming hybridised excitons can be found in a lot of bilayer systems, such as bilayer MoS₂ [Ger19, Slo19, Car19, Nie19], bilayer MoSe₂ [Sun20], MoSe₂/WS₂ [Ale19], WSe₂/WS₂ [Tan21], MoS₂/WS₂ [Kie20], MoSe₂/WSe₂ [McD21], or MoTe₂/MoSe₂ [RT19]. A particularly interesting system for hybridised excitons is homobilayer MoS₂. Homobilayer indicates a naturally 2H-stacked bilayer. Atomic orbital hybridisation of the two spin-like valence bands leads to IE with a large oscillator strength [Dei18, Ger19]. The resulting IE with its hybridised hole state is sketched in Figure 2.4b. The optical response of homobilayer MoS₂ is discussed in detail in Chapter 5 and Chapter 6.

IX are typically found in heterostructures with a type-II band alignment as shown in Figure 2.4d. For such a staggered band alignment, one monolayer has the energetically lowest conduction band state while the other one has the highest valence band state. After exciting an electron-hole pair in either monolayer, charges tunnel between the layers to reach their respective minimal energy state. The charge transfer happens on a sub-picosecond timescale [Hon14, Ceb14] which is much faster than the IX lifetime and also the intralayer exciton recombination time [Mil17]. After the tunnelling event, an IX is formed at an energy lower than the two intralayer exciton energies. This process is sketched in Figure 2.4d. IX energies are usually between the infrared and near-infrared energies. Even though the electron and hole are separated in space, IX still have a very large binding energy of over 200 meV [Wil17] enabling room temperature experiments [Unu18]. Unlike the strong oscillator strength of IE in e.g. bilayer MoS₂, IX in heterobilayers have a negligible oscillator strength. IX have been observed using photoluminescence spectroscopy in several material combinations with a type-II alignment like MoS₂/WSe₂ [Kun18, Kar19, Hua20], MoS₂/WS₂ [Che16, Oka18], WS₂/WSe₂ [Wan16, Jin19a, Mon21], or MoSe₂/WSe₂ [Riv15,

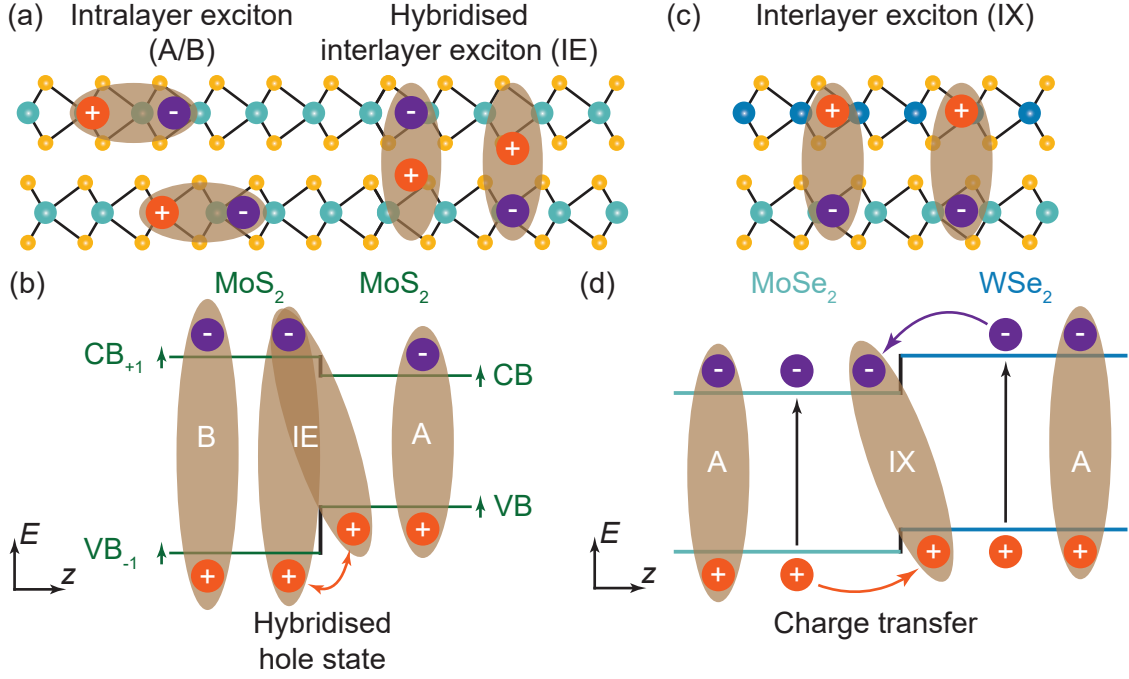


Figure 2.4. Schematic of intralayer and interlayer excitons. (a,b) Intralayer A- and B-excitons and hybridised interlayer excitons (IE) in homobilayer MoS₂ sketched (a) in the crystal structure and (b) in the bandstructure. Intralayer excitons consist of electrons and holes confined in the same layer. IE consist of an electron confined to one of the two layers and a hole that is delocalised across both layers. The hybridised hole state is a consequence of atomic orbital hybridisation in the valence bands of the two layers [Ger19]. CB₊₁ (VB₋₁) indicates the higher (lower) energy conduction (valence) band. (c) Interlayer exciton (IX) sketched in the crystal structure of a type-II MoSe₂/WSe₂ heterobilayer. IX consist of an electron residing in MoSe₂ and a hole in WSe₂. (d) Formation process of IX depicted in the bandstructure of the heterobilayer. The valence band maximum is located in the WSe₂ layer, while the conduction band minimum is located in the MoSe₂ layer. Exciting an intralayer exciton in either layer leads to an efficient charge transfer between the layers (indicated by the coloured arrows) and ultimately to the formation of IX.

Riv16, Nag17b, Mil17, Ros17, Han18, Hsu18, Via19, Fö19, Jau19, Sey19, Tra19, Cia19].

It is important to note that IX are formed with electrons and holes both located near the K (K') point in the Brillouin zone. As discussed in Chapter 2.2, other points in the Brillouin zone like Γ or Q are influenced by the number of layers. This leads to a hybridisation of the atomic orbitals of the two layers at the Γ and Q points. In the following discussion, the focus lies on the most-studied heterobilayer MoSe₂/WSe₂ which is also the system investigated in this thesis. Several studies of IX in MoSe₂/WSe₂ argue that the conduction band minimum is at the Q point and not at the K point [Mil17, Han18, Fö21]. Additionally, the stacking of two crystals leads to the formation of a moiré pattern which influences the properties of IX. The main implications of the moiré potential will be explained in the next section. Due to this complex heterobilayer system, the interpretations of the physical

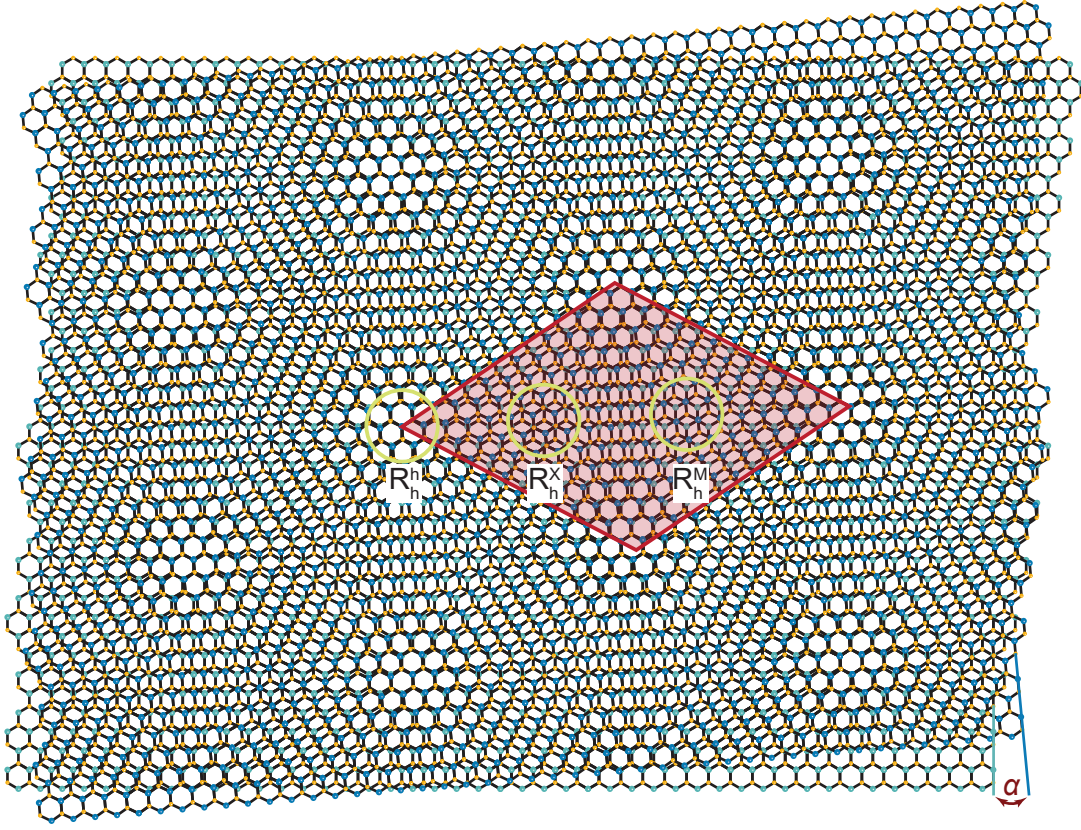


Figure 2.5. Moiré superlattice formed when stacking two TMD monolayers at an angle α on top of each other. Here, monolayer MoSe₂ and WSe₂ with a very similar lattice constant are stacked at a twist angle of $\alpha = 5^\circ$. Therefore, the moiré periodicity $a_{\text{moiré}} \approx 3.8$ nm. The supercell of the moiré superlattice is highlighted with the red shaded area. There exist three high-symmetry points with a \hat{C}_3 rotational symmetry (three-fold rotational symmetry): R_h^h , R_h^X , and R_h^M . R indicates 3R-stacking (near 0° stacking). The superscript μ (hexagonal centre h, chalcogen atom X, or metal atom M) indicates the site of the MoSe₂ layer that is aligned with the hexagon centre (h) of the WSe₂ layer. These high-symmetry points are explained in more detail in Figure 2.6.

origin of the IX are still widely discussed [Tra20]. In Chapter 4, the properties of IX in a MoSe₂/WSe₂ heterobilayer are discussed and the real and momentum space origin is determined.

2.6 Moiré effects in twisted TMD heterobilayers

Upon stacking two TMD monolayers with a different lattice constant and/or at a specific twist angle on top of each other, the two crystal lattices will overlap forming an interference pattern, a so-called moiré pattern. The moiré effect is illustrated in Figure 2.5 where monolayer MoSe₂ and WSe₂ are stacked with a twist angle of $\alpha = 5^\circ$. The moiré supercell is shaded in red. Assuming a very small lattice mismatch, the periodicity of the superlattice

can be approximated as [RP18]

$$a_{\text{moiré}} \approx \frac{a_{0,W}}{\sqrt{\alpha_{\text{rad}}^2 + \delta^2}}, \quad (2.6)$$

with the lattice constant mismatch $\delta = \frac{|a_{0,\text{Mo}} - a_{0,W}|}{a_{0,W}}$ and α_{rad} being the twist angle in radian. Due to the small lattice mismatch of TMDs (see Table 2.1) the periodicity is mainly given by the twist angle. For very small twist angles, the moiré periodicity can reach up to several hundred nanometers which is much larger than the monolayer lattice constant or the exciton radii.

Similar to bulk TMDs, a heterobilayer can have two extreme stacking angles: 3R/R stacking (near 0° twist) or 2H/H stacking (near 60° twist). The influence of the moiré pattern on the excitonic properties strongly depends on the stacking configuration [Yu18, Hua22]. The studied heterobilayer in this thesis has a nearly R-stacked configuration ($\approx 3^\circ$ twist). Therefore, the discussion in this theory chapter focuses on IX in R-stacked MoSe₂/WSe₂ heterobilayers.

In this section, several moiré effects will be discussed. Following the crystal symmetry, the optical selection rules in the bilayer are modified significantly as presented in Subsection 2.6.1. After introducing the moiré potential in Subsection 2.6.2, the moiré excitons residing in this potential are discussed in Subsection 2.6.3. It is shown that the stacking angle is very crucial for the excitonic properties. Finally, atomic reconstruction is presented in Subsection 2.6.4.

2.6.1 Optical selection rules in a moiré superlattice

Inside the moiré supercell, there exist three high symmetry points where the three-fold rotational symmetry (\hat{C}_3) is preserved. These points are shown in Figure 2.5 and are labelled as R_h^h , R_h^X , and R_h^M [Yu17]. The superscript μ (hexagonal centre h, chalcogen atom X, or metal atom M) indicates the site of the MoSe₂ layer (electron layer) that is aligned with the hexagon centre (h) of the WSe₂ layer (hole layer) as indicated by the subscript. The side and top view of the atomic stacking configuration at each symmetry point are shown in the top row of Figure 2.6.

As in the monolayer, the optical selection rules for excitons depend on the Bloch phase winding under the C_3 rotation. The C_3 rotation eigenvalue of the Bloch function depends on the electron layer rotation centre (h, X, M) for a fixed hole layer centre (h) [Yu17]. First, the transitions at the K point are discussed. Contrary to the monolayer, the spin-flip (spin-triplet) transitions in a heterobilayer are dipole-allowed with a similar magnitude as spin-conserved transitions because of the broken out-of-plane mirror symmetry [Yu18, Tra20]. As a result of the Bloch phase shift, the spin-conserved IX transition at R_h^h

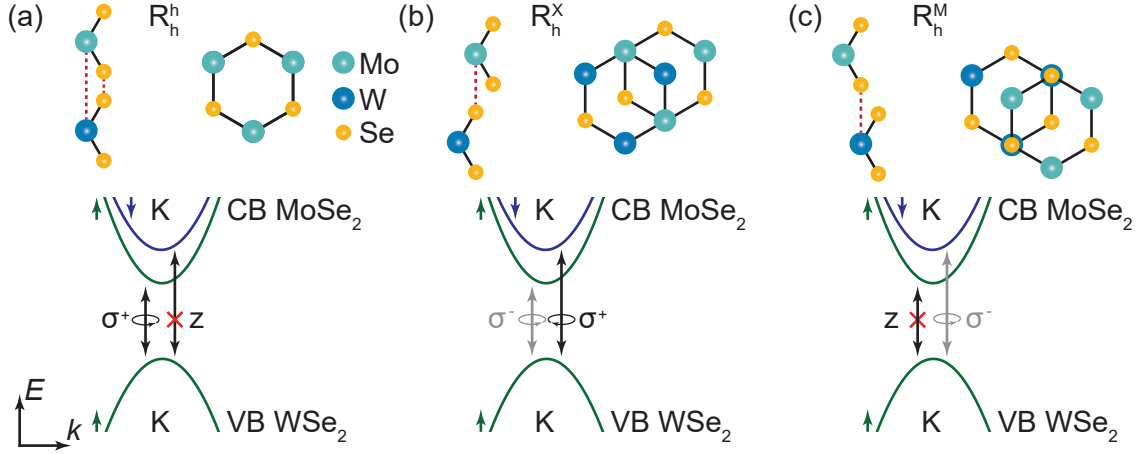


Figure 2.6. High-symmetry points in the moiré superlattice and their corresponding optical selection rules at the K point of an R-stacked MoSe₂/WSe₂ heterobilayer. (a) For R_h^h , the two hexagons are aligned with metal and chalcogen atoms on top of each other. The spin-conserved transition is σ^+ polarised, while the spin-flip transition only couples to photons polarised in-plane (z). (b) For R_h^x , the chalcogen atom of the MoSe₂ layer is on top of the hexagon centre of WSe₂. The spin-conserved (spin-flip) transition couples to σ^- (σ^+) polarisation. (c) For R_h^m , the metal atom of the MoSe₂ layer is on top of the hexagon centre of WSe₂. The spin-conserved (spin-flip) transition couples to in-plane (σ^-) polarisation. To get the selection rules for the K' point, all σ^+ and σ^- polarisations need to be swapped. The figure is adapted from References [Yu18, Tra19].

(R_h^x) couples to σ^+ (σ^-) polarised light. The spin-flip IX transition at R_h^h (R_h^x) couples to in-plane (σ^+) polarised light. The spin-conserved (spin-flip) transition at R_h^m couples to in-plane (σ^-) polarised light [Yu15, Yu17, Wu18]. All selection rules are summarised in the bottom row of Figure 2.6. The K' selection rules follow from time-reversal symmetry. As a result, all σ^+ and σ^- polarisations need to be swapped on going from K to K'. In between the high-symmetry points, the selection rules vary continuously in the whole moiré supercell [Yu15].

2.6.2 Moiré potential

In addition to the modified selection rules, the moiré pattern also leads to a real space variation of the distance between the two layers and the IX energies with the extrema located at the high-symmetry points [Yu17, Wu18]. The resulting theoretical layer separation δd and moiré potential for a bilayer with zero twist angle are plotted in Figure 2.7a. The layer separation of a heterobilayer measured with scanning tunnelling microscopy (STM) is roughly a factor of three larger than the theoretical prediction [Zha17a]. The lowest IX energy is at the R_h^x point. The moiré potential magnitude strongly depends on the twist angle of the bilayer [Bre20a]. The potential depth of the minimum IX energy point for R stacking (60 – 100 meV) is calculated to be larger than for H stacking (~ 20 meV)

[Wu18, Tra19, Bre20b].*

IX can therefore be seen as particles residing in this real space moiré potential. The IX movement in this potential then strongly depends on the size of the moiré supercell or in other words on the exciton radius as compared to the distance between the potential minima. Additionally, the diffusion of IX also depends on the exciton density (filling of the potential) and the temperature [Wan21a]. IX are localised in the moiré potential at small twist angles and/or small exciton densities; the IX diffusivity increases for larger twist angles and/or higher exciton densities [Yua20, Cho20, Wan21a]. If IX are strongly confined, or not, has a big influence on the optically dominant IX in the bilayer as will be discussed in the next subsection.

2.6.3 Moiré excitons

The moiré pattern also influences the crystal properties in momentum space as sketched in Figure 2.7b. In a bilayer, the two Brillouin zones of each monolayer are rotated by the real space twist angle α as well. This leads to a momentum difference of ΔK of the K and K' valleys in each layer, respectively. The momentum conservation of IX then depends on ΔK and the reciprocal lattice vectors of the upper and lower layer. The whole k space behaviour of intra- and interlayer excitons near the K/K' point can be folded into the so-called moiré mini Brillouin zone (mBZ) [Wan17c, Wu18]. The distance between the mBZ centre γ and the hexagon corners κ/κ' is ΔK . Recently, the emission of IX inside the mBZ has been measured experimentally in momentum space using femtosecond photoemission momentum microscopy [Sch22]. It should be noted that if the stacking angle is too far away from 0° or 60° then the interlayer coupling (efficiency of the charge transfer) is reduced and therefore the optical emission is quenched significantly [Nay17].

The resulting zone-folded moiré mini IX bands strongly depend on the twist angle. Figure 2.7c shows the moiré IX bandstructure for a small twist angle of 1° which exhibits flat bands [Wu18, Nai20, Guo20, Bre20b]. Flat bands are possible in TMD bilayers for a large range of angles where the exact angles depend on the materials used for the bilayer. The optically active excitons are at the γ point and have their real space origin at R_h^X . The deep confinement of IX at small twist angles leads to multiple exciton resonances at the same location as sketched in Figure 2.7a bottom. This situation is very similar to semiconducting quantum dots. Exciton ground and excited states are observed with alternating optical selection rules [Tra19]. The ground state has the σ^- polarisation of the spin-conserved transition at the R_h^X point [Wu18, Bre20b]. Localised IX in a moiré potential could for example be used to realise an ordered array of quantum dots with highly

*The intralayer exciton energy is also modified through the moiré pattern [Yu17]. Intralayer moiré excitons have been experimentally determined in bilayer heterostructure [Zha18, Jin19b]. However, the exact origin of intralayer excitons in the moiré superlattice is still under discussion [Tra20].

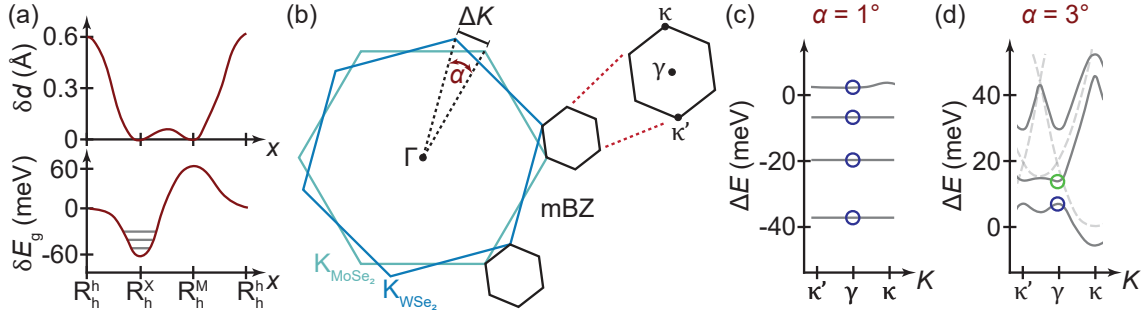


Figure 2.7. (a) Layer separation δd (top) and interlayer bandgap variation δE_g along the high-symmetry points in the moiré superlattice at zero twist angle. (b) Schematic of the moiré mini Brillouin zone (mBZ) for a MoSe₂/WSe₂ heterobilayer at a twist angle of α . K and K' valleys are separated in momentum by ΔK . The momentum difference between the centre of the mBZ γ and the hexagon corners κ and κ' is also ΔK . (c,d) Sketch of the moiré interlayer exciton minibands for a twisted MoSe₂/WSe₂ heterobilayer at (c) $\alpha = 1^\circ$ and (d) $\alpha = 3^\circ$. For very small twist angles, the deep exciton potential at R_h^X (R_h^h) leads to multiple confined interlayer exciton states with a flat band (see also (a) bottom). For larger twist angles, the bands are almost parabolic and follow the zone-folded bands of free excitons closely (light grey dashed lines). Hybridisation of the free exciton bands leads to avoided crossings at the intersection points. Optically active exciton states spatially located at R_h^X (R_h^h) are marked with an open blue (green) circle. The sketch in (a) top is adapted from Reference [Yu17]. The sketches in (a) bottom and in (c,d) are adapted from Reference [Bre20b].

tunable properties [Yu17, Sey19, Nai20]. The quantum nature of moiré-trapped IX has already been confirmed experimentally [Bae20].

The IX mini bands for a slightly larger twist angle of 3° are shown in Figure 2.7d. On increasing the angle, the flat bands change to nearly parabolic bands. The parabolic bands indicate delocalised states. The resulting bands (dark grey lines) follow the zone-folded bands of the free excitons (light grey dashed lines) closely [Bre20b]. The hybridisation of excitons with a different centre of mass leads to avoided crossings in the bandstructure. The strong mixing can be seen as standing waves localised at different symmetry locations.* The lowest-energy (second lowest-energy) optically active IX at the γ point originates from R_h^X (R_h^h) coupling to σ^- (σ^+) polarisation [Bre20b].

The twist angle is therefore a very important tuning knob in bilayer TMDs. IX are either confined in a deep moiré potential, delocalised, or some state in-between. Their state strongly influences the optical response of the bilayer. Additionally, only K/K' excitons are considered in the moiré exciton picture; potentially energetically lower momentum-indirect Q-K exciton transitions are neglected [Gil18]. It is important to understand all these different microscopic pictures when discussing IX in bilayers.

*Here, two interlayer states mix resulting in two IX with electron and hole still localised in either layer. This is in contrast to certain hybridised IE which are formed when the intralayer and interlayer moiré mini bands hybridise [Ale19, RT19, Bre20a].

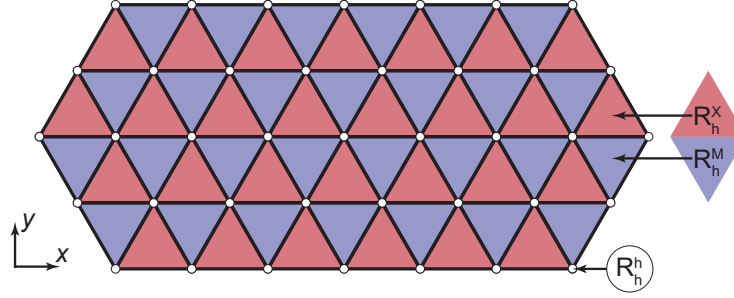


Figure 2.8. Periodic atomic reconstruction (AR) in R-stacked TMD bilayers for small twist angles. Below a certain twist angle, the energy gain from forming low-energy and high-symmetry points (R_h^X and R_h^M) outweighs the energy cost of twisting the layers into the high-symmetry configurations. After AR, the bilayer shows alternating triangular domains with R_h^X and R_h^M symmetry. This is a significant deviation from the moiré pattern shown in Figure 2.5 where a rigid lattice is assumed. The triangular domain size is very position and twist-angle dependent and can vary from 5 nm up to ~ 300 nm [Sus19, Ros20, Wes20].

2.6.4 Atomic reconstruction of bilayers

So far the bilayer system has been treated as two rigid monolayers. In reality, atomic reconstruction (rearrangement of atoms in each layer) happens between the two layers at small twist angles. The reconstruction leads to significant changes in the crystal structure of the bilayer system. Certain high-symmetry stackings of the two layers are energetically much more favourable than others. Therefore, atomic reconstruction occurs if the energy gain of forming a preferred crystal orientation overcomes the energy cost of twisting the layers into said orientations [Car18, Wes20]. Atomic reconstruction has been theoretically and experimentally shown in bilayer graphene [Ald13, Wij15, Yoo19, McG20] and bilayer TMDs [Car18, Sus19, Ros20, Wes20, Sun20, Luo20, Hal21, And21, Li21, Sha21a]. The critical twist angle, below which the reconstruction takes place, is hard to determine. Studies suggest that reconstruction is likely to happen for angles below 2° [Ros20, Wes20] while there appears to be a rather large transition region (2° - 6°) between pure reconstruction and pure moiré [Qua21]. However, these numbers might depend on the materials used for the bilayer.

An atomically reconstructed R-stacked TMD bilayer is sketched in Figure 2.8. Two alternating triangle domains of the low-energy and high-symmetry points R_h^X (red) and R_h^M (blue) are formed. R_h^h domains are pushed to the corners of the triangles. Both triangles are rather strain-free. This means that the strain resulting from the twisting mainly acts in the boundaries between the domains (black lines) [Wes20]. The domain size of the triangles can vary from 5 nm up to ~ 300 nm due to the strong position and twist angle dependency [Sus19, Ros20, Wes20]. Generally speaking the smaller the twist angle is, the larger the domain sizes are. H-type stacked bilayers have only one lowest-energy stacking symmetry

which forms hexagonal domains [Car18, Ros20]. It is not clear yet as to how much hBN encapsulation influences the atomic reconstruction [Tra20].

An open question is to what extent atomic reconstruction influences the optical properties of TMD bilayers. The optical selection rules of the reconstructed high-symmetry domains are the same as described in Subsection 2.6.1 [Woz20]. However, the correlation of the optical properties with the atomic structure is not an easy task [And21]. From an experimental point of view, it is interesting to correlate atomic reconstruction to the excitonic properties measured via photoluminescence spectroscopy. Currently, atomic reconstruction is usually studied optically only with Raman spectroscopy which allows the measurement of certain low-frequency phonon processes that only take place in reconstructed areas [Pur16, Hol20]. These processes are discussed in more detail in Appendix Chapter C.

2.7 Excitons in electric or magnetic fields

External electric or magnetic fields can be used to manipulate and tune certain properties of excitonic particles. Experimentally, these fields are easily accessible and tunable. Therefore, measurements utilising these fields are an integral part of this thesis. Studying the excitonic response to external fields is an important step toward understanding the optical properties of TMDs. Since a 2D material system is studied and therefore excitons that exist in a 2D confinement, the orientation of the external field with respect to the 2D plane is crucial. Generally, one can distinguish the response of excitons to an out-of-plane field along the z -direction and an in-plane field at an arbitrary direction in the x - y -plane. In this thesis, only the response to out-of-plane fields is studied. In the following, some of the most important consequences for excitons in external out-of-plane fields will be discussed. For completeness, some influences of in-plane fields will also be mentioned.

2.7.1 Electric field

In an external electric field \vec{F} , excitons experience an energy shift ΔE given by

$$\Delta E = -\vec{\mu} \cdot \vec{F} - \vec{\beta} \cdot \vec{F}^2, \quad (2.7)$$

where $\vec{\mu}$ is the excitonic dipole moment and $\vec{\beta}$ is the excitonic polarisability. This effect is called the quantum-confined Stark effect (QCSE) [Mil84]. The vector notation implies that this effect is present for both out-of-plane and in-plane electric fields. For a non-zero excitonic dipole moment (e.g. for interlayer excitons), the linear term dominates the energy shift for experimentally accessible electric fields.

Intralayer excitons have a near-zero out-of-plane dipole moment ($\mu_z \simeq 0$) leading to a quadratic QCSE determined by the polarisability. The out-of-plane polarisability in monolayer MoS₂ is roughly $\beta_z = 8 \times 10^{-10}$ D m V⁻¹ which translates to negligible energy

shifts [Roc18]. Interlayer excitons on the other hand have a non-zero out-of-plane dipole moment μ_z defined by the effective interlayer separation of the electron and hole. Applying an out-of-plane electric field can lead to very large linear energy shifts of these excitons (see Chapter 4 and Chapter 5).

The large response of interlayer excitons to external electric fields can for example be utilised to study exciton dynamics [Unu18, Unu19, Cho20, Wan21a]. Another interesting approach is to trap interlayer excitons by creating a lateral variation of the vertical electric field through nano-patterning of the gate electrodes [Sch11, Sha21b]. On account of the repulsive dipole-dipole interaction between interlayer excitons, it should be possible to electrostatically trap a single exciton [Sch13a] or a single exciton-polariton [Del19, MM19]. However, nano-fabricating a trap with a size comparable to the exciton is a very challenging task due to the very small interlayer exciton diameter of ~ 5 nm [Kar22]. Appendix A discusses the challenges of fabricating small traps and shows two procedures that are used to pattern holes (35 to 50 nm) into few-layer graphene.

An out-of-plane electric field additionally influences the interlayer exciton lifetime by changing the wave function overlap of electron and hole. The interlayer excitonic lifetime is inversely proportional to the wave function overlap squared [Kö88, Phi89, Ale90]. Depending on the sign of the electric field, the interlayer exciton lifetime can be tuned from 1 ns to 500 ns [Jau19].

The in-plane polarisability of intralayer excitons is much larger than the out-of-plane polarisability due to the lack of confinement. For monolayer MoS₂, $\beta_{x,y} = 3 \times 10^{-7}$ D m V⁻¹ which is roughly a factor 1000 larger than β_z [Cav18]. Using in-plane electric fields in monolayer TMDs might prove an interesting alternative route to trapping neutral excitons [Thu22]. A negative side effect of an in-plane electric field may be the ionisation of excitons. The field strength necessary for ionisation can be estimated by comparing the electric field drop along the exciton Bohr radius with the exciton binding energy [Die19]. Because of the extremely large binding energy and the small Bohr radius of (interlayer) excitons in TMDs, ionisation of excitons requires very large lateral fields which are not reached in most experiments. The ionisation of excitons can become important in the more traditional 2D semiconductor systems (e.g. III-V quantum wells) [Die19].

2.7.2 Magnetic field

At zero magnetic field, the K and K' valley exciton energies are degenerate (see Figure 2.9). An out-of-plane magnetic field B_z lifts the valley degeneracy by breaking time-reversal symmetry [Li14, Sri15, Aiv15, Mac15]. The electronic bands shift in energy according to the valley Zeeman effect [Mit15, Wan15a]. The total Zeeman energy shift of a band has three contributions:

- Spin: $\Delta_s = \frac{1}{2}g_s\mu_B s_z B_z \simeq \mu_B s_z B_z$, with $g_s \simeq 2$ being the free-electron g factor, μ_B

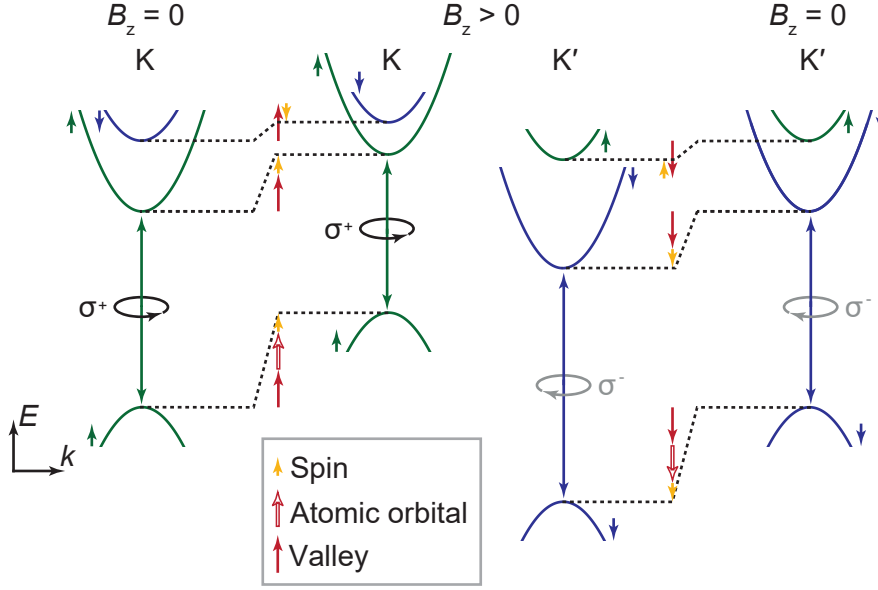


Figure 2.9. Bandstructure of a TMD monolayer in an external magnetic field B_z perpendicular to the 2D plane. Electronic bands shift in energy due to valley, atomic orbital, and spin contributions as illustrated by the coloured arrows. The magnetic field lifts the degeneracy of K and K' excitons; the energy of the σ^+ (σ^-) transition decreases (increases). The corresponding excitonic g -factor can be estimated to be -4.

being the Bohr magneton, and $s_z = \pm 1$ being the pseudospin operator perpendicular to the monolayer [Kor14].

- Atomic orbital: $\Delta_\alpha = \mu_B m_l B_z$, with m_l being the orbital magnetic moment. $m_l = 0$ for the conduction bands while $m_l = 2$ (-2) for the K (K') valley valence band [Aiv15].
- Valley: $\Delta_v = \mu_B \alpha^{c,v} \tau_z B_z$, with $\tau_z = +1$ ($\tau_z = -1$) being the valley quantum number at K (K') and $\alpha^{c,v} = \frac{m_0}{m_{e,h}}$ determining the valley magnetic moment defined by the different effective masses of electrons m_e and holes m_h in the conduction and valence band [Mac15].

The detailed magnetic field-induced energy shifts of the lowest-energy bands in a monolayer are sketched in Figure 2.9. The coloured arrows representing the three contributions are sketched on roughly the same scale. The total Zeeman shift of an exciton in a magnetic field depends on the energy shift difference of the contributing valence and conduction bands. The spin contributions cancel out for spin-conserving transitions. Additionally in a monolayer, the effective electron mass in the conduction band is roughly equal to the effective hole mass in the valence band (see Table 2.1). Therefore, the valley contributions cancel each other out. The only relevant Zeeman shift is due to the orbital magnetic moment of the valence band. The energy shift is equal to $-2\mu_B B_z$ ($+2\mu_B B_z$) for the spin-conserving interband transitions in the K (K') valley.

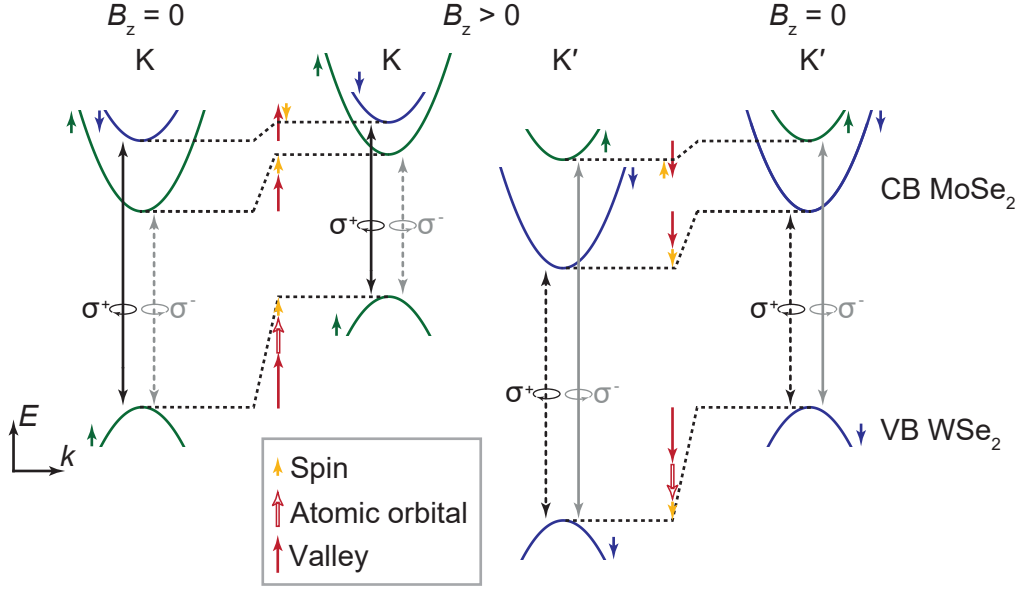


Figure 2.10. Bandstructure evolution of an R-stacked MoSe₂/WSe₂ heterobilayer in an external magnetic field B_z perpendicular to the 2D plane. The optical selection rules are the ones for R_h^X symmetry as it is the stacking with the lowest interlayer energy (see Figure 2.6). Electronic bands are shifting in energy due to valley, atomic orbital, and spin contributions as illustrated by the coloured arrows. The spin-conserving (spin-flip) transition is sketched as the dashed (continuous) vertical lines. The excitonic g -factor of the spin-conserving (spin-flip) transition can be estimated to be +6 (-10).

The valley Zeeman shift of the excitons scales linearly with the applied magnetic field. The slope of the shift is different for each valley. It is useful to define the valley Zeeman splitting ΔE between the two valleys as

$$\Delta E = E^{\sigma^+} - E^{\sigma^-} = g\mu_B B_z, \quad (2.8)$$

where g is the intervalley excitonic g factor and E^{σ^+} (E^{σ^-}) is the transition energy of the left (right) circularly polarised transition [Aro21].

Figure 2.9 illustrates that the K (K') valley A-exciton shifts to a lower (higher) energy in a monolayer TMD. The resulting g factor can be estimated to be -4. This estimation is in line with our results on monolayer A-exciton g factors (see Chapter 4). An extensive overview of measured g factors in TMD monolayers can be found in Reference [Woz20]. Deviations from a g factor of -4 are usually attributed to the difference of electron and hole masses. The B-exciton g factor is also measured and calculated to be -4 [Sti16a, Woz20].

The excitonic g factor is a very important property which helps the identification of interlayer excitons in bilayers. In homobilayer MoS₂, the hybridised interlayer exciton has a g factor of $\sim +7$ which makes it clearly distinct from intralayer resonances (see Chapter 5). In heterobilayers, the interlayer exciton g factor g_{IX} strongly depends on the local stacking

order and the spin configuration of the corresponding exciton. For example, measuring g_{IX} is a method to distinguish between R- and H-stacked bilayers with $g_R = +6$ and $g_H = -13$ [Nag17b, Woz20].

Figure 2.10 shows the band evolution of an R-stacked MoSe₂/WSe₂ heterobilayer in a perpendicular magnetic field. Note that the valley energy shift is larger in the valence band due to the smaller hole mass in WSe₂ as compared to the conduction band electron mass in MoSe₂ (see Table 2.1). Using $m_e = 0.58m_0$ and $m_h = 0.36m_0$, a band energy shift of roughly $-1\mu_B B_z$ ($+1\mu_B B_z$) is estimated at the K (K') point due to the valley contribution. The optical selection rules in Figure 2.10 are taken from the lowest energy R_h^X symmetry point. Using the simple considerations from above, g_{IX} can be estimated to be +6 (-10) for the spin-conserving (spin-flip) transition. At the R_h^H point, the swapped selection rules lead to a g_{IX} of -6 (+10) for the spin-conserving (spin-flip) transition. The strong dependence on the local crystal symmetry makes measuring g_{IX} a valuable tool to identify the interlayer exciton origin. In contrast, the main exciton g factor g_{IX} in a H-stacked sample is ~ -13 [Nag17a]. An extensive overview of measured and calculated g factors in a MoSe₂/WSe₂ heterobilayer can be found in References [Woz20, Fö21].

In addition to the linear Zeeman energy shift, excitons also experience a diamagnetic energy shift that scales with B_z^2 [Wal98]. The diamagnetic shift coefficient depends on the size of the exciton. By measuring the quadratic energy dependence one can therefore determine the exciton radius [Sti16a]. Due to the strong exciton confinement and hence the small radius, diamagnetic shifts only become apparent at very large magnetic fields (60 T). Typical intralayer 1s exciton radii are determined using the diamagnetic shifts to be on the order of 1-2 nm [Gor19]. The 2s exciton radius is on the order of 5-8 nm [Aro17, Zip18, Wan20b]. The large radius of 2s/3s excitons makes them an ideal sensor to study optically for example correlated electronic states in TMD bilayers [Xu20] or the fractional quantum Hall effect in graphene [Pop22]. A monolayer TMD sensor is placed close to the layers of interest. The large 2s/3s excitons are very sensitive to the dielectric environment and can therefore detect changes in the charge state of the sample [Raj17, Raj19].

The lifted valley degeneracy in a magnetic field may also influence the polarisation dynamics of excitons. For monolayer WSe₂, the magnetic field does not visibly influence the valley polarisation of neutral excitons [Mit15, Wan15a]. In contrast, the valley polarisation of neutral excitons in monolayer MoSe₂ is strongly influenced by B_z [Wan15a].

In tungsten-based TMDs, the excitonic ground state is optically dark (spin-flip transition) for excitation/detection perpendicular to the monolayer. However, some of these dark excitons can couple to light that is polarised perpendicular to the plane (z-polarisation) which corresponds to excitation/detection parallel to the monolayer [Wan17a]. Another way to study these dark transitions is by applying an in-plane magnetic field $B_{x,y}$. $B_{x,y}$ mixes

bright and dark states due to a mixing of the two spin states in each band [Mol17, Zha17b]. The bright dark splitting in WSe₂ (WS₂) is found to be 40 meV (55 meV) [Wan17a]. Interestingly, the dark exciton state in the seemingly bright MoS₂ also lies 14 meV below the bright exciton [Rob20].

2.8 Optically probing correlated electronic states

The interaction and hybridisation effects between electrons and holes in/between the individual layers of 2D materials may allow the study of strongly correlated electronic states. A notable example is twisted bilayer graphene where correlated insulator states, superconductivity, and ferromagnetic phases have been observed [Cao18a, Cao18b, Ker19, Lu19, Sha19]. Recently, experiments in twisted bilayer TMDs also showed strongly correlated insulating states and the formation of Wigner crystals [Reg20, Wan20a, Tan20b, Shi20, Xu20, Zho21, Hua21, Li21]. A Wigner crystal is an ordered, crystalline state of the charge carriers in the solid-state [Zho21]. Depending on the filling factor and the moiré potential in TMD bilayers, the Wigner crystal takes different forms [Reg20]. The TMD crystal symmetry allows the realisation of a triangular Hubbard model [Wu18] which could be used as a condensed-matter quantum simulator [Ken21].

The possibility to probe the correlated electronic states optically is very exciting. Therefore, it is interesting to study the interaction of excitons with charges in the moiré potential. Recently, several research groups found experimental evidence of moiré trions that could be used as a possible probe of the correlated states [Wan21b, Liu21, BG21]. As mentioned before, another option to probe the correlated state is by using the large 2s/3s excitons in a TMD monolayer sensor placed next to the system of interest [Xu20, Pop22].

The formation of correlated states is not only limited to TMD bilayer systems. In TMD monolayers, the Coulomb interaction between electrons can dominate over all other energy scales. This can lead to the formation of a Wigner crystal of electrons as experimentally demonstrated in monolayer MoSe₂ [Smo21]. A particularly interesting case is monolayer MoS₂ where the conduction band splitting is very small (see Table 2.1). On account of strong Coulomb interaction and electron-electron exchange between the valleys, electrons will form a spin-polarised/ferromagnetic state at small to moderate charge carrier densities [Roc19]. The ferromagnetic electronic state is probed by monitoring the excitonic response upon charging the monolayer. On increasing the charge carrier density, the ferromagnetic state undergoes a first-order phase transition which will be discussed in more detail in Chapter 7.

*“All that is gold does not glitter,
Not all those who wander are lost;”*
J. R. R. Tolkien, The Fellowship of the Ring
(1954)

Chapter 3

Sample fabrication and experimental methods

In the beginning, there is nothing but a few crystals and a silicon wafer. In the (happy) end, there is a finished heterostructure that has the potential to push the boundaries of 2D semiconductor physics forward. In-between, there are a lot of challenges that need to be overcome and a lot of techniques that need to be mastered. This chapter tries to fill in the voids such that a happy end is within reach.

Section 3.1 shows how to exfoliate and to identify flakes of 2D materials. Then, the stacking of the flakes into a van der Waals heterostructure is explained in Section 3.2. The stacking of 2D layers is at the core of 2D research and an art form in itself. When stacking two different TMD monolayers on top of each other the crystal alignment becomes important. Therefore, Section 3.3 introduces second harmonic generation as a method to align two monolayers for stacking. The electrical gating methods and the corresponding electrostatics for the different heterostructure devices are shown in Section 3.4. The finished heterostructure is studied with optical characterisation techniques like absorption or photoluminescence spectroscopy which are presented in Section 3.5. Afterwards, the influence of thin-film interferences on the optical properties of TMDs inside a heterostructure will be discussed in Section 3.6. Lastly, Section 3.7 shows the complete confocal microscope setup used to study the properties of TMDs.

3.1 Exfoliation and flake identification

2D materials consist of atomically thin layers weakly bound by van der Waals forces. Exploiting the weak interlayer forces, the top layers of a bulk crystal can be torn off using adhesion tape. This rather simple method enables the isolation of even a single 2D layer.

Material	Type	Source
MoS ₂	Natural	SPI Supplies
MoSe ₂	Synthetic	HQ Graphene
WSe ₂	Synthetic	HQ Graphene
Graphite	Natural	NGS Nanographit
hBN	Synthetic	K. Watanabe and T. Taniguchi [Tan07]

Table 3.1. Bulk crystals used in this thesis.

This process is called mechanical exfoliation or the Scotch tape method. Table 3.1 lists the sources of all bulk crystals used for exfoliation in this thesis.

The detailed exfoliation process used in this thesis is shown in Figure 3.1. A bulk crystal is thinned down on a master tape (Nitto tape ELP BT-150-LC, Nitto) by folding the tape and taking it apart again several times. Usually, the desired flake thickness is reached after folding four to eight times. Too much applied force or the folding process itself (bending of the tape) might lead to a fragmentation of the flakes. Therefore, one should take care that no big flake pieces are in the folding edge. Additionally, it is usually not recommended to fold flakes on top of other flakes in the thinning down process.

The exfoliation onto the substrate is not done with the master tape but with a second exfoliation tape that is pressed onto the master tape. Ideally, when peeling off the exfoliation tape slowly, the flakes cleave again such that the new top surface has not been in contact with any tape and is therefore clean. In Figure 3.1 the exfoliation tape used is again the Nitto tape. Another option is to use a thin polydimethylsiloxane (PDMS) film (Gelfilm WF-25-X4, Gel-Pak) as the exfoliation tape. Using PDMS reduces the tape residues as compared to the Nitto tape. However, the exfoliation yield is much smaller for the PDMS film.

The exfoliation tape is pressed onto one (or more) diced and cleaned Si/SiO₂ chip(s). The tape is removed slowly cleaving the flakes again creating a clean top surface as before. The chip then has a few flakes of all thicknesses and sizes and tape residue on its surface. To find suitable flakes on the chip an optical microscope is used. The chip is scanned systematically with an x5 or x10 objective until a suitable flake is found. Figure 3.1(i) shows a microscope image of a MoS₂ monolayer with a x100 objective. Usually, the desired flakes are very thin (1-2 monolayers) which makes them hard to see in a microscope. However, using interference effects in the substrate, one can maximise the contrast of very thin flakes (monolayers) for a specific SiO₂ thickness [[Gor11](#), [Wan12](#)]. Typically, the SiO₂ thickness is either ~ 90 nm or ~ 285 nm.

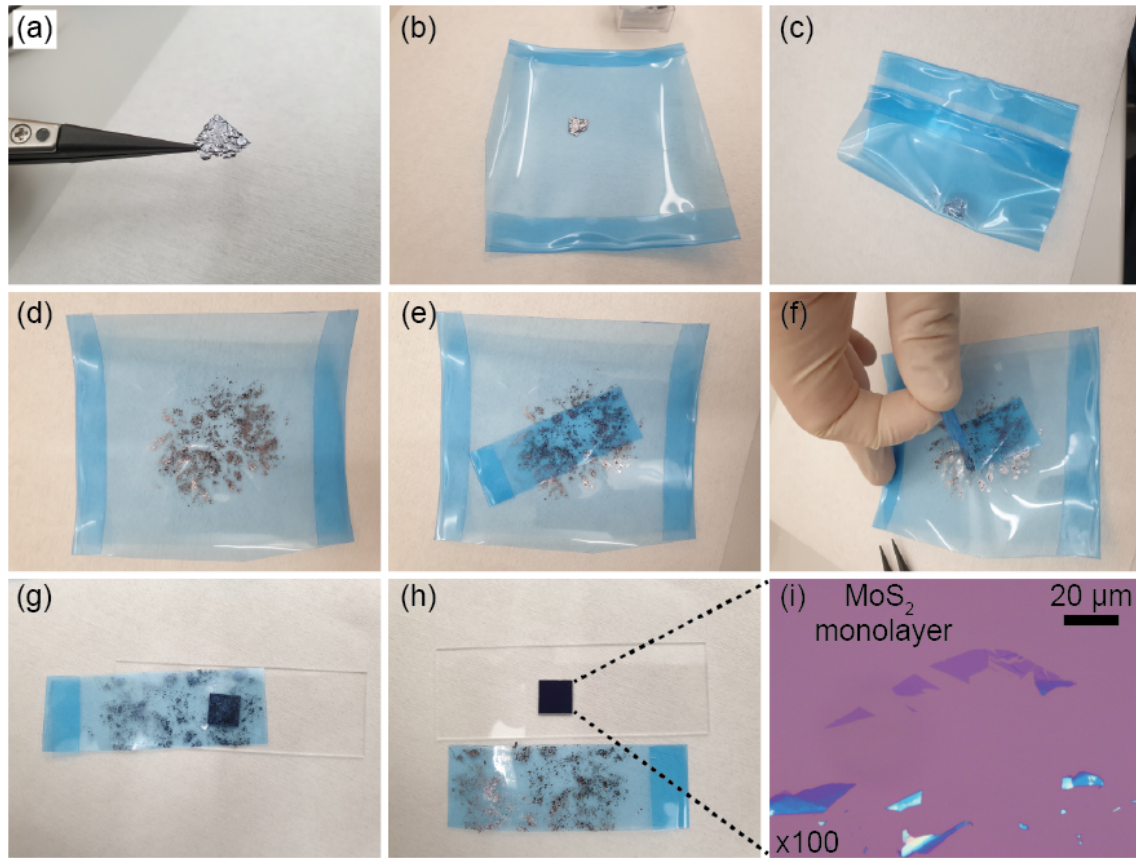


Figure 3.1. Mechanical exfoliation. (a) A bulk crystal (here: MoS_2) (b) is put on a master tape. After pressing the crystal onto the tape, the bulk crystal is removed such that some material is left on the tape. (c) The tape is folded several times to thin down the crystal (d) until the tape is covered with thin crystals. (e) The actual exfoliation tape is put on the master tape while slight pressure is applied. (f) The exfoliation tape is slowly peeled off and (g) pressed on top of a cleaned Si/SiO₂ (here: 285 nm SiO₂) chip with a mild force for a minute. (h) The tape is peeled off slowly from the chip. (i) Microscope image of a monolayer MoS_2 flake with an x100 objective.

A trained eye can spot TMD monolayers quickly while scanning the chip for suitable flakes. After a while of searching one can develop a feeling of which flakes are a monolayer and which are not. However, there are other methods to ensure one has found a monolayer. Using an atomic force microscope, the step height of a single layer can be measured. Another option is to measure the frequency difference between the out-of-plane A_{1g} and in the in-plane E_{2g}^1 Raman mode of the TMD flake (see Appendix C). The exact frequency difference is a fingerprint that can differentiate between mono- and few-layer TMDs [Lee10, Zha15]. Probably the most convenient way to confirm a monolayer is to utilise the fact that, unlike their few-layer and bulk counterparts, they are direct bandgap materials. The very bright luminescence of a TMD monolayer in response to a strong excitation can be imaged in the same optical microscope setup during flake searching. To this end, we

have expanded our microscope with a tungsten halogen lamp that can excite the exfoliated flakes. On excitation, a monolayer will glow very brightly as opposed to TMDs with larger thicknesses (see Appendix Figure B.1 for images of glowing flakes). The homogeneity of the luminescence in the monolayer region can be used as an indication of flake cleanness.

Tape residues are the main source of dirt on the chip and flake surface. It is important to select very clean flakes. Sometimes the residues are clearly visible in the optical microscope. However, especially for thicker flakes (e.g. hBN), residues, thickness steps, or cracks within the flakes are barely visible. These inhomogeneities can be detected using the dark field mode of our optical microscope.

Typically, there is a lot of back and forth between exfoliating and searching for good flakes. The exfoliation yield depends not only on a lot of the parameters used in the process but also on the used 2D materials. It is advised to constantly adjust parameters during exfoliation when the yield gets worse or is just not good enough. If, for example, the chip is generally quite dirty, then a new master tape might help. Other possibilities are to put the chip or the PDMS exfoliation tape into a UVO-cleaner (ultraviolet ozone). This step activates the surface and makes it more adhesive. Another option to increase the yield is to heat the chip with the exfoliation tape on top to 100 °C on a hot plate. Remove the chip with the tape from the heat and let it cool down before removing the tape. In the end, exfoliation is a flexible process that is constantly adapted through experience, intuition, and creativity.

3.2 Stacking van der Waals heterostructures

Different exfoliated 2D materials can be combined into a large van der Waals heterostructure with improved properties and the ability to control their properties electrically. However, for a high-quality sample, it is important to minimise the disorder in the system. The disorder can have many sources like polymer residues between the stacked flakes, strain, wrinkles, crystal defects, and trapped charges. There are two main ways to mitigate these effects: hBN encapsulation and the dry stacking technique.

Optical and electrical properties are strongly influenced by fluctuations of the surrounding dielectric environment [Raj19]. A uniform dielectric environment with no dangling bonds and atomically flat surfaces is achieved by encapsulating the active layers (e.g. graphene or TMDs) with two hBN flakes [Dea10]. hBN is an insulating 2D material and is used for nearly all high-quality samples. The hBN encapsulation improves the optical properties of TMDs significantly and is therefore essential [Cad17, Shr19].

The heterostructure quality can also be increased by using an appropriate stacking technique. A well-established way to stack is using the dry stacking technique [Zom14]. Here, a sticky polymer stamp is used to pick up flakes from the exfoliation chip. The stack is consequently assembled by picking up additional flakes starting from the top layer

to the bottom layer. Once the final layer is picked up the whole stack gets deposited onto a substrate. The main advantage of this method is that only the top layer of the stack will be in contact with the polymer. All other interfaces in the stack are therefore much cleaner which leads to an increased sample quality. All samples studied in this thesis are fabricated using an implementation of the dry stacking technique based on Reference [Zom14]. Subsection 3.2.1 describes the stamp fabrication followed by a description of the stacking setup in Subsection 3.2.2. The heterostructure design is discussed in Subsection 3.2.3. Finally, the stacking procedure is introduced in Subsection 3.2.4.

3.2.1 Polymer stamp

At the core of the dry stacking process is the stamp used for flake pick-up. The stamp consists of a piece of PDMS covered with a thin layer of poly-(bisphenol A-carbonate) (PC). Figure 3.2 shows and explains the step-by-step fabrication of the polymer stamp. The size of the PDMS base is roughly 5 by 5 mm with a thickness of 3 mm. The PDMS (184 silicone elastomer kit, Sylgard) is prepared by mixing the elastomer base and the elastomer curing agent with a weight ratio of 10:1 in a petri dish. The mix is rested for 30 min followed by a baking step at 65 °C for 55 min. The thin PC film is fabricated by uniformly sliding apart two glass slides with the liquid PC between them. For making the liquid PC (analytical standard pellets $M_W = 28.2$, Sigma-Aldrich), 0.8 g of the pellets are dissolved overnight in 20 ml chloroform under continuous stirring. The thin PC film is picked up by a doubled Scotch tape with a square window larger than the PDMS piece. Then, the tape with the PC window is carefully placed on top of the PDMS piece and fixed with additional Scotch tape. In order to avoid wrinkles in the PC film, some tension can be applied to the tape. The stamp is now finished and can be fixed to the stacking setup.

3.2.2 Stacking setup

The home-built stacking setup on top of a damped optical table with a mounted stamp is shown in Figure 3.3. The setup consists of two independent positioning stages, one for the sample and one for the stamp. The stamp can be positioned with an x-y-stage and the height is controlled by a z-stage. The sample is fixed on the sample holder by vacuum and can be moved laterally, rotated, and tilted using the respective stages. Additionally, the sample stage can be heated up to 190 °C using a home-built heater. The stacking process is imaged with an optical microscope (TH4-200, Olympus) equipped with three different objectives (x5, x10, and x20 magnification). The focus of the microscope is adjusted independently of the stamp and sample stage. The whole stacking process is done under ambient conditions and by hand - nothing in this setup is automated. There are, however, efforts in the 2D community to automate the stacking procedure to achieve a reproducible fabrication process [Lau22, Man22].

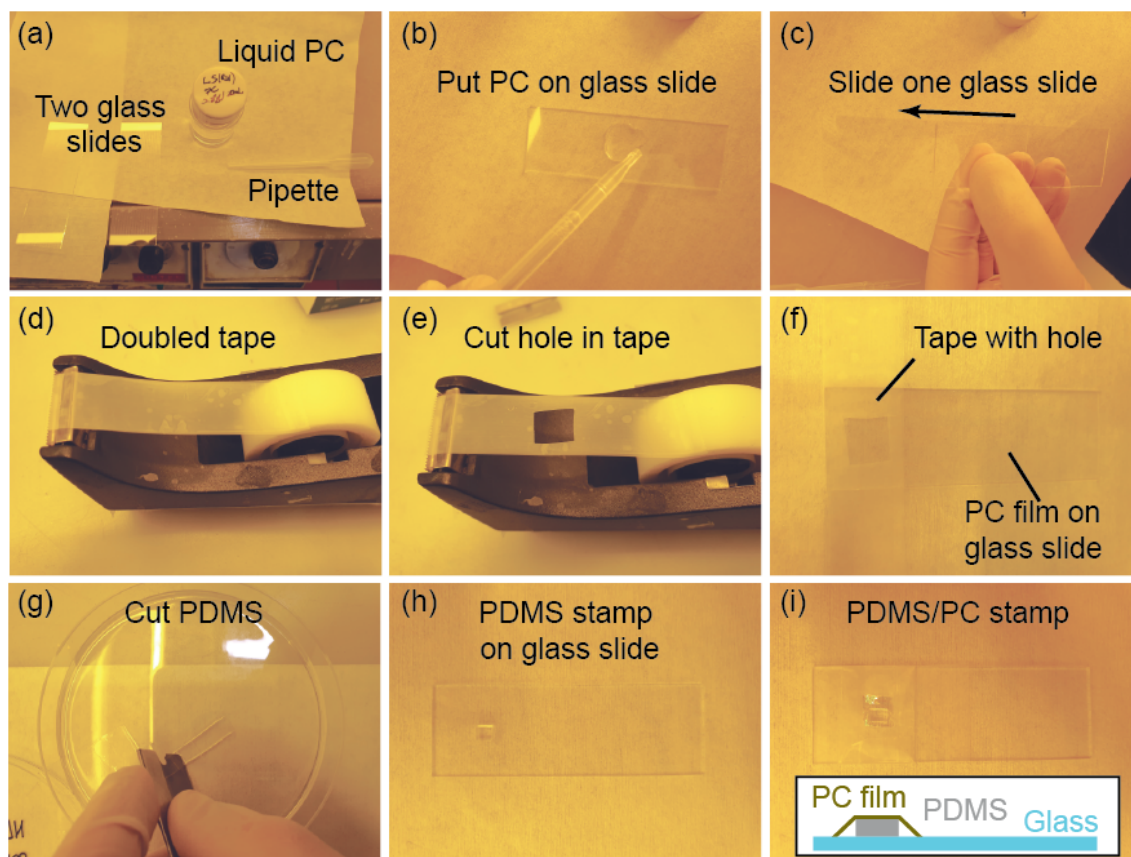


Figure 3.2. Preparation of the stamp used for flake pick-up. (a-c) Fabrication of a thin PC film. The glass slides are cleaned with acetone, IPA, and ethanol. Liquid PC dissolved in chloroform is put on a glass slide with a pipette. The second glass slide is pressed slightly on top of the first slide to create a uniformly distributed solution. One glass slide is uniformly slid to the side. This creates a thin PC film on each glass slide. The thickness of the film is important and depends on the amount of liquid, the pressure, and the sliding speed. (d) A commercial Scotch Magic tape is reinforced by doubling it. (e) A square hole is cut into the doubled tape. (f) The tape with the hole is put on top of the thin PC film. The tape is pressed slightly to ensure that the PC film sticks to it. The PC film is cut on the side of the tape. (g) A small piece of PDMS is cut and afterwards cleaned in acetone and IPA in an ultrasonic bath. Next, the thin side of the PDMS stamp is placed on a cleaned glass slide and put in a UVO cleaner for a couple of minutes. This not only cleans the PDMS surfaces but also makes the PDMS more sticky. (h) The PDMS is flipped so that the large surface is in contact with the glass slide. It should be ensured that the whole stamp sticks nicely to the glass. The stamp is put into the UVO cleaner for a few minutes. The tape with the hole is slowly peeled off from the PC-covered glass slide in (f). The thin film will usually stick to the tape. (i) The tape is carefully placed on the PDMS stamp such that the PC covers the whole PDMS. The PC film is fixed by using more Scotch tape around the edges of the glass slide. The inset in (i) shows a schematic side view of the finished stamp. As a final step, the stamp should be checked under a microscope to see if there are no wrinkles in the PC or big dirt pieces present.

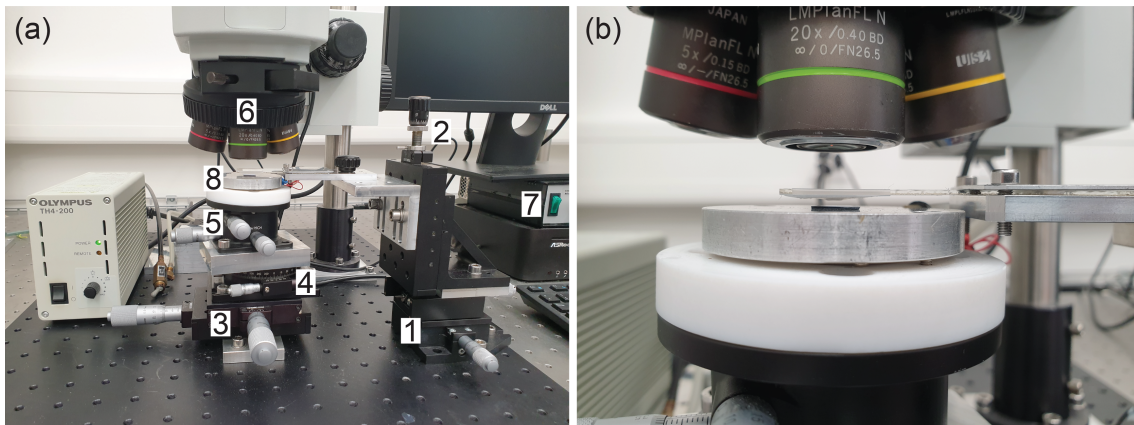


Figure 3.3. Stacking setup. (a) The setup is built on top of a damped optical table. The labelled components are 1 the stamp x-y-stage, 2 the stamp z-stage, 3 the sample x-y-stage, 4 the sample rotation stage, 5 the sample tilt stage, 6 the optical microscope, 7 the sample heater, and 8 the heatable sample stage. (b) Close-up of a mounted sample below the stamp. The sample is imaged by the microscope through the PDMS stamp. The substrate and the stamp are slightly tilted with respect to each other.

3.2.3 Planning a heterostructure

In addition to the hBN encapsulation of the TMD crystal, top and bottom few-layer graphene (FLG) flakes are often included in the final heterostructure design. Together with metal contacts or FLG contacts to the TMD, these layers act as electrodes which allow the control of the charge carrier density in the TMD layer and the external electric field perpendicular to the TMD layer. If only charge carrier control is desired the top FLG gate is usually left away and the bottom gate could either be a FLG flake or a p-doped silicon substrate. Often FLG gates, especially the bottom gate, are replaced by thin metal gates defined by electron-beam (e-beam) lithography. The electrostatic details of these device structures will be discussed in Section 3.4.

Ultimately, the stack will have five (six) different layers for monolayer/homobilayer (heterobilayer) samples.* The stacking of a working structure with this many layers is not a straightforward task especially considering the random sizes and shapes of the flakes after exfoliation. Usually, we exfoliate until we have several reasonably large and clean TMD layers and a few good-looking hBN and FLG flakes. Before starting the stacking process, the heterostructure is designed on a computer. For this, we insert microscope images of the flakes into Adobe Illustrator and outline their shape. Then, we begin to design the heterostructure by overlaying the different layers while considering the following things:

- The two FLG gates and the TMD layer(s) will be electrically contacted. Therefore one needs to place the insulating hBN such that there is no short-circuit formed

*The stack will have even more layers when one chooses to electrically contact the TMD layer with FLG instead of metal gates.

inside the stack.

- The metal contacts to the flakes should be planned. If a flake can not be contacted directly additional etching steps might need to be performed.
- Sometimes there are quite thick flakes next to the flake of interest. In this case, the contact line (the frontier line where the stamp touches the sample) should cross the thick flake after it crosses the TMD region (or not at all if possible).
- TMD monolayers are very hard to see through the stamp that already has picked up the top FLG and hBN. Flakes in the vicinity of the exfoliated TMD layer should also be marked as they can be used for alignment.
- If an exfoliated flake is close to the chip edge the pick-up direction becomes important. In this case, the contact line should approach the flake from the centre of the chip towards the edge.
- When stacking, things usually do not go according to plan and certain steps in the process might fail. Therefore, it is useful to exfoliate more flakes than needed. This allows an adjustment of the stacking plan.

3.2.4 Heterostructure stacking and contacting

Once a heterostructure is planned and the stamp is ready, the stacking procedure can start. The chip with the topmost flake is placed on the sample stage. After mounting the stamp, the flake is located with the optical microscope through the stamp and centred under a clean area of the PC film. There should be an angle of a few degrees between the stamp and the sample surface (see Figure 3.3b). The angle helps the pick-up process as the contact between stamp and chip happens at a smoother and slower pace. The stamp is lowered until there is contact with the chip. Upon lowering the stamp further, the contact line moves closer to the flake (see Figure 3.4a and Figure 3.4b). The whole flake is brought in contact with the stamp and the contact line is placed a few tens of micrometres past the flake. The sample stage is heated up to 90 °C which will cause the PDMS to expand. The stamp height is adjusted such that the contact line stays at the initial position. After 90 °C are reached, the heater is turned off. The PDMS will cool down and the contact line will slowly retract. The contact line will pass the flake and gently peel it off the substrate (see Figure 3.4c). The adhesion of the flake to the PC is larger than to the Si/SiO₂ substrate. Once the contact line stops moving and the flake is already picked up, the stamp can then be manually lifted.

This pick-up process is then repeated for the subsequent layers of the heterostructure. The subsequent flakes stick better to the already picked-up flake(s) than to Si/SiO₂ and

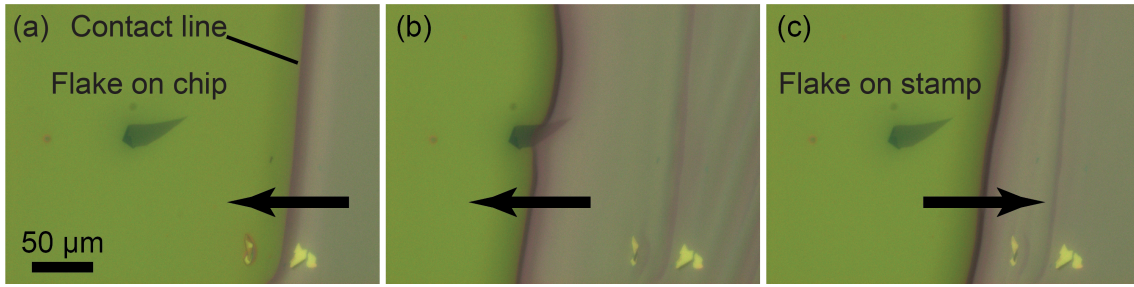


Figure 3.4. Flake pick-up with a stamp. (a) The stamp is lowered and brought into contact with the chip. Further lowering pushes the contact line towards the flake. (b) The contact line is pushed past the flake so that the whole flake is in contact with the PC. The sample stage is heated to 90 °C. The PDMS will expand on heating pushing the contact line further. This movement is counteracted by manually adjusting the stamp height such that the contact line stays at the initial position. After the stage reached 90 °C the heater is turned off. On cooling down, the PDMS will shrink slowly. (c) The contact line slowly retracts lifting the flake in the process. All images are taken with an x20 microscope objective.

are therefore lifted off. For each layer, it is important to align the flake according to the stacking plan. The outline of each flake is drawn in the software of the microscope for an easier check of alignment. If a picked-up flake is slightly shifted or has a different angle the stacking plan should be adjusted accordingly. Upon lowering the stamp for the subsequent flakes, always switch the microscope focus between the flake(s) on the stamp and the flake on the chip. Check their alignment and adjust the two stages accordingly. Slowly go into contact and repeat the steps described above. If the contact line is close to the flake and the alignment is not optimal, lift the stamp out of contact again and realign accordingly. The more flakes are already picked-up with the stamp, the harder the alignment process will be. Sometimes the alignment process can last for several tens of minutes. When stacking, it is therefore important to be physically prepared with good mental focus and concentration.

The stacking is finished once the last layer is picked-up with the stamp. Now, the heterostructure is placed on a clean Si/SiO₂ substrate with pre-patterned alignment markers used for e-beam lithography. For the deposition, the angle between stamp and substrate is decreased. Once the stack is in contact with the chip, the stamp is lowered even further until the whole substrate is covered. The sample stage is heated to 190 °C for several minutes. At these high temperatures, the PC will melt. By slowly lifting the stamp, the PC will detach from the PDMS and stay on the substrate covering the stack. Afterwards, the final substrate is heated for 10 minutes at 200 °C on a hotplate to relax potential stress in the PC film. The molten PC film is then dissolved in chloroform overnight. The chloroform is removed in IPA and the chip is blow-dried with nitrogen. In case some layers are electrically shorted or FLG gates are buried below hBN, reactive ion etching (RIE) can be used (see Appendix A).

The FLG gates and the active layer(s) are contacted from the top by evaporated metal gates of either Ti (5 nm)/Au (45 nm) or Cr (5 nm)/Au (45 nm). For a high stack, the Au thickness should be adjusted to be larger than the stack height. The gates are defined by e-beam lithography. The detailed recipes can be found in Appendix A. After deposition of the gates, the sample is annealed at 150 °C in a vacuum for at least twelve hours. Thermal annealing tends to decrease the contact resistance and can help to increase the heterostructure quality. For the device electrostatics, we determine the top and bottom hBN thicknesses using atomic force microscopy (AFM). As the last step, the sample is glued and wire-bonded (Au- or Al-wire) onto a chip carrier.

To make the stacking easier and more fault tolerant we sometimes fabricate a stack in two separate parts instead of picking up the whole stack in one go. The bottom part consists of the bottom FLG gate and the bottom hBN. On top of these two layers, the metal contacts to the TMD layers can be conveniently fabricated using e-beam lithography and subsequent metal deposition. The metal contacts consist of Ti (10 nm)/Au (20 nm) based on a recipe developed in Reference [Pis18]. The top part starts by picking up the top gate and ends with the active layer(s). The stacking is done in the same way as described above. When both halves are finished, the top part is deposited onto the bottom part after careful alignment. An advantage of this method is that if one part of the stack fails during fabrication, not the whole sample is lost. A disadvantage is that only the top interface of the TMD layer will be clean as the top surface of the bottom hBN has been in contact with the polymer stamp. However, when stacking a heterobilayer sample, the interface between the two monolayers is clean, which is very important for the interlayer exciton formation.

3.3 Heterobilayer alignment using second harmonic generation

The stacking angle of a heterobilayer has a big impact on its properties, as discussed in Section 2.6. Therefore, precise control of the stacking angle is very important. Usually, the two TMD monolayers are aligned such that their crystallographic axes are at an angle of modulo 60°; the K valleys are aligned in momentum space. If a certain moiré period is desired then the angle can be adjusted accordingly. For the crystal alignment, it is important to determine the crystallographic axes. During exfoliation, the flakes tend to break along the main crystal directions. This means that their edges often have an angle of modulo 60°. One can then align the edges of two monolayers and stack them together. This method is very crude and sometimes the edges have contradicting angles or no clear edges. A much better and more reliable method to determine the crystal directions is to use second harmonic generation (SHG).

SHG is a nonlinear optical process where two photons with angular frequency ω are

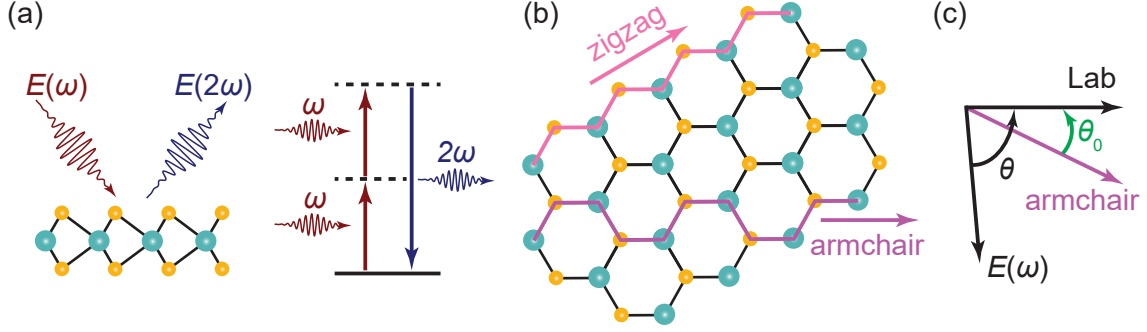


Figure 3.5. (a) Schematic of the second harmonic generation (SHG) process. The TMD layer is excited by a laser with frequency ω . Two of these photons are converted into one photon with doubled frequency 2ω . For TMD monolayers, the intensity of the SHG signal is dependent on the crystal orientation relative to the linear polarisation axis of the laser. (b) Illustration of the armchair and zigzag crystal directions in a monolayer TMD. (c) Sketch of the angle relations of laser and armchair axis in our SHG setup. The Lab(oratory) axis is defined as the 0° axis in the setup. The linear laser polarisation is rotated by a half-wave plate with an angle of θ . The armchair axis of the monolayer is fixed at an angle θ_0 with respect to the Lab axis. In the measurement, θ is varied while θ_0 stays constant.

converted into one photon with angular frequency 2ω (see Figure 3.5a). In other words, SHG doubles the frequency of the photons. For a pulsed and linearly polarised laser excitation, the SHG intensity depends on the angle between the material's crystal directions and the laser polarisation [Li13]. Figure 3.5b sketches the armchair and zigzag crystal directions in a monolayer TMD. The linearly co- and cross-polarised SHG intensity, I_{\parallel} and I_{\perp} , can be written as [Li13]

$$I_{\parallel} = I_0 \cos^2(3\phi) \quad \text{and} \quad I_{\perp} = I_0 \sin^2(3\phi), \quad (3.1)$$

where ϕ is the angle between the armchair axis and the linear laser polarisation. Therefore, we can determine the crystallographic axes for different TMD monolayers using SHG and stack them accordingly.

We measure the SHG signal of crystals at room temperature using a home-built confocal microscope setup. A detailed description of our SHG setup can be found in Reference [Lei22]. The sample is excited by a tunable, mode-locked titanium sapphire (Mira 900-D, Coherent GmbH) laser with femtosecond pulses (~ 150 fs) at a repetition rate of 76 MHz. Dispersion effects in a long optical fibre stretch the pulse to 36 ps [Lei18]. Typically, we use an excitation wavelength of roughly 810 nm with a power of several mW. The linear polarisation of the laser is turned by a $\lambda/2$ waveplate mounted on a computer-controlled stepper motor rotation stage; the sample orientation stays fixed. The light is focused onto the sample with an x40 microscope objective (NA = 0.65). Only the co-polarised SHG signal I_{\parallel} at 405 nm is detected in our setup. Additionally, our setup can image the flake using a CCD camera under red LED excitation. This is important to correlate the armchair axis with

the flake image. We define a Lab(oratory) axis as the 0° axis in the setup. The laser angle θ is varied in the measurement while the armchair axis angle θ_0 stays constant. The angle relations are sketched in Figure 3.5c. Using these angles, we can rewrite I_{\parallel} from Equation 3.1 as

$$I_{\parallel} = I_0 \cos^2 [3(\theta - \theta_0)] . \quad (3.2)$$

A typical SHG measurement is shown in Figure 3.6a. The data points represent the integrated SHG intensity I_{\parallel} of monolayer MoSe₂ (red) or monolayer WSe₂ (blue). The two data sets are fitted by Equation 3.2 yielding an angle between armchair and Lab axis of $\theta_{\text{Mo}} = -16.5^\circ$ and $\theta_{\text{W}} = -26.5^\circ$. The six-fold crystal symmetry can be clearly observed where a maximum (minimum) in the “flower” plot occurs along the armchair (zigzag) axis of the monolayer.* Then, the orientation of the monolayer inside the TMD setup is imaged as shown in Figure 3.6b. The two monolayers can then be aligned for stacking by twisting one of them to align their armchair axes. Figure 3.6c illustrates the rotation of monolayer WSe₂ by $(\theta_{\text{Mo}} - \theta_{\text{W}}) + i \cdot 60^\circ$. The rotation angle is chosen with a suitable value of i either to maximise the overlap region or to leave enough space to contact each monolayer with electrical contacts. Hence, this step is incorporated into making the heterostructure stacking plan as described in Subsection 3.2.3. The two monolayers shown in Figure 3.6b are the ones used in the heterobilayer device studied in this thesis (see Chapter 4 and Appendix B). The accuracy of the angle determination is $\pm 0.2^\circ$ in our setup [Lei18]. The manual rotation and alignment of the two layers during stacking is probably more inaccurate than 0.2° and therefore the main source of twist angle misalignment.

It is important to note that only the six-fold symmetry can be determined by SHG. Therefore, a 0° (R-stacking) heterobilayer can not be distinguished from a 60° (H-stacking) heterobilayer during the fabrication process. In principle, measuring SHG on the finished heterobilayer sample enables the determination of the stacking orientation. Depending on the stacking type, the SHG signal in the bilayer region is suppressed or enhanced as compared to the SHG signal in the monolayer regions [Hsu14]. A more reliable way to determine the stacking orientation is to measure the optical response of the heterobilayer at low temperatures. The optical selection rules and photoluminescence signal of interlayer excitons are very different for R- and H-stacked heterobilayers as discussed in Section 2.6 and Chapter 4.

3.4 Heterostructure electrostatics

We study optoelectronic devices in either the single-gate or the dual-gate configuration (see Figure 3.7). Voltages applied to the gates allow the tuning of the charge carrier density n

*The angle-resolved SHG intensity is very symmetric in Figure 3.6a indicating zero strain. Strained monolayers would exhibit a strongly modified SHG intensity along one or more crystal directions [Men19].

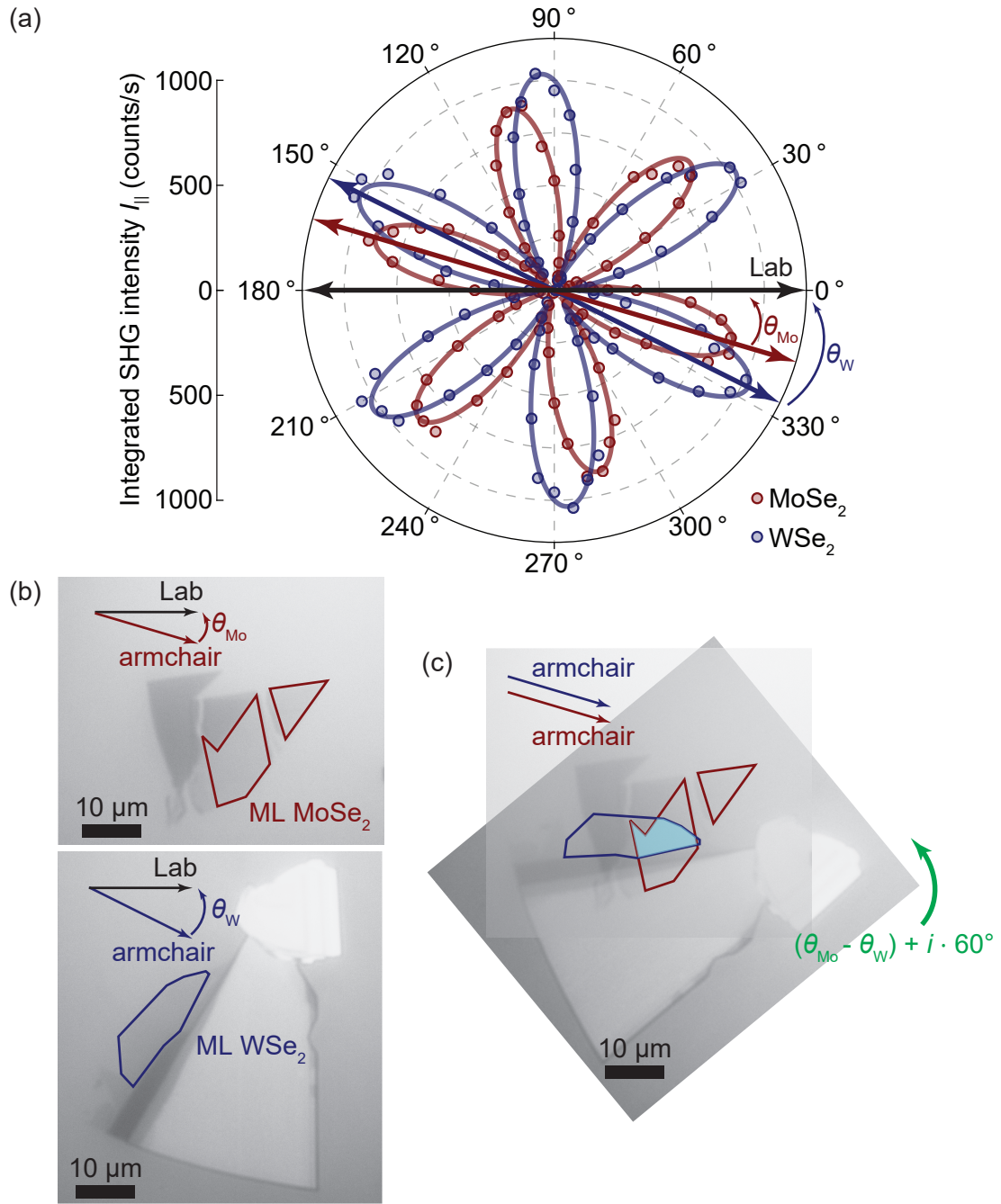


Figure 3.6. (a) Integrated SHG intensity $I_{||}$ co-polarised to the laser polarisation as a function of angle θ for monolayer MoSe₂ (red) and monolayer WSe₂ (blue). A six-fold symmetry is observed where the maxima are located along the armchair axes and the minima along the zigzag axes of the crystal. The SHG intensity is fitted by equation 3.2 and plotted as the coloured lines. From the fit we find $\theta_{\text{Mo}} = -16.5^\circ$ and $\theta_{\text{W}} = -26.5^\circ$. (b) Orientation of the two monolayers in the SHG setup. The image is taken with a CCD camera under red LED excitation of the sample. The two monolayer regions are outlined by the coloured polygons. (c) Rotation of monolayer WSe₂ with respect to MoSe₂ in order to align the armchair axes of both layers and to maximise overlap region. The heterobilayer region is shaded in light blue.

in the TMD layer for a single-gate device. For dual-gating, the electric field perpendicular to the heterostructure F_z can be controlled in addition to n . The two hBN layers around the TMD layer not only increase the sample quality but also act as a dielectric spacer. hBN has a breakdown voltage of roughly 1.2 V/nm [Hat15]. In experiments, we limit the applied voltages to 0.5 V/nm which usually shows no leakage current. For many measurements, we want to show the dependence of device properties on n and/or F_z . The calculation of n and F_z from the applied gate voltage(s) is modelled electrostatically and explained in the following.

3.4.1 Single-gate device

The electrostatics of a single-gate device can be described with a plate capacitor model [Roc19]. One electrode is the TMD layer while the other electrode is either (i) a p-doped Si or (ii) a FLG back gate as sketched in Figure 3.7a. In the simple model, the charge carrier density n can be calculated as

$$n = \frac{CV_G}{e}, \quad (3.3)$$

where C is the total capacitance per unit area, e is the electron charge, and V_G is the voltage applied to either of the electrodes. For a p-doped Si back gate, the capacitance is calculated by putting the hBN and SiO₂ capacitors in series:

$$C = \left(\frac{d_{\text{hBN}}}{\epsilon_0 \epsilon_{\text{hBN}}} + \frac{d_{\text{SiO}_2}}{\epsilon_0 \epsilon_{\text{SiO}_2}} \right)^{-1}, \quad (3.4)$$

where d_{hBN} and d_{SiO_2} are the thicknesses and $\epsilon_{\text{hBN}} = 3.76$ [Lat18] and $\epsilon_{\text{SiO}_2} = 3.9$ are the dielectric constants of hBN and SiO₂, respectively. ϵ_0 is the vacuum permittivity. For case (ii) with a FLG back gate, the device capacitance per unit area is simply

$$C = \frac{\epsilon_0 \epsilon_{\text{hBN}}}{d_{\text{hBN}}}. \quad (3.5)$$

3.4.2 Dual-gate device *

In comparison to only using one gate, the dual-gate device is a much more powerful system. Applying voltages at certain conditions to the top and bottom FLG gates allows independent control of charge carrier density and electric field. This is especially important in bilayer systems where one wants to study the excitonic transitions as a function of an electric field while keeping the charge carrier concentration close to zero.

We consider the electrostatic model schematically depicted in Figure 3.7b. The TMD layer(s) are modelled as two grounded conducting plates encapsulated by two insulating

*This section is partially adapted from the Supplement of Reference [Lei20].

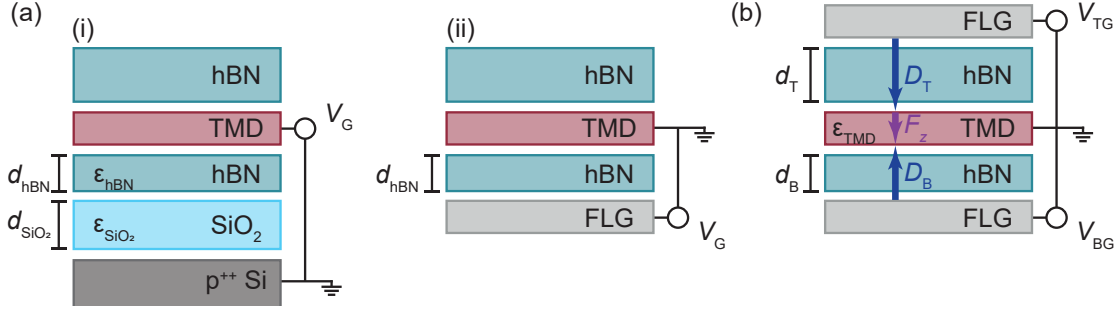


Figure 3.7. Heterostructure device schematics studied within this thesis. (a) Single-gate device with (i) p-doped Si or (ii) FLG as a back gate. On sweeping the gate voltage V_G of either gate while grounding the other gate, the charge carrier density in the TMD layer can be controlled. (b) Dual-gate device where voltages applied to the top and bottom FLG gates allow the independent control of carrier concentration and electric field F_z . $D_{\text{T,B}}$ are the top and bottom displacement fields. The thicknesses d and dielectric constants ϵ of the important layers are shown. This figure is adapted from Reference [Lei22].

hBN layers. Upon electrical gating, top and bottom displacement fields, D_T and D_B , respectively, lead to a net carrier doping n of the TMD, as well as an imposed interlayer displacement field D .

In our experiment, the displacement fields D_T and D_B are tuned independently by the top and bottom gate voltages, through the relations

$$D_T = C_T(V_{\text{TG}} - V_{\text{TG}}^0) \quad (3.6)$$

$$\text{and } D_B = -C_B(V_{\text{BG}} - V_{\text{BG}}^0). \quad (3.7)$$

Here, V_{TG} and V_{BG} are the voltages applied to the top and bottom gates, and V^0 is the effective offset voltage due to initial environmental carrier doping. Note, that the sample can start to be doped at an arbitrary combination of gate voltages. Hence, the values of V_{BG}^0 and V_{TG}^0 also depend on each other. To describe the capacitive system, we introduce the relevant geometric top and bottom gate capacitances per unit area as

$$C_T = \frac{\epsilon_0 \epsilon_{\text{hBN}}}{d_T} \quad \text{and} \quad C_B = \frac{\epsilon_0 \epsilon_{\text{hBN}}}{d_B}, \quad (3.8)$$

with d_T and d_B being the thicknesses of the top and bottom hBN layers as determined by AFM measurements.

Using the plate capacitor model, we can define the total applied electron density as

$$\begin{aligned} n &= n_T + n_B \\ &= \frac{1}{e} \left[C_T(V_{\text{TG}} - V_{\text{TG}}^0) + C_B(V_{\text{BG}} - V_{\text{BG}}^0) \right], \end{aligned} \quad (3.9)$$

where n_T and n_B are the carrier densities in the top and bottom layers. From Equation 3.8 and 3.9, the net carrier doping can be calculated to be

$$n = \frac{1}{e} \frac{\epsilon_0 \epsilon_{\text{hBN}}}{d_T} \left[(V_{\text{TG}} - V_{\text{TG}}^0) + \frac{d_T}{d_B} (V_{\text{BG}} - V_{\text{BG}}^0) \right]. \quad (3.10)$$

Now, we evaluate quantitatively the electric displacement in the system, assuming that there are no charges accumulated at the interfaces

$$\begin{aligned} D &= \frac{1}{2} \left[C_T (V_{\text{TG}} - V_{\text{TG}}^0) - C_B (V_{\text{BG}} - V_{\text{BG}}^0) \right] \\ &= \frac{1}{2} \epsilon_0 \epsilon_{\text{hBN}} \left[\frac{(V_{\text{TG}} - V_{\text{TG}}^0)}{d_T} - \frac{(V_{\text{BG}} - V_{\text{BG}}^0)}{d_B} \right]. \end{aligned} \quad (3.11)$$

The electric field across the TMD layer(s) can then be calculated to be

$$F_z = \frac{1}{2} \frac{\epsilon_{\text{hBN}}}{\epsilon_{\text{TMD}} d_B} \left[(V_{\text{TG}} - V_{\text{TG}}^0) - \frac{d_T}{d_B} (V_{\text{BG}} - V_{\text{BG}}^0) \right], \quad (3.12)$$

where we used $D = \epsilon_0 \epsilon_{\text{TMD}} F_z$, with ϵ_{TMD} being the dielectric constant of the TMD layer(s). An overview of the values for several ϵ_{TMD} can be found in Reference [Lat18]. For this thesis, we use a dielectric constant of 6.8 for homobilayer MoS₂ [Lat18] and 7.2 for the MoSe₂/WSe₂ heterobilayer [Kim15].

After comparing Equation 3.12 and 3.10 we find the condition

$$(V_{\text{TG}} - V_{\text{TG}}^0) = -\frac{d_T}{d_B} (V_{\text{BG}} - V_{\text{BG}}^0) = -\alpha (V_{\text{BG}} - V_{\text{BG}}^0), \quad (3.13)$$

where we can tune the electric field without changing the doping in the TMD. We use this gate voltage combination to study the optical response of a TMD as a function of purely tuning the electric field.

Similarly, the charge carrier density can be tuned significantly when using the same polarity for both voltages in Equation 3.13. On doping the sample, the electrostatic considerations for a bilayer TMD sample become more complicated than what has been discussed so far. The electric field across the bilayer then also depends on the charge carrier density in each layer [Pis19, Jau19]. This means that on sweeping the charge carrier density, the electric field will also be influenced. This makes the interpretation of experiments more difficult as one can not simply disentangle the effect of either electrical tuning knob.

3.5 Optical characterisation techniques

All van der Waals heterostructures studied in this thesis are characterised via optical spectroscopy. Optical spectroscopy is a powerful and non-invasive tool to study the

excitonic and even electronic properties of 2D semiconductors. Typically, the sample is excited by light from a laser or an LED and the sample response or the reflected light is collected and analysed. In our measurements, we focus on the two most widely used techniques: Absorption (or more specific white-light reflection) and photoluminescence (PL) spectroscopy. Other techniques would include SHG or Raman spectroscopy which we mainly use (if at all) during sample fabrication. A good overview of the different optical spectroscopy techniques and their application to 2D materials can be found in Reference [Shr21].

This section introduces the concepts of the absorption measurements in Subsection 3.5.1. It is shown how the measured reflectivity can be related to the absorption and how a good reference spectrum can be chosen. The basic concepts of PL spectroscopy and how it differs from absorption will be discussed in Subsection 3.5.2.

3.5.1 Absorption spectroscopy

In an absorption measurement, we are interested in the energies where a sample can absorb a photon and in how strong the resulting light-matter interaction is. In TMDs, the optical response is dominated by excitonic resonances. This means that absorption spectroscopy probes the intrinsic excitonic resonances of the material. Experimentally, the absorption is not probed directly but most of the time inferred from measuring the reflectivity.

Figure 3.8a shows a sketch of an absorption measurement. A broadband light source (white-light LED or supercontinuum laser) is used to illuminate the sample. If the light is on resonance with an optically-allowed excitonic transition the photon is absorbed. The absorption strength is governed by the oscillator strength which is a measure of the probability of an excitonic transition. Typically, van der Waals heterostructures are placed on Si/SiO₂ substrates which are not transparent and therefore reflect most of the light. In a simplified picture, the reflected light R from the sample is then missing the photons absorbed in the TMD layer(s) (red curve in Figure 3.8a). This allows for example to measure the excitonic Rydberg series [Che14]. In this simple case, we can write the relative relation between R and the imaginary part of the optical susceptibility $\text{Im}(\chi)$, a measure for the absorption, as

$$\text{Im}(\chi) \propto \frac{R - R_0}{R_0} = \frac{\Delta R}{R_0}, \quad (3.14)$$

where R_0 is the sample reference spectrum without the response from the TMD layer(s). $\frac{\Delta R}{R_0}$ is called the differential reflectivity.

Unfortunately, thin-film interferences at the interfaces inside the heterostructure can lead to a modification of the measured differential reflectivity. These interferences introduce a phase shift $\alpha(\omega)$ that depends on the angular frequency ω [Bac17]. To first order within our spectral range of interest, $\alpha(\omega) = \alpha$ is assumed to be frequency-independent. This

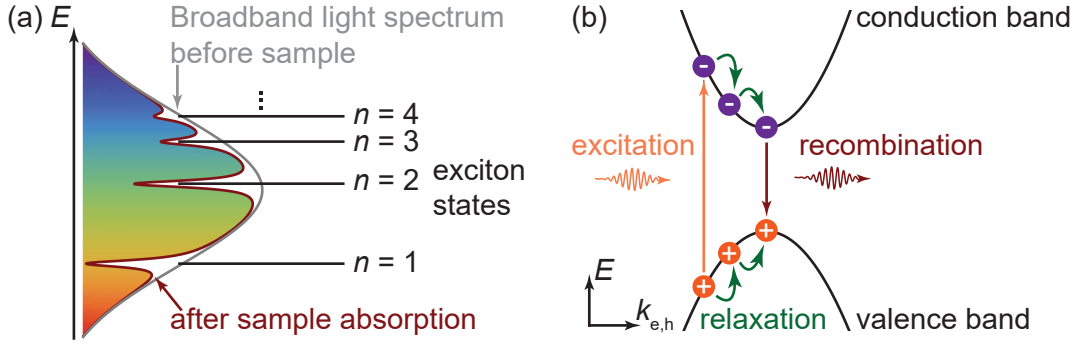


Figure 3.8. Sketches of (a) absorption and (b) photoluminescence (PL) measurements. (a) Absorption: A broadband light source illuminates the sample with an emission profile as sketched by the grey curve. At the resonance energy of the excitonic states, photons from the light source are absorbed. For TMDs, one typically measures the reflected signal R from the sample as indicated by the red curve. The absorption, described by the imaginary part of the optical susceptibility $\text{Im}(\chi)$, is determined from the differential reflectivity $(R - R_0)/R_0 = \Delta R/R_0$ using a Kramers-Kronig relation. R_0 is a reference reflectivity spectrum of the substrate. (b) PL: A laser excitation with an energy larger than the bandgap promotes an electron from the valence band into the conduction band leaving behind a hole in the valence band. Then, the bound electron-hole pair relaxes towards the lowest energy state where they recombine and emit a photon.

phase shift influences the actually measured absorption spectrum $\text{Im}(\tilde{\chi})$ as

$$\text{Im}(\tilde{\chi}) = e^{-i\alpha} \text{Im}(\chi) \propto \frac{\Delta R}{R_0}. \quad (3.15)$$

Following the detailed derivation in the Supplement of Reference [Roc19], one can relate $\text{Im}(\chi)$ of a TMD in a heterostructure to the experimentally measured differential reflectivity using the Kramers-Kronig relation:

$$\text{Im}(\chi) \propto \sin(\alpha) \frac{2}{\pi} \mathcal{P} \int_0^{\infty} \frac{\omega' \frac{\Delta R}{R_0}(\omega')}{\omega'^2 - \omega^2} d\omega' + \cos(\alpha) \frac{\Delta R}{R_0}. \quad (3.16)$$

The integral is calculated on the program Wolfram Mathematica using the trapezoidal rule where the integration range and step size are given by the resolution of the spectrometer. For a good choice of α , the differential reflectivity can then be transformed into $\text{Im}(\chi)$ where the resonances have a Lorentzian/Gaussian lineshape as shown in Figure 3.9b.

In order to obtain a good differential reflectivity spectrum, the choice of reference reflectivity R_0 is crucial. Reflections inside the optical setup lead to small interference patterns in the measured reflectivity. Ideally, these interferences should cancel out in the differential reflectivity. There are several ways to obtain a good R_0 . The most commonly used way is to detect the light reflected from a spot on the sample without the TMD layer(s). However, a heterostructure is very complex and layer thicknesses may change

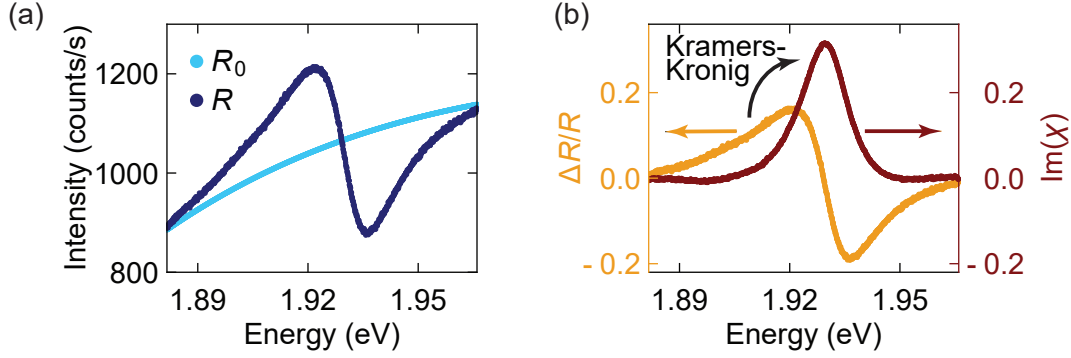


Figure 3.9. (a) Raw reflection spectrum R and reference spectrum R_0 around the A-exciton resonance in homobilayer MoS_2 . The spectra are recorded at $T = 4.2$ K and at the same sample position. R_0 is an interpolation of the raw reflection spectrum at a high electron concentration. (b) The differential reflectivity $\frac{\Delta R}{R_0}$ (orange) can be transformed into the imaginary part of the susceptibility $\text{Im}(\chi)$ using the Kramer-Kronig relation shown in equation 3.16. The perfect Lorentzian lineshape of the excitonic resonance in $\text{Im}(\chi)$ is achieved by accommodating thin-film interferences by using a phase factor of $\alpha = 1.54$ rad.

when moving to another sample position which would lower the quality of R_0 . A different thickness changes the optical path length slightly and the interference patterns do not cancel each other out. Another way is to acquire R_0 from the same spot as R which removes any interference pattern effects. In this case, one needs to get rid of the excitonic resonances in the reflected spectrum. This can be done in several ways. Our preferred method is to use/interpolate the raw reflectivity spectrum at a very high electron density (see Figure 3.9a). At these high doping levels, the oscillator strength is spread over a large spectral range and therefore negligible [Bac17]. Another possibility is to use several reflectivity spectra where the electric field or the charge carrier density is swept. If the spectra change significantly in the measurement, then their median can be used as R_0 . The last method is to use two spectra at a different F_z or n that each contains only one resonance at different energies. These spectra can then be combined into one R_0 spectrum.

The thin-film interferences can have a big impact on the optical properties of TMDs. They can influence the differential reflectivity shape, the amplitude, and the linewidth of excitonic resonances. Details on the interferences and how the differential reflectivity can be fitted just with the phase factor α will be discussed in Section 3.6.

Excitonic resonances can be modelled classically as optical dipoles where either the mass or the charge is oscillating. Using this model, the excitonic absorption can be modelled classically. The model for the absorption spectra of two excitons coupled together will be derived and discussed in Chapter 6.

3.5.2 Photoluminescence spectroscopy

In a PL measurement, the sample is excited by a photon with an energy larger than the bandgap which lifts an electron from the valence band into the conduction band. At the same time, a hole is created in the valence band. Due to the Coulomb interaction between electron and hole an exciton is formed. Then, the created excitons relax towards lower energies, for example through phonon emission. The process concludes with the recombination of the exciton by photon emission at an energy smaller than the excitation energy. The excitonic life cycle in a PL measurement is sketched in Figure 3.8b.

PL and absorption measurements can give very different information about the studied system. In absorption, the measured spectra are dominated by excitonic states with a high oscillator strength. This is not necessarily the case in a PL measurement. Here, states are dominating, where a lot of excitons have relaxed into [Shr21]. These are mostly states at lower (the lowest) energy which do not necessarily possess a high oscillator strength as is for example the case for type-II heterobilayers. While it is still possible to measure the high oscillator strength intralayer excitons in PL, they are much weaker than the low oscillator strength interlayer excitons (IX) at a much lower energy. Contrary, in an absorption measurement, these IX are very difficult to observe [Fö19].* In a PL process, there is a certain amount of relaxation time passing between the excitation and emission. During this time, excitons can for example relax in complex pathways, they can diffuse, or be trapped in defects or strained areas. These effects can not be easily modelled. Therefore, PL spectra are usually more complicated to interpret than absorption spectra.

3.6 Thin-film interference effects in heterostructures

Interference effects in a multilayered van der Waals heterostructure can lead to a big change in the light reflected/emitted from the sample. In Subsection 3.5.1 we introduced a phase factor α to account for these changes. In this section, the origin of this phase factor will be explained in more detail. Additionally, it will be shown how α can change the differential reflectivity lineshape between a Lorentzian and a dispersive shape. Lastly, the influence of the interferences on the excitonic linewidth and amplitude will be discussed.

In a simple picture, we have two reflectors inside a heterostructure: A TMD mirror at the excitonic resonance and a broadband reflector that is the superlattice that embeds the TMD. The reflections from the TMD and superlattice will interfere, which leads to a modification of the excitonic properties inside the TMD layer [Ivc05, Scu18]. The modified properties depend on the phase shift between the two reflected waves [Kar03], which is the factor α that we have already introduced. The value of α depends on the thickness and

*IX in a MoSe₂/WSe₂ heterobilayer have been detected in absorption using an electromodulation technique [Bar22]. The static IX dipole moment couples to an alternating electric field which periodically changes the IX energy and thus also the dielectric function.

refractive index of each layer in the superlattice. In a typical 2D heterostructure, these are the FLG, hBN, and SiO₂ layers. The SiO₂ layer thickness is fixed by the chip that is stacked upon. The FLG layers are usually quite thin so their influence on α is rather small and therefore neglected in the following. This leaves only the top and bottom hBN layers. By choosing the thickness of each hBN layer before stacking we can set α such that we achieve the desired excitonic properties.

The differential reflectivity of a TMD layer embedded in a heterostructure takes the following form [Smo19]:

$$\frac{\Delta R}{R_0} = A \cos(\alpha) \frac{\frac{\gamma}{2}}{(\omega - \omega_0)^2 + \frac{\gamma^2}{4}} + A \sin(\alpha) \frac{\omega_0 - \omega}{(\omega - \omega_0)^2 + \frac{\gamma^2}{4}} + C, \quad (3.17)$$

where ω_0 is the frequency, A is the amplitude, and γ is the linewidth of the excitonic resonance; C is a constant background. This lineshape is called a dispersive Lorentzian. For $\alpha = \pi$, a regular Lorentzian lineshape is recovered. By using α as an additional fitting parameter the experimentally measured differential reflectivity spectra can be fitted very well with Equation 3.17 [Bac18, Smo19].

Selecting certain hBN thicknesses before stacking can be important to control the properties of excitonic resonances. For example, some excitonic resonances might not be visible at all for one hBN thickness combination while they are perfectly visible for another combination [Rob18, Shr21]. Therefore, it is important to calculate the differential reflectivity before stacking. We calculate $\frac{\Delta R}{R_0}$ of a multilayer structure using a transfer-matrix method developed in Reference [Rob18]. The spectra are calculated with a script written by M. A. Semina and M. M. Glazov (Ioffe Institute, St. Petersburg). We consider a multilayer system of hBN/TMD/hBN/SiO₂ (285 nm)/Si from top to bottom. The TMD reflection coefficient r for a single excitonic resonance is given by

$$r = \frac{i\Gamma_0}{\omega - \omega_0 - i(\Gamma_0 + \Gamma)}, \quad (3.18)$$

with Γ_0 and Γ being the radiative and nonradiative dampings of the resonance. In the following, we will try to optimise the reflectivity of an excitonic resonance at $\omega_0 = 1.9$ eV with $\Gamma_0 = \Gamma = 1$ meV. The excitonic resonance should have a Lorentzian lineshape and a very small linewidth.

First, the differential reflectivity spectra for several top and bottom hBN thicknesses are calculated according to the transfer-matrix method. Then, one could manually check all the combinations and search for the excitonic resonance that looks best. Another option is to fit the calculated spectra using Equation 3.17 with $\frac{\gamma}{2} = \Gamma_0 + \Gamma$ where only Γ_0 is a fitting parameter; Γ is set to a constant value. Figure 3.10 shows the fit results for modelling the

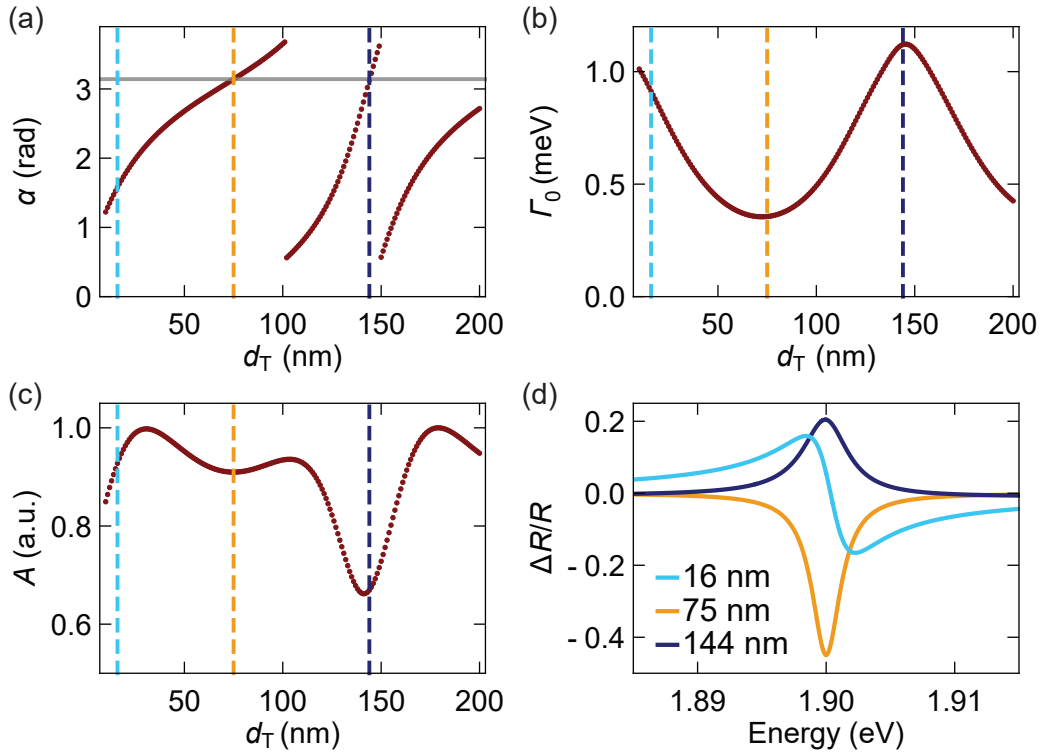


Figure 3.10. Fitted (a) phase shift α , (b) radiative linewidth Γ_0 , and (c) normalised amplitude A of the calculated differential reflectivity as a function of top hBN thickness d_T . The differential reflectivity is calculated for a constant bottom hBN thickness of 25 nm and fitted by Equation 3.17 with $0.5\gamma = \Gamma_0 + \Gamma$. (d) Differential reflectivity spectra for different d_T as marked by the coloured dashed lines in (a-c). The horizontal grey line in (a) indicates $\alpha = \pi$.

differential reflectivity calculated with a constant bottom hBN thickness of 25 nm and a varying top hBN thickness d_T . The phase shift α , the radiative linewidth Γ_0 , and the amplitude A vary significantly on sweeping d_T .^{*} There are two points where α comes close to a value of π as indicated by the orange and blue dashed lines in Figure 3.10a. However, the linewidths and amplitudes are quite different. Figure 3.10d shows three differential reflectivity spectra that highlight some extreme cases. For $d_T = 75$ nm (orange), a perfect Lorentzian spectrum with a nearly minimal linewidth and a strong amplitude is realised. In contrast, the spectrum at $d_T = 144$ nm (dark blue) has nearly the largest linewidth while having the same perfect Lorentzian lineshape. A purely dispersive lineshape is achieved at $d_T = 16$ nm (light blue) where $\alpha = 0.5\pi$. To summarise, the best excitonic properties are achieved for $d_T = 75$ nm when $d_B = 25$ nm. As can be seen from Figure 3.10, there is a certain region around the optimal condition which also yields good results. These thicknesses can then specifically be searched for when exfoliating hBN.

^{*}The excitonic energy also shows a variation as a function of d_T . In this case, the maximum energy difference is less than 1 meV.

Following the derivation of the optical reflection from a TMD embedded in a superlattice in Reference [Ivc05] we recover Equation 3.17 with a modified excitonic frequency $\tilde{\omega}_0$ and radiative linewidth $\tilde{\Gamma}_0$. $\tilde{\omega}_0$ and $\tilde{\Gamma}_0$ are given by

$$\tilde{\omega}_0 = \omega_0 - r_0 \sin(\alpha) \quad \text{and} \quad \tilde{\Gamma}_0 = \Gamma_0 [1 - r_0 \cos(\alpha)] \quad , \quad (3.19)$$

where r_0 is the reflection coefficient of the whole heterostructure without the TMD layer. The following relation holds: $R_0 = |r_0|^2$. r_0 can also be calculated using the transfer-matrix method. For $\alpha = \pi$, a large negative r_0 leads to a large reduction in linewidth. We find that the choice of top layer thickness is quite important. From the simulations we find that a good thickness is $d_T = \frac{\lambda_0}{4n_{\text{hBN}}}$, where λ_0 is the excitonic wavelength and n_{hBN} is the refractive index of hBN.

As an analogy, the TMD inside a heterostructure can be seen as a TMD inside an optical cavity. An emitter coupled to a cavity experiences a change in its spontaneous emission rate (radiative lifetime) [Pur46]. It has been shown that the excitonic lifetime is changed depending on the thickness of the hBN layers used for encapsulation [Fan19]. The change in lifetime goes hand in hand with a change in excitonic linewidth. A larger (smaller) lifetime leads to a decrease (increase) in linewidth. This means that at the smallest linewidth, the monolayer is placed at a node of the optical field inside the cavity [Fan19].

3.7 Experimental setup

The experimental setup is introduced in the following. Figure 3.11 shows a schematic of the complete setup.

Our confocal microscope setup is designed to study our samples either at room temperature (293 K) or cryogenic temperature (4.2 K). In this thesis, we only study heterostructures at cryogenic temperatures. The optical setup is modular and consists of three main parts: the microscope head, the microscope skeleton, and the sample holder. The sample holder is connected to the microscope head through the skeleton. The microscope head can easily be exchanged so that we can swap between absorption (Figure 3.11), PL (Figure 3.12), and Raman spectroscopy (see Appendix C). Additionally, the microscope heads can be modified to include polarisation resolution which can give insight into the spin and valley physics of TMDs.

The sample chip is glued onto a 20-terminal chip carrier with silver paint and contacted by Au/Ag wire bonding. The chip carrier is clipped into the sampler holder with 20 electric lines for contacting the sample. The electric lines are guided through the skeleton and connected to a digital-to-analog converter (DAC) from Basel Precision Instruments via a breakout box. The DAC is then used to control the voltages applied to the gates in the heterostructure. The sample holder is screwed on top of an x - y -scanner (ANSxy100,

attocube) for finetuning the studied sample position in a region of 30 μm by 30 μm . Three-dimensional positioning of the sample is achieved by using a set of three independent x -, y -, and z -piezo positioners (ANPx101 and ANPz101, attocube). The positioners are driven using an attocube ANC300 piezo controller. The stack of sampler holder and positioners is mounted in a titanium housing and attached to the bottom end of the microscope skeleton. For cryogenic measurements, the sample holder and skeleton are mounted in a tube which is evacuated and filled with helium exchange gas (25 mbar). The tube is then placed inside a helium bath cryostat (CryoVac) with a 9 T out-of-plane magnet. The length of the skeleton is chosen such that the sample sits in the centre of the magnetic field.

The microscope head is then put on top of the microscope skeleton. We use a confocal microscope system where we excite the sample and detect the emitted/reflected signal from the same position. The head consists of an excitation, a detection, and an imaging arm. Light (LED, laser) is coupled into the excitation arm from an optical fibre and collimated by an objective. The light is focused onto the sample by a microscope objective (x20/NA = 0.45 or x60/NA = 0.85, Microthek) with diffraction-limited spot size. The emitted or reflected light from the sample is collected by the same objective and sent into the collection arm with a 90:10 beamsplitter (90% is reflected). The signal is focused into a single-mode fibre with a collimating objective. The light is spectrally analysed by a spectrograph (Acton SP-2500, Princeton Instruments) and a liquid nitrogen-cooled charge-coupled device, CCD (Pylon 100BRX, Princeton Instruments). The spectrograph uses a grating with either 300, 600, or 1500 grooves/mm.

The absorption microscope head is shown in Figure 3.11. The sample is excited with a white LED (Osram warm white) through a multi-mode fibre. Polarisation control is achieved by inserting waveplates into the beam path. First, the light passes a linear polariser followed by a $\lambda/2$ liquid crystal (LC) variable retarder (LCC1411-A, Thorlabs). Applying an alternating current voltage to the LC with the liquid crystal controller (LCC25, Thorlabs) produces a $+\lambda/2$ or $-\lambda/2$ retardance of the initial beam. This turns the initial linear polarisation by $+45^\circ$ or -45° creating two perpendicular linear polarisations on demand. After passing an achromatic $\lambda/4$ waveplate either σ^+ or σ^- circularly polarised light is produced. The circular polarisation can simply be changed during an experiment by applying a different voltage to the LC retarder. A big problem is that the collected signal is very broadband which causes interference fringes (etaloning) on the CCD chip. To minimise the etaloning effects the light at the spectrometer input is defocused which spreads the light over a larger CCD chip area. The microscope head is generally aligned with a laser entering from a single-mode fibre (like for a PL measurement) instead of an LED. After the alignment, the excitation fibres are carefully changed and an absorption measurement can be started.

The PL microscope head is shown in Figure 3.12. The sample is excited with a red

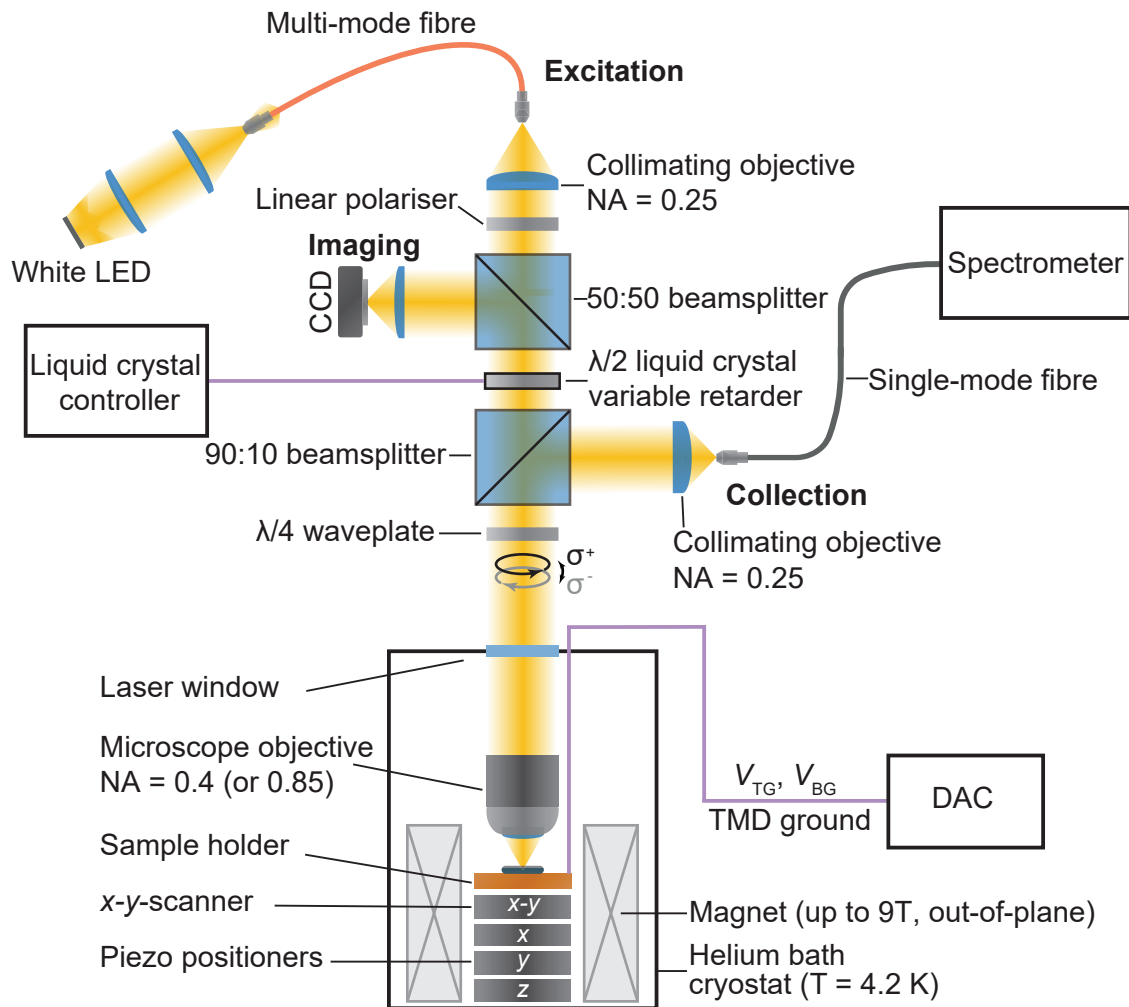


Figure 3.11. Confocal microscope setup used for the magneto-optoelectronic study of TMDs. The microscope head (top part) is designed to measure the reflectivity of the sample after exciting it with a white LED. In general, the head consists of an excitation, a detection, and an imaging arm. Polarisation optics in the excitation arm allow for exciting the sample with a specific circular polarisation. The signal from the sample is collected and sent to a spectrometer for spectral analysis. Parts of the microscope head are easily modified in order to measure other optical properties like PL (see Figure 3.12) or Raman (see Appendix C). The sample sits on piezo positioners inside a helium bath cryostat. Connection to a digital-to-analog converter (DAC) allows electrical control of the sample. The microscope skeleton connecting the sample holder to the microscope head is not shown in this sketch.

HeNe laser (632.8 nm, HNL050L, Thorlabs). The laser light is cleaned up after exiting the excitation fibre using two successive laser-line filters (narrow bandpass filter). The polarisation of the excitation laser is controlled in the same way as in the absorption microscope head. In a PL measurement, we want to additionally control the detected polarisation. To this extent, the signal from the sample passes the same $\lambda/4$ waveplate

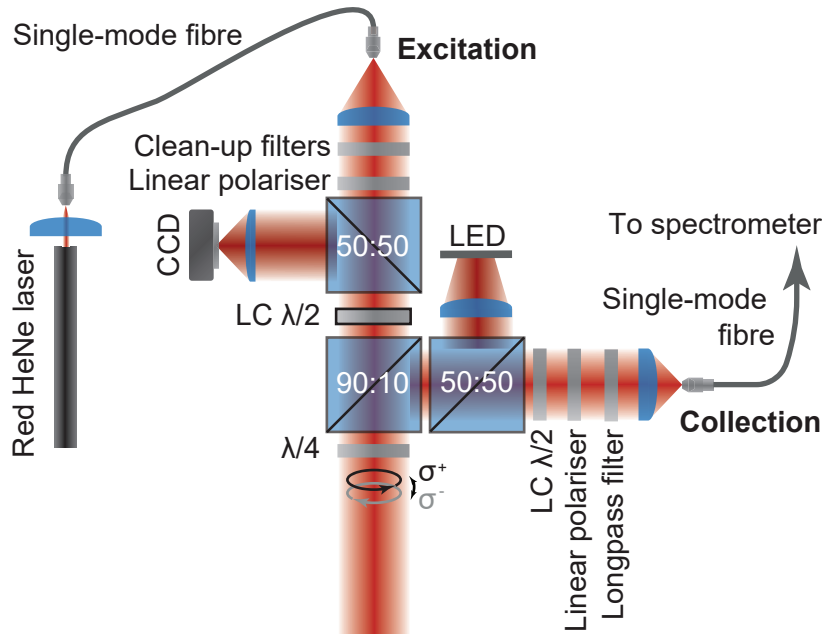


Figure 3.12. Microscope head used for PL measurements. The sample is excited with a red HeNe laser. Linear polarisers and waveplates in the excitation and detection arm enable measuring all circular polarisation combinations. The polarisation combinations can be changed easily during the measurement by applying a different voltage to each of the liquid crystal retarders. The 50:50 beamsplitter below the red LED is only inserted when imaging the sample.

before being directed into the detection arm. Here, the light passes another combination of LC $\lambda/2$ and linear polariser. On applying a certain voltage to the LC in the detection arm, either σ^+ or σ^- polarised light is detected. Before the light is coupled into the detection fibre, the reflected laser light is removed with a longpass filter. By using two LC retarders, full computer-controlled polarisation control is achieved. Applying the four different voltage combinations every possible excitation and detection polarisation combination can be realised.

The upper 50:50 beamsplitter is used to send light reflected from the sample to a CCD camera (Guppy Pro, Allied Vision) for imaging the sample surface. The light is focused onto the camera by an achromatic lens. The imaging is very important as it helps to locate the TMD region and position the sample accordingly. By exciting the sample with the white LED, we can image the sample automatically. For a PL measurement, a 50:50 beamsplitter is temporarily inserted into the detection arm to image the sample with a red LED (see Figure 3.12). Additionally, we use the camera to image the shape of the excitation laser to check the alignment of the microscope head.

*“Da steh ich nun, ich armer Tor!
Und bin so klug als wie zuvor.”*

J. W. v. Goethe, Faust I (1808)

Chapter 4

Interlayer exciton origin in a MoSe₂/WSe₂ heterobilayer

The photoluminescence (PL) emission from interlayer excitons in a twisted ($\sim 3^\circ$) and R-stacked MoSe₂/WSe₂ heterobilayer is studied as a function of excitation power, magnetic field, electric field, charge carrier density, and light polarisation.[†] A broad two-peak structure is observed over a large range of experimental parameters. It is shown that these two excitons correspond to a lower energy momentum-indirect transition and a larger energy momentum-direct transition, both confined to the moiré potential minimum. A momentum-indirect transition dominating the emission spectrum has so far only been demonstrated in H-stacked heterobilayers [Mil17, Bar22]. The properties of these two transitions (energy, intensity, effective dipole moment, g factor, and degree of circular polarisation) can be tuned as a complex function of the applied experimental parameters. For a specific parameter combination, the higher energy momentum-direct exciton dominates the emission spectrum. It is argued that, even at a seemingly large twist angle of $\sim 3^\circ$ (moiré period similar to exciton diameter), interlayer excitons are still confined to the moiré potential which governs their optical properties. Our results highlight the complex task of interpreting the photoluminescence spectra of interlayer excitons as their properties can be significantly and non-trivially tuned, even for a small change of experimental parameters.

Section 4.1 introduces interlayer excitons in type-II heterobilayers and discusses why it is interesting to study them. The device electrostatics are characterised in Section 4.2. In Section 4.3, the excitation-power dependent PL is presented. With the help of polarisation-resolved PL in a magnetic field, the interlayer exciton origin is proposed to be from a lower

[†]Lukas Sponfeldner fabricated the heterobilayer device. L.S. and Nadine Leisgang carried out the optical spectroscopy measurements. L.S. analysed the measurement data and interpreted the results.

energy momentum-indirect transition and a larger energy momentum-direct transition. Section 4.4 discusses the tunability of both interlayer exciton species as a function of several experimental parameters. Lastly, Section 4.5 summarises the results and gives a small outlook for the field of moiré interlayer excitons.

4.1 Introduction

In a type-II heterobilayer like MoSe₂/WSe₂, interlayer excitons (IX) can form due to an efficient charge separation [Riv15]. In a MoSe₂/WSe₂ heterobilayer, the electrons (holes) accumulate in the MoSe₂ (WSe₂) monolayer (see Section 2.5 for details on the IX formation). Due to the spatial separation of electron and hole, IX have a very defined dipole moment, allowing their energy to be tuned in external electric fields. The dipolar character can, for example, be utilised to study exciton dynamics [Unu18, Unu19, Cho20, Wan21a] or to trap a single IX by creating a lateral variation of the vertical electric field through nano-patterning of the gate electrodes [Sch13a, Sha21b]. The large IX dipole moment can lead to strong interactions between them and therefore macroscopic quantum correlations, like exciton condensation [Lai09, Fog14]. Recently, experimental evidence has been reported that IX show signatures of a degenerate many-body state [Wan19, Sig20].

An important degree of freedom for a TMD bilayer system is the twist angle between the two layers. A finite twist angle leads to a moiré pattern with its periodicity depending on the twist angle. A heterobilayer can have two extreme stacking angles: 3R/R stacking (near 0° twist) or 2H/H stacking (near 60° twist). The influence of the moiré pattern on the excitonic properties strongly depends on the stacking configuration. The heterobilayer studied in this chapter has a stacking angle of $\sim 3^\circ$ in the R-stacked configuration (see Section 4.3). The moiré pattern leads to a real space variation of the optical selection rules [Yu15] and the IX energies with the lowest IX energy located at the R_h^X point* [Yu17, Wu18]. Recently, atomic reconstruction has been experimentally observed in bilayer TMDs [Sus19, Ros20, Wes20, Sun20, Luo20, Hal21, And21, Li21, Sha21a]. At a small enough twist angle, the layers are reconstructing themselves as the energy gain from forming certain high-symmetry stackings is larger than the energy cost of twisting (see Section 2.6 for details on the atomic reconstruction). The atomic reconstruction also results – like the moiré pattern for larger twist angles – in a real space variation of the IX energies and their optical selection rules. For an R-stacked bilayer, the energy minimum in both cases is at the R_h^X point with the same optical selection rules [Woz20]. Therefore, it is hard to differentiate between effects originating from a moiré potential or from atomic reconstruction, especially as both patterns might coexist even on the same sample [Par21b].

*R indicates an R stacking of the bilayer. The superscript μ (hexagonal centre h, chalcogen atom X, or metal atom M) indicates the site of the MoSe₂ layer (electron layer) that is aligned with the hexagon centre (h) of the WSe₂ layer (hole layer) as indicated by the subscript.

Typically, in MoSe₂/WSe₂ heterobilayers two types of IX emission patterns are observed in PL spectroscopy: sharp resonances [Sey19, Bae20, Bai20, Li20] and broader (multi-peak) resonances [Tra19, Cia19, Ale20, Cal20, Wan20c, Fö21]. The sharp resonances are usually attributed to IX trapped inside several zero-dimensional moiré potential minima. The origin of the broad resonances is widely debated. There exist several different interpretations of the broad multi-peak structure, which will be further elaborated in Section 4.3. Determining the real space and momentum space origin of the observed peaks is not only important for the fundamental understanding of the heterobilayer system but also crucial for potential applications utilising the large IX tunability.

Here, we study the PL response of a gated R-stacked MoSe₂/WSe₂ heterobilayer as a function of several experimental parameters at a temperature of 4.2 K. We observe a broad double-peak structure in the whole studied parameter range, where we attribute the lower (higher) energy peak to originate from a momentum-indirect (momentum-direct) transition, both localised in the moiré potential minimum. We discuss the high tunability of several properties of both peaks, which have a complex dependence on the experimentally applied parameters.

4.2 Electrostatic device characterisation

A MoSe₂/WSe₂ heterobilayer is integrated in a dual-gate device with top and bottom gates for applying a static out-of-plane electric field F_z and controlling the charge carrier density n in the heterobilayer (see Appendix B for the device details). The two monolayers have been aligned by determining the crystallographic axes before the stacking using second harmonic generation (see Section 3.3). From a microscope image of the picked-up heterobilayer on a stamp, we estimate a stacking angle of $\sim 3^\circ$. By monitoring the MoSe₂ intralayer neutral and charged excitons, the MoSe₂ monolayer is found to be intrinsically n-doped with $n_0 = 1.2 \times 10^{12} \text{ cm}^{-2}$ (see Appendix B). When sweeping F_z we choose the top and bottom gate voltages such that we negate the intrinsic n-doping in the MoSe₂ monolayer.

The electrostatic control of the heterobilayer is demonstrated in Figure 4.1 and Figure 4.2. The large and linear energetic tunability of the IX (see Figure 4.2) shows that the electric field across the heterobilayer can be swept successfully. To confirm only a variation of F_z we monitor the intralayer excitons in the heterobilayer region with absorption spectroscopy. The left column in Figure 4.1a (Figure 4.1b) shows the σ^+ (σ^-) polarised absorption for the same electric field sweep as in Figure 4.2 with a larger F_z range. The lower (higher) energy resonance is the neutral MoSe₂ (WSe₂) exciton X_{Mo}^0 (X_{W}^0). The constant neutral exciton energy and the large absorption strength are a sign that only F_z is varied while the charge carrier density is kept constant and small.

Upon doping a TMD monolayer, the neutral excitons blueshift and lose oscillator strength

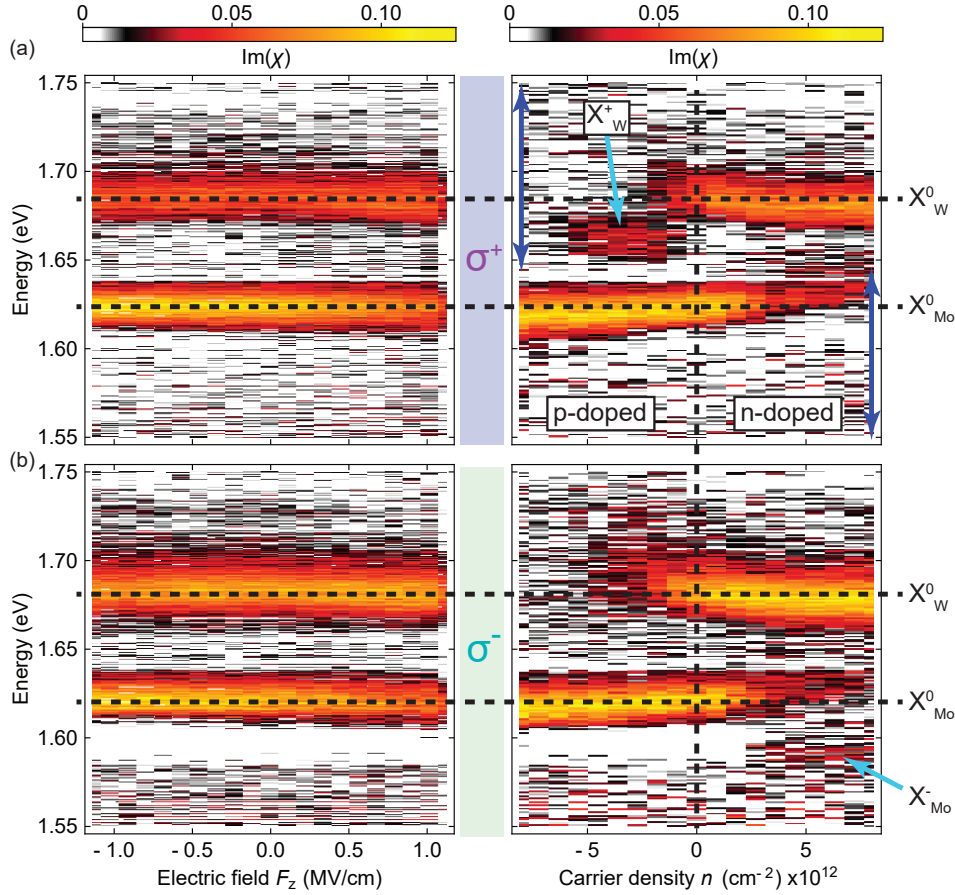


Figure 4.1. (a) σ^+ and (b) σ^- -polarised absorption measurements of the intralayer excitons at an out-of-plane magnetic field of 9 T for either only a varying electric field F_z (left column) or only a varying charge carrier density n (right column). The spectra are recorded in the heterobilayer region of the sample. The dashed horizontal lines indicate the energies of the intralayer excitons X_{Mo}^0 and X_{W}^0 in each monolayer. On sweeping only the electric field (left column), the exciton energy stays constant and no signs of charge doping are detected. On doping the bilayer with electrons (holes), the charges accumulate in the MoSe₂ (WSe₂) layer leading to a blueshift and a loss in oscillator strength of the X_{Mo}^0 (X_{W}^0). Due to the shifted electronic bands at high magnetic fields, the negatively charged X_{Mo}^- (positively charged X_{W}^+) does only appear in σ^- (σ^+) polarisation. The reference reflectivity spectrum R_0 for each polarisation is the sum of the spectra at the highest p- and n-doped density as indicated by the two dark blue double arrows in the top right colour map.

[Bac17, Roc19]. This is also the case in our heterobilayer system as shown in the right column in Figure 4.1. X_{W}^0 vanishes at a much lower density as X_{Mo}^0 . X_{Mo}^0 (X_{W}^0) stays strong and constant in energy in the p-doped (n-doped) region as all holes (electrons) accumulate in the opposite layer due to the type-II alignment of the monolayers. Additionally, we observe the appearance of the negatively charged X_{Mo}^- (positively charged X_{W}^+) in σ^- (σ^+) polarisation when n-doping (p-doping) the bilayer. The charged excitons appear only in one polarisation due to the applied out-of-plane magnetic field of 9 T. These measurements

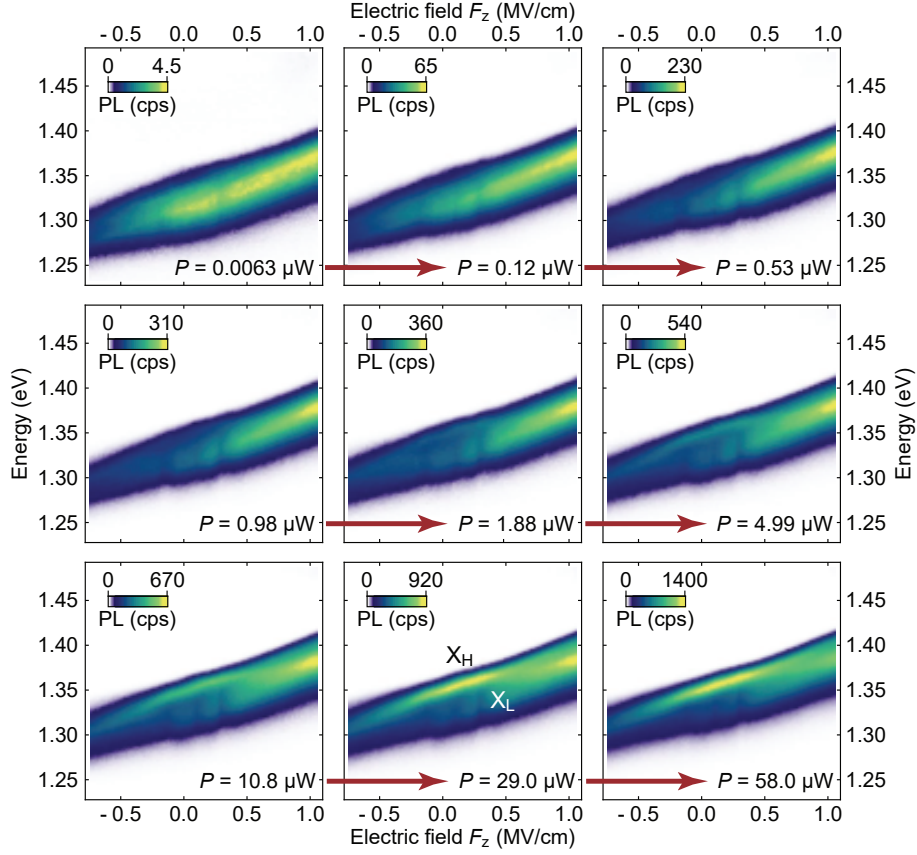


Figure 4.2. Excitation power P dependent Stark tuning of the IX by sweeping the electric field F_z at close-to-zero charge carrier density. An exciton with a small linewidth (X_H) energetically above a broad excitonic resonance (X_L) becomes dominant for an increasing excitation power.

confirm that we can tune the charge carrier density inside the heterobilayer.*

4.3 Two interlayer exciton species

We study the evolution of the IX spectra as a function of F_z and excitation laser power P using PL spectroscopy. The sample is excited with a red HeNe laser (632.8 nm) and the PL signal is collected (see Section 3.11 for the detailed experimental setup). Figure 4.2 summarises the whole measurement series. These measurements are conducted at zero magnetic field with no polarisation resolution. In each measurement, F_z is swept for a close-to-zero n . Between each measurement, P is increased from 0.0063 μW to 58.0 μW in eight steps. At first glance, two exciton peaks are visible that linearly shift with the applied F_z . The lower energy exciton X_L has a large linewidth. On increasing P , a higher energy exciton X_H with a smaller linewidth becomes more pronounced.

*Changing the doping probably also influences F_z across the heterobilayer due to the accumulated charges in each layer [Pis19, Jau19].

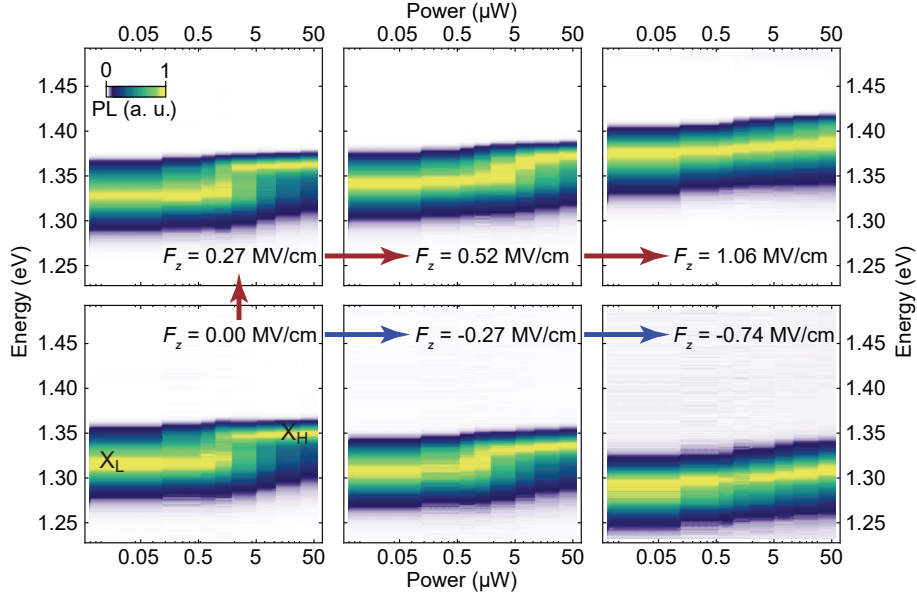


Figure 4.3. Normalised PL spectra as a function of laser power for different applied electric fields. The colour-maps are replotted from the data shown in Figure 4.2. Each individual spectrum is normalised by its maximum PL intensity. At small electric fields, the appearance of the higher-energy peak X_H is clearly visible. X_H becomes the dominating peak for higher powers at small fields.

Figure 4.3 offers a different view of the double-peak structure, where the colour-maps shown in Figure 4.2 are replotted as a function of power. Each spectrum is normalised by its maximum PL intensity. At small electric field values, the two exciton peaks are clearly visible. For an increased power, X_H gains intensity until it becomes the dominant exciton at the highest powers. For a more positive F_z , the power when X_H appears is increased. At the largest positive F_z (top right colour-map in Figure 4.3), the maximally used power is not enough for X_H to dominate the spectrum.

To gain a quantitative insight into the behaviour of the two IX peaks, each spectrum is fitted by the sum of two Gaussians. Figure 4.4a shows an example spectrum of the two excitons at zero electric field and a power of 4.99 μW . The corresponding fit of X_H (X_L) is plotted in blue (orange). Figure 4.4b shows the extracted peak energies as a function of power. On increasing the power, the peak energies increase due to dipole-dipole interactions as will be discussed in more detail in Subsection 4.4.2. The extracted peak intensities are plotted in Figure 4.4c. At small powers, X_H has a smaller intensity than X_L . At a power of $\sim 5 \mu\text{W}$, X_H becomes the exciton with the largest intensity. Figure 4.4d shows the extracted full width at half maximum (FWHM) of each peak. Apart from the smallest power, the FWHM of each peak stays rather constant with power. The FWHM of X_L is roughly twice as large as X_H .

To further study the two IX species, we employ polarisation-resolved PL measurements

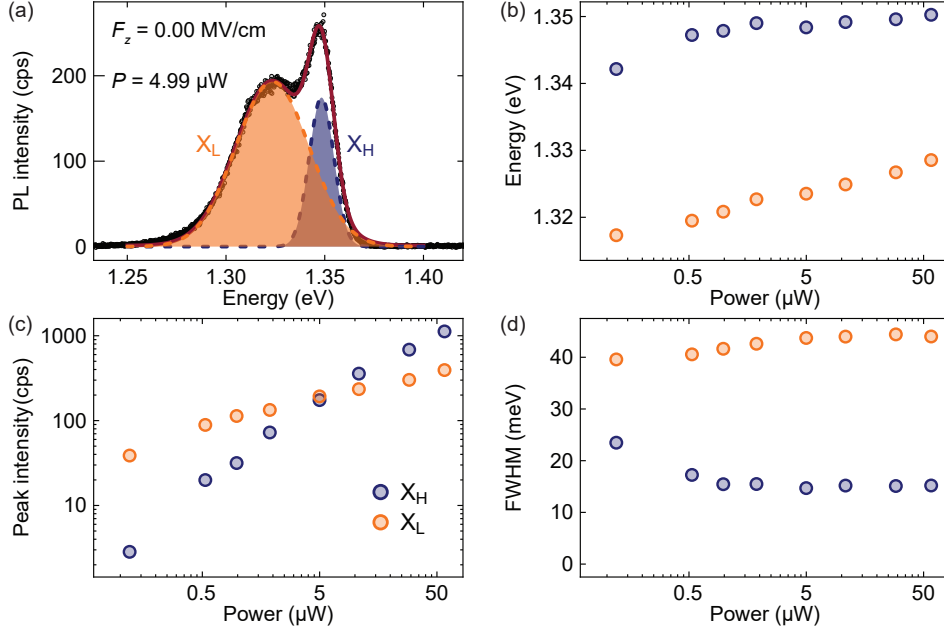


Figure 4.4. (a) PL spectrum of the low-energy peak X_L and the high-energy peak X_H at zero electric field and a power of $4.99 \mu\text{W}$. Each spectrum is fitted by a sum of two Gaussians. (b-d) Power dependence of the fitted (b) peak energies, (c) peak intensities, and (d) the full width at half maximum (FWHM). X_H (X_L) is colour-coded in blue (orange).

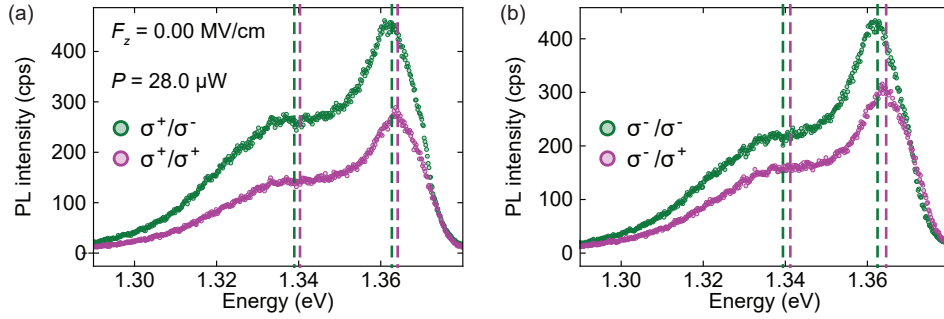


Figure 4.5. Polarisation-resolved PL spectra at a magnetic field of 9 T. The spectra are recorded at zero electric field and with a power of $28.0 \mu\text{W}$. PL spectra for a (a) σ^+ -polarised and (b) σ^- -polarised excitation. The spectra with σ^+ -polarised (σ^- -polarised) detection are coloured in purple (green). For both excitation polarisations, the σ^- -polarised detected signal is larger. The dashed vertical lines indicate the fitted peak energies of each exciton. For both exciton species, the σ^+ -polarised energies are larger than the σ^- -polarised energies resulting in positive g factors.

in an out-of-plane magnetic field of $B_z = 9$ T. In a magnetic field, the exciton energy shifts, leading to an energy difference $\Delta E^{+,-} = E^{\sigma^{+,-}/\sigma^+} - E^{\sigma^{+,-}/\sigma^-}$ between the σ^+ -polarised and σ^- -polarised PL signal for an excitation with σ^+ and σ^- polarisation, respectively. A measure for the energy difference is the excitonic g factor $g^{+,-} = \frac{\Delta E^{+,-}}{\mu_B B_z}$,

with $\mu_B = 58 \mu\text{eV}/\text{T}$ being the Bohr's magneton (see Section 2.7). Additionally, the integrated intensity $I^{\text{excitation/detection}}$ of an exciton depends on the polarisation. To quantify this dependence, we define the degree of circular polarisation (DOCP) as

$$\text{DOCP}^{+,-} = \frac{I^{\sigma^{+,-}/\sigma^+} - I^{\sigma^{+,-}/\sigma^-}}{I^{\sigma^{+,-}/\sigma^+} + I^{\sigma^{+,-}/\sigma^-}}. \quad (4.1)$$

The combined information of DOCP and g factor helps determine the real space origin of IX in the moiré potential (see Section 2.6).

The polarisation-resolved PL spectra for σ^+ -polarised (σ^- -polarised) excitation are shown in Figure 4.5a (Figure 4.5b). The measurements are done at zero electric field and with $P = 28.0 \mu\text{W}$. We extract a g^+ (g^-) of +2.7 (+4.0) and a DOCP^+ (DOCP^-) of -0.25 (-0.17) for X_H with a σ^+ -polarised (σ^- -polarised) excitation. For X_L , we extract a g factor of +2.7 (+3.5) and a DOCP of -0.29 (-0.16) with a σ^+ -polarised (σ^- -polarised) excitation.* A positive g factor and a negative DOCP confirm the R-stacking of the studied heterobilayer and likely originate from excitons at the R_h^X point in the moiré structure (see Section 2.6) [Woz20, Joe21, Hol22, Smi22]. The same sign of DOCP and g factor for both exciton species points towards a shared real space origin in the moiré potential [Yu17, Woz20, Fö21]. The converse argument then says: the excitonic doublet origin probably lies in momentum space.

A doublet IX structure as observed in our measurements has been seen in a lot of other experiments. The two peaks have been interpreted as singlet and triplet IX showing opposite circular polarisation [Cia19, Jau19, Zha19, Wan20c]. The excitonic doublet in Reference [Cia19], however, is likely to originate from different points in the sample due to the opposite energetic ordering of their positive and negative g factors [Woz20]. Others interpret the excitonic doublet as two momentum-indirect IX with opposite DOCP [Han18] or as IX and corresponding IX trion [Cal20]. Another interpretation is that X_H and X_L originate from a momentum-direct KK and a momentum-indirect QK transition, respectively [Mil17, Gil18, Bar22].[†] Other possibilities include impurity-bound IX complexes [Via19] and peaks with alternating DOCP attributed to the ground and excited states confined in a single moiré potential minimum [Tra19]. Lastly, Alexeev et al. found that wrinkles form in the monolayers during the stacking process leading to strain-redshifted PL emission of highly linearly polarised excitons confined to the wrinkles [Ale20]. Similar

*Note that the DOCP at zero magnetic field depends on the laser wavelength: the closer the laser energy is to the MoSe₂/WSe₂ A-exciton energy, the larger the absolute DOCP value is [Han18, Hsu18]. The laser used in our measurements is very off-resonant. Hence, we were not able to resolve the exciton polarisation at a magnetic field of 0 T. For an increasing magnetic field, the DOCP of IX in an R-stacked heterobilayer becomes more negative even for an off-resonant excitation [Hol22], see also Figure 4.20.

[†]We use the following notation for the excitonic transitions: The first (second) letter indicates the origin of the electron (hole) in the bandstructure.

results were found by Bai et al. who attribute the highly linear PL emission to IX confined in a striped one-dimensional (1D) moiré potential [Bai20].

The triplet/singlet IX, the alternately polarised IX confined in the moiré potential, and the doubly momentum-indirect QK IX are an unlikely origin of X_H and X_L as they both exhibit the same sign in their DOCP (see Figure 4.5). Impurity-bound IX are also an unlikely explanation as we counteract the initial doping in the MoSe₂ monolayer using our gating scheme (see Appendix B). By keeping the heterobilayer at a very small and constant charge carrier density, the trion interpretation for X_L seems unlikely as well. Additionally, density-dependent PL spectra discussed in Subsection 4.4.6 make the trion picture improbable. Strained regions in the bilayer as an IX origin is much more difficult to assess. Unfortunately, we don't have direct access to the structural information of the heterobilayer (e.g. using an atomic force microscope) as it is already capped with hBN and FLG flakes. We perform measurements resolving the linear polarisation of the IX and find a small polarisation dependence (see Figure 4.6). The degree of linear polarisation (DOLP) of 0.08 (0.19) for X_H (X_L) is smaller than the ones measured by other groups [Ale20, Bai20]. However, we measure a finite DOLP, albeit small, and therefore cannot fully exclude strain effects from wrinkles influencing the IX origin.

It should be noted that strain is probably present in the studied heterobilayer as the two monolayers likely undergo atomic reconstruction for small twist angles (see Section 2.6). The excitonic emission possibly comes from the R_h^X point in the moiré potential which becomes a triangular domain upon atomic reconstruction [Sus19, Ros20]. These domains (5 nm up to 300 nm) are rather strain-free with the strain accumulated in the boundaries between the domains [Wes20]. In a typical optical experiment, the signal is collected from multiple domains of varying sizes which makes it difficult to find the exact influence of the atomic reconstruction on the excitonic properties [Hua22].

In a recent study by Barré et al., the oscillator strength of IX is determined for the first time in absorption using an electromodulation technique [Bar22]. By comparing absorption and PL measurements, they find that the lowest energy exciton observed in PL originates from the momentum-indirect QK transition while the IX measured in absorption stem from the momentum-direct KK transition [Bar22]. The study in Reference [Mil17] reaches the same conclusion as to the origin of the excitonic doublet structure. Exactly the same trends as shown in Figure 4.4 have been observed by Miller et al. (compare to Figure 2 in Reference [Mil17]). The intensity behaviour of the two IX as a function of excitation power as depicted in Figure 4.4c can be explained by the state-filling of the constituent particles, electrons and holes. In reality, the KK transition is slightly momentum-indirect.* The finite twist angle between the layers introduces a small momentum mismatch between the valence

*Despite the small mismatch we refer to the KK transition as a momentum-direct transition.

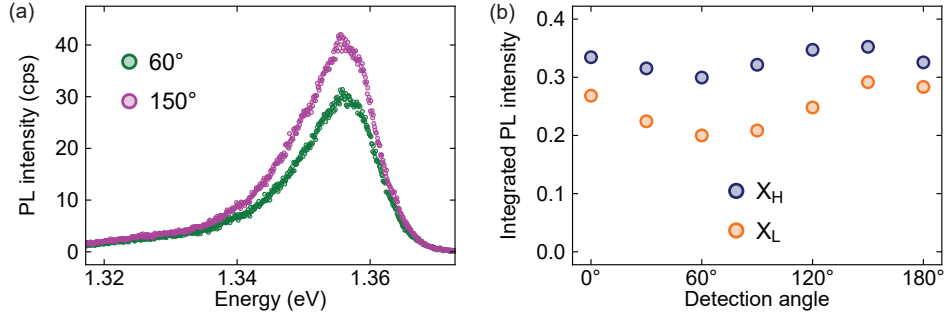


Figure 4.6. (a) Linear polarisation-resolved PL spectra along the direction corresponding to the minimum (green) and maximum (purple) PL intensity. The spectra are recorded at zero electric field and a power of 34.3 μW . The measurements have been done with zero voltage applied to each gate meaning that the intrinsically n-doped MoSe₂ is not neutralised. The n-doping of the bilayer explains the smaller relative intensity of X_L as compared to the spectra shown in Figure 4.5 for a similar excitation power. To measure the linearly polarised response of the bilayer, we insert a linear polariser (LPVIS050-MP, Thorlabs) and a $\lambda/2$ waveplate (947 nm 0-order, B. Halle) into the detection arm of the microscope head. The detection angle of 0° corresponds to the linear polarisation direction of the excitation laser. The detection angle δ is set by manually turning the linear polariser to an angle of δ and the half-waveplate to $\delta/2$. The half-waveplate keeps the linear polarisation direction sent to the spectrometer constant. (b) Integrated PL intensities of X_H and X_L for several detection angles. Defining the degree of linear polarisation (DOLP) as $\text{DOLP} = \frac{I_{\max} - I_{\min}}{I_{\max} + I_{\min}}$, with $I_{\max, \min}$ being the largest and smallest integrated PL intensity, respectively. We extract a DOLP of 0.08 (0.19) for X_H (X_L).

and conduction band extrema in the WSe₂ and MoSe₂ layer, respectively. On increasing the power, more IX are excited leading to a density blueshift (see Subsection 4.4.2) and a filling of the electron-hole states. For an increased phase-space filling of the constituent electrons and holes, the KK transition becomes much brighter as states with a sufficiently large kinematic momentum are occupied [Mil17]. The same effect is achieved by doping the bilayer system with electrons and thus filling up the conduction band states (see Subsection 4.4.6). The QK transition is much more momentum-indirect and radiative recombination is therefore assisted by phonon emission [Bar22]. A possible candidate could be the recently measured Q→K phonon ($E = 15$ meV) in monolayer WSe₂ [Par21a], which agrees well with theoretical phonon energies in a heterobilayer [Mah22]. Using these considerations, it can be explained why the QK exciton dominates the PL signal at low powers, while the KK exciton starts to dominate at larger powers. The peak assignment is strengthened as the phonon-assisted momentum-indirect QK exciton has twice the linewidth of the KK exciton due to electron-phonon interactions (see Figure 4.4d) [Mil17].

On decreasing the excitation power, some groups observed the transition to multiple very sharp (~ 100 μeV) IX resonances [Sey19, Bae20, Bai20, Li20]. These narrow peaks probably originate from the confinement in a moiré potential at small twist angles ($\sim 1^\circ$; moiré periodicity > 19 nm). At these small twist angles, the electronic bands in the

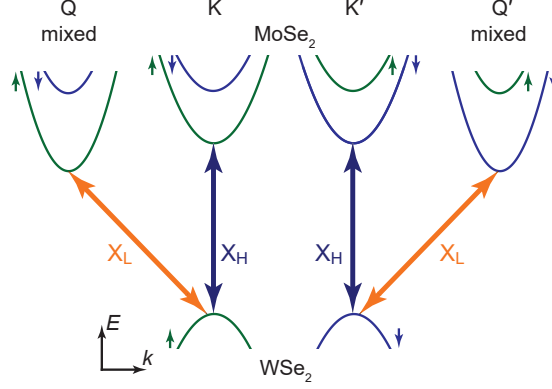


Figure 4.7. Sketch of the proposed IX doublet origin. X_L originates from the momentum-indirect QK transition; X_H originates from the momentum-direct KK transition. The electronic valence (conduction) bands at K are purely localised in the WSe_2 ($MoSe_2$) monolayer while the bands at Q are hybridised between the two layers. Note, that the band ordering of the higher energy spin-split bands at Q and K is not clear [Mil17, Gil18, Han18, Bar22].

moiré mini Brillouin zone are flat [Wu18, Nai20, Guo20, Bre20b] and the moiré period is large enough such that IX trapped in the potential minima do not feel each other (see Section 2.6). As can be seen in Figure 4.2 we observe rather broad IX peaks even down to a power as low as 6.3 nW. The moiré periodicity in our sample is roughly 6.3 nm, which is comparable to the size of IX [Kar22]. Therefore, the IX trapped in the moiré potential interact with each other leading to the observed broadened resonances.

Based on the argumentation above, we propose that the two-peak structure observed in our measurements originates from the QK (X_L) and KK (X_H) transitions as sketched in Figure 4.7. The electronic valence and conduction bands at K are purely localised in the respective monolayer; the bands at Q are hybridised [Han18]. While the previous studies have been done with an H-stacked $MoSe_2/WSe_2$ heterobilayer [Mil17, Bar22], our results show that also in an R-stacked heterobilayer the lowest energy transition is momentum-indirect. In addition to the findings of Miller et al. our measurements provide a detailed study of the relation and tunability of the two exciton species as a function of excitation power, magnetic field, electric field, charge carrier density, and light polarisation as will be discussed in the next section.

4.4 Momentum-indirect and momentum-direct interlayer exciton tunability

In this section, we analyse the momentum-indirect and momentum-direct IX species as a function of several experimental tuning parameters. We find that, for a specific combination of these parameters, the momentum-indirect X_H dominates the PL spectrum. The influence of excitation power, magnetic field, electric field, and charge carrier density on the excitonic

properties is a complex interplay of many effects that we will untangle in this section.

The peak intensities of X_H and X_L cross at a certain power as discussed in Subsection 4.4.1. Subsection 4.4.2 introduces the excitonic density blueshift and the resulting consequences for X_H and X_L. In Subsection 4.4.3, the influence of power and electric field on the Stark tuning of both excitons is presented. The energy difference as a function of power and F_z is shown in Subsection 4.4.4. So far, the discussion in the subsections uses data extracted from the measurement series shown in Figure 4.2. In Subsection 4.4.5, the excitonic response in an external magnetic field is studied and the extracted g factors and DOCP are presented. This section concludes in Subsection 4.4.6 with a discussion of the IX optical response as the charge carrier density in the heterobilayer is tuned.

4.4.1 Crossover power

The peak intensities of each exciton are analysed for a large electric field range. Figure 4.8a (Figure 4.8b) shows the peak intensity of each exciton at $F_z = -0.27$ MV/cm ($F_z = 0.52$ MV/cm), similar to Figure 4.4c. The intensity evolution of X_H and X_L is fitted by a power function. Figure 4.8e shows the extracted intensity scaling exponent as a function of F_z . The exponent is constant for X_L. For X_H, the exponent is constant and slightly decreasing at larger negative electric fields. The intensity scaling of X_H is much larger than that of X_L. Therefore, at a certain excitation power, the X_H intensity goes above the X_L intensity, which can be explained by the state-filling argument discussed before. Hence, the intensity crossover is robust over a large range of F_z values. The crossover power is extracted from the intensity fits and plotted in Figure 4.8f. For small electric field values, the crossover power is rather constant between 6 and 8 μ W. For larger positive fields, the crossover power increases drastically. At large negative fields, the crossover power also seems to increase.

The increased crossover power at large positive F_z could be linked to the peak intensity evolution as a function of F_z (see Figures 4.8c,d). On sweeping from negative to positive F_z values, the intensity of X_L constantly increases. In the same sweeping direction, the exciton energy increases, which means that the constituent electron and hole are pushed together spatially by the electric field. This leads to a slightly larger overlap of electron and hole wave functions and, therefore, a larger radiative recombination rate [Jau19]. Hence, the X_L gains intensity due to the increased radiative recombination rate. The same argumentation can be applied to the X_H intensity for negative and small positive F_z . For large positive F_z , the X_H intensity starts to decrease. The decrease hints at an increasing non-radiative decay channel for X_H, whose microscopic nature needs to be studied further. Both the decreasing X_H intensity and increasing X_L intensity lead to an increased crossover power for large positive F_z .

The onset of an increasing crossover power at large negative F_z could be a consequence

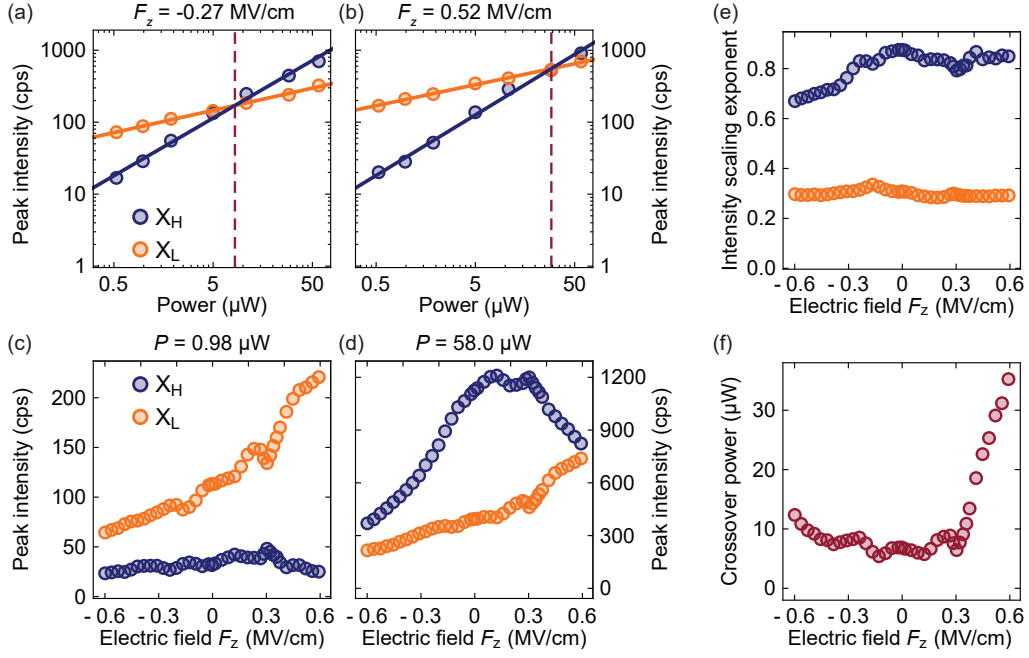


Figure 4.8. Fitted peak intensities of both peaks as a function of power for (a) $F_z = -0.28 \text{ MV/cm}$ and (b) $F_z = 0.54 \text{ MV/cm}$. Each intensity evolution is fitted by a power function $y = ax^b$. The resulting fit is indicated by the orange and blue lines. At the crossover power, the X_H intensity becomes larger than the X_L intensity. The crossover power is indicated by the vertical dashed red lines. (c,d) Peak intensity of the two peaks as a function of F_z for (c) $P = 0.98 \mu\text{W}$ and (d) $P = 58.0 \mu\text{W}$. (e) Intensity scaling exponent b and (f) crossover power extracted from the fits indicated in (a,b).

of the smaller energy difference of X_H and X_L for an increased field (see discussion in Subsection 4.4.4). The smaller separation makes fitting the data more difficult.

4.4.2 Excitonic density blueshift

On increasing the excitation power and therefore the IX density, the IX energy blueshifts [Neg00, Sch13b, Riv15, Nag17b]. This blueshift is also visible in our experiments for both exciton species. Figure 4.9a (Figure 4.9b) shows the density blueshift as a function of power for $F_z = 0.00 \text{ MV/cm}$ ($F_z = 0.59 \text{ MV/cm}$). At zero electric field, the blueshift of X_L is much larger than that of X_H , while they are similar at large F_z .

To explain the origin of the blueshift we turn to the dipolar nature of the IX. All IX dipole moments are aligned in the same direction, either parallel or antiparallel to F_z . Two aligned dipoles have a dipolar interaction energy W that is related to the exciton-exciton distance $r_{\text{IX-IX}}$ as $W \propto r_{\text{IX-IX}}^{-3}$ [Sch13b]. Increasing the exciton density for a higher excitation power leads to a smaller $r_{\text{IX-IX}}$ and therefore a larger exciton energy.

Using a simple plate capacitor model, the IX blueshift can be related to the IX density [Sch08, Lai09]. Assuming no free charge carriers, the formation of IX leads to two oppositely

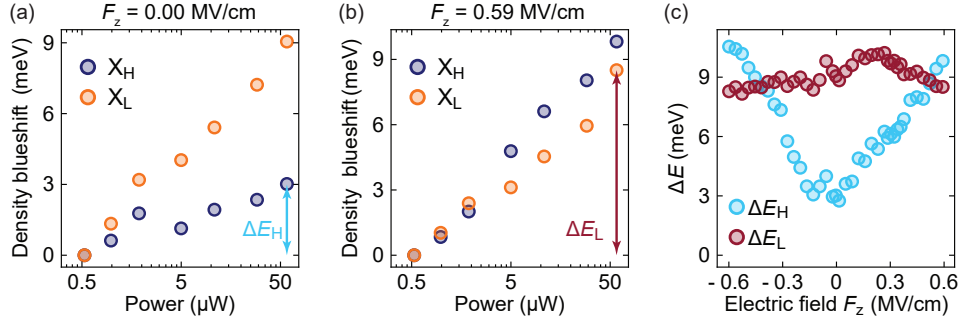


Figure 4.9. (a,b) Density blueshift of each exciton for (a) zero electric field and (b) a large positive electric field. All data points are subtracted by the respective absolute energy of the exciton at the lowest power ($P = 0.53 \mu\text{W}$). (c) Density blueshift ΔE for each exciton at the highest excitation power. ΔE_H and ΔE_L are indicated by the double arrows in (a) and (b).

charged layers at a distance d with a charge carrier density of n_{IX} . The creation energy of an additional IX is then increased due to the presence of the other IX [Lai09]. The density blueshift ΔE can be modelled as [But99]

$$\Delta E = \frac{e^2 d}{\epsilon_0 \epsilon_{\text{TMD}}} n_{\text{IX}}. \quad (4.2)$$

However, this simple approach neglects exciton-exciton interactions, which leads to an underestimation of the IX density [Sch08]. Equation 4.2 allows us to estimate the order of magnitude of the IX density. The blueshift of IX might also be influenced by IX diffusion to potential minima [Nag17b]. However, the moiré potential impedes the diffusion, which also depends on the IX lifetime [Cho20]. Phenomenologically, we take the IX blueshift with power as a sign of a density increase.

Figure 4.9c shows the maximum density blueshift of each exciton as a function of the electric field. The maximum blueshift is calculated as the difference between the exciton energy at $P = 58.0 \mu\text{W}$ minus the energy at $P = 0.53 \mu\text{W}$. The blueshift of X_L stays rather constant over the whole F_z range, with a value of ~ 9 meV. For X_H , the blueshift is small (3 meV) at low fields, while it increases for an increasing F_z until it becomes even larger than the blueshift of X_L .

First, we try to estimate the maximum IX density in our system. It should be noted that according to equation 4.2 the IX density at the lowest measured power is equal to zero. However, this cannot be the case as we detect PL signal. For the maximum blueshift of 10 meV, $d = 0.6$ nm and $\epsilon_{\text{TMD}} = 7.2$ [Kim15], we find an IX density of $n_{\text{IX}} = 6.6 \times 10^{11} \text{ cm}^{-2}$. Our estimate is probably reasonable as the measured blueshift for the used laser powers is very comparable to other observed blueshifts of IX [Nag17b, Joe21]. We can compare this density to the density of the moiré unit cells and therefore the density

of the potential minima for the IX (see Section 2.6). For a twist angle of 3° , the moiré period $a_{\text{moiré}} = 6.3$ nm corresponds to a potential minima density of $n_{\text{moiré}} = 2.5 \times 10^{12}$ cm $^{-2}$. $n_{\text{moiré}}$ is slightly larger than n_{IX} for our experimental conditions. Even for the largest powers used in our experiments, the moiré potential is likely not completely filled. In other words, the properties of both exciton species are governed by moiré effects. Bai et al. observe an intensity crossover similar to Figure 4.8 and argue the origin is due to IX leaving the moiré traps [Bai20]. Our density estimate makes this an unlikely explanation for the IX origin.

Next, we try to discuss the F_z -dependent blueshift behaviour of X_{H} . For low fields, ΔE_{H} has a value of 3 meV, roughly a factor of three smaller than ΔE_{L} (see Figure 4.9c). On increasing F_z in either polarity, ΔE_{H} increases linearly until it becomes even larger than ΔE_{L} . The linear increase can be modelled by the power-dependence of the X_{H} polarisabilities (see Figure 4.10e) or of the X_{H} dipole moments (see Figure 4.12c and discussion in the next subsection). Let us assume that the X_{H} density n_{H} at low fields is constant for the whole F_z range, as is the case for X_{L} . Then, the power-dependent blueshift in Equation 4.2 can be written as a function of F_z as

$$\Delta E_{\text{H}}(F_z) = \frac{e^2 d}{\epsilon_0 \epsilon_{\text{TMD}}} n_{\text{H}} - \Delta \mu_z F_z - \Delta \beta_z F_z^2, \quad (4.3)$$

with $\Delta \mu_z$ ($\Delta \beta_z$) being the dipole moment (polarisability) difference between the power of interest and the smallest power. Note that $\Delta \mu_z$ and $\Delta \beta_z$ depend on the excitation power. Plugging in the values for the dipole moments for $F_z < 0$ ($F_z > 0$) from the fit with two linear Stark shifts, the resulting ΔE_{H} at the largest field values is ~ 11 meV (~ 10 meV), which agrees well with the extracted ΔE_{H} values in Figure 4.9.

The X_{H} density is a factor three smaller than the X_{L} density. This relation is a reasonable observation as X_{L} is the lowest energy state in the system. Additionally, X_{L} has a longer radiative lifetime than X_{H} due to its momentum-indirect nature [Mil17].

4.4.3 Stark tuning of interlayer excitons

The peak energies of each exciton as a function of F_z are shown in Figures 4.10a and 4.12a for $P = 0.53$ μW , in Figure 4.10b for $P = 4.99$ μW , and in Figures 4.10c and 4.12b for $P = 58.0$ μW . Especially for X_{H} , there is a visible ‘‘kink’’ in the energy evolution at a slightly negative F_z . A kink and, therefore, a seemingly sudden change in the ‘‘slope’’ of the energy shift is also visible in F_z sweeps done by other groups [Cia19, Jau19, Sha21b]. In all three experiments, the larger Stark shift is in the smaller energy region, as in our experiment. Only L. A. Jauregui et al. mention a nonlinearity in the energy shift of 10% and attribute it to charging effects due to uncompensated gating without a more detailed investigation [Jau19]. Another explanation could be the transition to an exciton

originating from a different position in the moiré potential with a modified interlayer distance (see Section 2.6). However, this possibility is ruled out by the polarisation-resolved measurements shown in Subsection 4.4.5.

To understand this peculiar behaviour of the IX in more detail, we interpret the energy evolution in two different ways: First, we fit the energies using the quadratic Stark shift formula as shown in Equation 2.7. Typically for IX, the quadratic term in the energy shift is neglected. We find that the nonlinear tuning of X_H is due to a giant excitonic polarisability, which can be rationalised to a certain extent by theoretical calculations. Second, we fit the energies of X_H and X_L by two separate linear functions in the negative and positive F_z range. The slopes for X_H change significantly on changing the voltage polarity, which could be a consequence of the rigid dipolar nature of the IX.

The real microscopic explanation might be more complex than the two simple analysis cases discussed in the following. However, we believe that the giant excitonic polarisabilities are the most likely explanation for the observed IX energy shifts. In the end, both analysis methods yield similar conclusions that agree well with our interpretation of the IX origin.

Quadratic Stark shift

The quadratic fits to the IX energies with the function $E_0 - \mu F_z - \beta F_z^2$ are shown in Figures 4.10a-c. The fits describe the energy evolution of both peaks reasonably well. The extracted zero field energies E_0 as a function of power are shown in Figure 4.11a and they follow pretty much the same trend as the energies shown in Figure 4.9a. Both IX energies blueshift due to the increased exciton density for higher powers as described in the previous subsection.

The extracted dipole moments as a function of power are plotted in Figure 4.10d. The dipole moments of both excitons stay rather constant with the X_H dipole moment being slightly larger than the dipole moment of X_L. The average dipole moment of X_H (X_L) is 0.48 $e \cdot \text{nm}$ (0.42 $e \cdot \text{nm}$). These values are slightly smaller than the expected interlayer spacing [He14] and are also slightly smaller than other studies of dual-gated MoSe₂/WSe₂ heterobilayers [Jau19, Sha21b, Bar22]. However, these experimental studies only fit the energy shift with a purely linear function and therefore neglect the effect of the IX polarisability on the energy shift.

The dipole moments of X_L are smaller than those of X_H. This is in line with the interpretation of X_L as a momentum-indirect exciton, where the electron is hybridised [Han18, Phi19, Bar22]. The hybridisation effectively decreases the distance of electron and hole and therefore also decreases the dipole moment (see also the analysis of the IE Stark shift in homobilayer MoS₂ discussed in Chapter 5) [Jun23]. Our results also agree very well with a recent study where the momentum-direct KK excitons measured in absorption

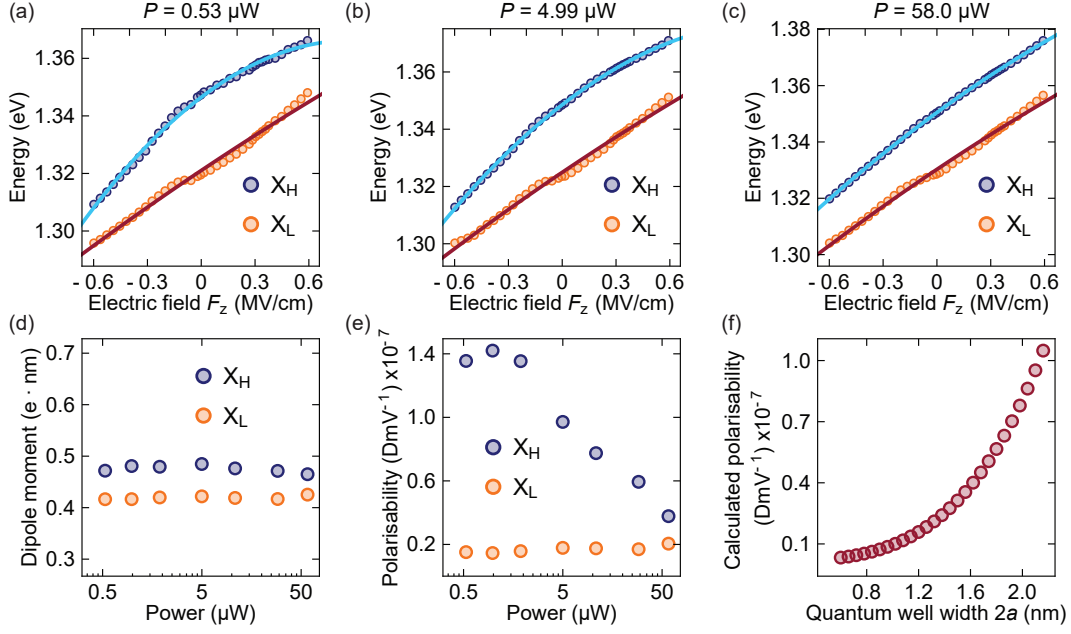


Figure 4.10. Fitting the linear and quadratic Stark shift. Extracted peak energies of X_H and X_L at (a) low and (b) medium laser power, and (c) high laser power. Each resonance is fitted by a quadratic function $E_0 - \mu F_z - \beta F_z^2$ over the whole F_z range, where μ is the IX dipole moment and β is the IX polarisability. (d) Extracted dipole moments $|\mu|$ as a function of power. (e) Extracted polarisabilities β as a function of power. (f) Calculated excitonic polarisability of a finite-barrier quantum well according to Equation 4.4 as a function of quantum well width $2a$.

exhibit a larger Stark shift than the lower-energy momentum-indirect QK excitons, which dominate the PL spectrum [Bar22]. We expand on this interpretation and show that for a specific combination of electric field and laser power, the PL spectrum can be dominated by momentum-direct IX.

The extracted polarisabilities as a function of power are plotted in Figure 4.10e. The polarisability of X_L stays constant with an average value of $0.17 \times 10^{-7} \text{ D m V}^{-1}$. The X_H polarisability is larger at low powers with roughly $1.4 \times 10^{-7} \text{ D m V}^{-1}$ and decreases with increasing power, approaching the polarisability of X_L . In order to get a feeling for the magnitude of excitonic polarisabilities and what they are influenced by, we first discuss the measured polarisabilities in two similar systems. The out-of-plane polarisability of A-excitons in monolayer MoS_2 is $8 \times 10^{-10} \text{ D m V}^{-1}$ [Roc18]. Going to bilayer MoS_2 , the A-exciton polarisability is increased to $6.4 \times 10^{-9} \text{ D m V}^{-1}$ (see analysis in Section 6.4 in Chapter 6). Following this trend and as we will discuss below, an effectively increased confinement width leads to an increased excitonic polarisability. For IX, it is therefore reasonable to assume an even larger polarisability due to their confinement in two monolayers, unlike the intralayer A-exciton.

Next, we try to calculate the polarisability of an exciton confined to a finite-barrier

	MoSe ₂ [Ras15]	WSe ₂ [Ras15]	hBN [SC13]
E_{cbm} (eV)	3.82	3.72	2.30
E_{vbm} (eV)	5.57	5.37	7.20

Table 4.1. Calculated conduction (valence) band edge offsets E_{cbm} (E_{vbm}) from the vacuum for monolayer MoSe₂, monolayer WSe₂, and hBN. For MoSe₂ and WSe₂, the two numbers given in Reference [Ras15] for each offset are averaged.

quantum well with a width of $2a$ and a potential barrier height of V_0 following an analytic model developed by T. G. Pedersen in Reference [Ped17]. The analytical form of the polarisability can be written as [Ped17]

$$\beta = \beta_0 \frac{k(15 - 4k^2) + 3 \cot k [5 - 4k^2 + (4k^2 + 5 \cot^2 k + 8k \cot k - 3) \cot^2 k - 4k \cot k]}{12k^4(k + \cot k)}, \quad (4.4)$$

with k being the wave number inside the well. The prefactor β_0 is given by

$$\beta_0 = \frac{e^2 m^* a^4}{\hbar^2}, \quad (4.5)$$

where e is the electron charge and m^* the effective mass. Additionally, a normalised potential barrier w is defined as

$$w = \frac{2m^* a^2 V_0}{\hbar^2}. \quad (4.6)$$

Following the energy boundary condition, the wave number can be calculated numerically via [Ped17]

$$k^2 (1 + \tan^2 k) = w^2. \quad (4.7)$$

For the calculation of the polarisability, we take m^* as the free electron mass. Using the average conduction and valence band offsets between each monolayer and hBN, V_0 is estimated to be 1.60 eV. The valence and conduction band offsets of each layer with respect to the vacuum are summarised in Table 4.1.

The polarisability calculated with Equation 4.4 as a function of quantum well width is shown in Figure 4.10f. For an increasing quantum well width, the polarisability increases in a nonlinear manner. Taking a width of 1.2 nm, we calculate a polarisability of 0.16×10^{-7} D m V⁻¹, which agrees very well with the measured polarisability of X_L. It should be noted that also a smaller confinement potential leads to a larger polarisability. Additionally, near-degenerate and dipole-coupled states in two coupled quantum wells can lead to an even larger polarisability [Cro18, Ped19]. Using all the considerations above, it is not unlikely to achieve calculated IX polarisabilities as large as 1.4×10^{-7} D m V⁻¹.

The X_H polarisability is larger than the polarisability of X_L . Again, the root of this observation probably lies with X_L being a hybrid IX: the effective confinement potential width of X_L is probably different than for X_H due to the hybridised electrons. Therefore, if the confinement is smaller, then the polarisability of X_L is also smaller (see Figure 4.10f).

Lastly, we discuss the power dependence of the three parameters extracted from the quadratic fits. At a small exciton density, we can rewrite the total exciton energy E as

$$\begin{aligned} E(F_z) &= E_0 - \mu F_z - \beta F_z^2 \\ &= E_0 - (\mu + \beta F_z) F_z \\ &= E_0 - \hat{\mu} F_z , \end{aligned} \quad (4.8)$$

with a modified dipole moment $\hat{\mu}$ that depends linearly on F_z . In the low power limit, we can determine the unmodified dipole moment μ and polarisability β of the IX. The rather different polarisabilities of X_H and X_L again point towards the conclusion that the origin of these two excitons is fundamentally different.

At a larger exciton density, the total energy is modified by the density blueshift ΔE shown in Equation 4.2. Using $ed = \hat{\mu}$, the total exciton energy is given by

$$\begin{aligned} E(F_z, n_{IX}) &= E_0 + \frac{e n_{IX}}{\epsilon_0 \epsilon_{TMD}} \hat{\mu} - \hat{\mu} F_z \\ &= \tilde{E}_0 - \tilde{\mu} F_z - \tilde{\beta} F_z^2 , \end{aligned} \quad (4.9)$$

with the modified parameters

$$\tilde{E}_0 = E_0 + \frac{e n_{IX}}{\epsilon_0 \epsilon_{TMD}} \mu , \quad (4.10)$$

$$\tilde{\mu} = \mu \left(1 - \frac{e n_{IX}}{\epsilon_0 \epsilon_{TMD}} \frac{\beta}{\mu} \right) = \mu \left(1 - \Delta E \frac{\beta}{\mu^2} \right) , \quad \text{and} \quad (4.11)$$

$$\tilde{\beta} = \beta . \quad (4.12)$$

For the modified zero field energies in Equation 4.10, the simple density blueshift formula from Equation 4.2 is recovered. The modified dipole moment $\tilde{\mu}$ in Equation 4.11 depends linearly on the exciton density or in other words the density blueshift. Taking a maximum density blueshift of 3 meV (9 meV) for X_H (X_L) and μ and β at the lowest excitation powers, we find $\tilde{\mu} = 0.96\mu$ ($\tilde{\mu} = 0.98\mu$). Therefore, the modification of the dipole moment as a function of power is negligible as is observed in our measurements in Figure 4.10d. In other words, there is a large contribution to the linear term from μ itself, such that any n -related effects are hard to detect. The polarisability in Equation 4.12 is not modified at all as a function of exciton density. This is in contrast to the experimental observations, where β depends on the excitation power (see Figure 4.10e). The evolution of each quadratic fit

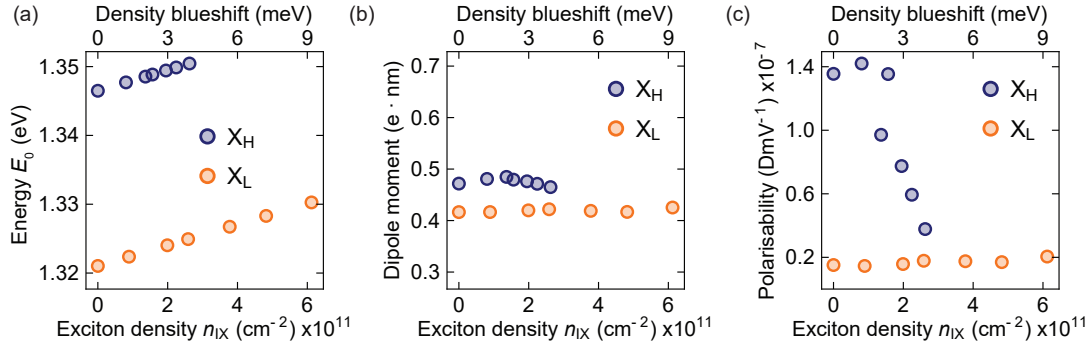


Figure 4.11. Plotting the quadratic fit parameters from Figure 4.10 as a function of the exciton density n_{IX} . Extracted (a) zero field energies E_0 , (b) dipole moments, and (c) polarisabilities of each IX as a function of n_{IX} . The exciton density is calculated from the density blueshift with Equation 4.2. Note that the maximum blueshift of X_H is much smaller than the maximum blueshift of X_L . We also want to stress that Equation 4.2 only gives a rough estimate of the IX density. Therefore, the error of the calculated n_{IX} is potentially large.

parameter as a function of exciton density n_{IX} is shown in Figure 4.11.

If we assume the gating of the layers to be responsible for the change in the X_H polarisability, the X_L polarisability should also be affected. However, this is not observed in our experiments, which makes uncompensated gating an unlikely explanation.

To summarise, we can determine the dipole moment and the polarisability for both excitons at low power, which strengthens the microscopic assignment of the peaks. Furthermore, the simple model to describe the total exciton energy as a function of electric field and exciton density can explain the behaviour of the zero field energies and the dipole moments as a function of power very well. However, the model fails to capture the power dependence of the polarisability. Compared to μ , β is smaller, so the quadratic term might be more sensitive to any n -dependent effects. The origin of this behaviour could lie with the increased dipole-dipole interactions as the power increases. The dipole-dipole interaction scales with the product of two dipole moments. Maybe this product could lead to a term that modifies the polarisability as a function of exciton density. So far, we have taken n_{IX} to be independent as a function of the electric field. A dependence of these two parameters on each other could also influence the energy scaling of each IX. Considering all these excitonic effects in a complex environment, the microscopic behaviour of the polarisability power dependence is not yet fully understood and warrants further detailed studies.

Two separate linear Stark shifts

Now, the IX energies are fitted with two separate linear functions in the positive and negative field range, respectively. The resulting linear fits are shown in Figure 4.12a (Figure 4.12b) for a low (high) power. Figure 4.12c plots the extracted dipole moments of

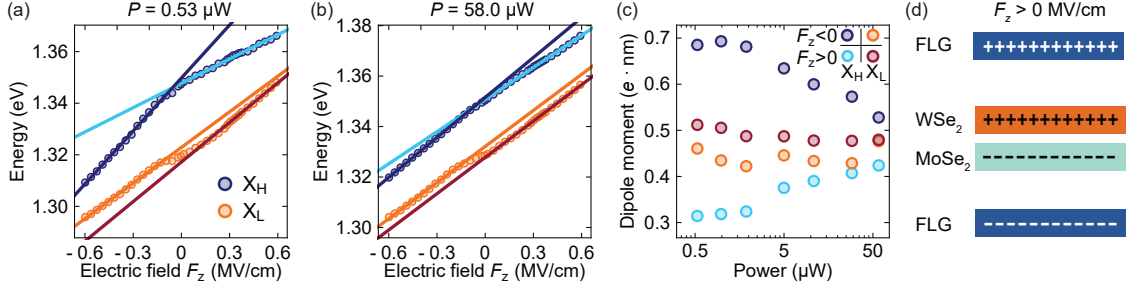


Figure 4.12. Fitting only the linear Stark shift in two regimes. Extracted peak energies of X_H and X_L at (a) low and (b) high laser power. Each resonance is fitted by two linear functions in the positive and negative F_z range. For X_H , the dark blue (light blue) line corresponds to a linear fit from -0.60 to -0.20 MV/cm (-0.02 to 0.59 MV/cm). For X_L , the orange (red) line corresponds to a linear fit from -0.60 to -0.20 MV/cm (0.09 to 0.59 MV/cm). (c) Extracted dipole moments $|\mu|$ as a function of power. (d) Sketch of the charges on each layer for positive electric fields with IX being present in the heterobilayer. Due to the rigid dipolar character of the IX, a second plate capacitor is formed in the centre.

X_H and X_L in the positive and negative F_z range as a function of power. The two dipole moments of X_L have a similar value and stay rather constant for an increasing power. For X_H , the power strongly impacts the two dipole moments. At low powers and in the negative field range the Stark shift of X_H is the largest. The value of $\sim 0.7 e \cdot \text{nm}$ agrees very well with the expected interlayer spacing [He14] and with other studies of dual-gated $\text{MoSe}_2/\text{WSe}_2$ heterobilayers [Jau19, Sha21b, Bar22]. Increasing the power at negative fields leads to a decrease in the effective dipole moment. This could explain the measured dipole moment of $0.5 e \cdot \text{nm}$ using a large laser power of $200 \mu\text{W}$ in Reference [Cia19]. However, the experiments are hard to compare in detail as probably also the excitation laser wavelength and the laser spot size influence the Stark shifts.

There is a large difference in the dipole moments of X_H for positive and negative fields, which leads to the kink in the energy evolution (see Figure 4.12). At the lowest power, there is roughly a factor of two difference between the dipole moments. For an increasing power, both dipole moments seem to converge towards a shared intermediate dipole value of $\sim 0.5 e \cdot \text{nm}$. This value roughly corresponds to the dipole moment of X_L . While the X_H dipole moment is affected by the field polarity, the X_L dipole moment is not, which again excludes uncompensated gating as an origin of the kink.

We propose a different possible explanation for the energy kink. The formation of IX can be seen as the accumulation of photogenerated electrons and holes in opposite layers. Then, the two monolayers act as a second plate capacitor where the plates are oppositely charged (see sketch in Figure 4.12d). For positive F_z values, the hole (electron) layer is closer to the gate with an applied positive (negative) voltage. In this configuration, the IX feel less than the applied voltage to each gate and therefore their effective Stark shift

is reduced. For negative F_z values, the hole (electron) layer is closer to the gate with an applied negative (positive) voltage. Following the same train of thought as above, this configuration could lead to an increased effective Stark shift. In other words, the kink in the IX energy could be a consequence of the asymmetry in the plate capacitor polarity due to the rigid dipolar nature of the IX.

The question remains why the X_L dipole moment is not affected as much as the X_H dipole moment on changing the field polarity. The hybridised exciton nature of X_L might lead to a less defined accumulation of charge carriers in opposite layers, which in turn leads to a reduced impact of the monolayer plate capacitor on the X_L dipole moments.

As is the case for the quadratic fit, the dipole moments of X_L are smaller than those of X_H without an effectively reduced dipole moment (for negative F_z). Even by using another fitting routine, the different dipole moments agree well with the interpretation of X_L as a hybridised momentum-indirect IX.

On increasing the power, the X_H dipole moment decreases (increases) for negative (positive) fields, while the X_L dipole moment stays rather constant. As discussed above, understanding the power dependence of the energy shifts is a complex task and more studies are needed to understand the microscopic origin in detail.

In the low power limit ($P \rightarrow 0$), the effect of the large initial field reduction should vanish and the dipole moments for positive and negative fields should become similar. For the lowest excitation power of 6.3 nW (see Fig. 4.2 top left), an X_L dipole moment of $0.43 e \cdot \text{nm}$ ($0.47 e \cdot \text{nm}$) is extracted for $F_z < 0$ ($F_z > 0$). The dipole moment difference is slightly smaller than the difference of $0.05 e \cdot \text{nm}$ at a power of 530 nW. Even for the lowest used power, there is still a finite difference in the X_L dipole moments. However, the measured data indicates a decreasing difference for $P \rightarrow 0$. Unfortunately, X_H is too weak at low powers to estimate a dipole moment.

4.4.4 Energy difference of the two excitons

In this subsection, we analyse the extracted energy difference of X_H and X_L . Figure 4.13a shows the energy difference as a function of F_z for several excitation powers. Figure 4.13b (Figure 4.13c) plots the energy difference as a function of power for a decreasing (an increasing) F_z value. For low F_z values, the energy difference is continually decreasing with the strongest decrease at the smallest fields. This decrease at small fields can be explained by the density blueshift difference of X_H and X_L (see Figures 4.9a,c).

For an increase of F_z in either polarity, the energy difference decreases for all powers with the largest decrease being at small powers. Additionally, the energy difference decreases stronger for negative fields as compared to positive fields. The two aforementioned observations can be modelled purely by the difference in Stark shifts of X_H and X_L for positive and negative F_z (see Figure 4.12c).

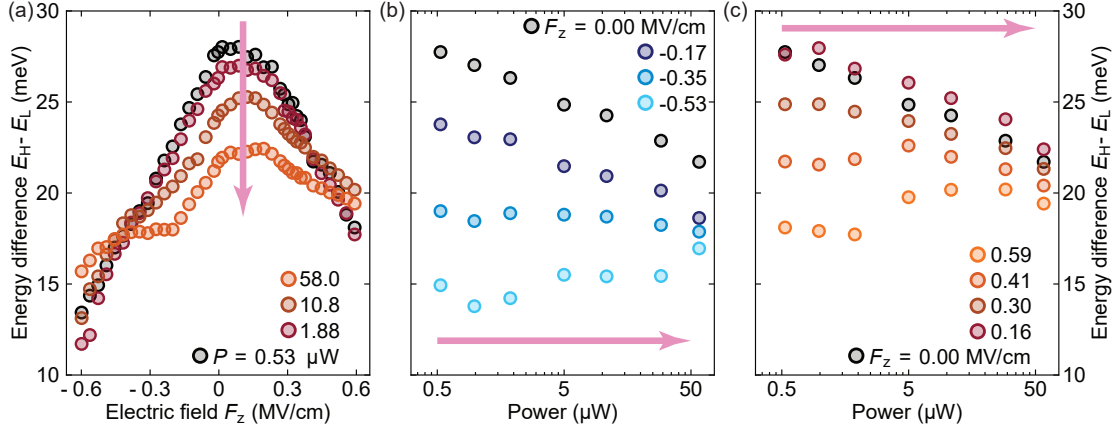


Figure 4.13. (a) Energy difference $E_H - E_L$ between the two excitons as a function of electric field for several excitation powers. (b,c) Energy difference as a function of power for several (b) decreasing and (c) increasing electric fields. The pink arrows are a visual aid and indicate the sweep direction from low to high power.

For a large positive or negative F_z value, the absolute energy difference stays almost constant (even a slight increase) for an increase in power as can be seen in Figure 4.13b and Figure 4.13c. This constant energy difference as a function of power originates from a similar density blueshift of X_H and X_L at high fields (see Figures 4.9b,c).

4.4.5 Excitonic response in a magnetic field

In this subsection, we study the polarisation-resolved optical response of the heterobilayer in an external out-of-plane magnetic field of 9 T. First, we look at the intralayer X^0 excitons in the heterobilayer region with absorption spectroscopy (see Figure 4.14). Each spectrum is fitted as the sum of two Lorentzians. From the extracted energies, a g factor for the MoSe_2 X_{Mo}^0 of $g_{\text{Mo}} \approx -4.5$ and for the WSe_2 X_{W}^0 of $g_{\text{W}} \approx -5.4$ is extracted. Both extracted g factors are slightly larger than the value of roughly -4 as expected for monolayer A-excitons (see Section 2.7). A possible reason could be that the g factors are altered due to moiré or atomic reconstruction effects in the heterobilayer.

Now, we turn to the IX response in a magnetic field. Figure 4.15 shows polarisation-resolved PL spectra for a varying F_z and with a power of 28.0 μW . With this high power, the X_H can clearly be seen. The bottom row of Figure 4.15 shows the total integrated DOCP⁺ (DOCP⁻) for an excitation with σ^+ (σ^-) polarised light. The total DOCP stays rather constant and negative with slight oscillations for both polarisations. DOCP⁺ is a bit more negative than DOCP⁻. A negative DOCP means that the most PL signal collected is emitted in σ^- polarisation as can be seen in the colour-maps as well. The spectra in Figure 4.15 are fitted as the sum of two Gaussians and the peak energies and integrated peak intensities are extracted for X_H and X_L . The polarisation-resolved g factors

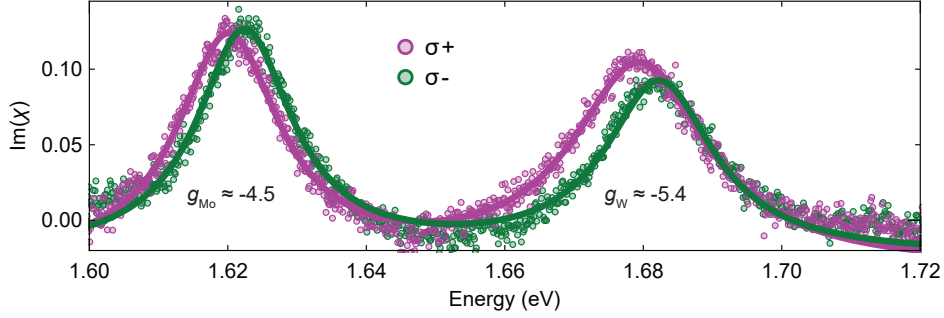


Figure 4.14. Polarisation-resolved absorption spectra of the intralayer X^0 excitons of monolayer MoSe₂ and WSe₂ in the heterobilayer region at a magnetic field of 9 T. The coloured lines are a fit to each spectrum consisting of the sum of two Lorentzians. Using the energy difference between the σ^+ and σ^- resonances, a g factor for the MoSe₂ X_{Mo}^0 of $g_{\text{Mo}} \approx -4.5$ and for the WSe₂ X_{W}^0 of $g_{\text{W}} \approx -5.4$ are calculated. The reference spectra R_0 is taken in the same way as described in Figure 4.1.

and DOCP are calculated for both exciton species and plotted as a function of F_z in Figure 4.16a and Figure 4.16b, respectively.

For both excitons and both excitation polarisations we extract a positive g factor. The relative behaviour of both g factors is very similar for each excitation polarisation. The X_{H} g factor stays small and rather constant for negative fields, while it increases for positive fields to up to nearly +10 (+8) for σ^+ (σ^-) excitation. For X_{L} , the g factor is slightly larger (smaller) than the X_{H} g factor for negative (positive) F_z . However, the X_{L} g factor increases for an increasing F_z in any polarity.

In an R-stacked heterobilayer, the energetic minimum in the moiré potential lies at the R_{h}^{X} point [Yu17]. The lowest energy KK transition g factor is estimated to be +6 (see Section 2.7). At least at small fields, the measured X_{H} g factor is slightly smaller than this estimate and also smaller than other recently measured g factors [Sey19, Cia19, Joe21, Hol22, Smi22]. For the momentum-indirect QK transition at the R_{h}^{X} point, Förg et al. calculate a g factor +8.6 [Fö21], which is quite a bit larger than what we extract from our measurements. They find a smaller g factor of +4 for the spin-conserving momentum-indirect $\text{K}\Gamma$ transition, where the hole state at Γ is slightly hybridised between the layers [Fö21]. The $\text{K}\Gamma$ transition is slightly lower in energy than KK, but higher in energy than QK [Fö21]. Further studies will be needed to determine if the origin of the momentum-indirect transition could be from $\text{K}\Gamma$. The F_z dependence of both g factors is very complex. In a recent study on homobilayer MoS₂, it was found that the g factors of hybridised interlayer and intralayer excitons depend on the energy detuning between them [Lor21]. Another possibility could be the change of effective hole and electron masses or the orbital composition as a function of F_z . To conclude, the spread in experimentally determined and theoretically calculated [Woz20, Fö21] g factor values, together with the non-trivial behaviour of the g factors as a function of F_z , warrants further detailed studies.

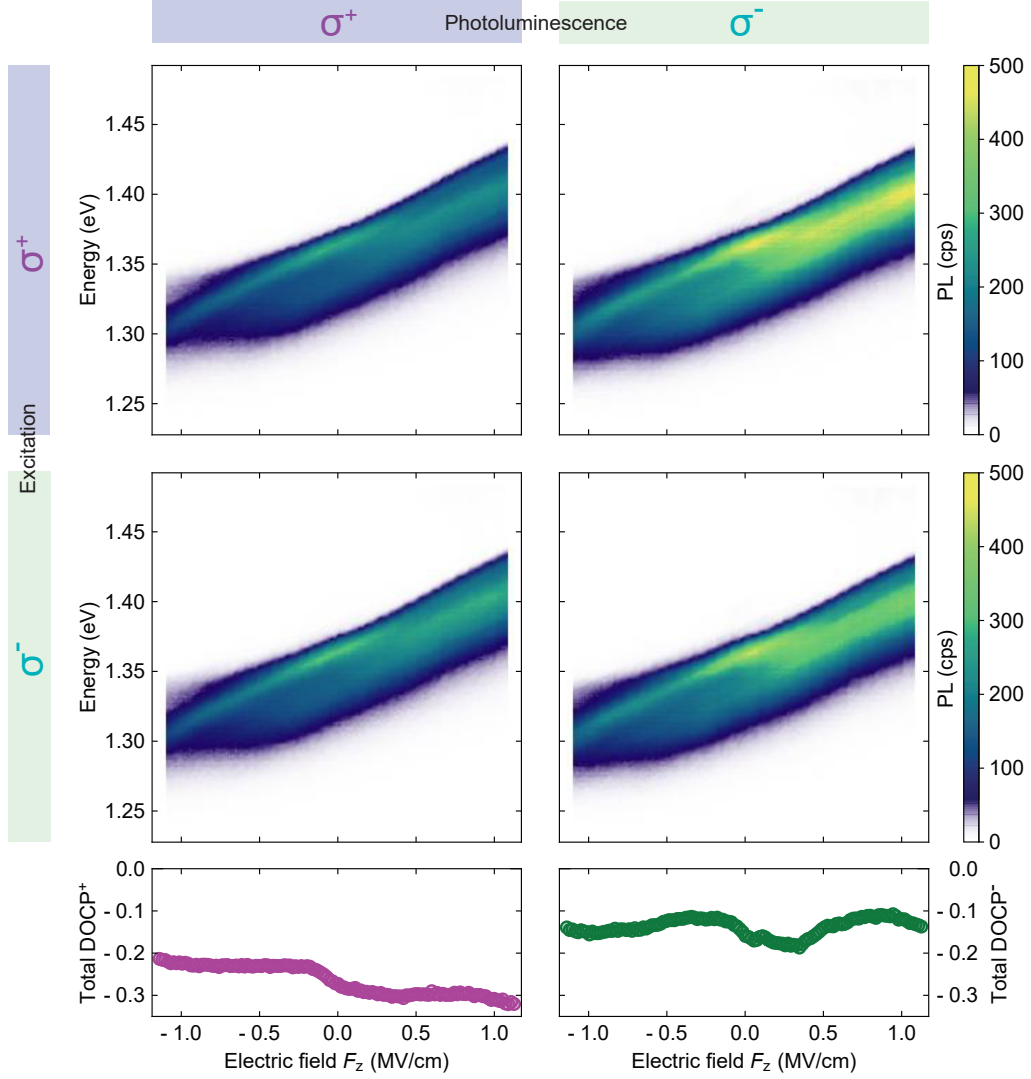


Figure 4.15. Polarisation-resolved PL spectra as a function of the electric field F_z at a magnetic field of 9 T and with a power of 28.0 μW . The gatesweeps correspond to the sweep shown in Figure 4.3 bottom middle. The spectra shown and fitted in Figure 4.5 have been extracted from these gatesweeps. The bottom row shows the total $\text{DOCP}^{+,-}$ for a $\sigma^{+,-}$ excitation as a function of F_z , respectively.

The DOCP of the individual IX is plotted in Figure 4.16b. All extracted DOCP values are negative, indicating a preferred PL emission in σ^- polarisation. For an excitation with σ^+ polarisation, an emission in σ^- is in line with an emission from the spin conserving transitions at the R_h^X point [Wu18, Bre20b]. On excitation with σ^- , the moiré selection rules dictate a σ^+ -polarised PL signal (see Section 2.6). However, we detect mostly σ^- -polarised emission which means there must be an efficient mechanism that flips both the electron and hole spins. The lowest electronic bands in a positive magnetic field are sketched in Figure 4.17. The Zeeman splitting of the electron and hole in a magnetic

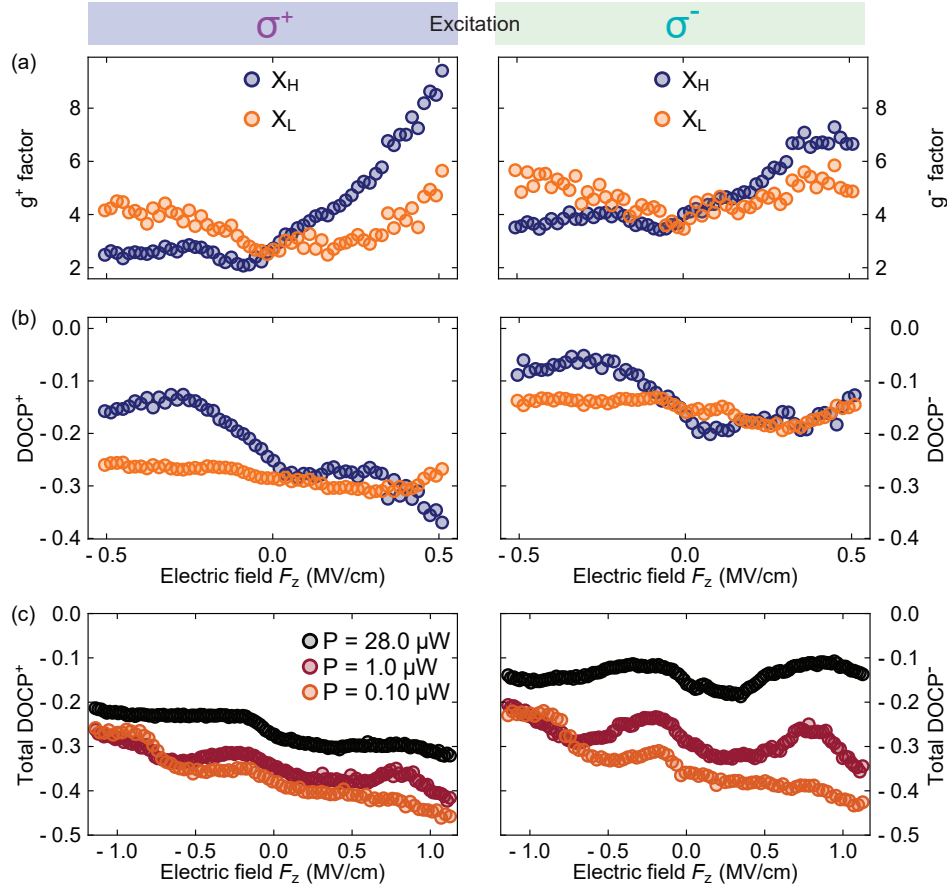


Figure 4.16. Polarisation-resolved (a) g factor and (b) DOCP extracted by fitting the spectra in Figure 4.15 by a sum of two Gaussians. (c) Total DOCP as a function of F_z for several excitation powers. The black points correspond to the data shown in Figure 4.15.

field is given by $\Delta E_{e,h} = g_{e,h} \mu_B B_z$, respectively. Using $m_e = 0.58m_0$ and $m_h = 0.36m_0$ [Kor15] we estimate an electron (hole) g factor of $g_e = 5.4$ ($g_h = 11.6$). At a magnetic field of 9 T, the estimated single particle g factors lead to an energy difference between the conduction and valence bands at K and K' of $\Delta E_e = 2.8$ meV and $\Delta E_h = 6.1$ meV, respectively. Under the measurement conditions, the Zeeman-split hole states are therefore twice as far apart in energy as the electron states. This energy difference can be related to the valley/spin relaxation time $\tau_{e,h}$ as [Mai93, Bla94, Wor96, Tra96]

$$\frac{1}{\tau_{e,h}(B_z)} = \frac{\alpha \Delta E_{e,h}^3}{\left| \exp\left(\frac{\Delta E_{e,h}}{k_B T}\right) \right|} + \frac{1}{\tau_0} \frac{\Gamma^2}{\Gamma^2 + \Delta E_{e,h}^2}, \quad (4.13)$$

with α being a parameter adjusting the strength of the first term, k_B being the Boltzmann constant, τ_0 being the zero field relaxation time, and Γ being a width parameter of the

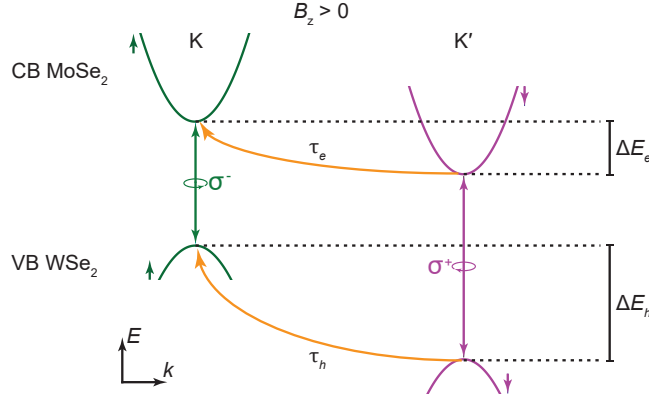


Figure 4.17. Sketch of the lowest electronic bands at the K and K' point in a positive magnetic field. In an R-stacked heterobilayer, the K (K') valley IX emits in σ^- (σ^+) polarisation. The transition in the K' valley has a larger energy than in the K valley resulting in a positive g factor. The valence band energy difference ΔE_h is roughly twice as large as the conduction band Zeeman splitting ΔE_e . $\tau_{e,h}$ are the electron and hole valley/spin scattering times, respectively. For simplicity, we only show the scattering of the charge carriers towards the lowest IX energy state, which explains our experimental findings.

second term. The first term describes a direct one-phonon process [Orb61]. The second term is due to the electron-hole exchange interaction and is only important when both states are close together in energy [Sur18]. At a magnetic field of 9 T, the first term dominates over the second term [Sur18] as the band energy splittings come close to the energies with a large phonon density of states [Mah22]. The electron scattering in the MoSe₂ layer could be mediated by the flexural acoustic ZA(K) mode [Jeo20].

Using Equation 4.13, we can explain the observed negative DOCP with σ^- excitation. For an off-resonant excitation at zero magnetic field, the observed DOCP is close to zero (see also Figure 4.20). On increasing the magnetic field, the overall DOCP is influenced by the energy differences and the ratio between τ_e and τ_h . ΔE_h becomes larger twice as fast as ΔE_e , meaning that the scattering time for holes is much faster than for electrons (see equation 4.13). For σ^+ excitation, the majority of IX end up in the K valley without a spin-flip leading to a σ^- -polarised IX emission. For σ^- excitation, most electrons and holes relax to the K' valley without a spin-flip. However, the fast relaxation time and the large energy gain make the hole and electron scattering to the K valley very likely. Hence, IX tend to scatter from K' to K leading to a σ^- -polarised IX emission. Scattering from the smaller Zeeman state to the larger Zeeman state is less probable as has been observed in monolayer MoSe₂ [Wan15a] and MoSe₂/WSe₂ heterobilayers [Nag17a, Hol22, Smi22]. The scattering also likely takes place after the formation of the IX as the tunnelling process is very fast (< 1 ps) [Hon14, Ceb14]. The above considerations also explain the overall smaller DOCP⁻ as compared to DOCP⁺ (see Figure 4.16). While the discussion above only considers K and K' valleys, the same arguments should hold for the Q and Q' valleys.

As seen in Figure 4.16b, the X_H DOCP exhibits the small oscillations in F_z of the total DOCP (see black data points in Figure 4.16c). The X_L DOCP decreases slightly from negative to positive fields and starts to increase at the largest positive F_z values. The same trend can be seen for the X_H DOCP except at high positive fields where the X_H DOCP decreases (increases) for a σ^+ (σ^-) excitation. The DOCP as a function of F_z seems to follow the behaviour of the g factors. An increase in the g factor could lead to larger $\Delta E_{e,h}$ and faster $\tau_{e,h}$. Therefore, the DOCP would become more negative, as the scattering from K' to K would become more effective. This correlation, however, would mean that the electron and hole g factor change differently as a function of F_z . The origin of this correlation may be the topic of future studies.

Finally, we show the total DOCP as a function of F_z for several laser powers (see Figure 4.16c). The general trend is that for a decreasing excitation power, the measured total DOCP becomes more negative for either excitation polarisation. The same trend has been observed recently by Förg et al. without discussing the origin of this trend in detail [Fö21]. We argue that the higher state-filling at larger powers leads to an effectively decreased $\Delta E_{e,h}$ and therefore a smaller overall DOCP. Additionally, the DOCP is altered by the influence of the electric field on the IX lifetime. A larger energy at positive fields leads to a drastically decreased IX lifetime (roughly one order of magnitude) [Jau19]. The much smaller lifetime leaves less time for the IX to flip their spin, thus increasing (decreasing) the DOCP⁺ (DOCP⁻). This would explain the bigger influence of the power on the DOCP in positive fields as compared to negative fields.

4.4.6 Tuning the charge carrier density

Lastly, we study the IX behaviour on tuning the charge carrier density in the heterobilayer. Figure 4.18 shows the polarisation-resolved carrier density gatesweeps done with a power of 28.0 μW and at a magnetic field of 9 T. For small and negative n , we observe a strong low energy X_L, while the X_H becomes more prominent on increasing the density. This behaviour can be seen in Figure 4.19a where the extracted peak intensities are plotted as a function of n . Similarly to the electric field gatesweeps, a peak intensity crossover is observed on increasing the charge density. In fact, the crossover happens already at very low electron densities. This is in line with the state-filling argument of the charge carriers. Through the increased Fermi level, states with sufficiently large kinematic momentum are filled, allowing a more efficient X_H recombination. The same effect has been proposed by Miller et al. where they estimate a crossover density of $4 \times 10^{11} \text{ cm}^{-2}$ [Mil17], very similar to our observed crossover behaviour. Generally, on increasing the n-doping, the peak intensities become smaller, probably due to a larger non-radiative decay channel through the interactions with electrons. On p-doping, there seems to be no intensity crossover. Maybe the valence band maximum at the Γ point is much higher in energy than at the K

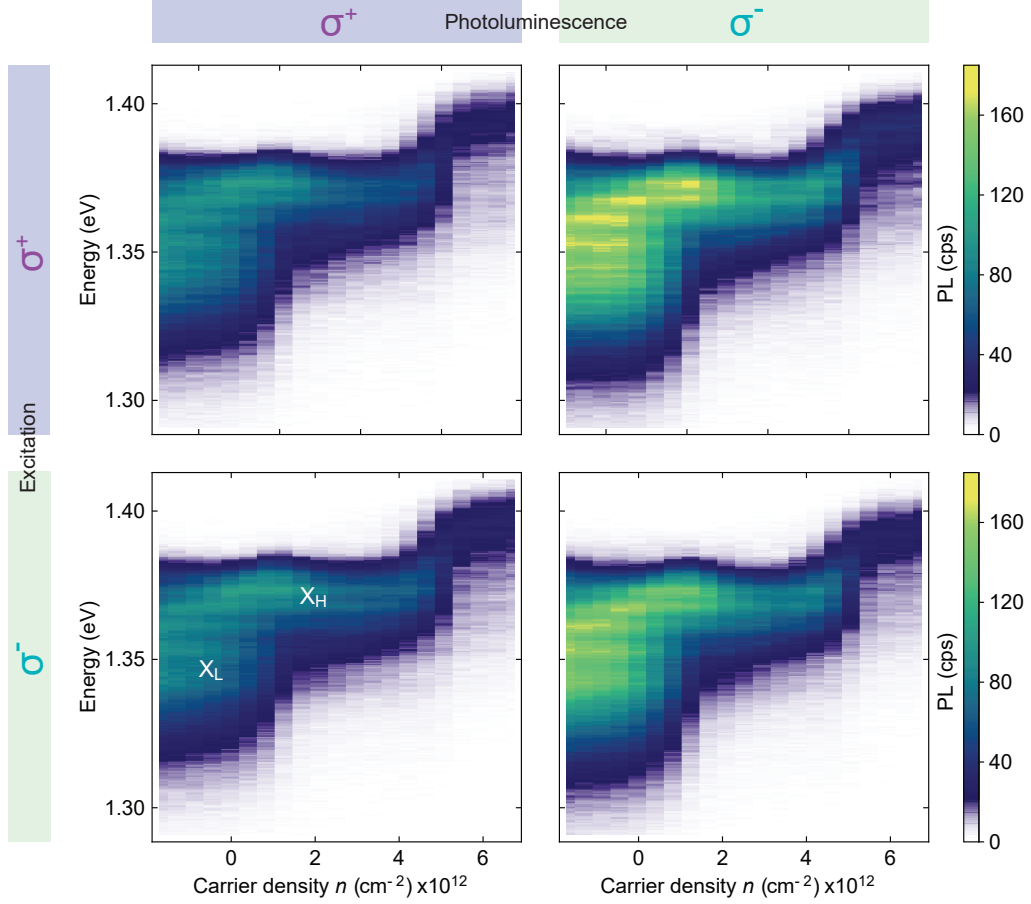


Figure 4.18. Polarisation-resolved PL spectra as a function of charge carrier density n at a magnetic field of 9 T and with a power of 28.0 μW . We scan the gate voltages as $V_{\text{TG}} = 0.68 V_{\text{BG}} + 3.36$ V. According to the simple electrostatics formula for F_z discussed in Section 3.4, this voltage combination corresponds to a moderate and a rather constant F_z of 0.20 MV/cm.

point [Bar22]. Then, for the studied densities, the holes would be mostly filled into the Γ point leading to a small state-filling at the K point.

On increasing the density to over $5 \times 10^{12} \text{ cm}^{-2}$, both peaks suddenly seem to blueshift by about 20 meV. The question arises if both of the peaks still originate from the QK or the KK transition or if they come from IX from higher energy bands due to the large state-filling. Possible transitions would include the triplet KK transition, the momentum-indirect and spin allowed $K'K$ transition, or a transition from the R_h^H point. To answer this question we extract the g factor (Figure 4.19b) and the DOCP (Figure 4.19c) as a function of the density.

Similar to the F_z dependence, we observe a strong variation of the g factors. At the highest densities, a positive g factor of roughly +4 (+6) for σ^+ (σ^-) excitation. The expected g factor of the triplet KK transition is negative and large (-11 [Woz20, Fö21]),

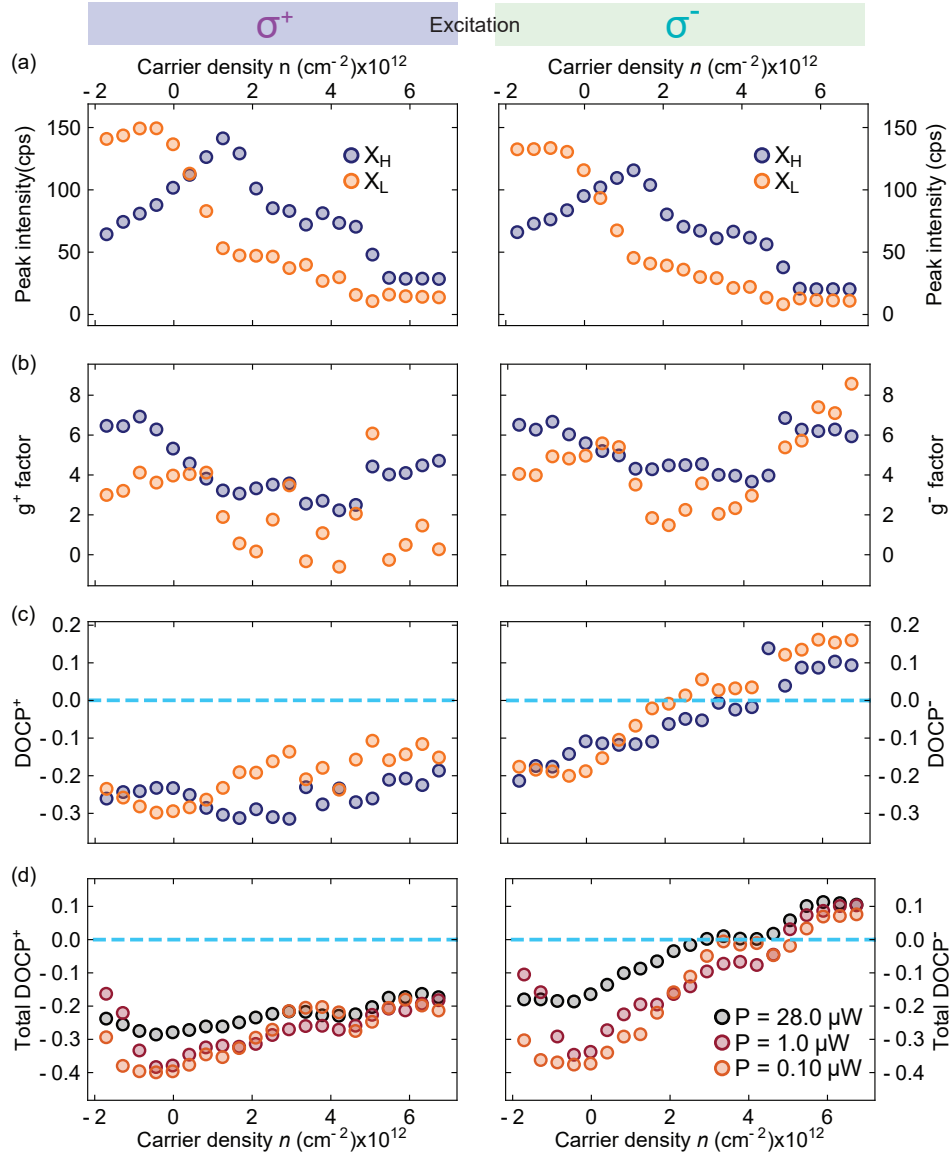


Figure 4.19. (a) Peak intensity by fitting the spectra in Figure 4.18 by a sum of two Gaussians for a σ^- detection, polarisation-resolved (b) g factor and (c) DOCP as a function of carrier density n . (d) Total DOCP as a function of n for several excitation powers. The black points correspond to the data shown in Figure 4.18. The horizontal dashed line in (c) and (d) indicates a DOCP of zero.

while it is positive and large for the spin conserving K/K transition (+13 [Fö21]). For an exciton at the R_h^H point, the g factor is estimated to be -6 [Woz20]. In the monolayer WSe₂ valence band [Gus18] and the monolayer MoSe₂ conduction band [Lar18], the hole and electron g factors are enhanced at the K point at the smallest n , respectively.* The enhancement is due to strong Coulomb interactions, which become screened for an

*It is not clear if this applies to Q point in the same way since it is a hybridised state.

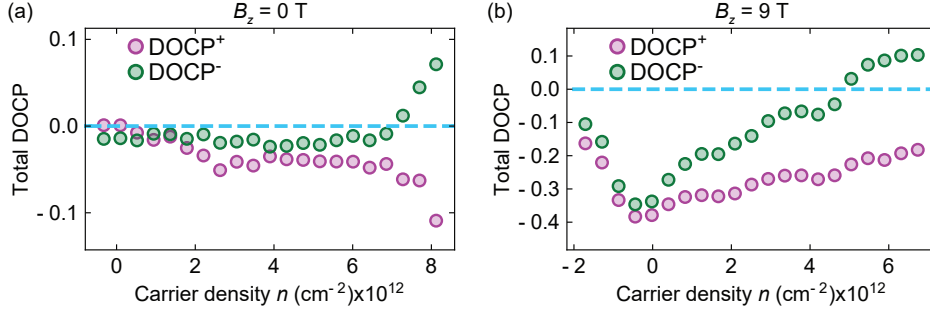


Figure 4.20. Total DOCP as a function of carrier density n with a power of $1.0 \mu\text{W}$ at a magnetic field of (a) 0 T and (b) 9 T . The measurements at 0 T have been performed with a slightly different gate voltage scheme: $V_{\text{TG}} = 0.68 V_{\text{BG}} + 5.04 \text{ V}$, which corresponds to $F_z = 0.37 \text{ MV/cm}$.

increased density. This means that for an increased p-doping (n-doping), the hole g factor g_h (electron g factor g_e) decreases. Using $g_X = g_h - g_e$, the excitonic g factor should decrease for a negative n , while g should increase for a more positive n . At the highest fields, we observe an onset of this behaviour. For moderate n-doping, the X_H g factor oscillates slightly. This behaviour could be related to an ordered crystalline electronic state [Reg20, Wan20a, Tan20b, Shi20, Xu20, Zho21, Hua21, Li21]. Near partial fillings of the moiré potential, interactions between the excitons might be influenced, leading to a change in the effective charge carrier mass. However, the exact influence of the crystalline electronic state on the IX properties is still not clear and warrants further studies. Furthermore, the X_L g factor behaves very differently depending on the excitation polarisation. For σ^+ excitation, it even goes down to a value of zero. As already mentioned in the previous subsection, further studies are needed to understand the g factor evolution in detail.

While the DOCP is negative for small n for both peaks, increasing the density leads to a peculiar behaviour: the DOCP^- crosses from negative to positive values, while the DOCP^+ decreases in magnitude only slightly and stays negative – even at the largest densities. This behaviour is reproduced for several excitation powers as plotted in Figure 4.19d. The triplet KK transition and the transition at the R_h^H point should be co-polarised [Bre20b], which is the opposite of the observed cross-polarised behaviour. Taking the g factor and DOCP findings, we exclude the possibility of a different IX origin for the peaks at a high carrier density.

To investigate the origin of the sudden IX blueshift and the clearly cross-polarised emission at high densities, we compare the DOCP of a density sweep at 0 T and at 9 T (see Figure 4.20). As mentioned before, we observe a very small DOCP at 0 T due to the excitation laser being very off-resonant. Despite the slightly different applied gate voltages, the emission becomes cross-polarised at large n independent of the magnetic field. At 0 T , the DOCP^+ even becomes more negative. The onset of a clear cross-polarised

emission happens at a larger density for $B_z = 0$ T as compared to $B_z = 9$ T. In the previous subsection, we argue that an increased state-filling leads to a larger scattering time and therefore a smaller value of DOCP in a magnetic field. This effect can also be observed in the total DOCP shown in Figure 4.19d. The above argument works well in a large magnetic field (see Figure 4.20b). However, we observe the cross-polarised PL even at 0 T, where we would expect a DOCP of roughly zero (see Figure 4.20a). Hence, the clear cross-polarised emission at large n must have a different origin.

The onset of cross-polarisation corresponds in both cases to the region of the sudden IX blueshift. At these high electron densities, the excitonic energies could be shifted due to band renormalisation effects, which however usually lead to a redshift [Ste14, Kat18]. Another possibility is a sudden change in the effective electric field that would increase the effective dipole moment of the excitons and thus their energy. As discussed in the previous section, a larger IX energy results in a smaller lifetime [Jau19]. On top of that, the lifetime is reduced even more by the presence of additional charge carriers [Jau19]. The much smaller lifetime reduces the spin-flip chance of the IX. This results in a measurable cross-polarisation, even for off-resonant excitation at 0 T. The cross-polarised behaviour is a hallmark of the moiré potential minimum in R-stacking. A similar behaviour can be seen in the electric field sweeps (see Figure 4.16c), especially for a large power: for high IX energies (positive F_z), the DOCP shifts in opposite directions depending on the excitation polarisation. Additionally, the total DOCP in a magnetic field shows oscillation with the carrier density (see Figure 4.19d and Figure 4.20b). These oscillations could be potentially due to special electron filling ratios of the symmetric moiré potential [Zho21].

Unlike other reports, we do not observe the formation of trions at an energy below the IX energy on n-doping the heterobilayer [Jau19, Bae21, BG21, Liu21, Wan21b].

4.5 Conclusion and outlook

In this chapter, we studied the origin of interlayer excitons in an R-stacked MoSe₂/WSe₂ heterobilayer using photoluminescence spectroscopy as a function of excitation power, magnetic field, electric field, charge carrier density, and light polarisation. We observe a two-peak structure over the studied large range of experimental parameters. The high energy peak has a small linewidth, while the low energy peak has roughly double the linewidth. At low powers, the low energy peak dominates the emission spectrum. Above a certain excitation power, the high energy peak dominates the emission spectrum. Using a state-filling argument [Mil17], we attribute the low energy peak to a momentum-indirect QK transition and the high energy peak to a momentum-direct KK transition. Increasing the excitation power leads to a larger phase-space filling of the constituent particles, electrons and holes, activating the momentum-direct transition. So far, this peak combination has only been observed in H-stacked heterobilayers [Mil17, Bar22]. For the first time, we

observe QK and KK IX in an R-stacked MoSe₂/WSe₂ heterobilayer.

Further, we show that the properties of these two peaks (energy, intensity, effective dipole moment, g factor, and degree of circular polarisation) can be tuned as a complex function of the applied experimental parameters. Over the whole parameter range, the interpretation of momentum-indirect and momentum-direct IX can explain most of the observed dependences. Some of the more complex experimental observations, like the g factor behaviour as a function of F_z and n , warrant further studies. For a specific combination of experimental parameters, the momentum-indirect KK transition dominates the emission spectrum. Additionally, we discuss the IX energy shifts in an electric field, which can be potentially explained by giant excitonic polarisabilities. This is an important observation: typically, polarisabilities are neglected when discussing IX Stark shifts. Finally, we show that moiré effects still influence the optical properties of IX even for larger twist angles, where sharp IX emission lines are not observed.

Our study indicates that care has to be taken when studying IX in a MoSe₂/WSe₂ heterobilayer as their properties can be significantly and non-trivially tuned, even for a small change of experimental parameters. This is especially important when trying to optically probe the correlated electronic states in the heterobilayer moiré potential [Liu21] or when studying degenerate many-body states [Sig20] at the onset of excitonic Bose-Einstein condensation [Sno02]. The momentum-indirect exciton being the lower energy particle might play an important role when trying to trap a single exciton in an electrostatic trap, creating a highly tunable single photon emitter [Sch13a, Sha21b].

One of the most important experimental parameters, the twist angle, determines if the electronic bands in the mini Brillouin zone are flat or parabolic (see Section 2.6). Typically, moiré effects are discussed in the small twist angle regime, where the IX exhibit multiple narrow peaks [Sey19, Bae20, Bai20, Li20]. We propose that the broader peaks at larger twist angles ($\sim 3^\circ$) are still confined to the moiré potential. Only for even higher exciton densities as studied in this chapter, IX escape the moiré potential [Wan21a]. A moiré periodicity similar to their size leads to interactions and, therefore, a broad resonance, while each IX is still confined at a potential minimum.

At the root of the many different interpretations for the IX origin exists still a big problem: the moiré supercell (or an atomically reconstructed area) size is much smaller than typical optical measurement areas ($\sim 1 \mu\text{m}^2$). Therefore, most optical experiments average over many moiré supercells. Hence, it is difficult to determine the role of a single moiré supercell (reconstructed area), as spatial inhomogeneities and defects alter the excitonic properties quite significantly on short length scales. For future studies, it will be important to develop optical near-field measurement techniques that allow the study of an isolated single supercell (reconstructed area) [Hua22].

*“Nature’s imagination far surpasses our own.”
Richard Feynman (1965)*

Chapter 5

Giant Stark splitting of an exciton in bilayer MoS₂

Adapted from:

N. Leisgang*, S. Shree*, I. Paradisanos*, L. Sponfeldner*, C. Robert, D. Lagarde, A. Balocchi, K. Watanabe, T. Taniguchi, X. Marie, R. J. Warburton, I. C. Gerber, and B. Urbaszek,

“Giant Stark splitting of an exciton in bilayer MoS₂”,
Nature Nanotechnology **15**, 901 (2020)[†]

*These authors contributed equally.

Transition metal dichalcogenides (TMDs) constitute a versatile platform for atomically thin optoelectronics devices and spin-valley memory applications. In monolayers optical absorption is strong, but the transition energy is not tunable as the neutral exciton has essentially no out-of-plane static electric dipole [Roc18, Ver19]. In contrast, interlayer exciton transitions in heterobilayers are widely tunable in applied electric fields, but their coupling to light is considerably reduced (see Chapter 4). In this work, we show tuning over 120 meV of interlayer excitons (IE) with high oscillator strength in bilayer MoS₂. These shifts are due to the quantum confined Stark effect [Mil84]. Here, the electron is localised to one of the layers yet the hole is delocalised across the bilayer. We optically probe the interaction between intra- and interlayer excitons as they are energetically

[†]N.L. fabricated device 1; S.S. and I.P. fabricated device 2 and sample 3. N.L. and L.S. performed optical spectroscopy measurements on device 1; S.S. and I.P. measured device 2 and sample 3. N.L., L.S., S.S., and I.P. analysed the optical spectra and interpreted the results. I.C.G. performed and interpreted the DFT GW+BSE calculations.

tuned into resonance. Interlayer excitons interact strongly with intralayer B-excitons as demonstrated by a clear avoided crossing, whereas the interaction with intralayer A-excitons is considerably weaker. Our observations are supported by beyond-standard density functional theory calculations including excitonic effects. In MoS₂ trilayers, our experiments uncover two types of interlayer excitons with and without in-built electric dipoles, respectively. Highly tunable excitonic transitions with large in-built dipoles and oscillator strengths will result in strong exciton-exciton interactions and therefore hold great promise for nonlinear optics with polaritons.

The material system homobilayer MoS₂ and its excitonic resonances are introduced in Section 5.1. Then, the Stark effect tuning of the IE is shown in Section 5.2. After discussing the excitonic Zeeman splitting in Section 5.3, the tuning of the inter- and intralayer excitons into resonance is presented in section 5.4. Section 5.5 shows theoretical calculations of the electric field effects on the excitonic resonances. Section 5.6 discusses experiments and calculations for interlayer excitons in a MoS₂ trilayer. Finally, this chapter is concluded with a summary and outlook in section 5.7.

5.1 Introduction

The optical properties of transition metal dichalcogenides (TMDs), such as MoS₂ and WSe₂, are governed by excitons, Coulomb bound electron-hole pairs [Che14, Wan18a]. High quality van der Waals heterostructures show close-to-unity, gate-tunable reflectivity of a single MoSe₂ layer [Scu18, Bac18], variation of the transition energies of interlayer excitons over a broad wavelength range in heterobilayers [Riv15, Joe21] and valley polarised exciton currents [Unu19].

In heterobilayers, the interlayer exciton is formed with the electron either in the top or in the bottom layer depending on the initial stacking [Riv15]. Reports on interlayer excitons in heterobilayers rely mostly on photoluminescence emission [Nag17b, Fö19, Riv15, Unu19, Joe21] as interlayer absorption is very weak. In 2H-stacked MoS₂ homobilayers, the situation is different. First, a strong feature in the absorption up to room temperature was observed in earlier studies on MoS₂ bilayers [Slo19, Cal18, Ger19, Nie19, Car19] and interpreted as an interlayer exciton, as theoretically predicted by Deilmann and Thygesen [Dei18]. Second, in principle, two energetically degenerate interlayer excitons can form with the electron residing in either the top or the bottom layer [Pis19], whereas the hole is delocalised [Gon13].

The band structure of homobilayer MoS₂ at the K point is sketched in Figure 5.1a. Exfoliated homobilayer MoS₂ exhibits a 2H-stacking, *i.e.* the top layer (L₂) is rotated by 180° with respect to the bottom layer (L₁), which results in the spin-ordering of the bands being inverted in L₂ compared to L₁. Intralayer A-excitons (B-excitons), form between the VB (VB₋₁) state and the CB (CB₊₁) state. For the interlayer excitons IE₁ (IE₂), the

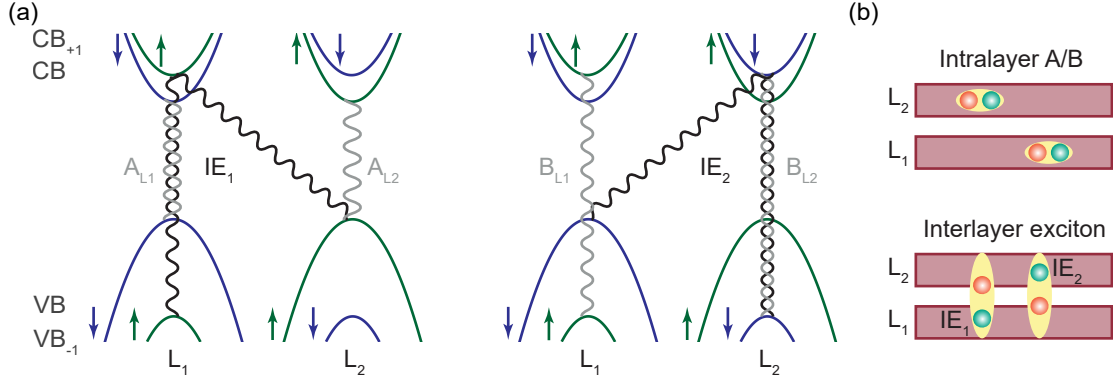


Figure 5.1. Band diagram and schematics of intralayer and interlayer excitons in homobilayer MoS₂ (a) at the K point and (b) in real space (adapted from [Ger19]). Intralayer resonances A and B correspond to excitons where the electron and the hole reside in the same layer. Intralayer excitons can form in each of the two layers, denoted by the subscript L₁ (L₂) for layer 1 (layer 2). Interlayer excitons IE₁ and IE₂ consist of an electron confined in one layer and a hole delocalised over both layers. Wavy lines connect the states involved in the formation of the different excitonic complexes at the K point. (b) Spatial extent of intra- and interlayer excitons in the bilayer. The electrons (holes) are sketched in green (red).

hole contribution comes from the VB state of L₂ (L₁), partially hybridised with VB₋₁ of L₁ (L₂), while the well-localised electron lies in the CB₊₁ state of the other layer L₁ (L₂). The interlayer exciton contains, already in the absence of an applied electric field, a strong B-intralayer component, explaining its large oscillator strength (see also [Dei18, Ger19]). The spatial extent of intra- and interlayer excitons in homobilayer MoS₂ is sketched in Figure 5.1b.

Here, we investigate excitons in bilayer MoS₂ with both strong light-matter interaction and high tunability in external electric fields. Our experiments focus on momentum-direct intralayer and interlayer excitons originating from valence and conduction bands around the K point.

5.2 Energetic tunability of interlayer excitons

We integrate MoS₂ homobilayers in devices (1 and 2) with top and bottom gates for applying a static out-of-plane electric field F_z (see Appendix B for an overview of the samples and their fabrication process). Figure 5.2a shows an optical microscope image of device 1. We utilise a dual-gate device structure as sketched in Figure 5.2b to change F_z while keeping the charge carrier density low and constant. A weak broadband source is illuminating the device locally. The optical reflectivity was measured at low temperature ($T = 4.2$ K) using a home-built confocal microscope (see Chapter 3.7). The imaginary part of the optical susceptibility $\text{Im}(\chi)$, a measure of the absorption, was deduced from the differential reflectivity signal $\frac{\Delta R}{R_0}$, $\Delta R = R - R_0$, using a Kramers-Kronig relation, where R is the reflectivity spectrum obtained on the MoS₂ flake and R_0 is the reference spectrum

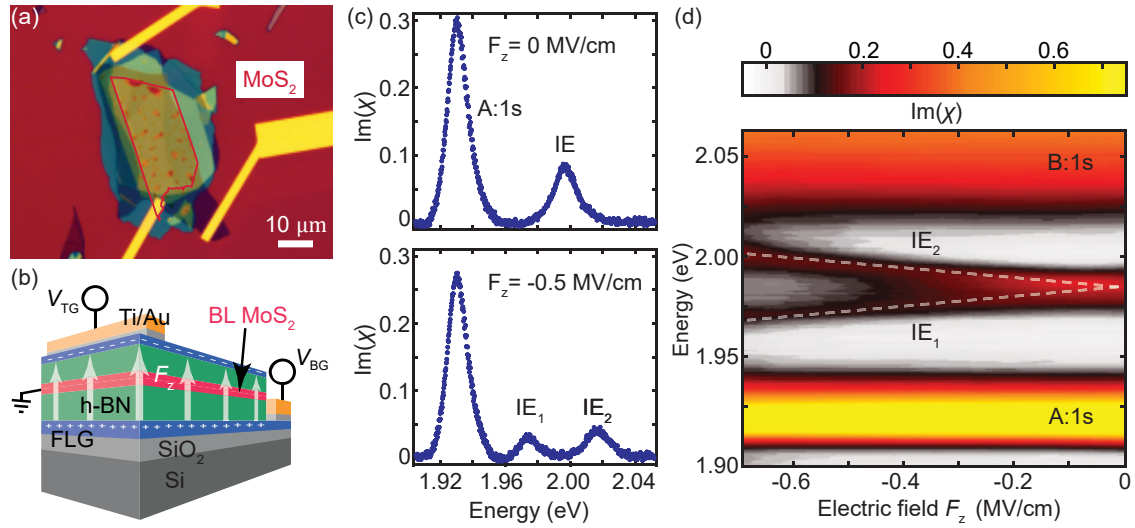


Figure 5.2. (a) Microscope image of device 1 highlighting the bilayer MoS₂ region. (b) Three-dimensional schematic of device 1, consisting of a MoS₂ homobilayer encapsulated between two hexagonal boron nitride (hBN) flakes. Few-layer graphene (FLG) serves as top and bottom gate, while a direct Ti/Au contact to the MoS₂ is used to ground the bilayer. Voltages to the top and bottom gates (V_{TG} and V_{BG}) are applied to create a uniform electric field F_z across the device. (c) Typical absorption spectra recorded without ($F_z = 0$ MV/cm) and with ($F_z = -0.5$ MV/cm) an applied electric field, extracted from Figure 5.3a. (d) Colour-map of the absorption spectra of a bilayer MoS₂ heterostructure (device 2 showing the Stark shift of the interlayer excitons at small electric fields. The intralayer A- and B-excitons (A:1s and B:1s) and the two branches of the interlayer A-resonances (IE₁ and IE₂) are labelled.

obtained at a high electron density (see Chapter 3.5.1 and Appendix Section D.1 for a detailed description).

Figure 5.2d and Figure 5.3a show typical absorption spectra as a function of the electric field F_z , recorded on device 2 and device 1. Three prominent transitions can be clearly identified at zero electric field ($F_z = 0$ MV/cm): the intralayer A- and B-excitons (A:1s and B:1s) near 1.93 eV and 2.10 eV, respectively, and the interlayer A-exciton (IE) at 2.00 eV [Ger19]. On applying an external electric field F_z , the IE splits into two well-separated branches, as seen in Figure 5.2c for $F_z = -0.5$ MV/cm. Using the area under the peaks in Figure 5.2d as a rough measure of the relative absorption strength (we take A:1s as 100%), we see that at $F_z = 0$ MV/cm the IE is about 30% compared to the intralayer A:1s. Remarkably, at finite electric fields $F_z = -0.5$ MV/cm, the absorption strength does not vanish but remains rather strong, with a combined 24% from IE₁+IE₂ relative to the A:1s. Our experiments clearly show that the absorption peak IE, initially at 2.00 eV, corresponds to interlayer exciton resonances with out-of-plane oriented electric dipoles: The carriers clearly do not reside within the same layer. For the intralayer excitons, on the other hand, the energy shift with applied electric field is negligible, as in the case for excitons

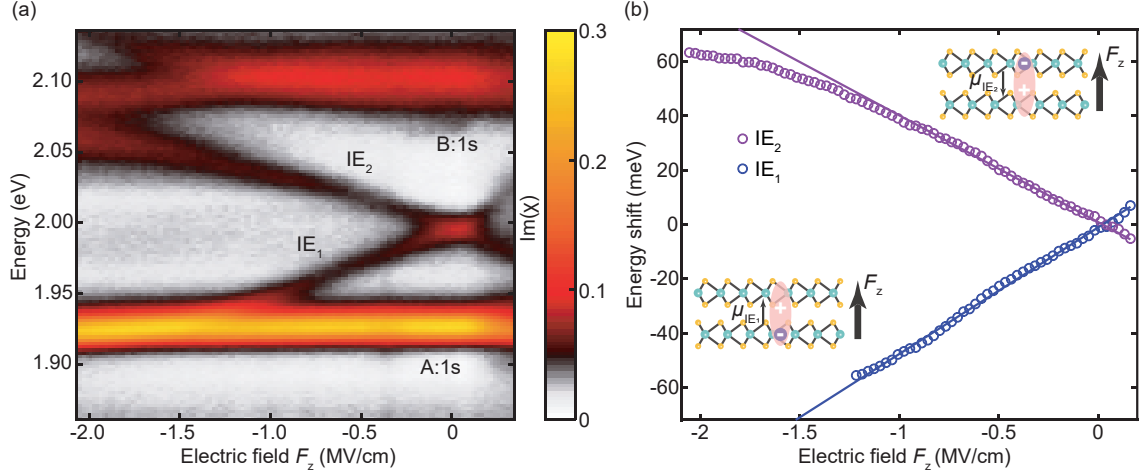


Figure 5.3. (a) Colour-map of the absorption spectra of device 1 as a function of the electric field F_z applied perpendicular to the heterostructure. (b) Stark shift of the interlayer A-excitons as a function of F_z , extracted from the spectra in panel (a). The solid blue and purple lines are linear fits to the experimental data points at small/moderate electric fields ($F_z = 0.1$ MV/cm to $F_z = -1$ MV/cm). Insets show schematics of interlayer excitons in homobilayer MoS₂. An electron localised in one layer interacts with a hybridised hole state to form an interlayer exciton. The direction of the dipole moment depends on the location of the electron, either in the bottom (μ_{IE_1}) or top (μ_{IE_2}) layer.

in monolayers [Roc18, Ver19]. As F_z is increased, the energy difference between the IE₁ and IE₂ states reaches a value of ~ 120 meV, covering a wide spectral range, spanning the energy range between the intralayer A- and B-excitons.

For small to moderate electric fields, before significant interaction between the interlayer states and the A- and B-excitons, we observe a linear energy shift with F_z for both peaks, IE₁ and IE₂, suggesting a first-order Stark shift caused by the static electric dipole moments across the MoS₂ bilayer (Figure 5.3). In Figure 5.3b we plot the transition energies extracted from Figure 5.3a as a function of the applied field F_z and perform a linear fit. We extract large dipole moments of $\mu_{\text{IE}_1} = (0.47 \pm 0.01) e \cdot \text{nm}$ and $\mu_{\text{IE}_2} = (-0.39 \pm 0.01) e \cdot \text{nm}$ with e being the electron charge. Applying higher electric fields in our experiment, we discover that the shifts deviate from a simple linear Stark shift, reflecting, as discussed below, very different interactions of the interlayer excitons with the A- and B-intralayer excitons. For the analysis of device 2, shown in Figure 5.2d, we extract a dipole value with a lower bound of about $0.3 e \cdot \text{nm}$.

In terms of the magnitude, the large extracted dipole moments are similar to results on interlayer excitons in MoSe₂/WSe₂ heterobilayers as determined by photoluminescence [Unu19, Nag19, Riv15, Joe21]. For comparison with other homobilayer systems, interlayer excitons have very different characteristics depending on the TMD material [Wu13, Jon14]. For WSe₂ bilayers, reports on interlayer excitons focus on transitions indirect in momentum

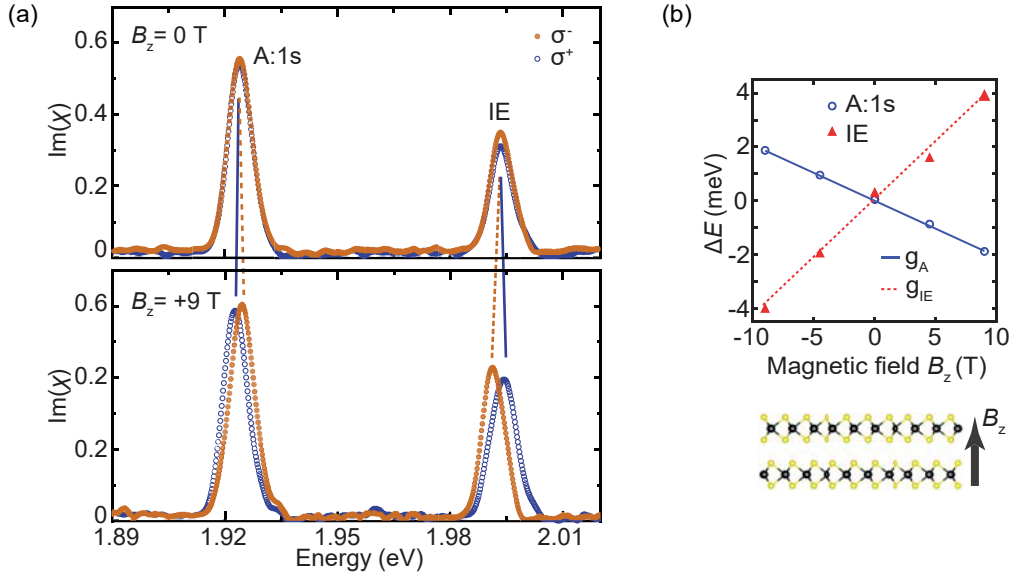


Figure 5.4. Magneto-optics of bilayer MoS₂ at zero electric field ($F_z = 0$ MV/cm). (a) Polarisation-resolved absorption spectra of bilayer MoS₂ (device 3) at $B_z = 0$ T (top) and $B_z = +9$ T (bottom). The orange and blue curves correspond to σ^- - and σ^+ -polarisation. Intra- and interlayer A-excitons (A:1s and IE) are labelled. (b) Energy difference ΔE between the two circular polarisations for the intralayer (blue) and interlayer (red) excitons at different magnetic fields B_z measured in device 1. The g factors of the two transitions are extracted from linear fits. The intralayer A-exciton has a negative g factor, $g_A = -3.6 \pm 0.1$, while the interlayer excitonic g factor is approximately twice as large with opposite sign, $g_{IE} = 7.4 \pm 1.1$. The errors in the g factors represent a 95% confidence interval that is calculated from the uncertainty of the fitting parameter.

space linked to the indirect band gap energetically below the direct K-K transitions [Lin18, Wan18b]. In the case of MoSe₂, K-K interlayer excitons are observed with similarities to the case of MoS₂, but with significantly lower oscillator strength [Hor18, Shi20, Sun20]. This is mainly due to the larger valence band spin-orbit splitting of MoSe₂ compared to MoS₂, which makes hole delocalisation over both layers and hence the formation of interlayer excitons less favourable [Gon13]. Signatures of interlayer excitons in bulk 2H MoSe₂ have been reported, but the same study did not find K-K interlayer exciton signatures for bulk 2H WSe₂ [Aro18].

5.3 Excitonic Zeeman splitting in a magnetic field

We confirm the interlayer character of the IE_{1,2} excitons also in magneto-optics: Interlayer excitons show a larger g factor with opposite sign compared to intralayer excitons [Aro17].

Magneto-optics is a powerful tool for line identification and transition energy tuning [Nag19]. Applying a magnetic field B_z perpendicular to the sample plane lifts the valley degeneracy (valley Zeeman effect) and allows the measurement of the intra- and interlayer

exciton g factors. Figure 5.4a shows the polarisation-resolved absorption spectra of bilayer MoS₂ (device 3) without (top) and with (bottom) an external magnetic field. At $B_z = 0$ T (top), there is no difference between the two circular polarisations (σ^+ - and σ^-), while at $B_z = +9$ T (bottom), the valley degeneracy is lifted. For a more detailed analysis of the Zeeman splitting, magneto-optical measurements were performed on device 1 for different magnetic field values (at $F_z = 0$ MV/cm), presented in Figure 5.4. The intralayer exciton A:1s, which exhibits a negligible Stark shift, shows a negative Zeeman splitting of about 2 meV at $B_z = +9$ T, which changes sign as the magnetic field direction is reversed. The Zeeman splitting for the interlayer exciton IE is about 4 meV at $B_z = +9$ T, and the sign is opposite compared to the intralayer case. The Zeeman splittings of the two excitonic transitions are defined as $\Delta E_A = E(\sigma^+) - E(\sigma^-) = g_A \mu_B B_z$ and $\Delta E_{IE} = g_{IE} \mu_B B_z$ with $E(\sigma^+)$ and $E(\sigma^-)$ being the transition energies for the two circular polarisations, g_A and g_{IE} are the excitonic g factors, and $\mu_B = 58 \mu\text{eV/T}$ is the Bohr's magneton. From the data presented in Figure 5.4b, we deduce a negative Landé g factor of around -3.6 for the intralayer exciton A:1s and a positive g factor of about $g_{IE} \approx 7.4$ for the interlayer exciton [Slo19]. These g factors, g_A and g_{IE} , are obtained from linear fits of ΔE versus B_z , divided by μ_B in Figure 5.4b.

The larger Zeeman splitting of interlayer excitons with opposite sign compared to intralayer excitons has been observed for other multilayer systems [Aro17]. The valley contributions to the Zeeman splitting for an optical transition within the same layer cancel (at least partially) for intralayer excitons, whereas they are additive for interlayer excitons. A more detailed discussion of excitonic Zeeman splittings is given in Subsection 2.7.2.

The reflectivity contrast, constructed as the difference between the differential reflectivity spectra recorded for σ^+ - and σ^- -polarisation ($\Delta R/R_0(\sigma^+) - \Delta R/R_0(\sigma^-)$), gives also information about the g factors (sign and amplitude) of the individual resonances. Figure 5.5a maps the differential reflectivity contrast between σ^+ - and σ^- -polarisation at $B_z = +9$ T when applying an external electric field across the MoS₂ bilayer. As can be deduced from our polarisation-resolved absorption measurements at zero electric field, dips in the reflectivity contrast spectra correspond to excitonic resonances with negative g factors ($g < 0$), positive values are related to resonances exhibiting a positive g factor ($g > 0$). Figure 5.5b compares the absorption (top) and differential reflectivity contrast spectrum (bottom) at zero electric field ($F_z = 0$ MV/cm), extracted from the colour-map in Figure 5.5a along the blue dashed line. The intralayer A:1s and B:1s exciton resonances (with negative g factors) and the interlayer exciton (IE) resonance (with positive g factor) can be identified. Additionally, a transition ~ 30 meV below the intralayer B:1s exciton (at $F_z = 0$ MV/cm) can be observed, labelled as BIE. This small feature, highlighted by the black dashed square in Figure 5.5a, can be uncovered in the reflectivity contrast plot, as the difference in reflectivity between σ^+ - and σ^- -polarisation is nearly zero for

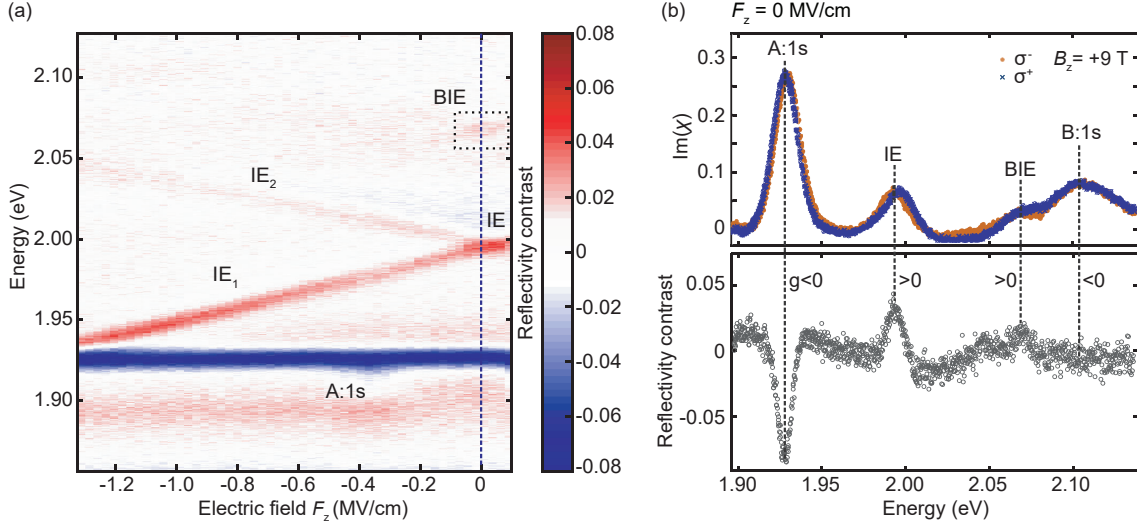


Figure 5.5. Absorption and differential reflectivity contrast in a magnetic field ($B_z = +9$ T). (a) Colour-map of the differential reflectivity contrast between σ^+ - and σ^- -polarisation ($\Delta R/R_0(\sigma^+) - \Delta R/R_0(\sigma^-)$) at $B_z = +9$ T on applying an external electric field across the MoS₂ bilayer (device 1). A negative value, corresponding to a dip in the differential reflectivity contrast spectrum, reflects a negative g factor, while a positive value reflects a positive g factor. In this panel, we can also observe a transition ~ 6 meV below the intralayer B-exciton (at $F_z = 0$ MV/cm), labelled as BIE. (b) Absorption (top) and differential reflectivity contrast spectrum (bottom) at zero electric field ($F_z = 0$ MV/cm). The bottom panel shows the data extracted along the blue dashed line in (a). The intralayer A- and B-excitons (A:1s and B:1s) and the two interlayer resonances (IE and BIE) are labelled.

the B-intralayer exciton. This is due to the fact that the B-exciton transition is spectrally broad and its Zeeman splitting is small compared to its linewidth. The positive g factor of the BIE transition as well as its tunability with electric field clearly indicates an interlayer character [Slo19]. However, with increasing electric field, the BIE resonance loses oscillator strength and, thus, cannot be observed for higher field values than $F_z = -0.2$ MV/cm.

For interlayer excitons, Stark effect tuning over tens of meV could therefore be combined in principle with an additional magnetic field splitting of the two interlayer Zeeman states. Our knowledge about interlayer versus intralayer magneto-optics is crucial for the analysis and discussion of our bilayer and trilayer results.

5.4 Tuning interlayer and intralayer transitions into resonance

Owing to the very large tunability shown in Figure 5.2d and Figure 5.3a for the interlayer transition energy, we are able to tune the interlayer excitons into resonance with the A- and B-intralayer excitons. The interactions are very different. This can be directly seen by comparing Figure 5.6a ($IE_2 \leftrightarrow B$) with 5.6b ($IE_1 \leftrightarrow A$). A very detailed analysis of the

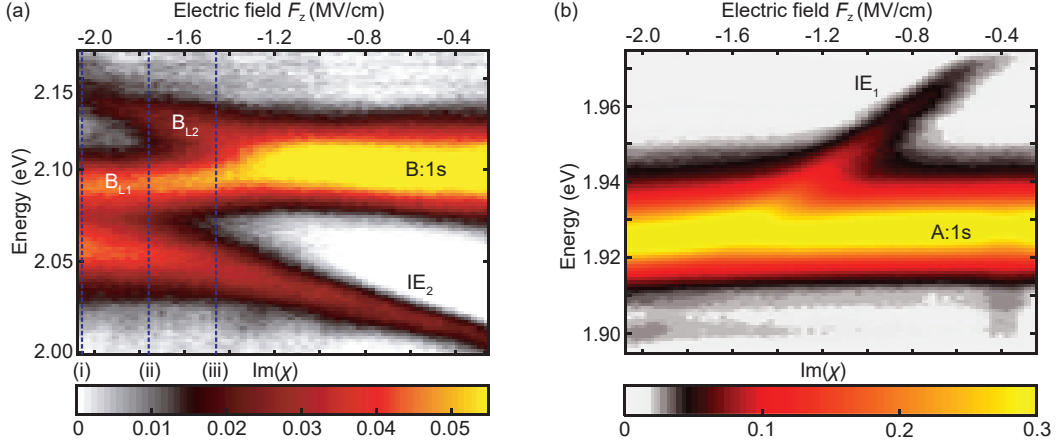


Figure 5.6. Electric field dependence in a magnetic field ($B_z = +9$ T). (a) Colour-map of the absorption spectra (σ^+ -polarisation) centred around the intralayer B-exciton. B_{L1} and B_{L2} are the intralayer excitons residing in layer 1 (L_1) and 2 (L_2), respectively. Dashed vertical lines show spectra reproduced in Figure 5.7c. Experiments were performed at $B_z = +9$ T for greater mechanical stability of the setup. (b) Colour-map of the absorption spectra (σ^+ -polarisation) centred around the intralayer A-exciton, showing a very small avoided crossing with IE_1 .

different couplings is given in Chapter 6.

In Figure 5.6b, the IE_1 transition merges with the A-exciton line at around -1.3 MV/cm; at the highest electric fields in these experiments, the absorption contrast of IE_1 decreases (a consequence of the large change to the dielectric constant induced by the strong A-exciton), falling below the noise. This points to a small avoided crossing of the weak IE_1 exciton with the strong A-exciton. On the one hand, the IE-A coupling is less than the linewidth of the A-exciton – if this were not the case then a clear avoided crossing would be visible. On the other hand, the coupling is not zero - there is clearly a change in the dispersion of the A-exciton at the electric fields where the IE and A-excitons are close in energy. This point can best be probed on samples with a smaller linewidth. Our estimate for the coupling of the IE-A excitons on the present sample is 5 ± 3 meV. Chapter 6 introduces a model based on two coupled and driven optical dipoles that gives us a better understanding of the IE-A coupling behaviour. Using this model, we find an absolute coupling strength of 3.5 meV which is in line with the estimate given above.

In contrast, tuning the upper interlayer branch IE_2 energetically close to resonance with the B-exciton leads to a clear avoided crossing, see data in Figure 5.6a and extracted transition energies in Figure 5.7a. For the B-exciton, we can distinguish two resonances associated with intralayer excitons in the two different layers L_1 and L_2 , labelled as B_{L1} and B_{L2} . The transition B_{L1} does not share any state with IE_2 as evidenced by a nearly constant transition energy and integrated absorption strength in this electric field range, see Figure 5.7b,c. Importantly, as IE_2 has a strong B_{L2} -intralayer component, see scheme in

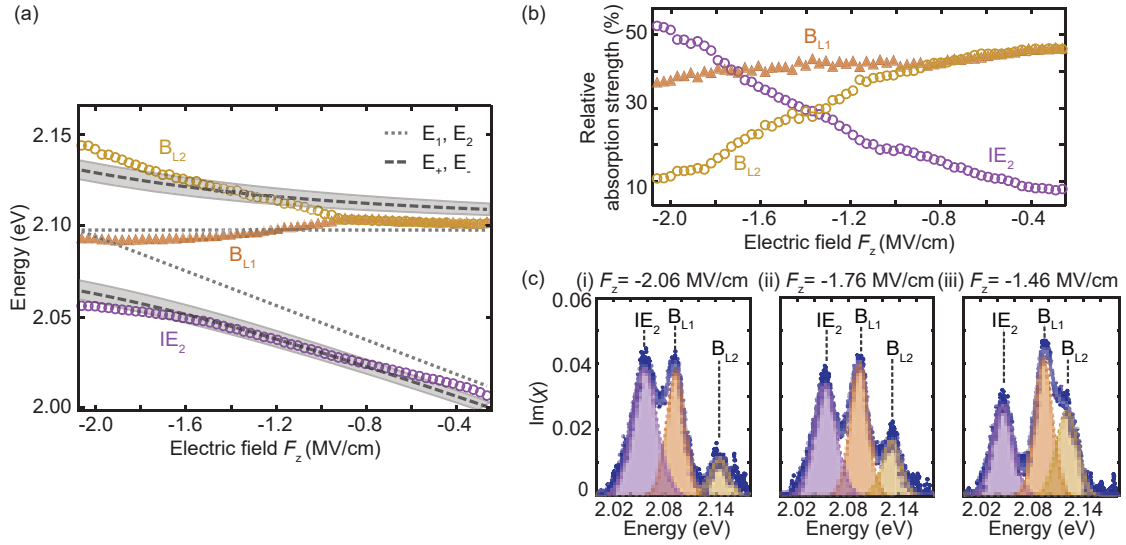


Figure 5.7. (a) Peak positions versus applied electric field extracted from spectra shown in Fig 5.6a, the transitions IE_2 and B_{L2} show a clear avoided crossing. The dotted lines show the peak energy evolution expected without coupling. E_1 is the mean energy of B_{L2} and E_2 is the unperturbed energy of IE_2 . The dashed lines are a fit to the two coupled eigenmode energies E_{\pm} using equation 5.2. The fit yields a coupling energy W of 33 ± 5 meV; the shaded area corresponds to the uncertainty in W . (b) Evolution of the integrated absorption strength of IE_2 , B_{L2} and B_{L1} confirming the mixing of IE_2 and B_{L2} ; here 100% corresponds to the sum of these three transitions. (c) Spectra from data of Fig 5.6a with the three-peak fit that determines the transition energies and the relative absorption strengths which are plotted in panels (a) and (b).

Figure 5.1a, these states interact strongly. There are two experimental signatures for strong coupling between B_{L2} and IE_2 . First, we observe a clear avoided crossing in Figure 5.7a on plotting the transition energies as a function of the applied field. Second, B_{L2} and IE_2 exchange strength - B_{L2} is initially strong but then weakens; IE_2 is initially weak but then strengthens, becoming the dominant exciton at large electric fields. This can be clearly seen in plotting the evolution of the absorption strength in Figure 5.7b.

The anticrossing of IE_2 and B_{L2} (Fig 5.7a) is modelled by a simple two-level system, taking into account the effect of an external perturbation (here the electric field) on this system. Two unperturbed resonances with energies E_1 and E_2 , respectively, are coupled by an interaction term W . The corresponding Hamiltonian of this two-level system can then be written as

$$H = \begin{pmatrix} E_1 & W \\ W & E_2 \end{pmatrix}. \quad (5.1)$$

Diagonalising the modified Hamiltonian after the perturbation and solving for the new

eigenstates E_{\pm} gives

$$E_{\pm} = \frac{1}{2}(E_1 + E_2) \pm \sqrt{\frac{(E_1 - E_2)^2}{4} + |W|^2} . \quad (5.2)$$

For our system, E_+ corresponds to the fitted energy of B_{L2} , and E_- corresponds to the fitted energy of IE_2 . Furthermore, we choose E_1 to be the mean energy of B_{L1} , constant in electric field. E_2 is set to be the unperturbed energy of IE_2 . The zero electric field energy of E_2 is extracted from the measurements. The Stark shift of E_2 is taken to be -0.47 e-nm, which is the shift extracted for IE_1 in Figure 5.3, but with opposite sign. Here, we assume the Stark shift of IE_1 , since its shift is expected to be closer to the unperturbed energy shift, a consequence of the strong IE-B coupling influencing the IE energies in a large energy range. In other words, the smaller Stark shift of IE_2 compared to IE_1 can be explained by the influence of the interaction W on the IE_2 resonance, already present for small electric fields.

In Figure 5.7a, the energies of B_{L2} and IE_2 are fitted simultaneously by Equation 5.2 with W being the only variable. The best fit is chosen to be the fit with the smallest minimum mean square error (MMSE). Note that the fit to the data with a two-level system is rather rigid and leads to a certain error. A source of error could be a small influence of the B_{L1} resonance on the overall interaction, which is not taken into account in our model. To accommodate for all uncertainties, we assume that the error interval of W includes all coupling strength values where the MMSE is within 50% of the minimum MMSE value. This calculation leads to an error of approximately ± 5 meV. Using this simple model gives us a coupling strength between the B_{L2} and IE_2 resonances of $W = (33 \pm 5)$ meV.

The simple two-level model can fit the energies of the coupled resonances very well. However, it does not describe the absorption strength evolution in the coupling region which is quite different for the IE-A and IE-B couplings (see Figure 5.6). Additionally for the IE-B coupling, at the F_z where the two transitions are closest in energy, the absorption strengths are quite different (see Figure 5.7b). In a classical avoided crossing one could expect that the two transitions have the same strength in this field. Therefore, a more detailed coupling model is developed and presented in Chapter 6, where we find that interference effects between the two coupled resonances can reproduce the measured absorption strength evolution.

5.5 Theoretical calculation of the electric field effects

The main observations of the experiments on devices 1 and 2 are (i) the splitting and very large energy shifts of the IE transitions in an applied electric field, (ii) anticrossing of the IE_2 with the B-intralayer exciton, and (iii) small avoided crossing of the IE_1 with the

A-intralayer exciton. The comparatively large Stark shift and the strong enough oscillator strength for absorption experiments have been initially discussed by Deilmann et al. [Dei18] using GW+BSE calculations. The target here, also using GW+BSE calculations, is to develop a semi-quantitative understanding of the observed effects (i) and (ii) by calculating the mixing of intra- and interlayer exciton components as a function of F_z . The approach is based on the inclusion of the applied electric field as a perturbation in the band structure calculations, similar to the approach in [Dei18, Fan16, Liu12]. Please note that only freestanding 2H MoS₂ bilayers are considered in the calculations, i.e. placed in vacuum, as the aim is to qualitatively reproduce the main trends. When applying an electric field, we observe a global shift for L_1 of the relevant conduction and valence bands at the K point down in energy with respect to L_2 , marked as ΔE_{Stark} (see Figure 5.8b for the electric field configuration and Figure 5.8c for a bandstructure schematic). A more realistic GW picture of this effect on the band structure is given in Appendix Section D.2. From the sketch in Figure 5.8c, it is thus clear that the IE transitions will split in energy: Transitions involving the L_2 valence bands and the conduction bands in L_1 will lower in energy, whereas transitions involving the L_1 valence bands and L_2 conduction bands will increase in energy.

After including excitonic effects, we are able to calculate the absorption (in Figure 5.8a) which looks very similar to our measurements at small electric fields (see Figure 5.2d). Figure 5.8d demonstrates how the IE transition energy changes, roughly linearly, with the applied electric field. At large electric field values of 5 MV/cm, we see two main groups of transitions: At the low energy side, the IE_1 is close to the A-exciton energy and, at the high energy side, the IE_2 is close to the B-exciton as in [Dei18]. Our calculations show relative IE oscillator strengths (versus A:1s) relatively close to experiments, despite neglecting the environmental dielectric constant variations. There are essentially no transitions in the energy range in-between. We refrain in our calculations to comment on any higher electric field values as our initial assumption to treat the electric field as a perturbation, in comparison with other energy splittings in the band structure, reaches its limits.

The exact nature and mixing of the absorption peaks, calculated in Figure 5.8a, contain information on the evolution of the exciton states with electric field (see Appendix Section D.2 Tables D.1 and D.2). We can use this knowledge to analyse the results in Figure 5.6: For finite electric fields, the intralayer A-exciton contains a very small IE component that remains small as the field increases. Our theory indicates very little mixing between the A-intralayer exciton and the IE, consistent with the experiments in Figure 5.6b. In Chapter 6 we show that the A-exciton is coupled indirectly to IE through the B-exciton. Concerning interactions with the intralayer B-exciton, the IE exciton, with a delocalised hole, is mixed with the intralayer B-exciton as they share the same valence states. This was suggested in [Ger19] to explain the surprisingly high oscillator strength of the IE transitions. In our calculations, we see that the mixing between the higher energy IE

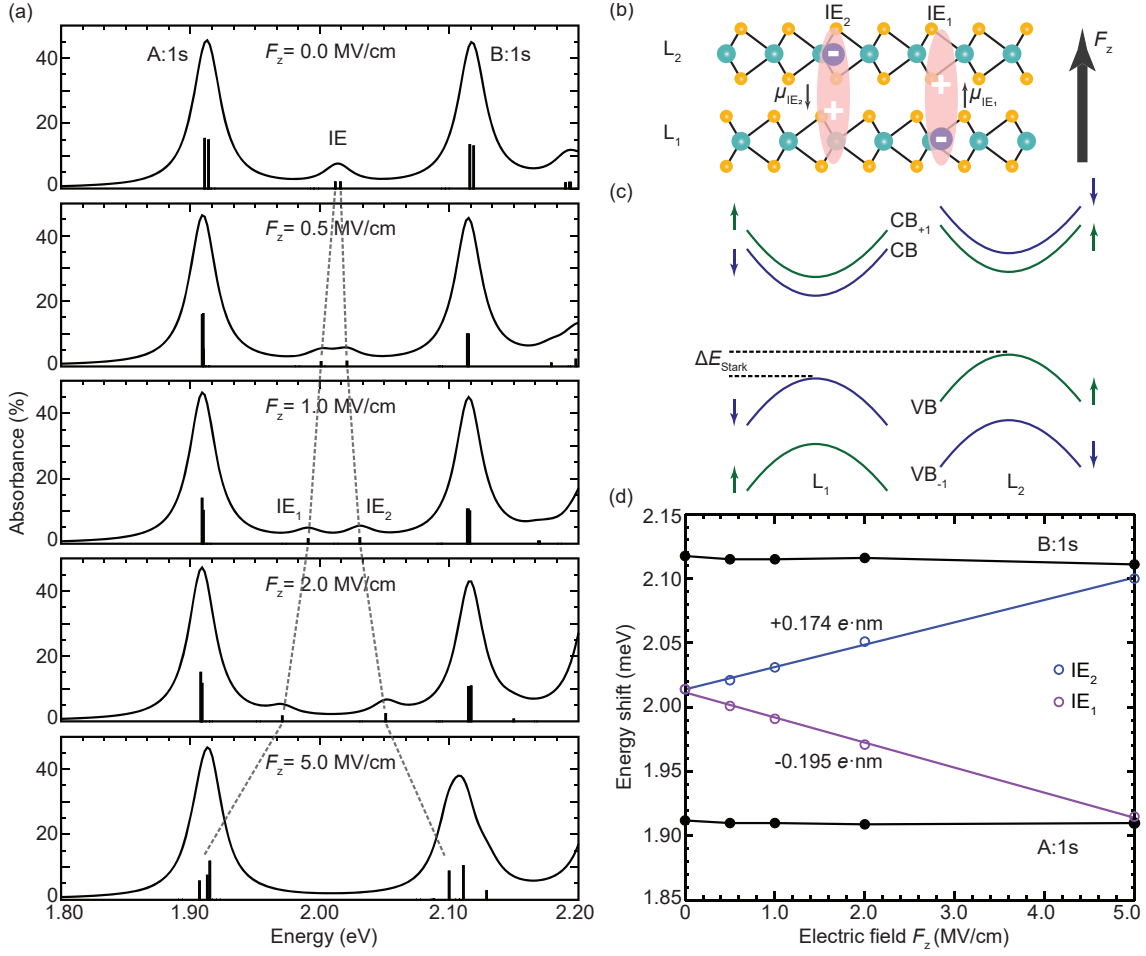


Figure 5.8. Beyond-DFT calculations of the electric field effects on the band structure and excitonic properties of a 2H MoS₂ bilayer. (a) Absorption spectra as a function of the applied electric field F_z . DFT-GW-BSE calculations determine both the excitonic energy position and absorption strength which are plotted as the vertical black lines. The numerical precision of the calculations is estimated to be of the order of ± 5 meV (see computational settings in Appendix Section D.2) such that any splitting below this value does not have any physical significance. For comparison with the experiment, an artificial broadening on the order of 10 meV is introduced for each transition. This results in the spectra shown with solid black lines; the three main transitions A:1s (intralayer A), IE (interlayer), and B:1s (intralayer B) are labelled. (b) Structural model of the 2H bilayer stacking and electric field direction. (c) Schematic of the band structure modification due to the application of F_z showing a global shift, denoted ΔE_{Stark} , between the distinct band structures of the two layers (see Appendix Section D.2 for detailed results on GW band structure calculations). (d) Evolution of the excitonic peak positions as a function of the electric field, and the corresponding dipole moment estimates for IE₁ and IE₂ excitons.

branch and the B-exciton becomes stronger as the electric field amplitude is increased (see Appendix Section D.2 for a detailed description of each component). We suggest that this clear admixture of the IE-exciton with the B-exciton in our calculations is the origin of the observed avoided crossing between IE₂ and B_{L2} shown in Figure 5.6a and Figure 5.7a,

as well as the enhancement of the absorption strength of IE₂, shown in Figure 5.7b. As IE₂ shares the same conduction band state only with B_{L2} and not with B_{L1}, there is an anticrossing between IE₂ and the B:1s resonance in L₂ (B_{L2}), but not the B:1s resonance in L₁ (B_{L1}). Our GW+BSE calculations therefore capture the main experimental findings, and aid our understanding of the interactions of the IE with the intralayer A- and B-exciton resonances, and the observed IE Stark shift. The calculated excitonic absorption strengths and their composition is discussed in more detail in Chapter 6.

5.6 Interlayer excitons in MoS₂ trilayers

The combined approach using experiments and theory is applied to uncover and manipulate novel exciton species in a more complex system, namely MoS₂ homotrilayers. In contrast to inversion symmetric MoS₂ bilayers, trilayers could be advantageous in nonlinear optics due to the broken inversion symmetry that gives rise to a non-vanishing second-order nonlinear susceptibility. In the trilayer system, we uncover additional types of interlayer excitons as compared to the bilayer in our experiment: At zero electric field, two different interlayer transitions appear in absorption, labelled IE* and IE in Figure 5.9a. We show absorption measurements as a function of the electric field and make a surprising observation: Whereas IE splits into two branches (IE₁ and IE₂) as for the bilayer studies, IE* does not show any measurable splitting and hence, a negligible or, at least, a very small in-built electric dipole moment. Interestingly, we make the same observation in our GW+BSE calculations, shown in Figure 5.9c.

We can explain the different behaviour in applied electric fields by analysing the microscopic origin of IE and IE* in our calculations (Appendix Section D.2). The schematic in Figure 5.9b shows these excitons to have very distinct characteristics: For the IE, two degenerate states form at zero electric field, i.e. IE₁ and IE₂. For IE₁, the electron is localised in the bottom layer and the hole is delocalised between the middle and bottom layers. For IE₂, the electron is localised in the top layer and the hole is delocalised between the middle and top layers. As such, IE₁ and IE₂ have a finite dipole moment, similar to the interlayer excitons in bilayers. We extract a dipole moment of $|\mu| \approx 0.15$ e-nm. This smaller value as compared to the bilayer can have its origin in the different dielectric environment and a more localised hole wavefunction. Admixture of intralayer with interlayer excitons does not change significantly over the investigated electric field range (see Appendix Section D.2 Table D.2).

For the IE* at slightly lower energy, the situation is different compared to IE: The electron is localised in the middle layer and the hole is delocalised over all three layers. This results in a negligible in-built electric dipole moment of IE* which translates into a non-resolvable Stark splitting of the transition in our measurements. The absence of a clear Stark shift might put the interlayer nature of IE* into question. To answer this, we have

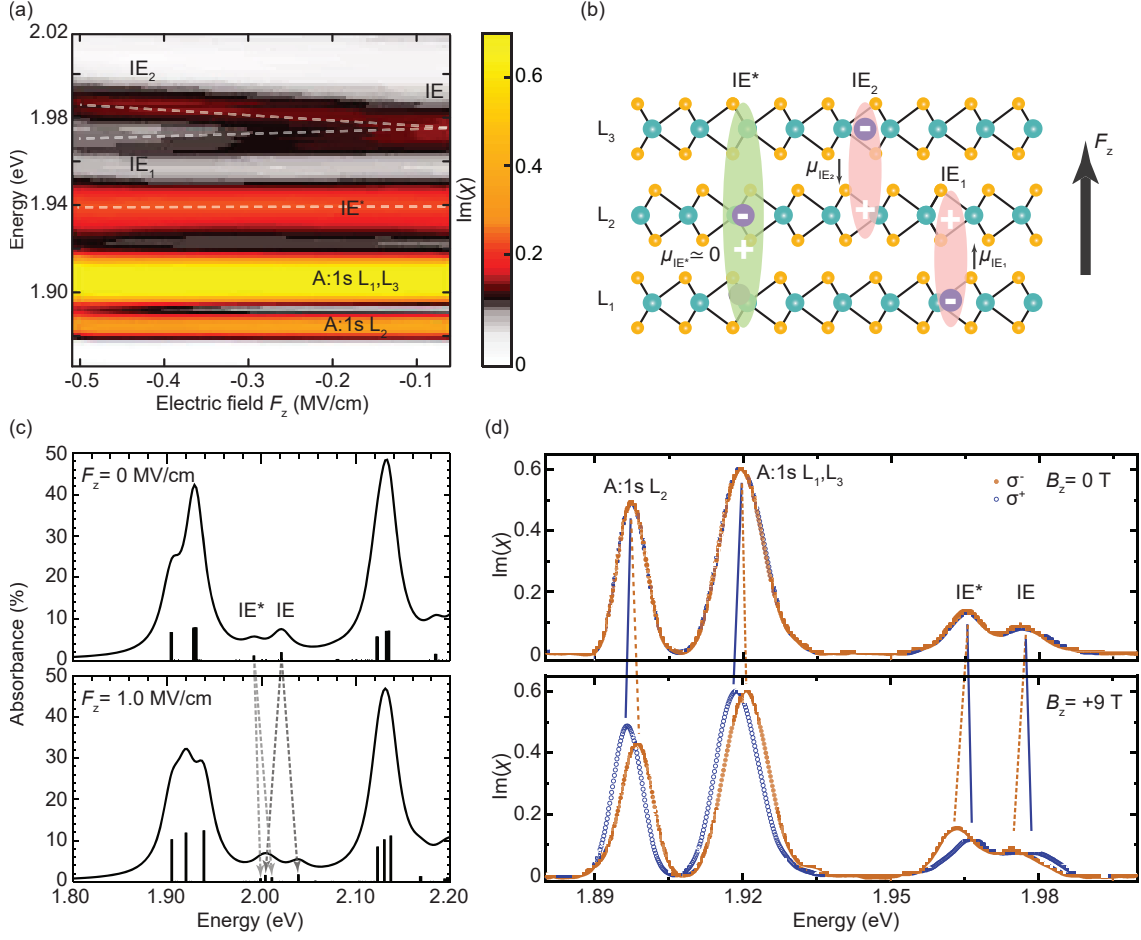


Figure 5.9. MoS₂ trilayer in an applied electric field. (a) Colour-map of the absorption spectra in device 2. (b) Schematic of the studied 2H-stacked trilayer representing the microscopic origin of IE and IE*. (c) Theoretical absorption spectra of a 2H MoS₂ freestanding trilayer without (top) and with (bottom) electric field. See Appendix Section D.2 for a detailed discussion of the trilayer band structure and the effect of the electric field on it. The Stark shifts of interlayer excitons IE and IE* are indicated by the grey arrows. (d) Magneto-optics on device 3 with small Zeeman splitting for intralayer excitons (A:1s) and large Zeeman splitting for interlayer excitons IE and IE* in magnetic fields of $B_z = +9$ T perpendicular to the monolayer plane.

performed magneto-optics, shown in Figure 5.9d. We observe for the intralayer excitons a Zeeman splitting of the order of 2 meV for $B_z = +9$ T and for IE and IE*, a Zeeman splitting of the order of 4 meV, with opposite sign compared to the intralayer transitions. Therefore, we confirm the interlayer character of these peaks. These results lead to an unusual situation for interlayer excitons: We observe a strong splitting in magnetic fields for IE*, but a very small Stark shift in electric fields.

5.7 Conclusion

In this chapter, the interlayer character of interlayer excitons in homobilayer MoS₂ has been confirmed by measuring their linear Stark shift in an applied electric field and by determining their excitonic g factor in a magnetic field. Unlike interlayer excitons in heterobilayers (see Chapter 4), interlayer excitons in bilayer MoS₂ possess a high oscillator strength. Furthermore, their transition energy can be tuned over 120 meV, more than 10 times their linewidth (see also [Lor21, Pei21]). We find two degenerate interlayer exciton states that have very large opposing dipole moments. Upon increasing the electric field, we can lift their degeneracy and bring them into resonance with the intralayer excitons. The coupling of the blue-shifted interlayer exciton with the intralayer B-exciton shows clear signatures of strong coupling. In contrast, the coupling of the red-shifted interlayer exciton with the intralayer A-exciton shows only a weak coupling. This allows us to conclude that the interlayer exciton has a strong B-exciton component in its wave function but a much smaller A-exciton component. We expect that at even higher fields than those in these experiments, the interlayer exciton will lie lower in energy than the A-exciton and will recover its absorption strength once it is sufficiently red-detuned from the A-exciton. The previous statement is confirmed by our exciton-exciton coupling model derived in Chapter 6. This will represent an advantageous scenario for applications: The ground-state exciton is long-lived and possesses both a large in-built electric dipole moment and a strong absorption.

For optoelectronics, the highly tunable excitons with an in-built dipole found here in MoS₂ bilayers are promising for exploring coupling to optical cavity modes, where excitons and photons can couple to form polaritons [Cri12, Sch18]. In III-V semiconductors very recently optical nonlinearities at a single polariton level have been detected [MM19, Del19]. Building on these promising proof-of-principle experiments further work on excitonic systems with stronger exciton-exciton interactions is desirable. This is the case for interlayer excitons in general in TMDs with an in-built static dipole. The interlayer excitons in the homobilayers investigated here have the crucial advantage of a high oscillator strength visible in absorption. Another promising system with strong nonlinear exciton-exciton interactions is a heterobilayer device with hybridised moiré excitons [Zha21].

*“If you can meet with Triumph and Disaster
And treat those two impostors just the same”
Rudyard Kipling, Rewards and Fairies (1910)*

Chapter 6

Capacitively and inductively coupled excitons in bilayer MoS₂

Adapted from:

L. Sponfeldner, N. Leisgang, S. Shree, I. Paradisanos, K. Watanabe, T. Taniguchi, C. Robert, D. Lagarde, A. Balocchi, X. Marie, I. C. Gerber, B. Urbaszek, and R. J. Warburton, “Capacitively and inductively coupled excitons in bilayer MoS₂”, *Physical Review Letters* **129**, 107401 (2022)[†]

The coupling of intralayer A- and B-excitons and interlayer excitons (IE) is studied in a two-dimensional semiconductor, homobilayer MoS₂. It is shown that the measured optical susceptibility reveals both the magnitude and the phase of the coupling constants. The IE and B-excitons couple via a 0-phase (capacitive) coupling; the IE and A-excitons couple via a π -phase (inductive) coupling. The IE-B and IE-A coupling mechanisms are interpreted as hole tunnelling and electron-hole exchange, respectively. The couplings imply that even in a monolayer, the A- and B-excitons have mixed spin-states. Using the IE as a sensor, the A-B intravalley exchange coupling is determined. Finally, we realise a bright and highly tunable lowest-energy momentum-direct exciton at high electric fields.

Section 6.1 introduces the phenomenon of exciton-exciton coupling and the material system of homobilayer MoS₂. The optical response of bilayer MoS₂ is presented in Section 6.2. A classical model of the excitonic coupling is developed in Section 6.3. In

[†]N.L. fabricated the sample. L.S. and N.L. performed optical spectroscopy measurements. L.S. and N.L. analysed the optical spectra and interpreted the results. L.S. developed the coupled dipole model. I.C.G. performed the GW+BSE calculations.

Section 6.4, the model is applied to the measured absorption in bilayer MoS₂. After showing the influence of the coupling sign on the excitonic absorption in Section 6.5, interference effects due to the coupling are discussed in Section 6.6. Theoretical calculations are presented in Section 6.7 that explain the microscopic origin of the exciton-exciton couplings. Section 6.8 discusses the intravalley exchange coupling of A- and B-excitons and how the coupling constant can be determined from the experiment. The chapter concludes with Section 6.9 where the results are summarised and an outlook is given.

6.1 Introduction

The elementary excitation at energies close to the band gap of a semiconductor is the exciton, a bound electron-hole pair. The exciton is a prominent feature of the linear optical response of a two-dimensional (2D) semiconductor, for instance monolayer MoS₂, even at room temperature [Mak10, Spl10]. This is a consequence of the giant exciton binding energies, hundreds of meV [Che14]. Excitons couple to each other leading to nonlinear optical effects [Wan15b, Jak16] and to condensation phenomena, the creation of states with macroscopic quantum-correlations [Kas06]. At the few-exciton level, exciton-exciton repulsion in a trap is a potential way to engineer a single-photon emitter [Del19, MM19].

Exciton-exciton couplings can arise via the charge of the constituent electrons and holes [Ciu98, Sha17, Erk21]. They can also arise should one of the constituents undergo tunnelling. The canonical example is the double quantum well in which molecule-like electronic states form via tunnelling between the two quantum wells [Fer90, Fox91, Siv12, And15]. Recently, molecule-like coupling has been discovered in bilayer 2D semiconductors [Ale19, Hsu19, Shi20, Sun20, Mer20, Zha20, Tan21, McD21].

Here, we probe exciton-exciton couplings in gated-homobilayer MoS₂. Previous work has revealed an interlayer exciton (IE) lying energetically between the intralayer A- and B-excitons [Ger19]. The intralayer excitons are doubly degenerate as an A and a B exist in each monolayer. The IE splits into two lines, IE₁ and IE₂, on applying a vertical electric field (F_z) [Lei20, Lor21, Pei21], evidence that the IE consists of a hole state delocalised across the two layers bound to an electron localised in one of the layers [Ger19, Pis19]. Avoided crossings were observed as IE₁ and A (IE₂ and B) are brought into resonance (see Chapter 5). We show here that at very high F_z the IE₁ becomes the momentum-direct exciton with the lowest energy; that the absorption strengths are sensitive to the phases (signs) of the IE₁-A, IE₂-B couplings; and that the IE enables the A-B coupling constant to be determined.

6.2 Optical response of homobilayer MoS₂

The device is constructed using bilayer MoS₂, Figure 6.1a. The studied sample is the same as device 1 in Chapter 5 albeit in a second cooldown cycle (see Appendix B for device

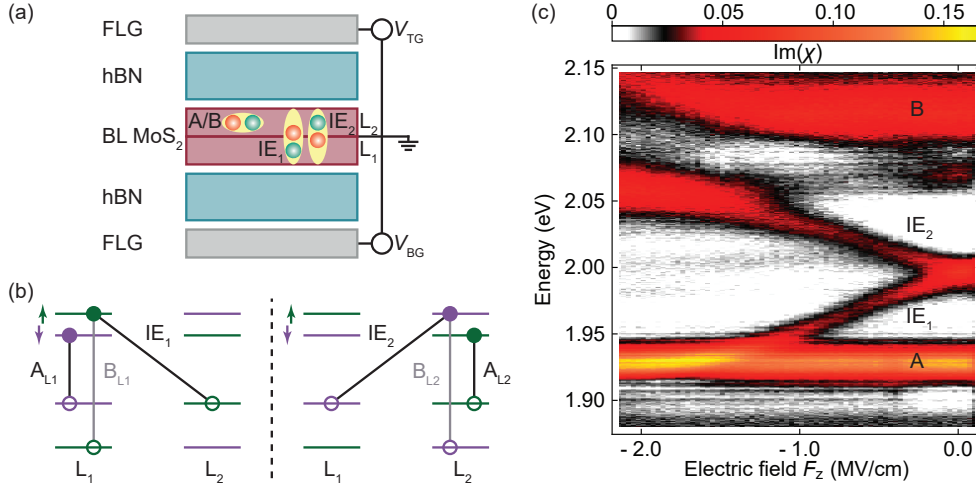


Figure 6.1. (a) Schematic of the van der Waals heterostructure consisting of a naturally 2H-stacked homobilayer MoS₂ embedded in hBN. The MoS₂ bilayer is electrically grounded. The voltages V_{TG} and V_{BG} applied to the top and bottom few-layer graphene (FLG) layers create a uniform electric field F_z across the bilayer. The spatial extents of the intralayer A- and B-excitons and the interlayer excitons (IE) are sketched. The electrons are depicted in green; the holes in red. The MoS₂ bottom (top) layer is denoted as L₁ (L₂). (b) Sketch of the important momentum-direct transitions in homobilayer MoS₂ at the K point. (c) Absorption (σ^+ polarisation) of homobilayer MoS₂ as a function of the applied electric field F_z over the whole energy range. The measurements were carried out at $T = 4.2$ K and magnetic field $B_z = 9$ T. For clarity, the uncoupled B_{L1} exciton and the uncoupled A_{L2} exciton are removed in a data processing step (see Appendix Chapter E.2). With the B_{L1} removed we can also observe a weak transition ~ 6 meV below the intralayer B-exciton (at small F_z). This transition corresponds to the higher-energy interlayer transition.

details). An exception is the measurement shown in Figure 6.1c and Appendix Figure E.8b which was recorded in the first cooldown cycle. The naturally 2H-stacked bilayer MoS₂ is embedded in hBN; few-layer graphene layers provide a back-contact and a top-gate; the MoS₂ layer is contacted. Results are presented as a function of F_z for the smallest possible electron density (n). The device is illuminated locally with a weak broadband source. The reflectivity is measured, using the response at large n as a reference, and converted into optical susceptibility using a Kramers-Kronig relationship (see Section 3.5.1).

At $F_z = 0$, the imaginary part of χ (which determines the absorption) shows three peaks: at low energy the intralayer A-excitons, at high energy the intralayer B-excitons, and in between, the IE, Figure 6.1c. These excitonic transitions are shown schematically in Figure 6.1a; the band structure at the K point is shown in Figure 6.1b. At high F_z , there is a clear avoided crossing between IE₂ and B; and a weak avoided crossing between the IE₁ and A, as discussed in Chapter 5.

At the highest F_z , IE₁ emerges on the low-energy side of A (Figure 6.2b). A zoomed-in spectrum of the IE₁ below the A-exciton is shown in Fig 6.2c. This means that the ground

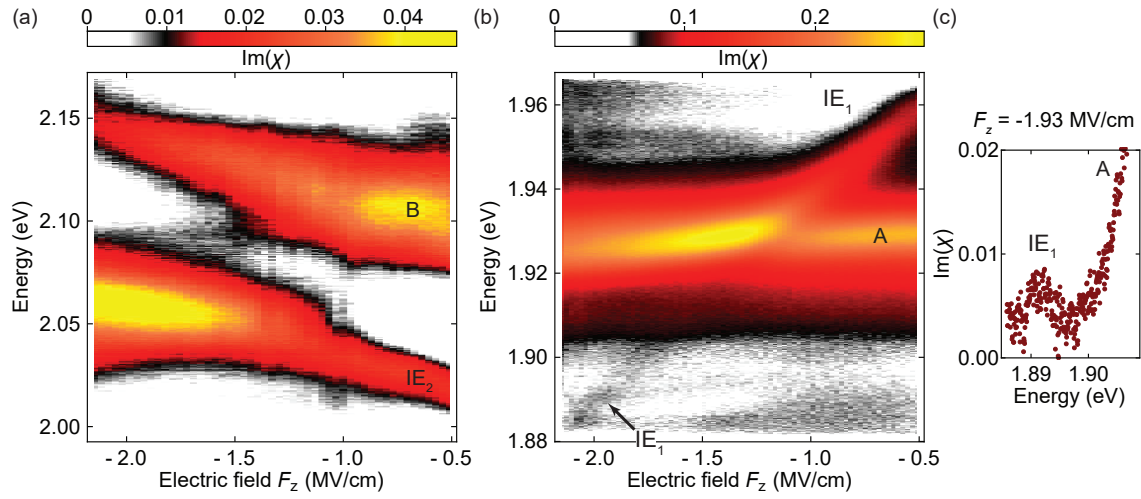


Figure 6.2. Detailed absorption maps (σ^+ polarisation) centred around (a) the B-exciton and (b) the A-exciton. The measurements were carried out at $T = 4.2$ K and magnetic field $B_z = 9$ T. For clarity, the uncoupled $\text{B}_{\text{L}1}$ exciton is removed from (a), and the uncoupled $\text{A}_{\text{L}2}$ exciton is removed from (b) in a data processing step (see Appendix Chapter E.2). (c) Zoomed-in spectrum at $F_z = -1.93$ MV/cm highlighting the IE_1 appearing just below the A-exciton. The spectrum is extracted from (b).

state exciton is both electric-field tunable and relatively bright. As explained below, we expect the IE_1 to become brighter as it is tuned further below A.

We now focus on the avoided crossings. At the IE-B avoided crossing, one of the B-excitons couples to the IE, the other does not. In Figure 6.2a and Figure 6.1c, we subtract the peak arising from the uncoupled B-exciton (see Appendix Chapter E.2). As discussed in Chapter 5, a simple two-level model describes the peak energies convincingly but not the relative intensities. Strikingly, at the F_z for which the two transitions are closest together in energy ($F_{z,0B}$), the intensities are quite different: the lower-energy transition is considerably stronger than the higher-energy transition. The IE-A coupling shown in Figure 6.2b is weaker than the IE-B coupling. One of the A-excitons couples to the IE, the other does not. The absorption from the uncoupled A-exciton is subtracted in Figure 6.1c and Figure 6.2b. The minimum energy separation of the peaks is smaller than the peak broadening. Nevertheless, the avoided crossing has a strong effect on the intensities: as F_z increases, the IE-like branch enters the avoided crossing with a relatively large intensity, but emerges with a much lower intensity. The IE-A intensity behaviour mimics the behaviour at the IE-B avoided crossing but with one crucial difference. The upper-IE is strong on the low-energy side of the B-exciton; the lower-IE is strong on the high-energy side of the A-exciton. Our target is to understand the origin of the different coupling behaviours.

6.3 Classical exciton-exciton coupling model

The optical susceptibility of a quantum well can be calculated from the semiconductor Bloch equations [Lin88, Koc06, Hau09, Kli12]. In this approach, the quantum well is treated quantum mechanically. The final result is identical to a completely classical approach in which the quantum well is treated as a 2D array of optical dipoles [Kar03]. Inspired by the success of the purely classical approach, we set up a heuristic description of the exciton-exciton coupling.

The excitonic couplings are modelled as the coupling of two driven oscillating optical dipoles. The dipole oscillation can be described by the oscillation of the dipole extension \vec{r} or by the oscillation of the charge \vec{q} . One can think of two frameworks which provide a classical analogue. In a mechanical system, two masses represent the dipoles, a spring represents the coupling. In an electrical system, two RLC circuits represent the dipoles, an impedance (either capacitor or inductor) represents the coupling. Both, the mechanical and the electrical system, can be described by equivalent equations of motion (see Appendix Section E.1). However, the experimental results discussed in this chapter study excitonic couplings. Therefore, we forge an analogy between mechanical (electrical) and optical systems. We show that excitonic coupling can be readily described by the mechanical model assuming a classical description of the driven excitons.

The coupling model of inter- and intralayer excitons driven by an external light field is sketched in Figure 6.3. The optical dipole representing the intralayer exciton (index 1) has a constant energy of $\hbar\omega_0$. The IE (index 2) is modelled by a dipole that has a tunable energy through the term $\hbar\Delta\omega$ with a total energy of $\hbar\omega_0 + \hbar\Delta\omega$. The two dipoles are coupled to each other through a complex coupling constant $\kappa = |\kappa| e^{i\phi}$ that carries a phase ϕ . The detuning $\hbar\Delta\omega$ is a linear function of the applied electric field F_z on account of the Stark effect. From experiments, we know that the energy crossing point occurs at $F_z \neq 0$. Therefore,

$$\hbar\Delta\omega = \mu (F_z - F_{z,0}) , \quad (6.1)$$

where μ is the static dipole moment and $F_{z,0}$ is the field at which the two bare energies match.

From the experiment, we also know that the sign of μ is positive for IE₁ and negative for IE₂. The two dipoles are driven by the external light field $\vec{E} = \vec{E}_0 \text{Re}(e^{i\omega t})$. The force of the field on the charge e is $e\vec{E}$. Each dipole has a different coupling strength $F_{1,2}$ to the light field and a dephasing constant $\gamma_{1,2}$.

The resulting equations of motion have the same form as the equations of motion of the mechanical system (see Appendix Section E.1). Therefore, the calculations and solutions of the mechanical system also hold for the excitonic system. The eigenenergies of the system

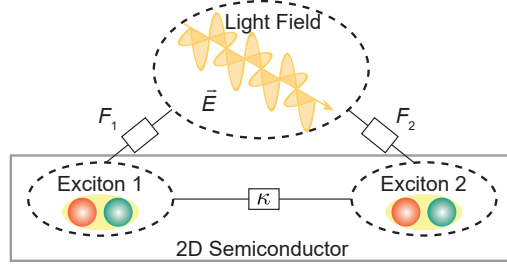


Figure 6.3. Sketch of two coupled excitons in a 2D semiconductor both driven by an external light field. The oscillator strength of each exciton is given by $F_{1,2}$; κ is the coupling constant.

are given by

$$\hbar\Omega_{\pm} \simeq \hbar \left(\omega_0 + \frac{1}{2}\Delta\omega \right) \mp \frac{1}{2} \sqrt{(\hbar\Delta\omega)^2 + 4\kappa^2}, \quad (6.2)$$

assuming $\hbar\omega_0 + \kappa \simeq \hbar\omega_0$, as $\hbar\omega_0 \gg \kappa$. It is important to note that Ω_{\pm} do not depend on $F_{1,2}$.

So far we have described the response of two individual dipoles coupling to each other. In practice, an array of dipoles exists in a semiconductor. In a completely classical approach, the quantum well is treated as a two-dimensional array of optical dipoles [Kar03]. Following this approach, the linear absorption $\alpha(\omega)$ of a quantum well is given by [Kar03]

$$\alpha(\omega) = \frac{2\gamma\Gamma_0^{\text{rad}}}{(\omega_0 - \omega)^2 + (\gamma + \Gamma_0^{\text{rad}})^2}. \quad (6.3)$$

The definition of the radiative coupling constant Γ_0^{rad} is

$$\Gamma_0^{\text{rad}} = \frac{1}{4A} \frac{e^2 f}{\epsilon_0 c m n}, \quad (6.4)$$

where f is the oscillator strength, n is the refractive index of the quantum well, c is the speed of light, and $1/A$ is the dipole area density. From Equation 6.3 we see that the solution of the quantum well absorption is additionally broadened by Γ_0^{rad} due to dipole-dipole interactions in the quantum well [Kir06, Kar03].

The absorption of an array of dipoles shown in Equation 6.3 has a similar form as the equation for the time-averaged dissipated power $\langle P \rangle$ of two coupled masses in the mechanical system (see Appendix Section E.1). Both equations are equivalent if we take the experimental dephasing $\gamma_{1,2}$ to be equal to the dephasing of the dipole array $\gamma + \Gamma_0^{\text{rad}}$. By comparing the two equations we find a linear relation between the absorption $\text{Im}(\chi)$ of two coupled dipoles and the dissipated power $\langle P \rangle$:

$$\text{Im}(\chi) = \frac{4e^2}{A\epsilon_0 c n |\vec{E}_0|^2} \langle P \rangle. \quad (6.5)$$

The absorption strength $I_{1,2}$ of each coupled optical dipole is then dependent on the energy detuning $\hbar\Delta\omega$, the coupling κ , and the oscillator strengths $F_{1,2}$. For all calculations, the prefactor $\frac{4\hbar e^2}{A\epsilon_0 cmn}$ is set to 1 eV. $I_{1,2}$ is given by

$$\begin{bmatrix} I_1 \\ I_2 \end{bmatrix} = \begin{bmatrix} (U_{11}F_1)^2 + (U_{12}F_2)^2 + 2U_{11}U_{12}F_1F_2 \cos \phi \\ (U_{21}F_1)^2 + (U_{22}F_2)^2 + 2U_{21}U_{22}F_1F_2 \cos \phi \end{bmatrix} \text{ eV}, \quad (6.6)$$

where U_{ij} are the elements of the transformation matrix \mathbf{U} as defined in Appendix Section E.1. These elements and therefore the absorption strength depend on the energy detuning, the coupling κ (magnitude and phase ϕ), and the oscillator strength ratio F_1/F_2 . The absorption is then modelled as

$$\text{Im}(\chi) = I_1 \frac{\frac{1}{2}\hbar\gamma_1}{(\frac{1}{2}\hbar\gamma_1)^2 + (\hbar\Omega_+ - \hbar\omega)^2} + I_2 \frac{\frac{1}{2}\hbar\gamma_2}{(\frac{1}{2}\hbar\gamma_2)^2 + (\hbar\Omega_- - \hbar\omega)^2}. \quad (6.7)$$

This is a significant result: the model predicts straightforward lineshapes.

In the experiment, the A-exciton has a quadratic Stark shift that is not negligible. Therefore, the quadratic shift of the A-exciton is included in the model when fitting the IE-A coupling. This is carried out by adding the term $-\beta_z F_z^2$ to the uncoupled energy of the optical dipole 1 representing the A-exciton with β_z being the excitonic polarisability. Then, the eigenenergies have an additional term depending on the quadratic energy shift of the optical dipole 1 (A-exciton). The eigenenergies are

$$\hbar\Omega_{\pm} = \hbar\omega_0 - \frac{1}{2}\beta_z F_z^2 + \frac{1}{2}\hbar\Delta\omega \mp \frac{1}{2}\sqrt{(\hbar\Delta\omega)^2 + 4\kappa^2 + 2(\beta_z F_z^2)^2 + 2\beta_z F_z^2 \hbar\Delta\omega}. \quad (6.8)$$

The absorption strength is given by Equation 6.6 with the matrix elements of the transformation matrix \mathbf{U} adjusted to include the quadratic terms in F_z (see Appendix Section E.1).

M. Kira and S. W. Koch calculate the linear absorption $\alpha(\omega)$ of a quantum well following the quantum mechanical semiconducting Bloch equations coupled to Maxwell's wave equation [Kir06]. Their result for the absorption is the same as the absorption of an array of oscillating dipoles in a two-dimensional plane derived in a classical way shown in Equation 6.3 [Kar03]. Therefore, the simple classical model derived in this section yields an equivalent result as a quantum mechanical approach.

To summarise, solving the equations of motion of a classical model of two coupled optical dipoles yields an analytic equation for both the eigenenergies $\hbar\Omega_{\pm}$ (Equation 6.2) and the absorption strengths (Equation 6.6) of the two eigenmodes. The complete derivation of the coupling model and a deeper discussion of its implications on the excitonic response is

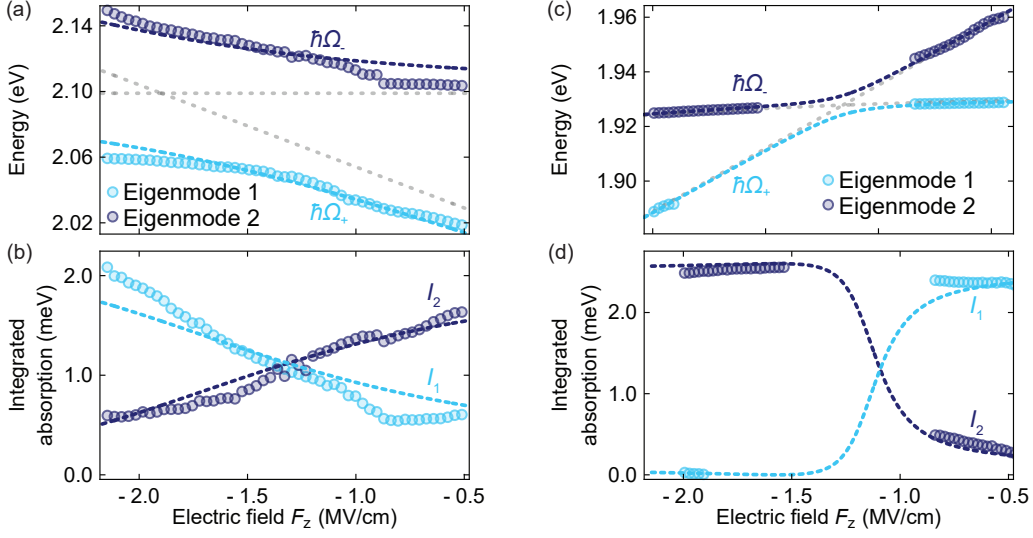


Figure 6.4. (a) Peak energies and (b) integrated absorption extracted from the IE-B absorption spectra shown in Figure 6.2a. The coloured dashed lines are fits to the energy according to Equation 6.2 for the eigenenergies $\hbar\Omega_{\pm}$. (c) Peak energies and (d) integrated absorption extracted from the IE-A absorption spectra shown in Figure 6.2b. As the coupling strength is much smaller than the linewidth of the A-exciton, only the spectra far from the crossing point can be fitted unambiguously. The coloured dashed lines are fits to the energy according to Equation 6.8 which includes the quadratic Stark shift of the A-exciton. All parameters extracted from the measured data are summarised in Table 6.1. The light grey dashed lines in (a) and (c) show the energy evolution with zero coupling.

shown in Appendix Section E.1.

6.4 Modelling the absorption in homobilayer MoS₂

Now, we try to model the experimentally observed IE-B and IE-A absorption spectra in Figure 6.2 using the classical model of two coupled optical dipoles. We extract the peak energy and the integrated absorption of each excitonic transition (see Appendix Section E.2 for the detailed fitting routine). Then, the energies are fitted with Equation 6.2 and the integrated absorption is fitted with Equation 6.6.

The classical model reproduces both the experimental IE-B peak energies (Figure 6.4a) and integrated absorption (Figure 6.4b) extraordinarily well provided the ratio of the oscillator strengths and the coupling constant are well chosen. The fits yield an oscillator strength ratio $F_1/F_2 \approx 5$ and an IE-B coupling strength of $\kappa = +35.8 \pm 3.6$ meV. The positive sign is inferred from a fitted coupling phase of $\phi = 0.0 \pm 0.3$ ($e^{i\phi} = +1$).

The IE-A avoided crossing (Figure 6.2) is described with the same model but with the energies appropriate to the lower IE-branch and the A-exciton along with a different choice of coupling constant. For the A-exciton energy, a quadratic Stark shift is included [Mil84]. The extracted energies and the corresponding fit according to Equation 6.8 are shown in

	$\hbar\omega_0$ (eV)	$ \kappa $ (meV)	ϕ	μ (e nm)	$F_{z,0}$ (MV/cm)
IE-A	1.930	3.517	π	0.4634	-1.119
IE-B	2.099	35.76	0	-0.5000	-1.898

	F_1	F_2	F_1/F_2	$\hbar\gamma_1$ (meV)	$\hbar\gamma_2$ (meV)	β_z (D m V ⁻¹)
IE-A	0.05008	0.009706	5.159	12	12	6.412×10^{-9}
IE-B	0.04645	0.009116	5.096	20	12	

Table 6.1. Parameters extracted from the measured data shown in Figure 6.2 and used for the calculation of the excitonic coupling model. For IE-B, $\hbar\omega_0$ is the mean value of the fitted uncoupled B_{L1} energies for all electric fields. $\hbar\gamma_{1,2}$ are set to make the calculated resonances have a comparable linewidth as in the experiments. All other parameters are extracted from the measured data using the coupling model Equations 6.2 and 6.6 (see Figure 6.4). For the IE-A coupling, the equations are adjusted to accommodate the polarisability β_z of the A-exciton. We estimate the random errors in all parameters deduced with the coupled dipole model to be $\pm 10\%$. The error of the coupling phase ϕ is estimated to be ± 0.3 .

Figure 6.4c. Our model reproduces also the IE-A avoided crossing very convincingly. The IE-A coupling is essential to describe the F_z -dependence of the intensities (see Figure 6.2b and Figure 6.4d). The fits yield an oscillator strength ratio $F_1/F_2 \approx 5$ and an IE-A coupling strength of $\kappa = -3.5 \pm 0.4$ meV. The negative sign is inferred from a fitted coupling phase of $\phi = \pi \pm 0.3$ ($e^{i\phi} = -1$). Additionally, the fit yields a polarisability of the A-exciton of $\beta_z = 6.4 \times 10^{-9}$ D m V⁻¹. The A-exciton polarisability in the bilayer is roughly a factor of 10 larger than the polarisability of A-excitons in a monolayer MoS₂ [Roc18]. In homobilayer MoS₂ the valence band of both layers are mixed [Ger19]. This leads to an increased effective quantum well width as compared to the monolayer which in turn also leads to an increased polarisability [Ped16].

The B-exciton can't be described nicely with a simple quadratic energy shift. Due to the large IE-B coupling, the B-exciton is influenced by the IE even at zero electric field. This influence alters the energy evolution of the B-exciton beyond the quadratic Stark shift.

Table 6.1 summarises the parameters for the IE-A and IE-B interactions extracted by the classical model fit. It should be noted that while we fit the measured data with several free parameters only three of them are needed to predict the absorption strength behaviour nicely: the magnitude and phase of the coupling constant and the ratio of the oscillator strengths. The other parameters can either be extracted from the eigenenergy fit with Equation 6.2 or directly be taken from the measured data.

The absorption spectra for the IE-A and IE-B couplings are calculated separately and added together to describe the full F_z -dependence, as shown in Figure 6.5b. Comparing

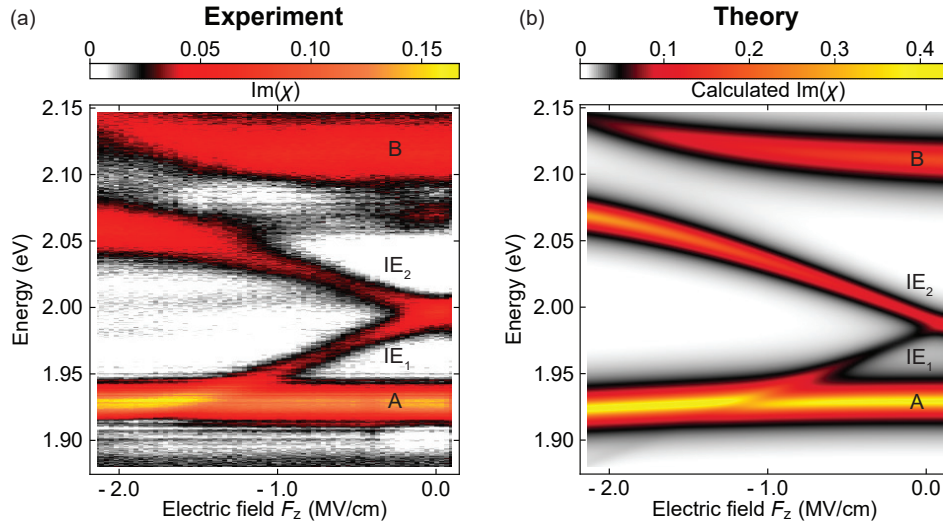


Figure 6.5. Comparison of experiment and theory. (a) Measured absorption of homobilayer MoS₂. The measurement is the same as shown in Figure 6.1c. (b) Colour-map of the calculated absorption $\text{Im}(\chi)$ as a function of electric field F_z with parameters extracted from model fits to the measured data in Figure 6.2. The parameters are listed in Table 6.1. Separate models are used to describe the IE-A and IE-B couplings. The $\text{Im}(\chi)$ is a sum of the two. The two colour-maps are interpolated to first order.

the calculated with the measured absorption in Figure 6.5a, we find an excellent agreement between experiment and classical theory.

6.5 Influence of the sign of the coupling strength on the excitonic absorption

This model unearths a crucial result: the IE-A coupling constant is of opposite sign to the IE-B coupling constant. The sign of the coupling constant is particularly important in determining the relative strengths of the absorption peaks.

Figure 6.6a shows the calculated average dissipated power of the IE-A and IE-B couplings with the same parameters as the calculations shown in Figure 6.4. Figure 6.6b shows the calculated dissipated power if the two coupling strengths have opposite signs. The two individual couplings are added together to highlight the IE “cage” (Figure 6.6a) and IE “anti-cage” (Figure 6.6b) behaviour. For the IE cage, the IE is weak “inside”, i.e. at energies between the A-like and B-like excitons, and strong on the “outside”; the IE anti-cage describes the opposite behaviour. By comparing the two calculations with the measured absorption shown in Figure 6.5a, it is clear that a negative coupling models the IE-A coupling, and a positive coupling models the IE-B coupling.

We interpret the sign of the coupling by making an analogy to driven, coupled RLC-circuits (see Appendix Section E.1). Two such circuits can be coupled via an impedance. The equations of motion are analogues of those describing the driven optical dipole. The

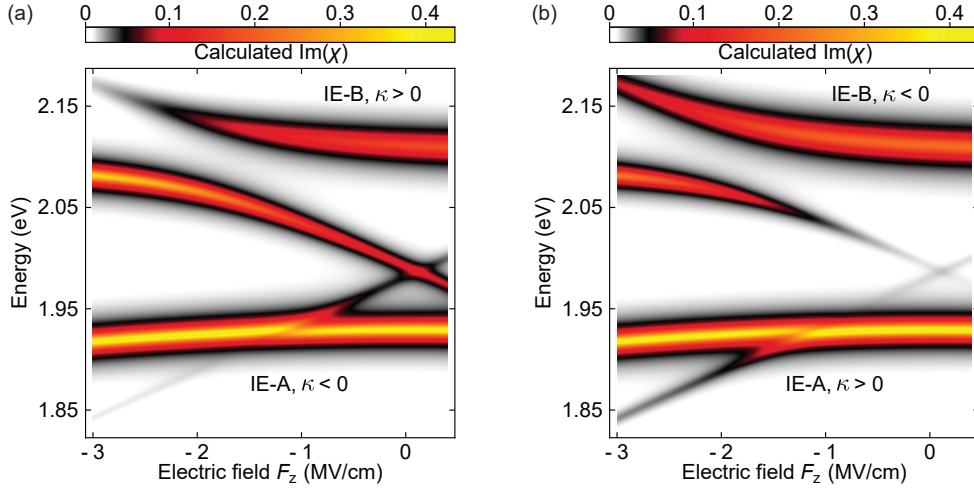


Figure 6.6. Colour-map of the calculated absorption $\text{Im}(\chi)$ of the IE-A and IE-B couplings as a function of electric field according to Equation 6.7. Separate models are used to describe the IE-A and IE-B couplings. The $\text{Im}(\chi)$ is a sum of the two in order to visualise the (a) IE “cage” and (b) IE “anti-cage”. The used parameters are the same as those extracted from fits to the data shown in Figure 6.4. The parameters are summarised in Table 6.1. The A-exciton energy is described with a quadratic Stark shift. The coupling constants in (a) have the same sign as determined through the model fit while each of the coupling constants in (b) have the opposite sign. The two colour-maps are interpolated to first order.

nature of the coupling impedance determines the sign of the coupling constant: coupling via a capacitance (inductance) results in a positive (negative) coupling constant. In this analogy, the IE-B coupling corresponds to a capacitive coupling. This suggests that, at a microscopic level, the IE-B coupling involves the movement of charge – it is consistent with hole tunnelling from one layer to the other [Ger19]. Conversely, the IE-A coupling corresponds to an inductive coupling. This points to a completely different coupling mechanism, as discussed in the next sections.

6.6 Constructive and destructive interference

The model provides an explanation for the F_z -dependent absorption strengths in Figure 6.5. We take the IE-A coupling as an example. Without a coupling, both IE and A respond directly to the driving field. A has the stronger response: the induced dipole moment is in-phase with the drive for energies well below the bare A-energy and out-of-phase for energies well above the bare A-energy (the standard behaviour for a driven harmonic oscillator). With a coupling, each eigenmode is a dressed state of IE and A. At detunings far from the avoided crossing, there is an A-like and an IE-like eigenmode. The IE-like mode is driven by two sources: the field acting directly on the IE, and via its coupling to A. Now the sign of the coupling plays a crucial role. If the coupling has a negative sign, then for energies above (below) the bare A-energy, these two terms have the same (opposite)

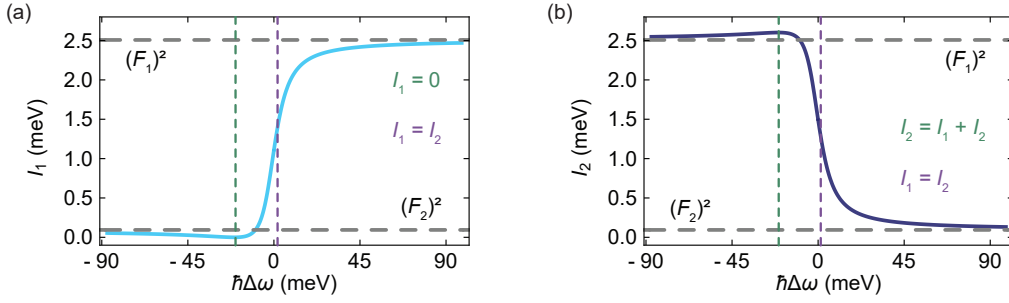


Figure 6.7. Plot of the absorption strength (a) I_1 and (b) I_2 calculated according to Equation 6.6 adjusted with the quadratic Stark shift of the A-exciton. The plots show the same curves as the fits to the measured data shown in Figure 6.4d as a function of detuning $\hbar\Delta\omega$. The parameters are summarised in Table 6.1. The horizontal dashed grey lines indicate the absorption strengths of the bare (i.e. uncoupled) excitons. The vertical dashed green lines indicate the detuning of the maximum/minimum absorption strength due to the constructive/destructive interference in each eigenmode. The vertical dashed purple lines indicate the detuning where the absorption strengths I_1 and I_2 are identical.

sign and interfere constructively (destructively). At a particular detuning, the destructive interference is complete and the absorption of one mode disappears.

Figure 6.7 shows the calculated absorption strengths $I_{1,2}$ according to Equation 6.6 using the same parameters as extracted for the IE-A coupling in Figure 6.4d. Here, the absorption strengths are plotted as a function of energetic detuning $\hbar\Delta\omega$ as defined in Equation 6.1. For large detuning, both absorption strengths approach the value of the respective oscillator strengths. This model also predicts destructive interference in eigenmode 1 (Figure 6.7a), constructive interference in eigenmode 2 (Figure 6.7b), for negative detuning and a negative coupling constant. The sign of κ determines which eigenmode experiences destructive interference. For $\kappa > 0$ ($\kappa < 0$) the higher (lower) energy mode shows destructive interference (see Figure 6.6). The maximum absorption strength in the eigenmode with constructive interference corresponds to the sum of the squared oscillator strengths $F_{1,2}$. The minimum absorption strength in the eigenmode with destructive interference is zero (see Figure 6.7). The effects of the constructive and destructive interference depend strongly on the coupling phase ϕ in the mixed term in Equation 6.6. Complete constructive (destructive) interference occurs only for a phase of exactly 0 or π . The more the phase is different from 0 or π , the less apparent is the effect of the interference.

Even at energies far from the avoided crossing, this interference has a strong effect on the IE-absorption. The picture inverts for a positive coupling, the IE-B coupling. In this case, the IE-like mode is boosted (suppressed) when it lies below (above) the bare B-energy. At $F_z = 0$, the IE is far from the avoided crossing with both A- and B-excitons but its absorption strength is boosted by its coupling to both A and B. In simple terms,

the dielectric constant at the IE-resonance is strongly influenced by the strong A- and B-resonances.

6.7 Microscopic origin of the two different exciton-exciton couplings

We look for a microscopic explanation for the different IE-A and IE-B couplings. To do this, we describe the band structure of bilayer MoS₂ at the GW-level (one-particle Green's function G , dynamically screened Coulomb interaction W), and use these states to construct excitons by solving the Bethe-Salpeter equation, BSE (see Appendix Section E.3 for computational details). The results describe the general behaviour of the experiments very well as revealed by a comparison of the calculated relative absorption strengths in Figs. 6.8b,c for IE-B and Figs. 6.8e,f for IE-A with the measured integrated absorption in Figs. 6.4b,d. Exact quantitative agreement is not expected as the model assumes that the MoS₂ bilayers are located in vacuum – it does not take into account the full dielectric environment. As in the experiment, the IE are relatively strong when they lie energetically between the bare A- and the bare B-resonances but weaker when they lie out of this energy window (Figure 6.8e and Figure 6.8f). In the following, we will discuss the GW+BSE results on the MoS₂ bilayer in detail.

6.7.1 IE₂-B_{L2} coupling

Figs. 6.8a-c summarise the results from the GW+BSE calculations for eigenmode 1 and eigenmode 2 of the IE₂-B_{L2} coupling. As already discussed in the main text, these two excitons couple strongly to each other. The evolution of the calculated relative absorption strength I_1 and I_2 as a function of electric field is shown as the cyan points in Figure 6.8b and Figure 6.8c, respectively. Upon tuning through the coupling region, a clear transfer of absorption strength between the two eigenmodes is visible. These GW+BSE results agree quite well with the measured absorption shown in Figure 6.2a and with the fitted absorption strength evolution shown in Figure 6.4b.

Figure 6.8b and Figure 6.8c also show the interband transition composition of the true excitonic eigenstates at each electric field step. The composition percentage indicates how much each interband transition contributes to the overall excitonic absorption strength. The involved interband transitions are colour-coded and shown in Figure 6.8a. The calculations reproduce nicely the layer character of each eigenmode upon tuning through the coupling region. Initially, eigenmode 1 (eigenmode 2) has a large interlayer IE₂, yellow (intralayer B_{L2}, blue) component. Upon increasing the electric field the IE₂ and B_{L2} percentages in each eigenmode change: one increases at the cost of the other one. Finally, at high electric fields, eigenmode 1 (eigenmode 2) has changed its layer character to an intralayer

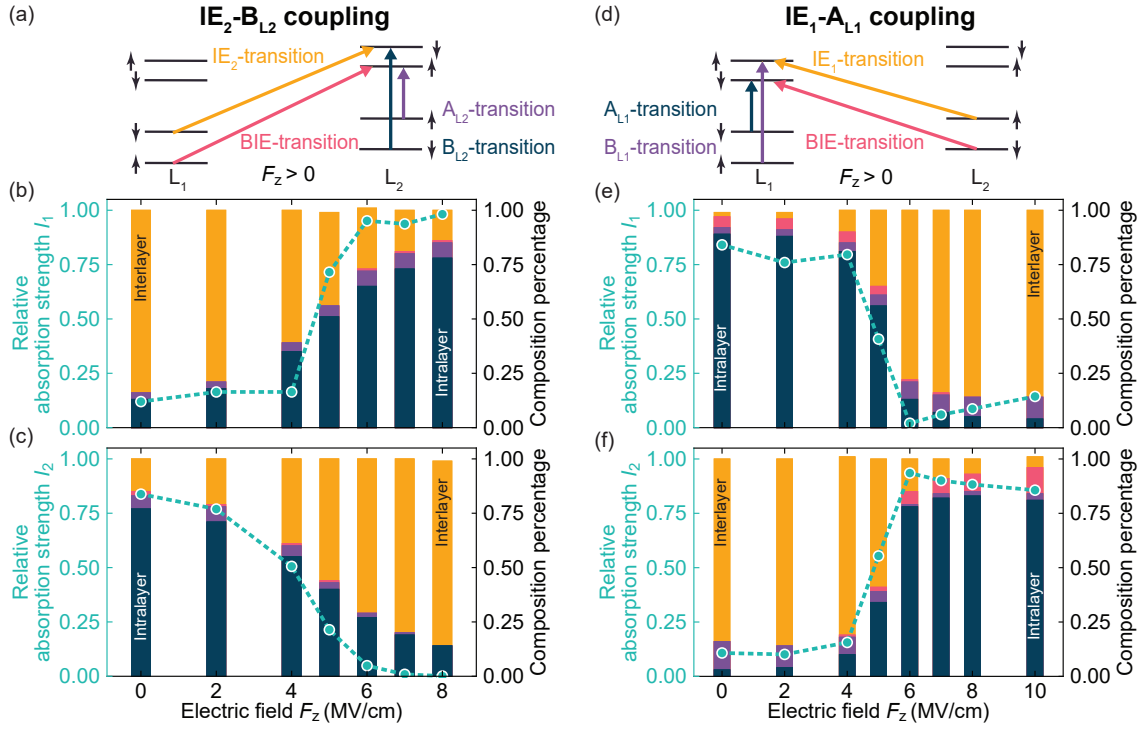


Figure 6.8. Main excitonic transitions contributing to (a) the IE-B dressed state and (d) the IE-A dressed state. They are sketched as the coloured arrows in the schematic band structure at the K point of bilayer MoS₂ at a finite positive electric field F_z . BIE denotes the higher-energy interlayer transition. (b,c) Relative absorption strength of (b) eigenmode-1 I_1 and (c) eigenmode-2 I_2 of the IE-B coupling as a function of electric field determined by GW+BSE calculations. (e,f) Relative absorption strength of (e) eigenmode-1 I_1 and (f) eigenmode-2 I_2 of the IE-A coupling as a function of electric field determined by GW+BSE calculations. The cyan dashed-line is a guide to the eye. The coloured bars in (b,c) and (e,f) indicate the composition percentage; the colours match those used in (a) and (d), respectively.

(interlayer) character. The swapping of the layer character of each eigenmode confirms the coupling of IE₂ and B_{L2} [Lei20].

6.7.2 IE₁-A_{L1} coupling

The IE-A coupling is presented in the same way as the IE-B coupling discussed in the previous subsection. Figs. 6.8d-f summarise the results from the GW+BSE calculations for eigenmode 1 and eigenmode 2 of the IE-A coupling. The evolution of the calculated relative absorption strength I_1 and I_2 as a function of electric field is shown as the cyan points in Figure 6.8e and Figure 6.8f, respectively. As for the IE-B case, there is a clear transfer of absorption strength between the two eigenmodes on tuning through the coupling region. The calculated absorption strengths agree quite well with the measured absorption shown in Figure 6.2b and with the fitted absorption strength evolution shown in Figure 6.4d.

The interband transition composition of the true excitonic eigenstates reveals a coupling of

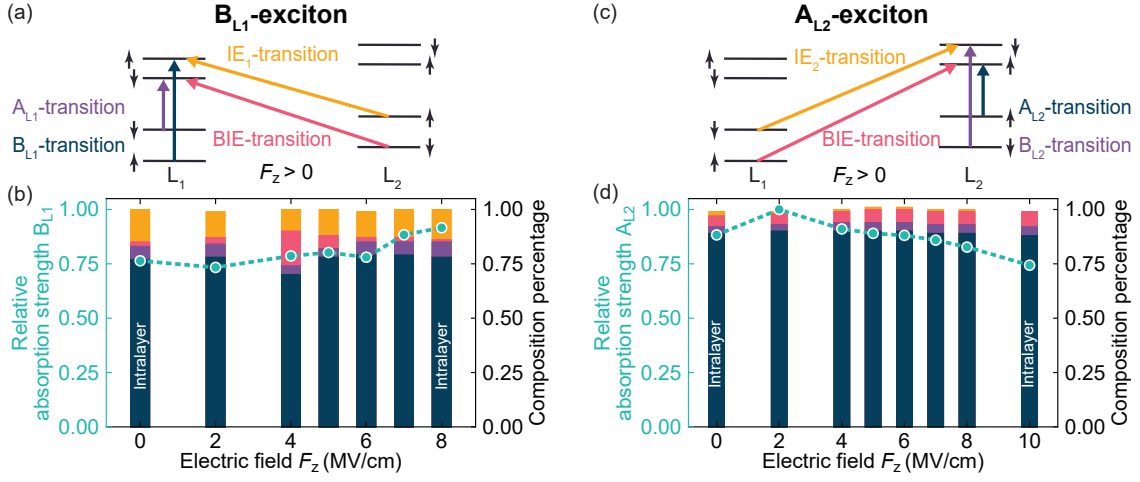


Figure 6.9. Main excitonic transitions contributing (a) to the true B_{L1} exciton and (c) to the true A_{L2} exciton. They are sketched as the coloured arrows in the schematic band structure at the K point of bilayer MoS_2 at a finite positive electric field F_z . Relative absorption strength of (b) B_{L1} and (d) A_{L2} as a function of electric field determined by GW+BSE calculations. The cyan dashed line is a guide to the eye. The coloured bars indicate the composition percentage at each electric field step; the colours in (b) and (d) match those used to denote the excitonic transition in (a) and (c), respectively.

the IE_1 and the A_{L1} -exciton through the swapping of the layer character of each eigenmode. As will be discussed in the next section, this mixing is due to a strong intravalley Coulomb exchange interaction.

6.7.3 B_{L1} exciton

To confirm that IE_2 only couples to B_{L2} , we will now look at the calculation results for the B_{L1} exciton. Figure 6.9a and Figure 6.9b summarise the calculated relative absorption strength of B_{L1} and its interband transition composition. The B_{L1} absorption strength stays constant over the whole electric field range. The interband transition composition shows several interesting features. First, the intralayer B_{L1} (blue) component dominates the oscillator strength and stays rather constant for all studied electric fields. These results are a confirmation that the B_{L1} exciton does not couple to the IE_2 exciton. Second, at 4 MV/cm the B-interlayer exciton (BIE, pink) component is increased as compared to lower and higher electric fields. An explanation could be that B_{L1} and BIE with opposite spin couple in a similar way as IE_1 and A_{L1} . From measurements we know that the BIE is energetically located just below the B-excitons at around 2.07 meV [Lei20]. An energetic crossing of B_{L1} and BIE could therefore be expected around this electric field range. Experimentally, we can't resolve this coupling due to the very small oscillator strength of the BIE and the probably small coupling strength to B_{L1} . Last, the true B_{L1} exciton retains a very large and rather constant IE_1 (yellow) component over the whole

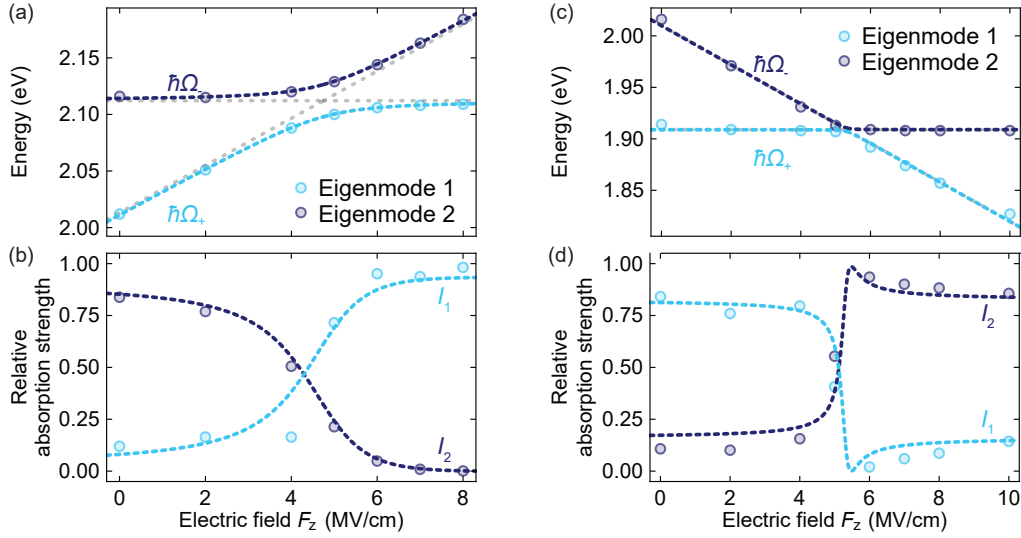


Figure 6.10. (a) Peak energies and (b) relative absorption strengths of the IE-B coupling determined by GW+BSE calculations. The coloured dashed lines are fits of the energy according to Equation 6.2 and fits to the oscillator strength according to Equation 6.6. (c) Peak energies and (d) oscillator strengths of the IE-A coupling determined by GW+BSE calculations. The coloured dashed lines are fits of the energy and to the oscillator strength with the same functions as in (a) and (b), respectively. The light grey dashed lines in (a) and (c) show the energy evolution with zero coupling. All parameters extracted from the calculated data are summarised in the text.

electric field range even though IE₁ is energetically detuned far away from the B-exciton. This indicates that the orbital hybridisation and consequently the large oscillator strength of the IE is not affected much in the studied electric field range. The IE oscillator strength is not diminished even after energetically tuning it below the A-excitons.

6.7.4 A_{L2} exciton

Next, we will discuss the GW+BSE results for the true A_{L2} exciton (see Figure 6.9c and Figure 6.9d). Similarly to the B_{L1} exciton discussed before, the absorption strength of A_{L2} and its composition stay constant over the studied electric field range. This confirms that the A_{L2} exciton does not couple to IE₁.

6.7.5 Applying coupled dipole model to GW+BSE results

The calculated GW+BSE excitonic peak energies and relative absorption strengths can also be fitted with the classical coupling model, similarly to the measured data shown in Figure 6.4. The energies are fitted with Equation 6.2 and the relative absorption strengths are fitted with Equation 6.6. The energy fit of the IE-B coupling shown in Figure 6.10a yields a coupling strength of $\kappa = +14.2$ meV, a B-exciton energy $\hbar\omega_0$ of 2.11 eV, a crossing point $F_{z,0}$ of 4.74 MV/cm, and a linear Stark shift μ of 0.21 e nm. The oscillator strength

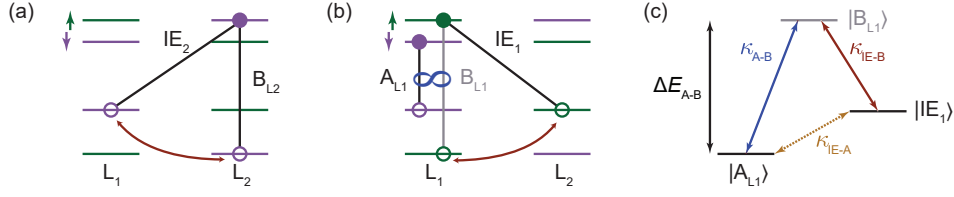


Figure 6.11. Band structure and schematics of excitons in homobilayer MoS₂ at the K point. (a) Sketch of the microscopic origin of the IE-B coupling mediated by hole tunnelling (red arrow). Sketch of the IE-A coupling (b) in the bandstructure and (c) in a transition diagram. IE and B are coupled ($\kappa_{\text{IE-B}}$, red arrow). A and B are coupled through intralayer exchange ($\kappa_{\text{A-B}}$, blue ∞ -symbol). Through the common coupling to B, IE and A are effectively coupled ($\kappa_{\text{IE-A}}$).

fit (Fig 6.10b) yields an oscillator strength ratio of $F_1/F_2 = 6.26$ and confirms the positive sign of the IE-B coupling.

The energy fit of the IE-A coupling shown in Figure 6.10c yields an absolute coupling strength of $\kappa = -1.7$ meV, an A-exciton energy $\hbar\omega_0$ of 1.91 eV, a crossing point $F_{z,0}$ of 5.31 MV/cm, and a linear Stark shift μ of -0.19 e nm. The oscillator strength fit (Figure 6.10d) yields an oscillator strength ratio of $F_1/F_2 = 2.27$ and confirms the negative sign of the IE-A coupling.

In addition to the measurement results, the coupled dipole model is also able to parameterise the results from the GW+BSE calculations quite well.

To summarise, our GW+BSE calculations show that the excitons observed in the experiment are mixed excitonic states rather than states consisting of a single excitonic transition. The true excitonic eigenstates are mixed states of multiple excitonic transitions.

6.8 Intravalley exchange coupling of A- and B-excitons

An analysis of the spin and orbital composition of the excitons explains both the IE-B and IE-A couplings. The IE-B coupling arises via hole tunnelling (see Figure 6.11a). In the bare B-state, the electron and hole are localised in one monolayer; in the bare IE-state, the electron is localised in the same monolayer but the hole is localised in the other layer. Hole tunnelling couples these two states (Figure 6.11a). The large IE-B coupling constant, $+35.8$ meV, reflects the efficient hole tunnelling.

Conversely, the IE-A coupling arises via a weak admixture between the A- and B-excitons in the same valley and layer, as shown schematically in Figure 6.11b and Figure 6.11c. This exciton admixture was proposed in Reference [Guo19] for MoS₂ monolayers and is found also in our bilayer calculations (Figure 6.8).^{*} This means that both IE and A couple

^{*}We study the composition of the true A- and B-excitons in the same valley in monolayer MoS₂ using GW+BSE calculations. Our calculations show that the A-exciton contains 4.3% of the B-transition, while the B-exciton contains 8.8% of the A-transition. Those values are in line with the ones reported in Reference [Guo19].

to B. IE and A then acquire an effective coupling, a second-order effect.

In this analysis, depicted in Figure 6.11c, the IE-A coupling is determined by

$$\kappa_{\text{IE-A}} = -\frac{\kappa_{\text{A-B}}\kappa_{\text{IE-B}}}{\Delta E_{\text{A-B}}}, \quad (6.9)$$

with the sign convention employed here and where $\kappa_{\text{IE-B}}$ is the IE-B coupling, $\kappa_{\text{A-B}}$ the A-B coupling, and $\Delta E_{\text{A-B}}$ is the energy splitting between A and B [L651]. The experiment measures $\kappa_{\text{IE-A}} = -3.5$ meV, $\kappa_{\text{IE-B}} = 35.8$ meV, and $\Delta E_{\text{A-B}} = -170$ meV. In turn, this determines $\kappa_{\text{A-B}}$. We find $\kappa_{\text{A-B}} = -16.6 \pm 2.5$ meV. In other words, by using the IE as a tunable probe, we are able to determine the A-B coupling energy. This is an important quantity – it arises even in a MoS₂ monolayer and determines to what extent spin is a good quantum number in the fundamental exciton [Wan17c, Guo19].

6.9 Conclusion and outlook

We study the coupling of intralayer A- and B-exciton and IE in homobilayer MoS₂ by measuring its optical response. The large Stark shift of the IE (see Chapter 5) allows tuning the resonances through the coupling region. A classical model based on two coupled optical dipoles is developed that successfully describes the IE-A and IE-B couplings. We state four main conclusions.

First, a 2D semiconductor system, homobilayer MoS₂, is discovered for which the lowest-energy momentum-direct exciton is both electric-field tunable and bright, gaining in absorption strength as the field is increased. This is not the case for a monolayer (bright but without field-tunability) or a heterobilayer (field-tunable but dim). This is potentially useful in transporting and trapping excitons with locally-varying electric fields.

Second, in homobilayer MoS₂, the IE and B-excitons couple via hole tunnelling; the IE and A-excitons couple via an exchange-induced A-B admixture. This difference results in coupling constants of opposite sign (IE-B coupling phase 0, IE-A coupling phase π). By using an electrical analogy, we find that IE-B couple capacitively while IE-A couple inductively. Hybridised intra- and interlayer excitons can be tuned into a regime where one eigenmode is as bright as the intralayer component yet retains the electric dipole moment of the interlayer component. This combination of properties is very useful for creating exciton- or polaron-polaritons with highly nonlinear optical properties [Tan20a]. Recently it has been shown that the neutral IE in homobilayer MoS₂ coupled to a cavity photon leads to highly nonlinear effects [Dat22, Lou22]. This is already a very nice result that establishes homobilayer MoS₂ as a promising material platform to use a single polariton as a single-photon emitter [MM19, Del19]. We propose that our results would allow us to push the IE-polariton results even further. At zero electric field, the IE has a large absorption strength and a significant electric dipole moment; the A-exciton has an absorption strength

5 times stronger than the IE but no electric dipole moment. By increasing the electric field the IE can be tuned such that it couples to the A-exciton. In the coupled system, two hybridised excitons can couple to a photon in a cavity. At an intermediate electric field, the layer character of the coupled excitons is a strong function of the electric field (Figure 6.8) and the higher-energy eigenmode has both the absorption strength of the A-exciton and an electric dipole moment due to its interlayer character. This opens up interesting possibilities to create bright yet strongly interacting exciton-polaritons.

Third, we determine the A-B coupling, a result which is also relevant for a monolayer. By using IE as a sensor, we can measure the A-B coupling precisely – experiments on a monolayer are much harder to interpret. We find an A-B coupling of -16.6 meV. Equivalently, the A-like eigenstate is $|A\rangle + \epsilon|B\rangle$ with $|\epsilon| \simeq 10\%$, and vice versa for the B-like eigenstate. The A-B coupling implies that spin is an imperfect quantum number for the A- and B-excitons in the same valley. This is a basic property of MoS₂.

Finally, we show that a measurement of the optical susceptibility enables not just the magnitude but also the phase of the exciton-exciton couplings to be determined (see Figure 6.6). The coupling model can be readily applied to other TMD bilayer systems where band hybridisation leads to mixed excitonic states [Ale19, RT19, Kie20, Sun20, Tan21, McD21].

We point out that the driven coupled oscillator model has a general validity – it is by no means limited to excitons in the optical domain. We note for instance that it describes the response of two coupled gatemons at microwave frequencies where a clear destructive interference is observed in the lower-frequency branch [Cas16] (compare Appendix Figure E.6 bottom right with Figure 4a in Reference [Cas16]).

The model shows how a weak resonance can be made visible by bringing it into near-degeneracy with a strong resonance. All that is required is a coupling between the two resonances. Furthermore, in the case of a weak coupling, although the energies are only slightly perturbed, the absorption strengths are strongly modified by the coupling. This sensitivity is very useful in cases where the couplings are potentially weak or completely unknown. Examples include hybrid systems, for instance, an exciton or a spin coupled to a mechanical mode.

“The pen is mightier than the sword if the sword is very short, and the pen is very sharp.”
Terry Pratchett, *The Light Fantastic* (1986)

Chapter

First-order magnetic phase transition of mobile electrons in monolayer MoS₂

Adapted from:

J. G. Roch, D. Miserev, G. Froehlicher, N. Leisgang, L. Sponfeldner, K. Watanabe, T. Taniguchi, J. Klinovaja, D. Loss, and R. J. Warburton, “**First-order magnetic phase transition of mobile electrons in monolayer MoS₂**”, *Physical Review Letters* **124**, 187602 (2020)[†]

Evidence is presented for a first-order magnetic phase transition in a gated two-dimensional semiconductor, monolayer MoS₂. The phase boundary separates a ferromagnetic phase at low electron density and a paramagnetic phase at high electron density. Abrupt changes in the optical response signal an abrupt change in the magnetism. The magnetic order is thereby controlled via the voltage applied to the gate electrode of the device. Accompanying the change in magnetism is a large change in the electron’s effective mass. The ferromagnetic phase is unstable at zero magnetic field due to the symmetry of spin-up and spin-down states. We show that a weak circularly polarised laser excitation leads to symmetry breaking and therefore a stable ferromagnetic phase even at zero magnetic field.

Section 7.1 introduces the concept of magnetic phase transitions and our material of interest, monolayer MoS₂. The photoluminescence emission of monolayer MoS₂ is discussed in Section 7.2. In Section 7.3, evidence is presented for a first-order magnetic

[†]J.G.R. fabricated device 1; L.S. fabricated device 2. J.G.R. and L.S. carried out the optical spectroscopy measurements on device 1; L.S. measured device 2. J.G.R. analysed the optical spectra of device 1. D. M. developed the first-order phase transition theory. L.S. analysed the measurement data of device 2 and interpreted the results.

phase transition based on the analysis of the measured photoluminescence. The effective electron mass in the ferromagnetic and paramagnetic phases is estimated in Section 7.4. In Section 7.5, experimental hints of an excitation laser-induced stable ferromagnetic phase at zero magnetic field are presented, based on the different trion states in monolayer MoS₂. Lastly, Section 7.6 summarises the results and gives a brief outlook for future experiments.

7.1 Introduction

Mobile electrons in a semiconductor can lower their energy by aligning their spins, a consequence of the Pauli principle. A ferromagnetic phase in which all electron spins point in the same direction was proposed originally by Bloch [Blo29]. Experimental verification of this prediction on two-dimensional (2D) electron gases in conventional semiconductors was elusive [Zhu03, Vak04] on account of disorder [Fin95, Yus00]. Recently however, ferromagnetic ordering of 2D electrons was reported in monolayer MoS₂ [Roc19], twisted-bilayer graphene [Sha19], and in AlAs quantum wells [Hos21]. Furthermore, ferromagnetic ordering of holes in a moiré superlattice was also recently observed in a WS₂/WSe₂ heterobilayer [Wan22]. A phase transition can be expected between a ferromagnetic state at low density and a paramagnetic state at high density. The behaviour on crossing the phase boundary is crucial: does the magnetisation turn on abruptly or does the magnetisation increase gradually?

In three-dimensional (3D) ferromagnets such as iron, the magnetisation grows gradually from zero on crossing the phase boundary. This is classified as a “second-order” phase transition. An abrupt change in the magnetisation, a “first-order” phase transition, is more striking and is observed in more exotic metals, so-called “quantum ferromagnets” [Bra16]. This is potentially much more useful in spintronics: a small change in a control parameter from one side of the phase boundary to the other results in a massive change in the magnetisation. In metallic systems, the control parameter is typically the temperature or pressure, neither convenient for fast and efficient switching from one phase to the other. This restriction is lifted in 2D semiconductors for which the electron density can be controlled over a wide range simply via a voltage applied to a gate electrode. However, magnetism of mobile electrons in 2D is different to that in 3D. On the one hand, mean-field theories, such as those of Bloch [Blo29] and Stoner [Sto38], are provably inadequate in 2D [Mer66, Los11]. On the other hand, corrections to Fermi liquid theory, effects which can result in a first-order phase transition, are predicted to be much more pronounced in 2D compared to 3D [Bel99, Chu04, Mas09, Bra16]. Experimentally, magnetic phase transitions of mobile electrons in 2D semiconductors are unexplored.

We focus on monolayer MoS₂, a 2D semiconductor in the transition-metal dichalcogenide (TMD) family. We present evidence for a first-order phase transition between a paramagnetic phase at high electron density and a ferromagnetic phase at low electron density. The

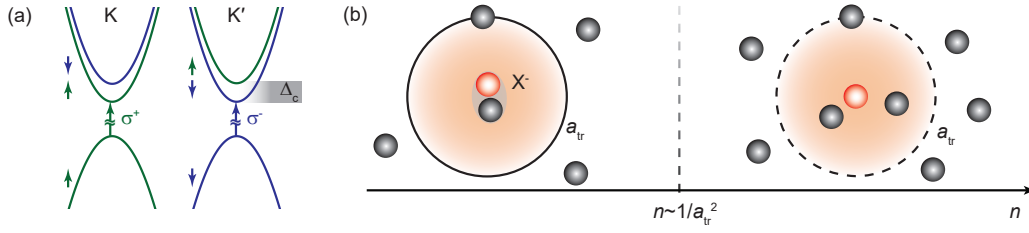


Figure 7.1. (a) Band structure and allowed optical transitions of monolayer MoS₂. (b) Schematic of a trion in a two-dimensional Fermi sea. The black circles denote conduction band electrons; the red circles a valence band hole. The trion (X⁻, Bohr radius a_{tr}) is bound (unbound) at low (high) electron density.

magnetism is thereby controlled electrically simply via the voltage applied to a gate electrode. Accompanying this abrupt change in magnetisation is an abrupt change in the electron effective mass, from a relatively small value in the paramagnetic phase to a large value in the ferromagnetic phase.

The conduction band structure of MoS₂ exhibits minima at the edges of the Brillouin zone, at the K and K' points [Mak10, Xia12, Kor14]. The spin- \uparrow and spin- \downarrow states are split by a small spin-orbit interaction, Δ_c (see Figure 7.1a). Calculations predict $|\Delta_c| = 3$ meV [Kor14]; experiments suggest $\Delta_c = 0.8$ meV [Mar17]. The bare electron mass is relatively large, $0.44m_0$ according to theory [Kor14]; the dielectric constant relatively small, such that the Bohr radius is just ~ 0.5 nm, only slightly larger than the lattice constant. Quantum effects in gated MoS₂ have recently been reported: conductance quantisation [Mar17], Shubnikov-de Haas oscillations [Pis18] and ferromagnetic spin-ordering [Roc19].

Here, a monolayer of MoS₂ is embedded between two hBN layers. Electrons are injected into the MoS₂ by applying a voltage to a metallic contact (see Appendix B for device details). The ground state of the mobile electrons is probed optically with photoluminescence (PL) and absorption spectroscopy. Right-handed (left-handed) circularly-polarised light σ^+ (σ^-) injects a spin- \uparrow (spin- \downarrow) hole at the K point (K' point) (see Figure 7.1a). This spin-valley selectivity is crucial: the optical probe represents a spin-sensitive probe of the electronic ground state. Furthermore, PL represents a local measurement: information is gleaned from a few-hundred-nanometre diameter region on the sample. On this length scale, inhomogeneous broadening in the optical response is small [Cad17, Aja17].

7.2 Photoluminescence emission of monolayer MoS₂

PL in the presence of a Fermi sea of electrons has been explored in a number of 2D semiconductor systems (GaAs [Fin95, Yus00], CdTe [Hua00], MoSe₂ [Sid17, Bac17]) and there is a model to describe it [Uen90, Haw91]. At very low n , PL arises from the recombination of tightly bound electron-hole pairs, excitons (X⁰). As n increases, X⁰ weakens and is replaced with a red-shifted peak, the trion (X⁻). The trion consists of

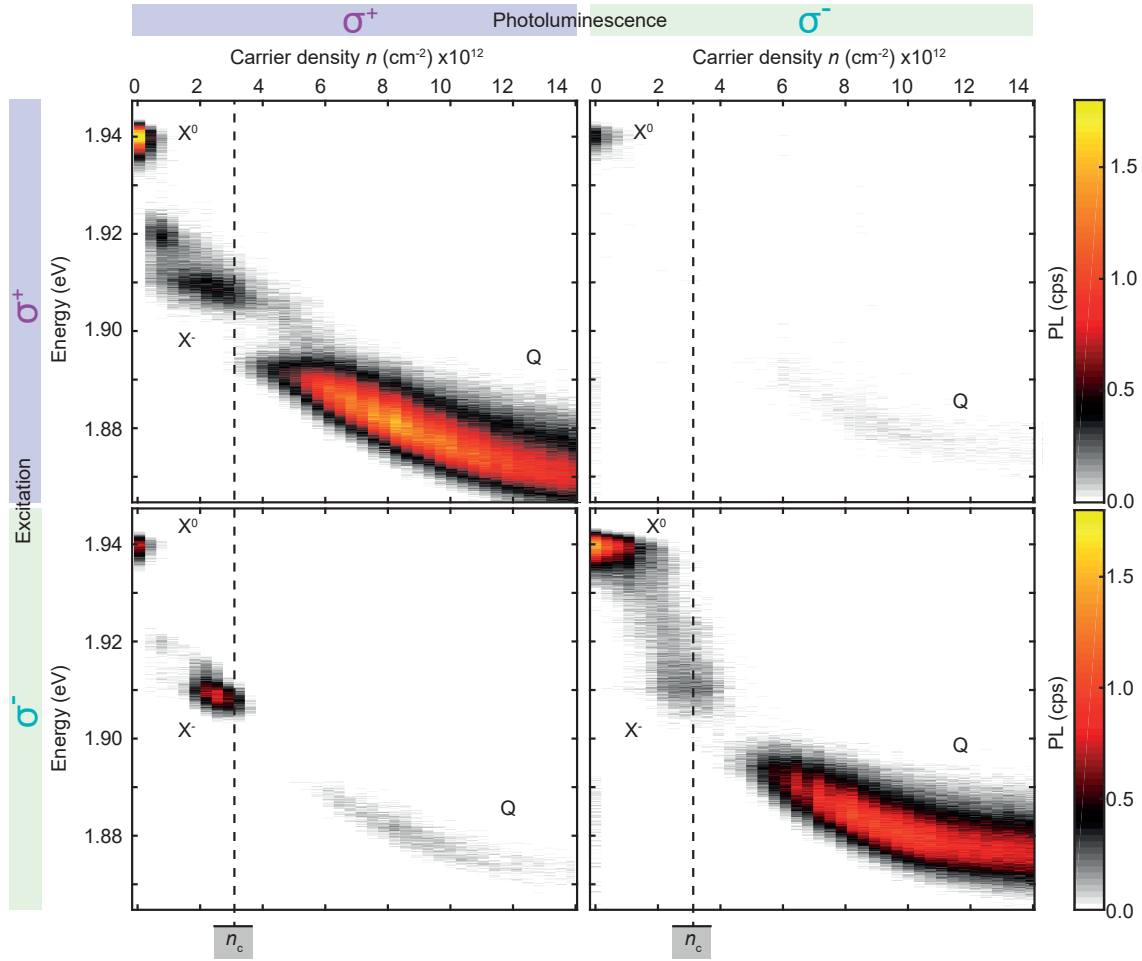


Figure 7.2. Photoluminescence of gated monolayer MoS₂ at 1.6 K and $B_z = 9.00$ T. The excitation is either σ^+ or σ^- ; the detection either σ^+ or σ^- : the top (bottom) row corresponds to σ^+ (σ^-) excitation; the left (right) column to σ^+ (σ^-) detection. n_c denotes the critical density. At $n = n_c$ there is a jump in the PL energy: the PL process changes from a trion (X^-) to a Mahan exciton (Q). For $n > n_c$, the PL process is largely polarisation-conserving. Conversely, for $n < n_c$, the PL is highly polarisation-nonconserving: σ^- excitation leads to strong σ^+ PL.

two electrons in a spin-singlet state and a hole, or, in more accurate language, the bound exciton-Fermi sea polaron [Sur01, Efi17]. At higher n , the trions become unbound. In a simple picture, this occurs once an electron from the Fermi sea resides “inside” the trion wave-function (see Figure 7.1b). In PL, the X^- peak evolves gradually into a broad peak, typically red-shifted with respect to X^- , the Mahan exciton [Mah67]. A key property of the Mahan exciton is the red-shift of PL with respect to absorption, $E_{\text{PL}} - E_{\text{A}} < 0$ [Uen90, Haw91]. In the single-particle limit for equal electron and hole masses (as for TMDs), this shift is twice the Fermi energy.

We turn to gated MoS₂. The absorption spectra at large out-of-plane magnetic field

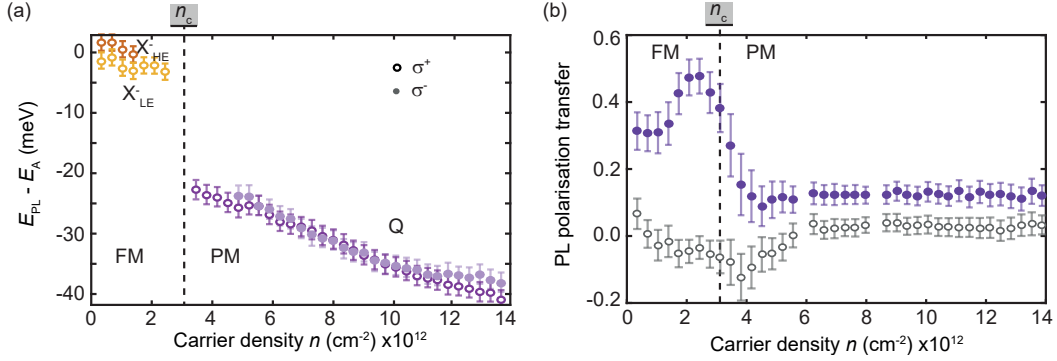


Figure 7.3. (a) The energetic separation between the PL and the absorption, $E_{\text{PL}} - E_{\text{A}}$ (measured either with σ^+ or σ^- polarisation), versus electron density at 1.6 K and $B_z = 9.00$ T. There are two trions, X_{LE}^- and X_{HE}^- (red and orange points, respectively) [Roc19]. The Q-peak is plotted for both polarisations (σ^+ and σ^- , open-purple and filled-purple points, respectively). (b) The PL polarisation transfer [$a_2/(a_1 + a_2 + a_3)$ (purple) and $a_3/(a_1 + a_2 + a_3)$ (white), see Equation 7.1], versus electron density. These plots determine $n_c = 3.0 \times 10^{12} \text{ cm}^{-2}$.

(two trions in σ^+ -polarisation but no trions in σ^- -polarisation) show that the spins are polarised (ferromagnetism) at low-to-intermediate densities [Roc19]. We focus here on PL. At $n \simeq 0$, the PL spectrum consists of a single sharp line corresponding to X^0 emission (Figure 7.2) [Che14]. On increasing n , X^0 weakens and is replaced with a red-shifted line, X^- (Figure 7.2) [Sid17, Bac17, Roc19]. At higher densities, X^- disappears and a broad peak (labelled Q in Figure 7.2) appears to the red. The Q-peak exhibits the large PL-absorption splitting characteristic of the Mahan exciton. These features follow the standard behaviour of PL in the presence of a Fermi sea. There is however a radically different feature. Strikingly, the smooth transition between trion (X^-) and Mahan exciton (Q) is missing: instead, there is an abrupt change from one to the other resulting in a “gap” in the PL spectrum (Figure 7.2). This signals an abrupt change in the Fermi sea: it is the first evidence for a first-order phase transition. The second evidence comes from the polarisation of the PL. We excite and detect in all four combinations of circular polarisation, presenting the results as a matrix (Figure 7.2). For the Q-peak, the response is overwhelmingly “diagonal”, i.e. polarisation-preserving: excitation with σ^+ (σ^-) results in σ^+ -polarised (σ^- -polarised) PL; Conversely, for X^- , there is a large “non-diagonal” response (σ^- -polarised excitation results in σ^+ -polarised PL yet σ^+ -polarised excitation results in a very weak PL signal), clear evidence for symmetry breaking. The switch from one symmetry class to the other is also abrupt as the density changes.

7.3 First-order magnetic phase transition

We plot $E_{\text{PL}} - E_{\text{A}}$ as a function of n (Figure 7.3a). Details on the absorption measurement can be found in Appendix F. There is an abrupt change at $3.0 \times 10^{12} \text{ cm}^{-2}$ signifying

an abrupt change in the nature of the PL process. Also, we analyse the polarisation dependence via:

$$\begin{pmatrix} P_+ \\ P_- \end{pmatrix} = \begin{pmatrix} a_1 + h & a_2 \\ a_3 & a_1 - h \end{pmatrix} \begin{pmatrix} L_+ \\ L_- \end{pmatrix} \quad (7.1)$$

where L_+ (L_-) is the σ^+ -polarised (σ^- -polarised) laser intensity, P_+ (P_-) the σ^+ -polarised (σ^- -polarised) PL signal. P_+ and P_- are integrated over the spectral window (Figure 7.2). The term a_1 describes the polarisation-preserving response. Terms a_2 and a_3 describe a transfer of the polarisation, from σ^- at the input to σ^+ at the output (a_2); from σ^+ at the input to σ^- at the output (a_3). There is one further term. In the experiment, a hole is injected either at the K point or at the K' point by choosing the polarisation. This works well but imperfectly. In an applied magnetic field, the hole can relax from the K' point to the K point, a process that is described by the term h . We define the ‘‘PL polarisation transfer’’ as $a_2/(a_1 + a_2 + a_3)$, i.e. the fraction of the total PL emitted in the polarisation-nonconserving channel. As a function of n , the PL polarisation transfer reaches values as high as 50% at intermediate density, decreasing rapidly between $n = 2.5 \times 10^{12}$ and $n = 3.5 \times 10^{12} \text{ cm}^{-2}$ (Figure 7.3b). The opposite polarisation-nonconserving process, $a_3/(a_1 + a_2 + a_3)$, is small at all n (Figure 7.3b). Both $E_{\text{PL}} - E_{\text{A}}$ and the PL polarisation transfer change abruptly at the same electron density. We identify a critical density of $n_c = 3.0 \times 10^{12} \text{ cm}^{-2}$ (Figure 7.3).

Without a magnetic field, the abrupt change in $E_{\text{PL}} - E_{\text{A}}$ is still clearly visible (see Appendix F) showing that there is still a phase transition at $n = n_c$ between states with different magnetic order. However, there is zero net magnetisation at $B_z = 0$ (zero polarisation transfer). At $B_z = 0$, we propose that for $n < n_c$ there are fluctuating ‘‘puddles’’ of spin- \uparrow and spin- \downarrow electrons such that the net magnetisation, averaged over time and space, goes to zero. This is consistent with the Ising symmetry of the system at low temperature: the spin-orbit interaction in the conduction band forces the magnetisation to lie either in the ‘‘up’’ or ‘‘down’’ direction but in the absence of an applied magnetic field, both directions are equally likely. The size of the ‘‘puddles’’ is much smaller than the extent of the spatial probe in this experiment [Fan21]. At $B_z = 0$ and $n > n_c$, the puddles disappear – there is no magnetic ordering whatsoever. This line of thinking explains the role of the magnetic field in these experiments – it establishes a quantisation axis, favouring either the ‘‘up’’ or the ‘‘down’’ direction, and it allows long-range magnetic order stabilising the ferromagnetic state.* In a large B_z but at $T = 30 \text{ K}$, there is evidence that

*We note that the Zeeman splitting even at $B_z = +9.00 \text{ T}$ is an order of magnitude smaller than the Fermi energy in these experiments precluding magnetic order via a paramagnetic response. Also, if the response were solely paramagnetic then a phase transition would not occur, ruling out a giant paramagnetism.

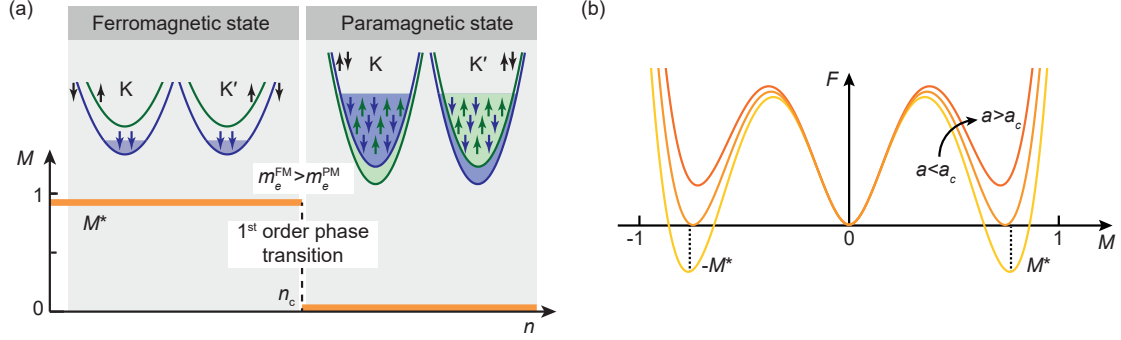


Figure 7.4. (a) The occupied bands in the ferromagnetic phase (left) and in the paramagnetic phase (right) along with the change in magnetisation at $n = n_c$. In the ferromagnetic phase, occupation of two bands with the same spin is favoured, a consequence of exchange. In the paramagnetic phase, all four bands are occupied. (b) The free energy F as a function of magnetisation fraction M for $F = aM^2 + bM^4 + c|M|^3$. The terms aM^2 and bM^4 are the Ginzburg-Landau terms; the nonanalytic term $c|M|^3$ arises from corrections to Landau's theory of the Fermi liquid. Plotted is F for constant b and c with $c < 0$ as a function of a . For $a < c^2/4b$ ($a > c^2/4b$), the global minimum of F lies at $M = 0$, a paramagnetic phase (large M , a ferromagnetic phase). The phase transition at $a = c^2/4b$ is first-order.

the phase transition survives (see Appendix F).

Our results are in agreement with recent theory [Mis19] which predicted spin-ordering (and not ordering in the valley index or combined spin-valley index [VdD18, Bra18]) and a first-order phase transition between ferromagnetic and paramagnetic phases. Both predictions in the theory depend on corrections to Fermi liquid theory which arise via infrared electron-hole excitations at the Fermi energy [Bel99, Chu04, Mas09]. This theory allows us to present a model which is fully consistent with the experimental results (Figure 7.4). For $n < n_c$, the two bands with spin- \downarrow are occupied resulting in a ferromagnetic state with a large spin polarisation [Roc19]; for $n > n_c$, all four bands are occupied, the ferromagnetism is destroyed and the spin polarisation disappears (Figure 7.4a). The free energy F depends on the magnetisation fraction M according to:

$$F = aM^2 + bM^4 + c|M|^3. \quad (7.2)$$

The first two terms represent the Ginzburg-Landau model which, alone, leads to a second-order phase transition. The third term is a non-analytic correction. Crucially, theory predicts a negative c for MoS₂ [Mis19]. Plots of F as a function of density (i.e. versus a) show how a negative c leads to a first-order transition between paramagnetic and ferromagnetic phases (Figure 7.4b). We stress that the first-order nature of the phase transition depends on the non-analytic correction: without it, the transition would be second-order.

7.4 Effective electron mass

In the ferromagnetic (FM) phase, we observe PL from the trion: the trion is bound; in the paramagnetic (PM) phase we do not observe PL from the trion: the trion is unbound. In other words, there is an abrupt change in the nature of the PL at n_c , from trion to Mahan exciton. This implies a profound change of the electron mass on passing from the FM to the PM phase. We analyse the simple concept (see Figure 7.1b). The Fermi sea reduces the trion binding energy E_T because all states with $k < k_F$ are occupied and become unavailable in constructing the trion wave function:

$$E_T = E_T^0 + \hbar^2 k_F^2 / 2\mu, \quad (7.3)$$

where k_F is the Fermi wave-vector, E_T^0 the trion binding energy in the limit $n \rightarrow 0$, and μ the reduced mass of an exciton and an electron. This result comes from the Suris model [Sur01] with the approximation $E_T^0 \gg \hbar^2 k_F^2 / 2\mu$.

In the FM [PM] phase, two [four] bands are occupied such that $E_T = 0$ at $n_{\text{FM}} = \mu E_T^0 / \pi \hbar^2$ [$n_{\text{PM}} = 2\mu E_T^0 / \pi \hbar^2$]. The experiment tells us that n_{FM} must be larger than n_c , and that n_{PM} must be smaller than n_c , i.e. $n_{\text{FM}} > n_{\text{PM}}$. This conundrum can only be resolved by a change in the reduced mass, $\mu_{\text{FM}} > 2\mu_{\text{PM}}$, i.e. a significant decrease in the electron mass on going from the FM to the PM phase. Taking $E_T^0 = 17$ meV [Roc19] and a hole mass of $m_h = 0.54m_o$ [Kor15], we find $m_e^{\text{FM}} > 0.65m_o$ and $m_e^{\text{PM}} < 0.40m_o$. The mass in the ferromagnetic phase (m_e^{FM}) is consistent with the value deduced from Shubnikov-de Haas oscillations at low density ($0.8m_o$) [Pis18]; the mass in the paramagnetic phase (m_e^{PM}) is consistent with the calculated bare electron mass ($0.44m_o$) [Kor14]. This analysis is consistent with general expectations that the mass is enhanced above its bare value in an interacting phase.

7.5 Stabilising the ferromagnetic phase at zero magnetic field

The next step is to stabilise the ferromagnetic phase without a large external magnetic field. The stabilisation could be achieved via coupling to an insulating 2D ferromagnet. A much more versatile method would be to use a circularly polarised pump laser, which has been demonstrated to create a stable FM phase in a WSe₂ monolayer [Hao22] or in a WS₂/WSe₂ heterobilayer [Wan22]. Hao et al. demonstrated for monolayer WSe₂, that the excitation with a σ^+ -polarised (σ^- -polarised) pump laser leads to the creation of excitons in the K (K') valley and therefore an excess of spin- \uparrow (spin- \downarrow) electrons. The imbalance between spin- \uparrow and spin- \downarrow electrons leads to a symmetry breaking between the two FM phases. The resulting FM phase is stable at zero magnetic field and can extend over the

whole sample region [Hao22]. While the laser-induced FM phase exists in WSe₂, it is not clear if this mechanism also works in MoS₂. In this section, evidence is presented that the PL response of monolayer MoS₂ indicates the formation of a stable FM phase, even when exciting the monolayer with a small laser power ($P < 0.5 \mu\text{W}$).

In order to explain the laser-induced FM phase, the trion states in monolayer MoS₂ are introduced in Subsection 7.5.1. The observation and the mechanism behind the FM phase at zero magnetic field are discussed in Subsection 7.5.2.

7.5.1 Trion states in monolayer MoS₂

Upon n-doping monolayer MoS₂, different trion states can form due to the spin- and valley-degree of freedom [Dru17, Zhu20]. In the following, we base our analysis of the trion states on Reference [Lei22], which takes full spin polarisation into account.* We limit the following analysis to a moderate carrier doping of $\sim 2 - 4 \times 10^{12} \text{ cm}^{-2}$.

In order to study the trions in a stable spin polarisation, we measure the polarisation-resolved PL response of monolayer MoS₂ (device 2) at a magnetic field of 9 T (see Figure 7.5). The polarisation behaviour of each peak reproduces the PL behaviour for device 1 in Figure 7.2 very well. Device 2 exhibits a good quality as the excitonic linewidth of $\sim 2 \text{ meV}$ is very close to the homogeneous limit [Cad17]. The polarisation behaviour of X⁰ reveals a large spin- and valley-depolarisation due to electron-hole exchange between the valleys [Cao12, Zen12]. We define the degree of circular polarisation of X⁰ (DOCP^{+,−}) for σ^+ and σ^- excitation as

$$\text{DOCP}^{+,-} = \frac{I^{\sigma^{+,-}/\sigma^+} - I^{\sigma^{+,-}/\sigma^-}}{I^{\sigma^{+,-}/\sigma^+} + I^{\sigma^{+,-}/\sigma^-}}, \quad (7.4)$$

where $I^{\text{excitation}/\text{detection}}$ is the integrated PL intensity of the X⁰. At $n = 0$, we extract a DOCP⁺ = 38.8% (DOCP[−] = −1.0%) for X⁰, which leads to a significant exciton transfer between the K and K' valleys.

In the moderate doping regime, there is a strong trion resonance T₃ that emits in σ^+ polarisation, independent of the excitation polarisation. For a σ^- -polarised emission, there is a weak resonance T₄ (no clear resonance) visible for an excitation with σ^- (σ^+) polarisation. In the following, we will argue that T₃ and T₄ are two different trions, where their appearance depends on the valley (polarisation) that is read out.

The polarisation resolved spectra in Figure 7.5 are fitted around the trion resonance by a single Lorentzian. Example spectra and the corresponding fits are shown in Figure 7.6a. The extracted peak energies are plotted in Figure 7.6b and the full widths at half maximum

*The first experimental observation of the three trion states, including the spin polarisation effect, was done by N. Leisgang and the theoretical description was made by N. Leisgang and D. Miserev. A detailed discussion and derivation of the trion states can be found in Reference [Lei22].

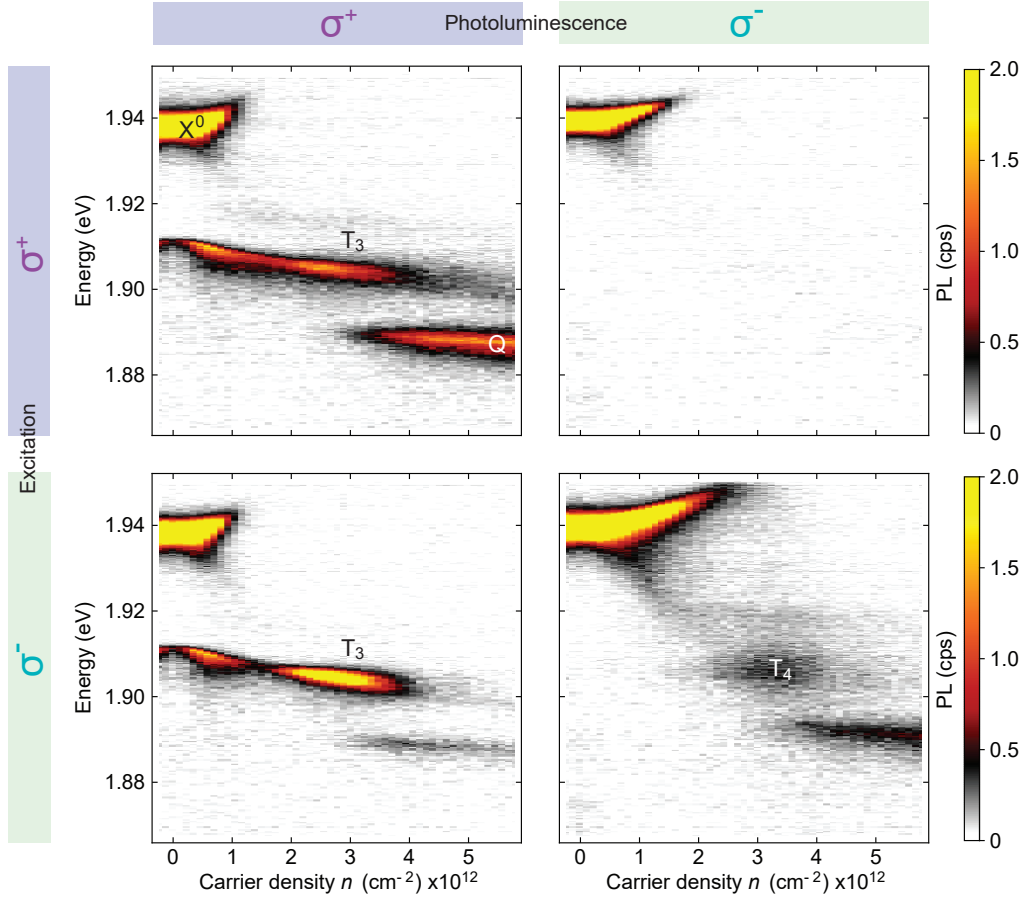


Figure 7.5. Polarisation-resolved PL of a different gated monolayer MoS₂ device (device 2) at 4.2 K, $B_z = 9$ T, and $P = 0.462$ μ W. The polarisation behaviour of each peak is similar to the one shown in Figure 7.2. The neutral exciton X^0 and the Mahan exciton Q are marked in the top left colour-map. The intravalley singlet trion T_3 only appears in cross-polarised emission, while the intervalley triplet trion T_4 appears in co-polarised emission.

(FWHM) are shown in Figure 7.6c. The energies linearly redshift for an increased doping according to Equation 7.3. Fitting a linear function to the energies we find a slope for T_3 of 1.51 meV/ 10^{12} cm⁻² (2.00 meV/ 10^{12} cm⁻²) for σ^+/σ^+ (σ^-/σ^+). For T_4 , the slope is 0.50 meV/ 10^{12} cm⁻² for σ^-/σ^- . According to Equation 7.3, the slopes are inversely proportional to the reduced trion mass. This would mean that the reduced trion mass of T_4 is roughly three times as large as that of T_3 . The difference in slopes might also be influenced by a different change in the effective trion masses as the Fermi level is increased [Zhu20]. The T_3 FWHM stays small and starts to increase for larger densities. For T_4 , the FWHM increases immediately until it starts to saturate at larger n . Generally, the T_4 linewidth is broader than that of T_3 . The two T_3 resonances behave very similarly in energy and FWHM as a function of n , while the T_4 resonance behaves rather differently.

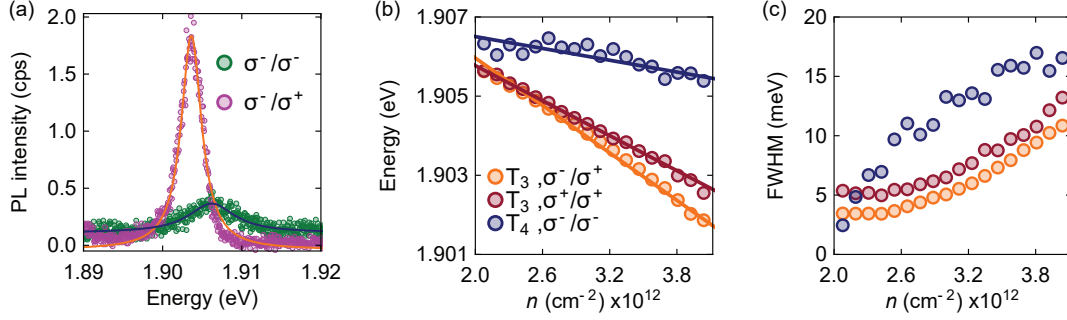


Figure 7.6. (a) Polarisation-resolved PL spectra extracted from Figure 7.5 at a carrier density of $n = 3.2 \times 10^{12} \text{ cm}^{-2}$ and a σ^- -polarised excitation. Each spectrum is fitted by a single Lorentzian. The orange (blue) curve shows the resulting fits for T_3 (T_4). (b,c) Polarisation-resolved carrier density dependence of the fitted (b) peak energies and (c) full width at half maximum (FWHM). The lines in (b) correspond to a linear fit of the energies. For T_3 , the slope is $1.51 \text{ meV}/10^{12} \text{ cm}^{-2}$ ($2.00 \text{ meV}/10^{12} \text{ cm}^{-2}$) for σ^-/σ^+ (σ^+/σ^+). For T_4 , the slope is $0.50 \text{ meV}/10^{12} \text{ cm}^{-2}$ for σ^-/σ^- .

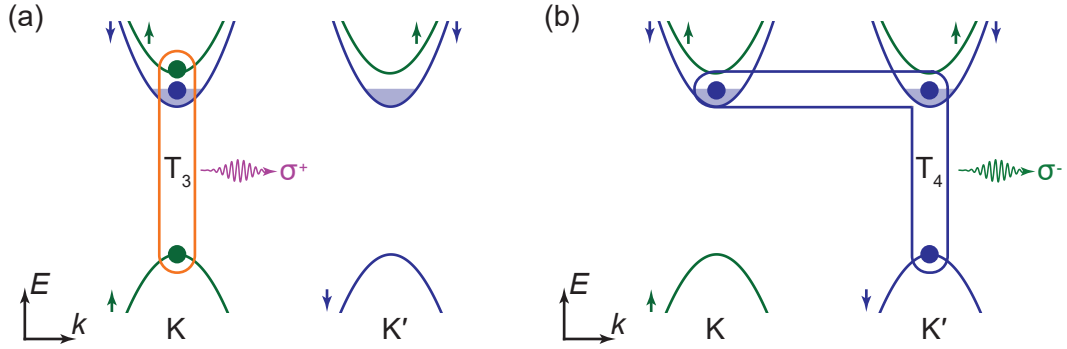


Figure 7.7. Sketch of the (a) intravalley spin singlet trion T_3 and (b) the intervalley spin triplet trion T_4 in a large and positive magnetic field leading to a spin- \downarrow polarisation. T_3 (T_4) is detected in σ^+ -polarised (σ^- -polarised) PL emission as it originates from the K (K') valley.

These differences are an indication that T_3 and T_4 correspond to different trion states.

The trion state T_3 is attributed to the intravalley spin singlet trion that emits in σ^+ polarisation as sketched in Figure 7.7a. The appearance of T_3 for either excitation polarisation is due to a significant valley- and spin-depolarisation [Cao12, Zen12].

The trion state T_4 is attributed to the intervalley spin triplet trion emitting in σ^- polarisation as sketched in Figure 7.7b. The larger linewidth and the smaller intensity of T_4 as compared to T_3 strengthen the interpretation of T_4 as a spin triplet resonance. For a σ^+/σ^- polarisation, the T_4 is not clearly visible. This can be explained by a suppressed exciton transfer to K' due to the presence of a spin- \downarrow Fermi sea at K' [Lei22].

For the explanation of the laser-induced spin polarisation as discussed in the next subsection, only the lowest energy trions, T_3 and T_4 , are important. Therefore, the other

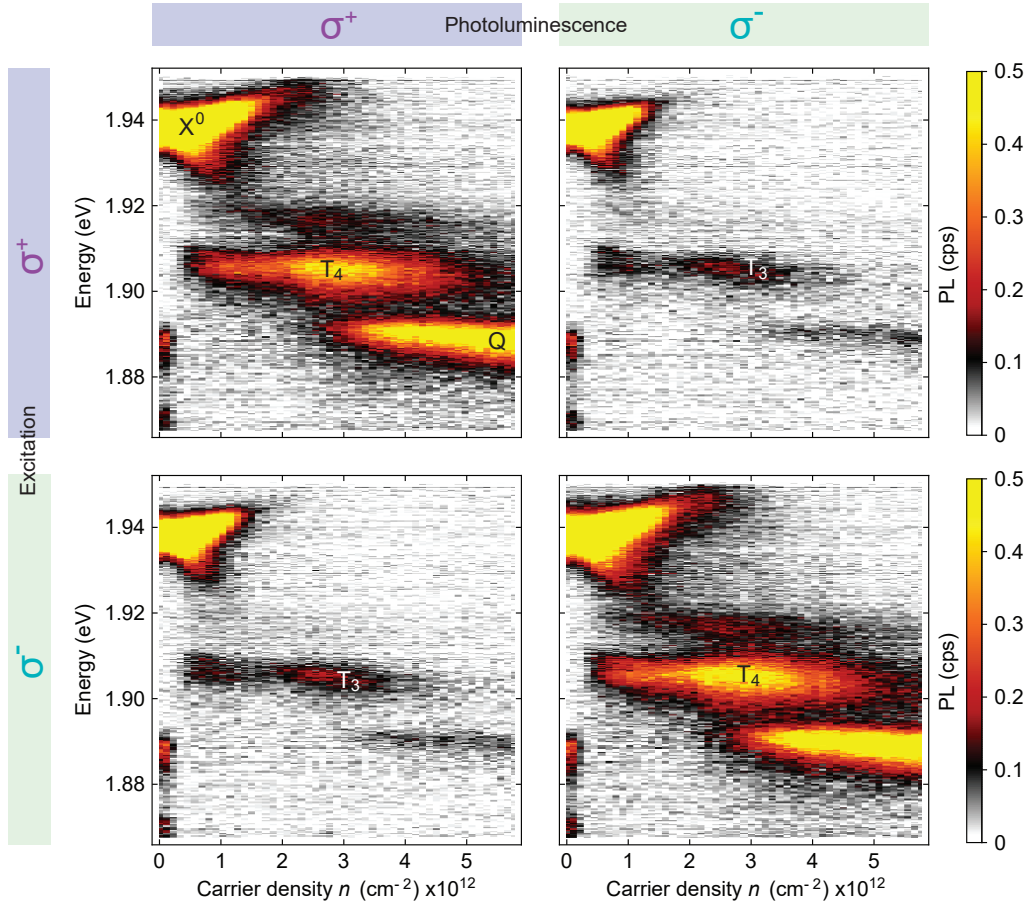


Figure 7.8. Polarisation-resolved PL of gated monolayer MoS₂ (device 2) at 4.2 K, $B_z = 0$ T, and $P = 0.409$ μ W. The neutral exciton X^0 and the Mahan exciton Q are marked in the top left colour-map. The intravalley singlet trion T_3 only appears in σ^+ -polarised emission, while the intervalley triplet trion T_4 appears in σ^-/σ^- emission.

two trion resonances formed in monolayer MoS₂ will only be briefly discussed. The two highest energy triions in the three trion structure are usually very weak and not observed at every sample position [Lei22]. These two peaks could not be clearly observed in device 2. Mostly, only one of these peaks is observed (see polarisation-conserving channels in Figure 7.5 and in Figure 7.8). The other peak could be masked by the strong X^0 or the lowest energy trion resonance. The proposed origin of these two peaks is the superposition $(|S_i\rangle + |T_0\rangle)/\sqrt{2}$ of an intervalley spin singlet trion $|S_i\rangle$ and an intervalley spin triplet trion $|T_0\rangle$, mixed with the corresponding dark state $(|S_i\rangle - |T_0\rangle)/\sqrt{2}$ [Lei22].

7.5.2 Laser-induced spin polarisation

Now, we turn to the polarisation-resolved PL response at a magnetic field of 0 T (see Figure 7.8). As compared to the PL signal at 9 T, the two co-polarised (cross-polarised)

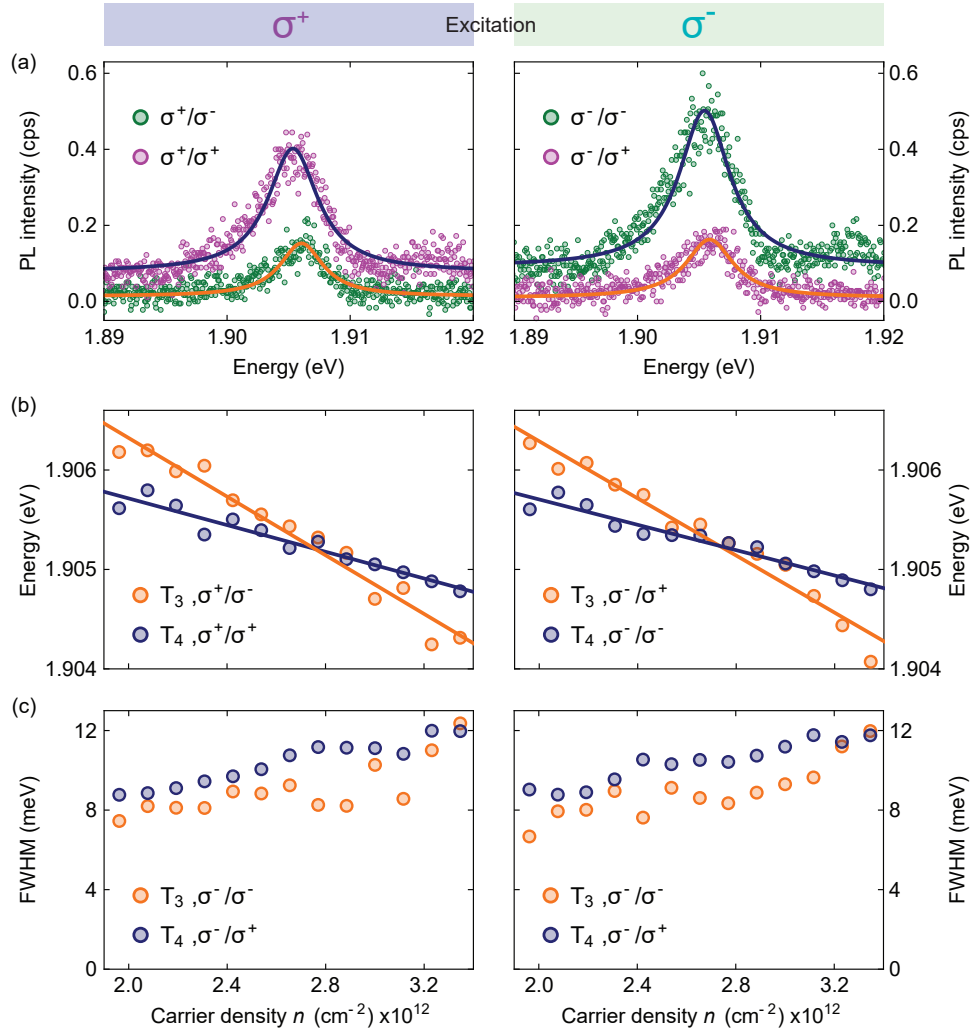


Figure 7.9. (a) Polarisation-resolved PL spectra extracted from Figure 7.8 at a carrier density of $n = 2.3 \times 10^{12} \text{ cm}^{-2}$. Each spectrum is fitted by a single Lorentzian. The orange (blue) curve shows the resulting fits for T_3 (T_4). (b,c) Polarisation-resolved carrier density dependence of the fitted (b) peak energies and (c) FWHM. The lines in (b) correspond to a linear fit of the energies. For T_3 , the slope is $1.47 \text{ meV}/10^{12} \text{ cm}^{-2}$ ($1.44 \text{ meV}/10^{12} \text{ cm}^{-2}$) for σ^+/σ^- (σ^-/σ^+). For T_4 , the slope is $0.67 \text{ meV}/10^{12} \text{ cm}^{-2}$ ($0.64 \text{ meV}/10^{12} \text{ cm}^{-2}$) for σ^+/σ^+ (σ^-/σ^-).

channels at zero magnetic field exhibit the same emission behaviour. At first glance, a similar response of the polarisation-conserving (non-conserving) channels excludes the possibility of spin polarisation. At zero magnetic field, the PL emission energy is almost the same independent of the detection polarisation (see Fig. 7.9b) but there is evidence that PL arises from different trions. We will show that a σ^+ (σ^-) excitation leads to a spin polarisation of spin- \uparrow (spin- \downarrow) electrons. Then, depending on the detection polarisation, either T_3 or T_4 is detected. Since the spin polarisation direction depends on the excitation

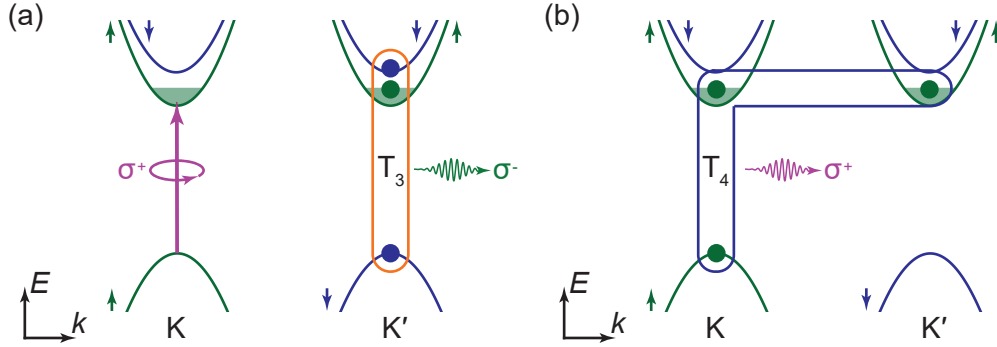


Figure 7.10. Sketch of the (a) intravalley spin singlet trion T_3 and (b) the intervalley spin triplet trion T_4 . A σ^+ -polarised excitation laser leads to an excess of spin- \uparrow electrons and therefore a favoured spin- \uparrow polarisation even at zero magnetic field. T_3 (T_4) is then detected in σ^- -polarised (σ^+ -polarised) PL emission as it originates from the K' (K) valley.

laser polarisation, the measured PL response is similar for the polarisation-conserving (non-conserving) channels. The low energy features around ~ 1.88 eV and at zero n appear at certain sample positions in device 2 and are probably due to defect states or potentially to phonon-assisted recombination of indirect excitons [Par22].

We fit the polarisation-resolved spectra in the moderate doping regime with a single Lorentzian around the trion resonance as shown in Figure 7.9a. The extracted peak energies are plotted in Figure 7.9b and the FWHM are shown in Figure 7.9c. The trion resonance in the polarisation-conserving channels exhibits an energy shift as a function of n which is roughly half the shift of the trion resonance in the polarisation non-conserving channels. The energy shift of the trion in the polarisation-conserving σ^+/σ^+ (σ^-/σ^-) channel is $0.67 \text{ meV}/10^{12} \text{ cm}^{-2}$ ($0.64 \text{ meV}/10^{12} \text{ cm}^{-2}$), which is very similar to the slope of $0.50 \text{ meV}/10^{12} \text{ cm}^{-2}$ observed for T_4 at 9 T. The slope for the polarisation non-conserving σ^+/σ^- (σ^-/σ^+) channel is $1.47 \text{ meV}/10^{12} \text{ cm}^{-2}$ ($1.44 \text{ meV}/10^{12} \text{ cm}^{-2}$), which is very similar to the slope of $1.51 \text{ meV}/10^{12} \text{ cm}^{-2}$ ($2.00 \text{ meV}/10^{12} \text{ cm}^{-2}$) observed for T_3 in the σ^+/σ^+ (σ^-/σ^+) channel at 9 T. Therefore, we attribute the trion in the polarisation-conserving (non-conserving) channels to be T_4 (T_3).

The T_4 emission intensity is comparable at 9 T and 0 T, while the intensity of the T_3 emission is much stronger at 9 T than at 0 T. Density-dependent absorption measurements have shown that the oscillator strength of the spin singlet trions in the σ^+ polarisation increases for an increasing magnetic field [Roc19]. The increase in oscillator strength is explained by a larger spin polarisation in a stronger magnetic field. The small T_3 emission intensity at 0 T could be an indication that the spins are only slightly polarised by the weak excitation laser. Hao et al. show that the degree of spin polarisation increases with increasing laser power until a saturation value is reached [Hao22]. Another indication for

an incomplete laser-induced spin polarisation at zero magnetic field could be the FWHM behaviour of T_3 . While the T_3 FWHM behaves differently compared to the T_4 linewidth at 9 T, the two linewidths are very similar at 0 T, with the T_3 linewidth being slightly smaller than that of T_4 (see Figure 7.9c). In order to quantify the degree of laser-induced spin polarisation and its influence on the intensity and FWHM of T_3 , the polarisation-resolved PL emission will need to be studied as a function of excitation power and magnetic field.

The polarisation-dependent detection behaviour of T_3 and T_4 can be explained with the sketches shown in Figure 7.10. Following a σ^+ -polarised laser excitation, an excess of spin- \uparrow electrons is excited in the K valley. Therefore, the spin- \uparrow bands in both valleys are pulled down as a surplus of spin- \uparrow electrons favours a spin- \uparrow polarisation. In this spin configuration, the intravalley spin singlet trion T_3 emits in a cross-polarised manner (see Figure 7.10a) and the intervalley spin triplet trion T_4 emits in a co-polarised manner (see Figure 7.10b). The same argumentation holds for an excitation with a σ^- -polarised laser but with reversed electron spins. The observed polarisation behaviour of a co-polarised T_4 and a cross-polarised T_3 can only be explained by assuming a laser-induced spin polarisation that is stable during the whole acquisition time of one spectrum.

7.6 Conclusion and outlook

In TMD monolayers, the Coulomb interaction between electrons can dominate over all other energy scales at cryogenic temperatures. Due to the strong Coulomb interaction and electron-electron exchange between the valleys, electrons form a ferromagnetic state at small to moderate charge carrier densities [Roc19]. The ferromagnetic electronic state is probed by monitoring the photoluminescence emission upon charging the monolayer. At a certain critical density, the ferromagnetic state undergoes a first-order phase transition to a paramagnetic phase. At the same critical density, a jump in the photoluminescence emission energy is observed, which allows an estimation of the different electron masses in the ferro- and paramagnetic phases. Furthermore, a careful study of the optical response at zero magnetic field enabled the observation of an excitation laser-induced ferromagnetic phase.

As an outlook, it is commented that, first, our work establishes monolayer MoS_2 as a platform for studying and exploiting interaction-driven physics. The combination of an ultra-small Bohr radius, spin and valley degrees of freedom, and a small spin-orbit interaction creates a rich test bed. Secondly, the ferromagnetic-to-paramagnetic phase transition can be directly probed with a sensitive state-of-the-art magnetometer [Mar22], such as individual magnetic nanowires [Mat20] or a magnetised pendulum atomic force microscope [Yil19]. Lastly, the first-order phase transition between ferromagnetic and paramagnetic phases enables the spin ordering to be controlled simply via a small change to a gate voltage, opening a route to fast and efficient electrical switching.

Our experiments show that it is possible to stabilise the ferromagnetic phase at zero magnetic field using a circularly polarised laser excitation. This is an important result as this removes the need to apply very large external fields for stabilisation of the ferromagnetic phase. The next step is to study the laser-induced ferromagnetic phase using absorption spectroscopy in a pump-probe experiment: a circularly polarised pump laser is fixed on a certain sample position, while the sample absorption is probed at a different position, similar to the experiments shown in Reference [Hao22]. By scanning the probe position on the sample, we can study the spatial extent of the laser-induced ferromagnetic phase. The separate spots also allow the use of a higher pump laser power. Additionally, the temporal dynamics can be probed: the laser can be abruptly turned on (off).

*“Irgendwo tief in mir bin ich ein Kind
geblieben”*

Peter Maffay, Nessaja (1983)

Chapter 8

Conclusion and outlook

The vast amount of different two-dimensional (2D) materials and the possibility of combining them into arbitrary multilayer structures provide an exciting playground for studying and exploiting novel physical phenomena. In this thesis, we have studied the physical properties of three different semiconducting transition metal dichalcogenide (TMD) systems using optical spectroscopy: MoSe₂/WSe₂ heterobilayer, MoS₂ homobilayer, and MoS₂ monolayer. The TMD systems are embedded in high-quality optoelectronic devices, which provide full control of the electrostatic environment. We have demonstrated that the excitonic response and the electronic ground state in these systems are highly tunable by either changing the carrier density and the electric field or by optical excitation.

In bilayer TMD systems, interlayer excitons with a permanent out-of-plane dipole moment can form, which enables a large energetic tunability due to the quantum confined Stark effect. These interlayer excitons are studied in a type-II MoSe₂/WSe₂ heterobilayer. Twisting the two layers leads to moiré and atomic reconstruction effects that dominate the excitonic properties. Using photoluminescence spectroscopy, two different types of interlayer excitons, originating from the same real space position in the moiré potential, are identified: one of momentum-indirect nature, the other of momentum-direct nature (Chapter 4). The properties of these two transitions (energy, intensity, effective dipole moment, g factor, and degree of circular polarisation) can be tuned in a non-trivial manner by the external experimental parameters.

The understanding of the interlayer exciton real and momentum space origin in heterobilayer systems is crucial for potential applications utilising their large tunability. These excitonic states can be used for example to optically probe the correlated electronic states in the moiré potential [Liu21] or to study degenerate many-body states [Sig20] at the onset of excitonic Bose-Einstein condensation [Sno02]. Another application could be to

use an electrostatically trapped single exciton as a highly tunable emitter of single photons [Sch13a, Sha21b]. However, interlayer excitons in type-II heterobilayers have a big disadvantage: while they are widely tunable by electric fields, their coupling to light is considerably weak (see Chapter 4).

In homobilayer MoS₂, we find hybridised interlayer excitons that combine a large tunability of their energy with a big oscillator strength. On increasing the electric field at close-to-zero carrier density, two interlayer resonances are found with opposite dipole moments, leading to a giant energetic tunability over 120 meV (Chapter 5). The large dipole moments are used to tune the interlayer excitons into resonance with the intralayer A- and B-excitons. In both cases, an avoided crossing is observed, indicating exciton-exciton coupling. A classical model of two coupled optical dipoles is developed that shows a good concordance with the experimentally measured couplings. The model reveals that the measured optical susceptibility determines both the magnitude and the phase of the coupling constants (Chapter 6).

Exciton-exciton coupling can lead to nonlinear optical effects [Wan15b, Jak16] and to condensation phenomena, for example, the creation of states with macroscopic quantum-correlations [Kas06]. The hybridised nature of interlayer excitons in homobilayer MoS₂ coupled to optical cavity modes leads to the creation of bright yet strongly interacting exciton-polaritons [Dat22, Lou22]. On account of these strong and repulsive non-linear interactions, homobilayer MoS₂ provides a promising platform to achieve polariton blockade, which can turn laser light into single photons [Del19, MM19].

The excitonic response of TMDs can also be used to probe the electronic ground state of the system. Injecting electrons into monolayer MoS₂ creates a 2D electron gas. The interaction of excitons with this electron gas can be probed using photoluminescence spectroscopy as a local spin- and valley-sensitive probe. At low charge carrier densities, the electrons in MoS₂ form a ferromagnetic phase on account of the strong Coulomb interaction and electron-electron exchange between the two valleys [Roc19]. We found evidence of a first-order phase transition from the ferromagnetic phase to a paramagnetic phase at a certain critical carrier density (Chapter 7). Therefore, spin ordering can be easily controlled by a small change of gate voltage, enabling efficient and fast electrical switching. However, these observations rely on an optical probe, which measures the magnetic phase only indirectly. A more direct way to observe this magnetic phase transition would be to quantify and image the magnetic field with a sensitive state-of-the-art magnetometer [Mar22], such as individual magnetic nanowires [Mat20] or a magnetised pendulum atomic force microscope [Yil19].

A fully ferromagnetic phase (spin-polarised phase) requires a symmetry breaking of the spin-up and spin-down states, which is typically achieved by applying large external magnetic fields. By using a circularly polarised excitation laser, we show that it is possible

to stabilise the ferromagnetic phase at zero magnetic field. Therefore, the electronic ground state can not only be controlled by electrical means but also optically. The local laser-induced symmetry breaking leads to a ferromagnetic phase that can extend throughout the whole sample [Hao22].

The field of 2D materials – TMDs in particular – offers seemingly endless possibilities to study novel physical phenomena like highly tunable (hybridised) interlayer excitons in moiré superlattices or ferromagnetic electronic ground states. There are still many things to discover and research on gated TMD devices will therefore remain interesting and exciting for years to come. In the end, we can finally answer Shakespeare’s famous question (“2D, or not 2D?”) with 2D!

Appendix

Fabrication recipes

Chapter 3 describes the fabrication steps to create a van der Waals heterostructure. In this appendix chapter, detailed fabrication recipes are provided.

A.1 Electron-beam lithography for etching and contacts

1. Design electron-beam (e-beam) mask of desired nanostructure with Adobe Illustrator
2. Spin-coat PMMA (AR-P 672.045) at 4000 rpm for 40 s with a ramp rate of 1000 rpm/s
3. Bake chip at 180 °C for 3 min
4. E-beam exposure to write predesigned structures ($V = 20$ kV and a dose of $550 \mu\text{C}/\text{cm}^2$)
5. Development in cold (~ 5 °C) IPA:DI water (7:3) for 60 s
6. Blow-dry with nitrogen

A.2 Reactive ion etching

Reactive ion etching (RIE) can be used to etch down certain layers in a van der Waals heterostructure. Potential uses are fixing an electrical short in the stack or freeing a FLG layer for contacting from the top if it was buried. Another option is to use RIE to pattern exfoliated flakes. This could be interesting for example when designing an exciton trap by patterning holes in graphene (see Section A.5). We use O_2 plasma to shape a heterostructure and an Ar/O_2 plasma to etch graphite.

A.2.1 O_2 plasma

1. O_2 (gas flow of 20 sccm) at a pressure of 40 mTorr and RF power of 60 W

2. Etching rates:
 - hBN: ~ 0.33 nm/s
 - Graphite: several layers per minute
 - SiO₂: ~ 1.66 nm/s

A.2.2 Ar/O₂ plasma

1. Ar/O₂ (gas flow of 22/8 sccm) at a pressure of 25 mTorr and RF power of 30 W
2. Etching rates:
 - Graphite: ~ 0.17 nm/s
 - SiO₂: ~ 1.12 nm/s

A.3 Fabrication of metal contacts

1. Load sample with developed PMMA mask into the Sharon e-beam evaporator
2. Deposit a sticking layer of Ti (5 nm) or Cr (5 nm) for the top contacts or Ti (10 nm) for contacts on the bottom half
3. Evaporate the desired thickness of Au
4. PMMA lift-off in acetone at 50 °C for a couple of hours
5. If necessary create an acetone flow using a syringe to remove residual metal
6. Put the sample into IPA and blow-dry with nitrogen

A.4 Drop-down PMMA coating of 2D materials

2D materials can be patterned using a combination of e-beam lithography and RIE. Unfortunately, during this process, the flake is heated up to 180 °C during the baking of the PMMA. This is a problem as the pick-up of 2D materials becomes more difficult after heating them to such temperatures. An example is shown in Figure A.1. A FLG flake with small holes etched into it is picked up by a stamp. During the process the flake rips apart and big pieces are stuck to the chip. To overcome this problem we developed a technique to spin-coat an exfoliated flake without heating it. The flake that needs to be patterned should be exfoliated on a chip with markers for alignment in the e-beam lithography.

1. Cut a large piece of Si/SiO₂ wafer ($> 3 \times 3$ cm)
2. Spin-coat dextran at 2000 rpm for 40 s with a ramp rate of 1000 rpm/s
3. Bake chip at 150 °C for 3 min

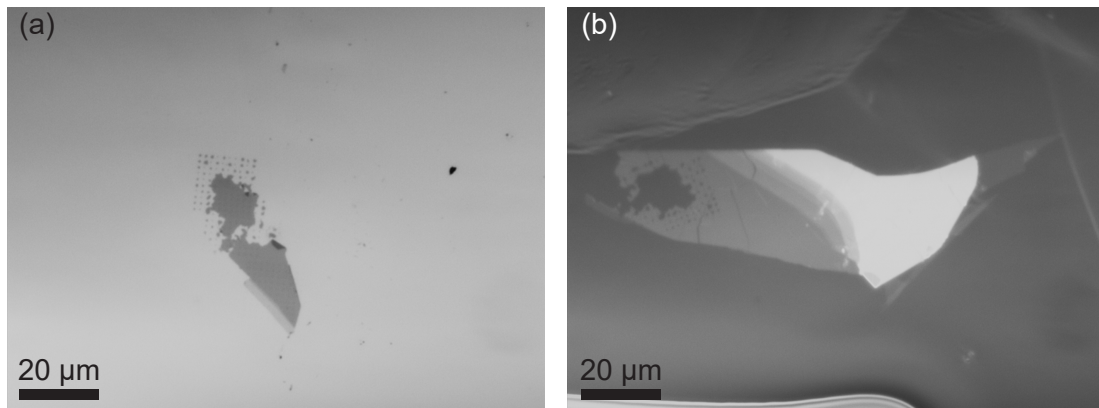


Figure A.1. Optical microscope images of a FLG flake with small holes etched (RIE) into it after trying to pick it up with a stamp. (a) Remains of the FLG flake on the chip it was exfoliated onto. (b) Picked-up part of the FLG flake on top of the stamp. Etched hole regions stuck to the chip ripping the flake apart during the pick-up process.

4. Spin-coat PMMA (AR-P 672.02) at 4000 rpm for 40 s with a ramp rate of 1000 rpm/s on top of the dextran-covered chip
5. Bake chip at 180 °C for 5 min
6. Cut a large square into the doubly spin-coated chip
7. Fill a petri dish with DI water and carefully slide the cut chip into the water
8. The dextran is dissolving which leaves the cut PMMA floating on top of the water
9. Take the chip with a nice exfoliated flake, flip it upside down, and drop it on the PMMA swimming on the water surface
10. Remove the chip from the water and bake it at 90 °C for 5 min to remove the residual water

Now, we have a flake coated in PMMA without having to heat it up to high temperatures. The PMMA usually has some wrinkles due to the crudeness of the drop-down. However, in most cases, the wrinkles are not at the position of the flake of interest.

A.5 Making nano-holes in graphene

A potential trap for interlayer excitons in a TMD heterostructure can be engineered when patterning one of the gate electrodes with small holes (30 to 50 nm diameter). It turns out that this is quite a difficult task. In the final stack, the patterned flake should either be on top of the stack or on top of an hBN spacer in order to be separated from the influences of the SiO₂ substrate. In this section, we will discuss two methods of how one could fabricate these small holes: RIE or focused ion beam (FIB) milling.

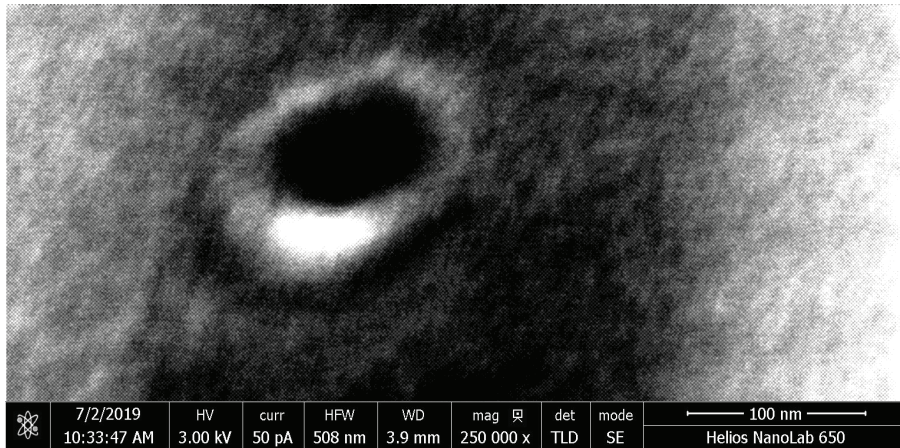


Figure A.2. SEM image of a hole that has been milled with Ga atoms into a FLG graphene flake. The image is taken with the FEI Helios NanoLab 650 SEM/FIB.

A.5.1 Etching

The flake of interest is covered in PMMA without heating the chip up according to the method explained in Section A.4. The holes are written with e-beam lithography. Subsequently, the developed chip is etched with RIE. For the etching to work, we found that the used PMMA thickness should be small; roughly two times the hole diameter. We spin-coat PMMA (AR-P 672.02) at 4000 rpm for 40 s with a ramp rate of 1000 rpm/s (~ 100 nm thick). Shanks et al. managed to fabricate 30 nm holes into a FLG top gate on an already finished stack using RIE [Sha21b].

A.5.2 Focused ion beam milling

1. Stack the FLG bottom gate on top of an hBN flake onto a conducting Si chip (p-doped) with markers with a small SiO_2 thickness (80 nm) for the FIB process
2. Load the sample into the FEI Helios NanoLab 650 SEM/FIB with a Ga-gun
3. Mill the holes (outer diameter 35 nm) in the FLG flake ($V = 30$ kV and $I = 7.7$ pA)
4. Remove sample from FIB and continue the stacking procedure described in Chapter 3

A scanning electron microscope (SEM) image of the resulting hole is shown in Figure A.2. While the hole size is quite close to the specified 35 nm, there is a ring formed around the hole. The details of the ring formation are not clear. Also, we do not know the exact influence this ring has on the optical properties of a TMD layer. We have studied a device with holes FIB-milled into the bottom FLG gate but unfortunately, we have seen no hints of interlayer exciton trapping.

Appendix **B**

Van der Waals heterostructure device details

At the core of this thesis are all the devices that allowed us to measure loads of interesting phenomena in two dimensions. Behind these few devices, there are also many other stacks where some electrical gates did not work, where the fabrication process has failed, or that have died prematurely (e.g. by electrostatic discharge). These failed attempts laid the foundation for building a device successfully. Fabricating a working van der Waals heterostructure device is a piece of art. Hence, credit is given to the creators of the devices essential for this thesis. In the following, fabrication and device details are provided.

B.1 MoSe₂/WSe₂ heterobilayer device

Chapter 4 describes the measurements conducted on one MoSe₂/WSe₂ heterobilayer dual-gate device. The individual monolayers were aligned using SHG to determine their crystallographic axes. The flakes depicted in the alignment process described in Section 3.3 are the monolayers in the studied device (see Figure B.1a). The device was stacked in three parts. First, the bottom FLG gate was placed on top of a thin hBN flake to shield the FLG flake from the potential SiO₂ charge noise. Holes (~ 35 nm diameter) were patterned into the FLG flake using FIB milling as described in Section A.2. The holes were separated by 1 μm in several 10x10 squares. Second, the bottom hBN is stacked on top of the FLG gate to finish the bottom part. Unfortunately, the hBN layer detached during the PC dissolving step and tore apart the FLG flake in the process. However, there was still a large enough and clean area of the remaining FLG flake to continue the fabrication process. The bottom contacts to the two TMD monolayers and the contacts to the bottom FLG gate were defined by e-beam lithography followed by metal deposition of Ti(10 nm)/Au(20 nm).

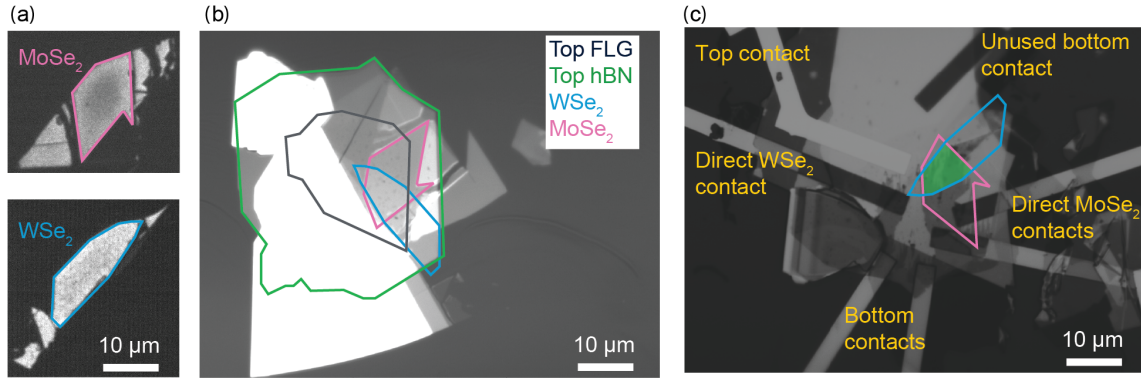


Figure B.1. (a) Optical microscope images of the MoSe₂ (top) and WSe₂ (bottom) monolayers under illumination with a tungsten halogen lamp. Their bright glow confirms their monolayer nature. (b) Optical microscope image of the fully picked-up top part of the stack (top FLG/top hBN/WSe₂/MoSe₂) on the PDMS/PC stamp. Note that the flakes are mirrored as the stamp has to be flipped for imaging. (c) Optical microscope image of the finished gated device. The heterobilayer region is shaded in green.

Third, the top part of the stack is picked up by a PDMS/PC stamp. Figure B.1b shows an optical microscope image of the fully picked-up top part. The top part is carefully placed on the bottom part. The finished stack is shown in Fig B.1c with the heterobilayer region highlighted in green. The big contact pads and the connection to the small bottom contacts consist of Ti(5 nm)/Au(45 nm).

Comparing the ideal overlap region defined on the computer before stacking with the two monolayers on the stamp (Figure B.1b) we can estimate a stacking angle of roughly $\sim 3^\circ$. As discussed in Chapter 4, the optical measurements indicate an R-stacking of the heterobilayer.

As mentioned before, the bottom FLG flake was patterned with nano-holes. Due to the ripping of the FLG flake, we could identify the hole 10x10 square by optical microscopy because the area around the holes tends to stick to the sample upon ripping (see Figure A.1). Based on the microscope images we estimate that a part of the heterobilayer is covered by FLG with holes and a part of the bilayer is covered by FLG with no holes.

The heterobilayer device is built in a dual-gate structure that allows sweeping of the electric field across the bilayer for a constant charge carrier density (see Section 3.4). For the determination of F_z and n , the top and bottom hBN thicknesses are measured by an atomic force microscope (AFM) to be $d_T = 25.2$ nm and $d_B = 36.7$ nm. For all calculations we take $\epsilon_{\text{hBN}} = 3.76$ [Lat18] and $\epsilon_{\text{TMD}} = 7.2$ [Kim15]. The effective offset voltage V^0 due to initial environmental charge carrier doping is determined by monitoring the intralayer exciton PL in the heterobilayer region as a function of top and bottom gate voltages V_{TG} and V_{BG} .

For the MoSe₂ monolayer, we monitor the PL intensity of the neutral and the charged

exciton. We find the highest intensity ratio of neutral versus charged exciton at the condition $V_{\text{TG}} = -0.68V_{\text{BG}} - 1.4$ V. When this condition is fulfilled the MoSe₂ monolayer is neutral. Or in other words, the intrinsic doping is neutralised by the electrostatically injected carriers [Ros13]. This argument is strengthened as the slope of the neutrality condition is nearly equal to the ratio of top and bottom hBN thicknesses $\alpha = \frac{d_{\text{T}}}{d_{\text{B}}} \approx 0.69$. Therefore, we sweep the voltages along the neutrality condition in our experiments when we only want to change F_z while keeping n small and constant. Using the neutrality condition, we determine the MoSe₂ monolayer to be intrinsically n-doped with $n_0 = 1.2 \times 10^{12}$ cm⁻². A voltage offset of $V_{\text{TG}}^0 = +1.4$ V is used for calculating all F_z and n values. The n-doped character is typical for Mo-based TMD monolayers [Mak13, Ros13]. The amplitude is smaller than the doping of a MoSe₂ layer in the heterobilayer region ($n_0 = 5 \times 10^{12}$ cm⁻²) measured by F. Violla et al. [Via19].

For the WSe₂ monolayer in our device, this condition is not so easily determined as the excitonic emission spectrum is more complicated and much weaker in intensity than the MoSe₂ spectrum. In Reference [Via19] they found that the WSe₂ layer is slightly p-doped ($n_0 = -2 \times 10^{11}$ cm⁻²) with a much smaller amplitude than the n-doped MoSe₂. However, from the electrostatics discussion in Chapter 4, we can conclude that the WSe₂ monolayer stays intrinsic when sweeping the voltages along the MoSe₂ neutrality condition.

B.2 Homobilayer MoS₂ devices *

Three separate structures were fabricated: Device 1 was prepared at the University of Basel, and device 2 and sample 3 were assembled at LPCNO Toulouse. For device 1, a PDMS stamp with a thin PC film was used to pick up individual layers from top to bottom. All flakes were previously mechanically exfoliated from bulk crystals on SiO₂ (285 nm)/Si substrates. Metal contacts to the MoS₂ and few-layer graphene (FLG) were patterned by electron-beam lithography and subsequent metal deposition of Ti(5 nm)/Au (45 nm) (see Appendix A). For device 2, 2H-MoS₂ crystals (2D Semiconductors), synthetic hBN and natural graphite were subjected to micromechanical cleavage on Nitto Denko tape [Nov05b], then exfoliated again on a PDMS stamp placed on a glass slide for optical inspection. Sequential deterministic stamping of the selected flakes was then applied to build the complete stack, aligned according to the position of the Au contacts pre-patterned onto the substrate. Sample 3, consisting of bilayer (BL) and trilayer (TL) MoS₂, was assembled following the same transfer steps as device 2.

Optical images of devices 1 and 2, and sample 3 are shown in Figure B.2a,b, and c. For the determination of the electric field values in the gated devices, the thicknesses of the individual hBN layers in devices 1 and 2 were measured by AFM ($d_{\text{T}} = 16.2$ nm and

*This section is partially adapted from the Supplement of Reference [Lei20].

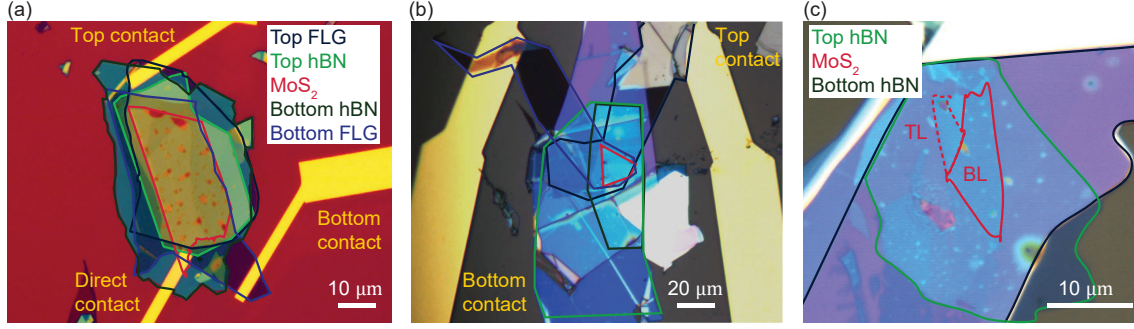


Figure B.2. Homobilayer MoS₂ device and sample structure. Optical microscope images of electrical gated (a) device 1 and (b) device 2, and (c) sample 3, consisting of bilayer (BL) and trilayer (TL) MoS₂.

$d_B = 21.5$ nm for device 1, and $d_T = 13$ nm and $d_B = 4$ nm for device 2). Device 1 is built in the dual-gate configuration which allows independent control of the electric field across the bilayer and the charge carrier density inside the bilayer (see Section 3.4).

Device 1 was fabricated by Nadine Leisgang; device 2 and sample 3 were fabricated by Shivangi Shree and Ioannis Paradisanos.

B.3 Monolayer MoS₂ devices

In this thesis, two different monolayer MoS₂ devices were studied: device 1 and device 2. Both of them were fabricated using the dry-stacking technique described in Chapter 3. Both samples use the method where they are stacked in two parts. The bottom part in device 1 consists only of an hBN flake; the bottom part in device 2 is FLG capped with hBN. The MoS₂ was contacted from the bottom by metal Ti(10 nm)/Au(20 nm) contacts that were patterned by e-beam lithography (see Appendix A), following Reference [Pis18]. In device 1, the big contact pads and the connection to the small bottom contacts consist of Ti(5 nm)/Au(45 nm). For device 2, we used a thickness of Ti(5 nm)/Au(105 nm) due to the very thick top hBN.

Device 2 uses a dual-gate device structure as sketched in Fig B.3b. An optical microscope image of the contacted stack is shown in Fig B.3c. Unfortunately, the bottom gate did not work during the first cooldown cycle, where all measurements on this device shown in this thesis were performed. This means device 2 has effectively the same structure as device 1: a single-gate structure. Device 1 uses a p-doped Si substrate as a back gate to dope the monolayer (see Figure B.3a), while device 2 uses a FLG top gate to do so. The charge carrier density in the device can be calculated with $en = C \cdot V_{G,TG}$ (see Section 3.7). The geometrical capacitance is $C = 11.1 \pm 0.5$ nFcm⁻² for device 1 and $C = 46.2 \pm 1.9$ nFcm⁻² for device 2.

For device 2, the hBN thicknesses were chosen such that the trion resonances at around 1.92 eV have a Lorentzian lineshape in an absorption measurement and a narrow linewidth.

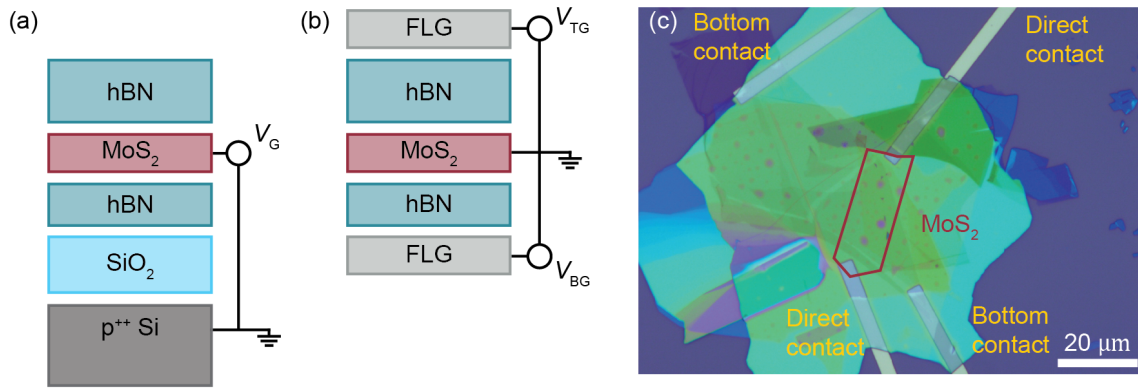


Figure B.3. Schematic of the homobilayer MoS₂ (a) device 1 and (b) device 2. For device 1, the p-doped silicon wafer serves as a global back gate. Device 2 is fabricated in a dual-gate device structure with hBN thicknesses optimised such that a resonance at 1.92 eV has a Lorentzian lineshape and narrow linewidth. (c) Optical microscope image of the gated device 2 consisting of monolayer MoS₂. The image is taken before the writing and deposition of the big contact pads and the metal contact to the top FLG gate.

To simulate the thicknesses needed we follow the procedure described in Section 3.6. The final sample has a bottom hBN thickness of $d_B = 21.5 \pm 2$ nm and a top hBN thickness of $d_T = 72 \pm 2$ nm.

Device 1 was fabricated by Jonas Roch.

Appendix

C

Raman spectroscopy

Raman spectroscopy is used to determine the vibrational modes of the TMD crystals. In the early days of 2D materials, Raman spectroscopy was used as a tool to determine the number of layers of an exfoliated crystal. The exact frequency difference between the out-of-plane A_{1g} and in-plane E_{2g}^1 Raman mode (see Figure C.1a) of the TMD flake is a fingerprint that can differentiate between mono- and few-layer TMDs [Lee10, Zha15].

Recently, Raman spectroscopy has been used to study atomic reconstruction effects in twisted TMD bilayer systems. In bilayer systems exist two low-frequency phonon processes: the interlayer breathing mode (IBM, Figure C.1b) and the interlayer shearing mode (ISM, Figure C.1c). The presence of an ISM ($\sim 20 \text{ cm}^{-1}$) indicates that atomic reconstruction has happened at the measured sample position [Hol20]. For larger angles, moiré phonons can be used to estimate the twist angle [Par21b].

In order to measure a potential low-frequency ISM in our heterobilayer device and

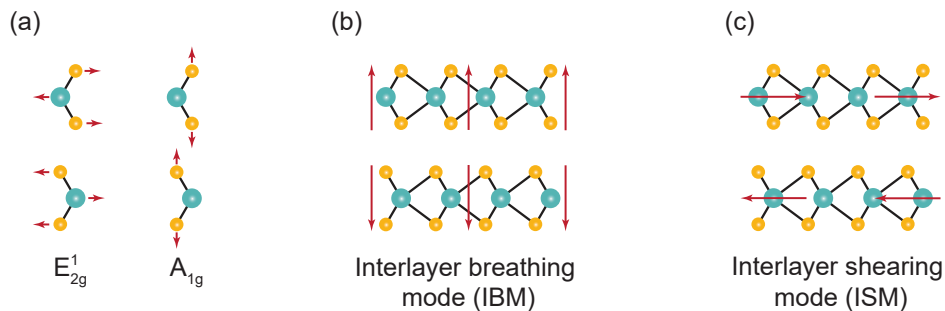


Figure C.1. Atomic displacements of important vibrational modes of TMD crystals. (a) Sketch of the in-plane E_{2g}^1 and the out-of-plane A_{1g} modes. (b,c) Sketch of (b) the interlayer breathing mode and (c) the interlayer shearing mode.

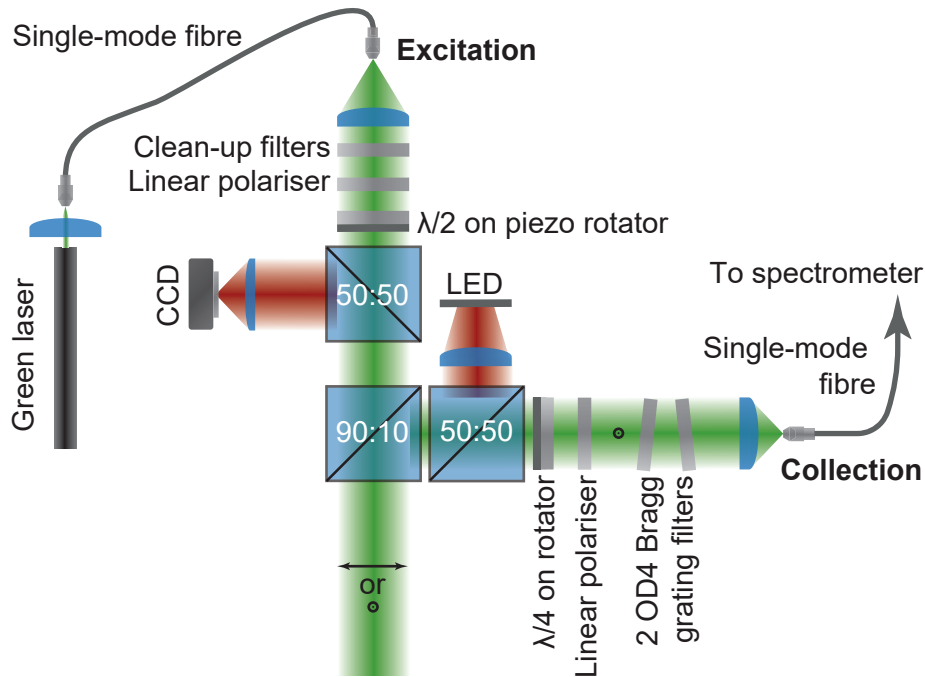


Figure C.2. Microscope head used for low-frequency Raman measurements. The sample is excited with a green laser (532 nm, ventus 532, Laser Quantum). To measure low-frequency Raman signals the laser background needs to be reduced. This is achieved with two methods put in series. First, a cross-polarisation scheme is employed where the linear polarisation of the exciting laser and the detected laser are orthogonal. This method achieves a large laser suppression [Kuh13, Ben21]. Fine-tuning of the alignment is achieved by using piezo rotators for turning the waveplates. Rotating the $\lambda/2$ waveplate by 90° additionally enables co-polarised measurements with a worse laser suppression. Second, the laser is further filtered by two consecutive OD4 Bragg grating filters (Optigrate) aligned at 6° with respect to the plane perpendicular to the laser propagation. The 50:50 beamsplitter below the red LED is only inserted when imaging the sample.

correlate its presence with PL measurements (see Appendix B) at cryogenic temperatures, we modified our microscope as shown in Figure C.2. The laser background is reduced through the combination of a cross-polarisation scheme and two consecutive OD4 Bragg grating filters. In the measurements, moderate laser powers of a few tens of μW are used to not damage the sample. Unfortunately, even for long integration times of several hours, no clear ISM signal could be measured. One of the reasons could be the hBN encapsulation, which tends to reduce the measurable Raman signal [Hol20]. A potential way to overcome this problem is by using resonant Raman scattering: exciting the sample with a laser energy close to an intralayer exciton resonance drastically increases the measured Raman signal [McD21].

Appendix **D**

Supplemental information to Chapter 5: “Giant Stark splitting of an exciton in bilayer MoS₂”

In Chapter 5, we performed absorption measurements to probe the optical response of homobilayer MoS₂ in two different laboratories. To strengthen and understand our experimental findings, beyond-DFT calculations were performed. In this appendix chapter, details of the experimental methods in each lab and the computational details are presented. This chapter is partially adapted from the Supplement in Reference [Lei20].

D.1 Experimental details

Experiments were performed independently in two different research laboratories in Basel and Toulouse using devices 1, 2, and 3. The reflectivity spectra of device 1 were recorded in Basel with the absorption setup described in Section 3.7 using a NA = 0.45 microscope objective. In order to evaluate the differential reflectivity $\Delta R/R_0$, we compare the reflectivity spectrum R obtained from the MoS₂ flake at a given electric field F_z with a reference spectrum R_0 . Sweeping the gate voltages V_{TG} and V_{BG} so that only the carrier concentration n_{tot} in the device is varied leads to significantly different reflectivity spectra. For device 1, we thus extrapolate the reference spectrum R_0 from the raw reflectivity spectrum at a high electron density $n_{tot} \approx 11.5 \cdot 10^{-12} \text{ cm}^{-2}$, where the oscillator strength is distributed over a large spectral range [Bac18]. Using Kramers-Kronig relation, the measured differential reflectivity data $\Delta R/R_0$ can be converted into the imaginary part of the optical susceptibility $\text{Im}(\chi)$ (see Section 3.5.1 for a more detailed description).

For devices 2 and 3, low temperature reflectance measurements were performed in

Toulouse in a home-built micro-spectroscopy setup constructed around a closed-cycle, low vibration attoDry cryostat with a temperature controller ($T = 4$ K to $T = 300$ K). For reflectivity, a halogen lamp with a stabilised power supply is used as a white light source, initially focused onto a pin-hole that is imaged on the sample. The reflected light is then dispersed by spectrometer and detected by a Si-CCD camera. Here, the differential reflectivity is defined as $\Delta R/R_0$, where R is the intensity reflection coefficient of the sample with the MoS₂ layers and R_0 is obtained from the same structure without the MoS₂. Note that the overall shape and amplitude of the differential reflectivity signal depends on thin-film interferences in the hBN layers [Rob18].

D.2 Beyond-DFT calculations

In this section, details of the beyond-DFT calculations are presented. The calculations were performed by Iann C. Gerber in Toulouse.

D.2.1 Computational details

The atomic structures, the quasi-particle band structures and optical spectra have been obtained from DFT calculations using the VASP package [Kre93, Kre96]. The plane-augmented wave scheme [Blo94, Kre99] has been used to treat core electrons. We have set the lattice parameter value of 3.22 Å for all the runs. A grid of $15 \times 15 \times 1$ k-points has been used, in conjunction with a vacuum height of 21.9 Å, for all the calculation cells. The geometry's optimisation process has been performed at the PBE-D3 level [Gri10] in order to include van der Waals interactions between layers. All the atoms were allowed to relax with a force convergence criterion below 0.005 eV/Å. Heyd-Scuseria-Ernzerhof (HSE) hybrid functional [Hey04, Hey05, Pai06] has been used as approximation of the exchange-correlation electronic term, including SOC, to determine eigenvalues and wave functions as input for the full-frequency-dependent GW calculations [Shi06] performed at the G_0W_0 level. The application of the electric field is done at this step, just before the GW calculation process, considering that at small/moderate electric field values, its application is only a small perturbation to the band structures. An energy cutoff of 400 eV and a Gaussian smearing of 0.05 eV width have been chosen for partial occupancies, when a tight electronic minimisation tolerance of 10^{-8} eV was set to determine, with a good precision, the corresponding derivative of the orbitals with respect to k needed in quasi-particle band structure calculations. The total number of states included in the GW procedure is set to 1280, in conjunction with an energy cutoff of 100 eV for the response function, after a careful check of the direct band gap convergence (smaller than 0.1 eV as a function of k-points sampling). Band structures have been obtained after a Wannier interpolation procedure performed by the WANNIER90 program [Mos08]. All optical excitonic transitions have been calculated by solving the Bethe-Salpeter equation [Han79, Roh98], using the twelve

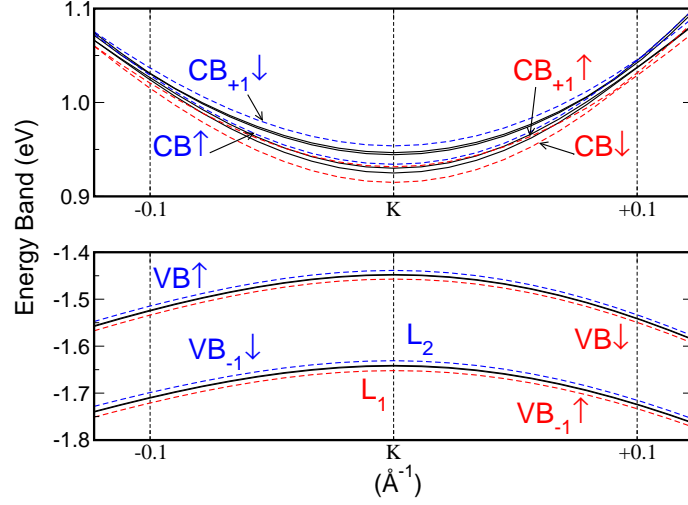


Figure D.1. Valence and conduction bands shifts induced by an electric field. G_0W_0 bandstructure of 2H MoS₂ bilayer in the vicinity of the K point, without (black lines) and with an applied electric field $F_z = 1$ MV/cm value (dashed lines). L_1 bands are in red, while L_2 bands are depicted in blue.

highest valence bands and the sixteen lowest conduction bands to obtain eigenvalues and oscillator strengths on all systems. From these calculations, we report the absorbance values by using the imaginary part of the complex dielectric function. By using such a computational setting, we obtained a good agreement in terms of A and B peak positions, as well as oscillator strength values, with the well-converged results of Qiu et al. [Qiu13] for MoS₂ monolayers.

D.2.2 Bandstructure modifications due to the electric field

As can be seen in Figure D.1, moderate electric field application on a free standing 2H MoS₂ bilayer shifts bandstructures from the two distinct layers by decreasing valence bands and conduction band energies for the layer L_1 lying at the highest electrostatic potential value while L_2 bands are upshifted. Mind that similar results were already reported in previous works using standard DFT calculations only [Ram11, Xia14, Lu17], confirmed here by our GW series of calculations.

In Figure D.2, the bandstructures of the trilayer case are reported. Interestingly, without electric field, L_1 and L_3 valence bands, more specifically VB and V_{B-1} , are both mixtures of Mo d_{xy} , $d_{x^2-y^2}$ with in-plane S p orbitals coming from both L_1 and L_3 layers. Thus, when making transitions implying those states (solid black lines in Figure D.2), holes will be delocalised over the top and bottom layers at the same time. By suppressing symmetry, with the application of an electric field, VB and V_{B-1} become more delocalised on each of the layers. Since our calculation cell is symmetric in the (Oz) direction, and since L_2 is located in the middle of it, its corresponding electrostatic potential is 0. This explains the

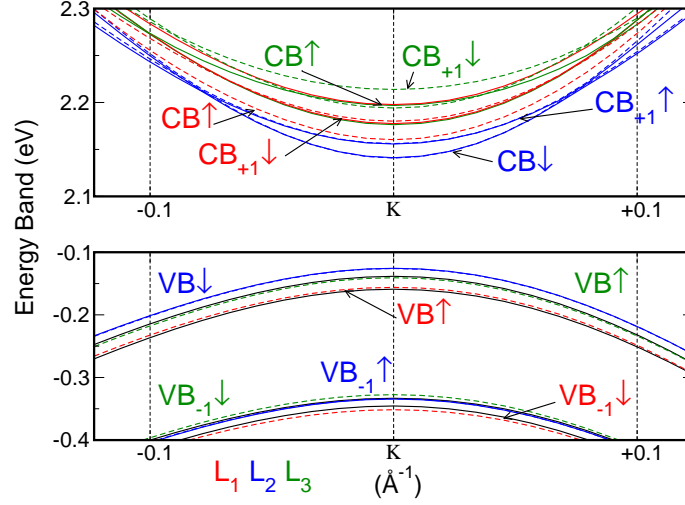


Figure D.2. Valence and conduction bands shifts induced by an electric field. G_0W_0 bandstructure of 2H MoS₂ trilayer in the vicinity of K point, without (solid lines) and with an applied electric field $F_z = 1$ MV/cm value (dashed lines). L₁ bands are in red, L₂ bands are blue and L₃ band are depicted in green.

Exciton	A	IE ₁	IE ₂	B
	$VB_{\uparrow}^{L_2} \rightarrow CB_{\uparrow}^{L_2}$	$VB_{\uparrow}^{L_2} \rightarrow CB_{+1,\uparrow}^{L_1}$	$VB_{\downarrow}^{L_1} \rightarrow CB_{+1,\downarrow}^{L_2}$	$VB_{-1,\downarrow}^{L_2} \rightarrow CB_{+1,\downarrow}^{L_2}$
0.0 (MV/cm)	5%	13%	13%	17%
	$VB_{-1,\uparrow}^{L_1} \rightarrow CB_{\uparrow}^{L_2}$	$VB_{-1,\uparrow}^{L_1} \rightarrow CB_{+1,\uparrow}^{L_1}$	$VB_{-1,\downarrow}^{L_2} \rightarrow CB_{+1,\downarrow}^{L_2}$	$VB_{\downarrow}^{L_1} \rightarrow CB_{+1,\downarrow}^{L_2}$
0.5 (MV/cm)	6%	12%	14%	18%
1.0 (MV/cm)	5%	11%	15%	19%
2.0 (MV/cm)	5%	10%	18%	23%

Table D.1. Decomposition of the oscillator strengths for 2H MoS₂ bilayer at the K point. Identification of the main electron-hole pairs related to the excitonic peaks are indicated in the first line. The percentage of the second most important contribution to the oscillator strength is given for four different electric field values, its physical nature is indicated in the second line for $F_z = 0$ MV/cm. CB and VB denote conduction band and valence band. L₁ and L₂ indicate transitions in layer 1 and 2, respectively.

absence of band shifts for the L₂ bands.

D.2.3 Decomposition of the excitonic oscillator strength

Bilayer case

From Table D.1, one can see that the A-exciton is not completely of pure intralayer exciton character, since a small amount (around 5%) of the oscillator strength is coming from the VB₋₁ of the other layer. This mixing does not vary with respect to the electric field. Note

Exciton	A:1s L ₂	A:1s L ₁ , L ₃	IE*
	$\text{VB}_{\downarrow}^{\text{L}_2} \rightarrow \text{CB}_{\downarrow}^{\text{L}_2}$	$\text{VB}_{\uparrow}^{\text{L}_{1,3}} \rightarrow \text{CB}_{\uparrow}^{\text{L}_{1,3}}$	$\text{VB}_{\uparrow}^{\text{L}_{1,3}} \rightarrow \text{CB}_{+1,\uparrow}^{\text{L}_2}$
0.0 (MV/cm)	6%	4%	10%
	$\text{VB}_{-1,\downarrow}^{\text{L}_3} \rightarrow \text{CB}_{\downarrow}^{\text{L}_2}$	$\text{VB}_{-1,\uparrow}^{\text{L}_2} \rightarrow \text{CB}_{\uparrow}^{\text{L}_{1,3}}$	$\text{VB}_{-1,\uparrow}^{\text{L}_2} \rightarrow \text{CB}_{+1,\uparrow}^{\text{L}_2}$
1.0 (MV/cm)	4%	8%	12%

Exciton	IE	B:1s L ₂	B:1s L ₁ , L ₃
	$\text{VB}_{\downarrow}^{\text{L}_2} \rightarrow \text{CB}_{+1,\downarrow}^{\text{L}_1}$	$\text{VB}_{-1,\uparrow}^{\text{L}_2} \rightarrow \text{CB}_{+1,\uparrow}^{\text{L}_2}$	$\text{VB}_{-1,\downarrow}^{\text{L}_{1,3}} \rightarrow \text{CB}_{+1,\downarrow}^{\text{L}_3}$
0.0 (MV/cm)	18%	13%	40%
	$\text{VB}_{\downarrow}^{\text{L}_2} \rightarrow \text{CB}_{+1,\downarrow}^{\text{L}_3}$	$\text{VB}_{\uparrow}^{\text{L}_1} \rightarrow \text{CB}_{+1,\uparrow}^{\text{L}_2}$	$\text{VB}_{-1,\downarrow}^{\text{L}_{3,1}} \rightarrow \text{CB}_{+1,\downarrow}^{\text{L}_3}$
1.0 (MV/cm)	12%	10%	23%

Table D.2. Decomposition of the oscillator strengths for 2H MoS₂ trilayer at the K point without electric field. Identification of the two main electron-hole pairs related to excitonic peaks and percentage of the second contribution to the total oscillator strength.

that no delocalisation of the electron is observed, as expected in this case, due to symmetry of the conduction band d_{z^2} nature [Gon13, Aka15, Kor15]. Interestingly, for the B-peak, originating mainly from $\text{VB}_{-1,\uparrow}^{\text{L}_1} \rightarrow \text{CB}_{+1,\uparrow}^{\text{L}_1}$ and $\text{VB}_{-1,\uparrow}^{\text{L}_2} \rightarrow \text{CB}_{+1,\uparrow}^{\text{L}_2}$ transitions, the interlayer contributions ($\text{VB}_{\uparrow}^{\text{L}_2} \rightarrow \text{CB}_{+1,\uparrow}^{\text{L}_1}$ and $\text{VB}_{\downarrow}^{\text{L}_1} \rightarrow \text{CB}_{+1,\downarrow}^{\text{L}_2}$) are already large for zero electric field and increase with enhanced electric field values. This means that the delocalisation of the hole, even in the B-excitons, becomes more pronounced with electric field. In contrast, the intralayer contribution to IE_1 tends to decrease with increasing electric field, while it increases for IE_2 , explaining the anticrossing regime observed between IE_2 and B lines.

Trilayer case

In Table D.2, the percentages of the second main electron-hole pair contribution to the first excitonic peaks are given for the trilayer case in the absence of an electric field. A-peaks are related to two different transitions, namely A:1s L₂ and A:1s L₁, L₃, as can be observed from magneto-optics measurements, reported previously [Ger19]. The contribution from the other layers to these oscillator strengths remains modest. The IE* peak clearly results from interlayer transitions, in which the electron lies in L₂, while the hole is delocalised over L₁ and L₃ (mediated by a small amount of intralayer L₂ coupling with good spin parity). For IE, the hole is almost exclusively in L₂. It couples with an electron largely localised in L₁ and in lesser extent in L₃. A first B-like exciton (B:1s L₂), composed of the corresponding L₂ VB and CBs, appears in the spectrum with a small contribution

from delocalised holes over $L_{1,3}$. Additional B-like transitions (B:1s L_1 , L_3), implying L_1 and L_3 VBs and CBs, also contribute to the spectrum. The effect of the electric field on the oscillator strength is also provided for an electric field value of $F_z = 1.0$ MV/cm. Interestingly, only IE^* and B:1s L_2 show significant changes in their transition composition: For both of them the intralayer contribution is reinforced by the application of the electric field, mainly due to the degeneracy lift of L_1 and L_3 VBs.

Appendix **E**

Supplemental information to Chapter 6: “Capacitively and inductively coupled excitons in bilayer MoS₂”

In Chapter 6, we studied the intralayer and interlayer exciton coupling in homobilayer MoS₂. Section E.1 derives the exciton-exciton coupling model in detail and discusses its consequences. The measurement data processing routines are described in Section E.2. Finally, the computational details of the GW+BSE calculations are presented in Section E.3. This chapter is partially adapted from the Supplement in Reference [Spo22].

E.1 Exciton-exciton coupling model

The excitonic couplings are modelled as the coupling of two driven oscillating optical dipoles. The dipole oscillation can be described by the oscillation of the dipole extension \vec{r} or by the oscillation of the charge \vec{q} . One can think of two frameworks which provide a classical analogue. In a mechanical system, two masses represent the dipoles, a spring represents the coupling. In an electrical system, two RLC circuits represent the dipoles, an impedance (either capacitor or inductor) represents the coupling. Both, the mechanical and the electrical system, can be described by equivalent equations of motion as shown below.

E.1.1 Equations of motion

First, we look at a mechanical system. We consider two driven and damped harmonic oscillators with a mass m_1 and m_2 and a spring constant of $k_1 = k$ and $k_2 = k + \Delta k$, respectively. The term Δk allows for the detuning of one oscillator with respect to the

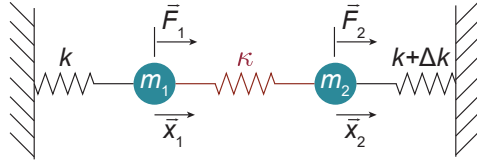


Figure E.1. Sketch of two masses m_1 and m_2 coupled by a spring with spring constant κ . m_1 has a spring constant of k , m_2 has a tunable spring constant of $k + \Delta k$. Each mass is driven by an external force $\vec{F}_{1,2}$ with different amplitudes. $\vec{x}_{1,2}$ describe the displacements of each mass.

other. The two oscillators are coupled by a spring with spring constant κ . The damping of each oscillator is described by γ_1 and γ_2 . The oscillators are externally driven by the forces \vec{F}_1 and \vec{F}_2 , respectively. A sketch of the mechanical system is shown in Figure E.1.

In the mechanical system, an oscillating force $\vec{F}_{1,2}$ induces a displacement $\vec{x}_{1,2}$ of the two masses $m_{1,2}$. For the following derivation, we assume $m_1 = m_2 = m$ and take $\vec{F}_{1,2} = F_{1,2} \vec{E}_0 \text{Re}(e^{i\omega t})$. $F_{1,2}$ is the mechanical oscillator strength of each mass. The matrix form of the equations of motion for this system is

$$\begin{bmatrix} \frac{d^2}{dt^2} + \gamma_1 \frac{d}{dt} + \frac{k + \kappa}{m} & -\frac{\kappa}{m} \\ -\frac{\kappa}{m} & \frac{d^2}{dt^2} + \gamma_2 \frac{d}{dt} + \frac{k + \kappa}{m} + \frac{\Delta k}{m} \end{bmatrix} \begin{bmatrix} \vec{x}_1 \\ \vec{x}_2 \end{bmatrix} = \begin{bmatrix} \frac{F_1}{m} \vec{E}_0 \text{Re}(e^{i\omega t}) \\ \frac{F_2}{m} \vec{E}_0 \text{Re}(e^{i\omega t}) \end{bmatrix} := \begin{bmatrix} \vec{L}_1 \\ \vec{L}_2 \end{bmatrix}. \quad (\text{E.1})$$

E.1.2 Decoupling the equations of motion

For an analytical solution to Equation E.1, we need to transform the equations of motion into the eigenvector basis. The two eigenmodes $\vec{r}_{1,2}$ are given by [Fri14]

$$\begin{bmatrix} \vec{x}_1 \\ \vec{x}_2 \end{bmatrix} = \mathbf{U}^{-1} \begin{bmatrix} \vec{r}_1 \\ \vec{r}_2 \end{bmatrix}, \quad (\text{E.2})$$

where the rows of the transformation matrix \mathbf{U} are the normalised eigenvectors of the matrix in Equation E.1. For simplicity, only the non-normalised eigenvectors will be shown in the following derivation. All calculations and plots shown in this thesis use the

normalised eigenvectors. The eigenvectors take the form

$$\vec{v}_1 = \begin{bmatrix} 1 \\ -\frac{1}{2} \frac{\Delta k}{\kappa} + \operatorname{sgn}(\Delta k) \frac{\sqrt{\Delta k^2 + 4\kappa^2}}{2\kappa} \end{bmatrix} \quad \text{and} \quad \vec{v}_2 = \begin{bmatrix} +\frac{1}{2} \frac{\Delta k}{\kappa} - \operatorname{sgn}(\Delta k) \frac{\sqrt{\Delta k^2 + 4\kappa^2}}{2\kappa} \\ 1 \end{bmatrix}. \quad (\text{E.3})$$

Introducing the ratio ρ between the detuning and coupling constant $\rho = \frac{\Delta k}{\kappa}$, we can write

$$\vec{v}_1 = \begin{bmatrix} 1 \\ -\frac{1}{2}\rho + \operatorname{sgn}(\rho) \sqrt{\frac{1}{4}\rho^2 + 1} \end{bmatrix} \quad \text{and} \quad \vec{v}_2 = \begin{bmatrix} +\frac{1}{2}\rho - \operatorname{sgn}(\rho) \sqrt{\frac{1}{4}\rho^2 + 1} \\ 1 \end{bmatrix}. \quad (\text{E.4})$$

We can write the transformation matrix \mathbf{U} as

$$\mathbf{U} = \begin{bmatrix} U_{11} & U_{12} \\ U_{21} & U_{22} \end{bmatrix} = \begin{bmatrix} 1 & -\frac{1}{2}\rho + \operatorname{sgn}(\rho) \sqrt{\frac{1}{4}\rho^2 + 1} \\ +\frac{1}{2}\rho - \operatorname{sgn}(\rho) \sqrt{\frac{1}{4}\rho^2 + 1} & 1 \end{bmatrix}. \quad (\text{E.5})$$

The angular eigenfrequencies of the system are given by

$$\Omega_{\pm} = \left(\frac{k + \kappa}{m} + \frac{1}{2} \frac{\Delta k}{m} \mp \frac{1}{2} \sqrt{\left(\frac{\Delta k}{m} \right)^2 + 4 \left(\frac{\kappa}{m} \right)^2} \right)^{\frac{1}{2}}. \quad (\text{E.6})$$

It is important to note that Ω_{\pm} do not depend on $\vec{F}_{1,2}$.

After transforming Equation E.1 with the matrix \mathbf{U} , we find two uncoupled differential equations for each of the eigenmode displacements \vec{r}_1 and \vec{r}_2 :

$$\begin{aligned} \left(\frac{d^2}{dt^2} + \gamma_1 \frac{d}{dt} + \Omega_+^2 \right) \vec{r}_1 &= \frac{\vec{E}_0}{m} (U_{11}F_1 + U_{12}F_2) \operatorname{Re}(e^{i\omega t}), \\ \left(\frac{d^2}{dt^2} + \gamma_2 \frac{d}{dt} + \Omega_-^2 \right) \vec{r}_2 &= \frac{\vec{E}_0}{m} (U_{21}F_1 + U_{22}F_2) \operatorname{Re}(e^{i\omega t}). \end{aligned} \quad (\text{E.7})$$

E.1.3 Frequency response of the coupled masses

Solving Equation E.7 for the eigenmodes \vec{r}_1 and \vec{r}_2 gives

$$\begin{aligned}\vec{r}_1 &= \frac{\vec{E}_0}{m} \frac{(U_{11}F_1 + U_{12}F_2)}{-\omega^2 + i\gamma_1\omega + \Omega_+^2} \text{Re}(e^{i\omega t}) , \\ \vec{r}_2 &= \frac{\vec{E}_0}{m} \frac{(U_{21}F_1 + U_{22}F_2)}{-\omega^2 + i\gamma_2\omega + \Omega_-^2} \text{Re}(e^{i\omega t}) .\end{aligned}\tag{E.8}$$

The mechanical response $f_{1,2}$ of each eigenmode is modified as a function of the ratio ρ through U_{ij} :

$$\begin{bmatrix} f_1 \\ f_2 \end{bmatrix} = \begin{bmatrix} U_{11}F_1 + U_{12}F_2 \\ U_{21}F_1 + U_{22}F_2 \end{bmatrix} .\tag{E.9}$$

For large detuning compared to the coupling strength ($\rho \gg 1$), the mechanical oscillator strength $F_{1,2}$ is recovered for each mass:

$$f_1(|\Delta k| \gg 1) = F_1 , \quad f_2(|\Delta k| \gg 1) = F_2 .\tag{E.10}$$

For a large positive detuning, the oscillator strengths shown in Equation E.10 are correct. For a large negative detuning, the oscillator strengths of the eigenmodes are swapped. To accomodate this problem, we need to change the transformation matrix \mathbf{U} upon changing the sign of the detuning Δk . Switching the rows in the transformation matrix \mathbf{U} yields the correct oscillator strengths at large negative detuning. The responses at large detuning are then:

$$\begin{aligned}f_1(|\Delta k| \gg 1) &= \begin{cases} F_1 , & \Delta k > 0 \\ F_2 , & \Delta k < 0 \end{cases} , \\ f_2(|\Delta k| \gg 1) &= \begin{cases} F_2 , & \Delta k > 0 \\ F_1 , & \Delta k < 0 \end{cases} .\end{aligned}\tag{E.11}$$

The full description of the transformation matrix \mathbf{U} is then:

$$\mathbf{U}(\Delta k > 0) = \begin{bmatrix} U_{11} & U_{12} \\ U_{21} & U_{22} \end{bmatrix}, \quad \mathbf{U}(\Delta k < 0) = \begin{bmatrix} U_{21} & U_{22} \\ U_{11} & U_{12} \end{bmatrix}. \quad (\text{E.12})$$

E.1.4 Calculation of the dissipated power

The dissipated power P in the system is given by the product of the velocity of the eigenmodes and the right hand side of the equations of motion, \vec{L} , in the eigenvector basis:

$$P(t) = \dot{\vec{r}}^T \mathbf{U} \vec{L}. \quad (\text{E.13})$$

The driving force oscillates as $\text{Re}(e^{i\omega t})$. Therefore, only the real part of the solution for $\vec{r}_{1,2}$ is relevant. After taking the real part and calculating the derivative of \vec{r} in time, we derive an analytical solution for the time-dependent dissipated power, P . We are interested in the steady-state solution of P . After averaging the total power P over time, the total average power $\langle P \rangle$ is given by

$$\begin{aligned} \langle P \rangle = & \frac{1}{2} \frac{|\vec{E}_0|^2}{m} (U_{11}F_1 + U_{12}F_2)^2 \frac{\gamma_1 \omega^2}{\gamma_1^2 \omega^2 + (\Omega_+^2 - \omega^2)^2} + \\ & \frac{1}{2} \frac{|\vec{E}_0|^2}{m} (U_{21}F_1 + U_{22}F_2)^2 \frac{\gamma_2 \omega^2}{\gamma_2^2 \omega^2 + (\Omega_-^2 - \omega^2)^2}. \end{aligned} \quad (\text{E.14})$$

The total average power can be seen as the sum of the average power of each of the two eigenmodes:

$$\langle P \rangle = \langle P_+ \rangle + \langle P_- \rangle. \quad (\text{E.15})$$

Assuming that $\kappa \ll k$ then $\frac{k+\kappa}{m} \simeq \frac{k}{m}$. Using this we can rewrite the term $(\Omega_\pm^2 - \omega^2) = (\Omega_\pm - \omega)(\Omega_\pm + \omega) \simeq (\Omega_\pm - \omega)2\omega$. Inserting this approximation into Equation E.14 yields:

$$\begin{aligned} \langle P \rangle \simeq & \frac{|\vec{E}_0|^2}{4m} (U_{11}F_1 + U_{12}F_2)^2 \frac{\frac{1}{2}\gamma_1}{\left(\frac{1}{2}\gamma_1\right)^2 + (\Omega_+ - \omega)^2} + \\ & \frac{|\vec{E}_0|^2}{4m} (U_{21}F_1 + U_{22}F_2)^2 \frac{\frac{1}{2}\gamma_2}{\left(\frac{1}{2}\gamma_2\right)^2 + (\Omega_- - \omega)^2}. \end{aligned} \quad (\text{E.16})$$

The average power is the sum of two Lorentzians centred around each of the eigenvalues Ω_{\pm} . This is a significant result: the model predicts straightforward lineshapes.

E.1.5 Linking the mechanical system to the optical response of coupled excitons

The experimental results shown in Chapter 6 study excitonic couplings. Therefore, we forge an analogy between the mechanical and optical systems. We show that excitonic coupling can be readily described by the mechanical model assuming a classical description of the driven excitons.

We model the coupling of inter- and intralayer excitons as two coupled oscillating optical dipoles driven by an external light field. The optical dipole representing the intralayer exciton (index 1) has a constant energy of $\hbar\omega_0$. The IE (index 2) is modelled by a dipole that has a tunable energy through the term $\hbar\Delta\omega$ with a total energy of $\hbar\omega_0 + \hbar\Delta\omega$. The two dipoles are coupled to each other through a coupling constant κ . The detuning $\hbar\Delta\omega$ is a linear function of the applied electric field F_z on account of the Stark effect. From experiments we know that the energy crossing point occurs at $F_z \neq 0$. Therefore,

$$\hbar\Delta\omega = \mu(F_z - F_{z,0}) , \quad (\text{E.17})$$

where μ is the static dipole moment and $F_{z,0}$ is the field at which the two bare energies match.

From the experiment we know that the sign of μ is positive for IE₁ and negative for IE₂. The two dipoles are driven by the external light field $\vec{E} = \vec{E}_0 \text{Re}(e^{i\omega t})$. The force of the field on the charge e is $e\vec{E}$. Each dipole has a different coupling strength $F_{1,2}$ to the light field and a dephasing constant $\gamma_{1,2}$.

The resulting equations of motion have the same form as the equations of motion of the mechanical system shown in Equation E.1. Therefore, the calculations and solutions of the mechanical system also hold for the excitonic system. The eigenenergies of the system are given by

$$\hbar\Omega_{\pm} \simeq \hbar \left(\omega_0 + \frac{1}{2}\Delta\omega \right) \mp \frac{1}{2} \sqrt{(\hbar\Delta\omega)^2 + 4\kappa^2} , \quad (\text{E.18})$$

assuming $\hbar\omega_0 + \kappa \simeq \hbar\omega_0$, as $\hbar\omega_0 \gg \kappa$.

For the eigenvectors, the ratio ρ is in this case defined as $\rho = \frac{\hbar\Delta\omega}{\kappa}$. The excitonic eigenmodes can be written as

$$\vec{r}_{1,2} = \frac{e\vec{E}_0 (U_{11,21}F_1 + U_{12,22}F_2)}{m (-\omega^2 + i\gamma_{1,2}\omega + \Omega_{\pm}^2)} . \quad (\text{E.19})$$

The result for the eigenmodes $\vec{r}_{1,2}$ from Equation E.19 is related to the dipole moment via

$$\vec{p}_{1,2} = e\vec{r}_{1,2} . \quad (\text{E.20})$$

So far we have described the response of two individual dipoles coupling to each other. In practice, an array of dipoles exists in a semiconductor. In a completely classical approach, the quantum well is treated as a two-dimensional array of optical dipoles [Kar03]. Following this approach, the linear absorption $\alpha(\omega)$ of a quantum well is given by [Kar03]

$$\alpha(\omega) = \frac{2\gamma\Gamma_0^{\text{rad}}}{(\omega_0 - \omega)^2 + (\gamma + \Gamma_0^{\text{rad}})^2} . \quad (\text{E.21})$$

The definition of the radiative coupling constant Γ_0^{rad} is

$$\Gamma_0^{\text{rad}} = \frac{1}{4A} \frac{e^2 f}{\epsilon_0 c m n} , \quad (\text{E.22})$$

where f is the oscillator strength, n is the refractive index of the quantum well, c is the speed of light, and $1/A$ is the dipole area density. From Equation E.21 we see that the solution of the quantum well absorption is additionally broadened by Γ_0^{rad} due to dipole-dipole interactions in the quantum well [Kir06, Kar03].

The absorption of an array of dipoles shown in Equation E.21 has a similar form as the equation for the average dissipated power $\langle P \rangle$ of two coupled masses in the mechanical system given in Equation E.16. Both equations are equivalent if we take the experimental dephasing $\gamma_{1,2}$ to be equal to the dephasing of the dipole array $\gamma + \Gamma_0^{\text{rad}}$. By comparing the two equations we find a linear relation between the absorption $\text{Im}(\chi)$ of two coupled dipoles and the dissipated power $\langle P \rangle$:

$$\text{Im}(\chi) = \frac{4e^2}{A\epsilon_0 c n |\vec{E}_0|^2} \langle P \rangle . \quad (\text{E.23})$$

The absorption strength $I_{1,2}$ of each coupled optical dipole is then dependent on the energy detuning $\hbar\Delta\omega$, the coupling κ , and the oscillator strengths $F_{1,2}$. For all calculations, the prefactor $\frac{4\hbar e^2}{A\epsilon_0 c m n}$ is set to 1 eV. $I_{1,2}$ is given by

$$\begin{bmatrix} I_1 \\ I_2 \end{bmatrix} = \begin{bmatrix} (U_{11}F_1 + U_{12}F_2)^2 \\ (U_{21}F_1 + U_{22}F_2)^2 \end{bmatrix} \text{eV} . \quad (\text{E.24})$$

The absorption is then modelled as

$$\text{Im}(\chi) = I_1 \frac{\frac{1}{2}\hbar\gamma_1}{(\frac{1}{2}\hbar\gamma_1)^2 + (\hbar\Omega_+ - \hbar\omega)^2} + I_2 \frac{\frac{1}{2}\hbar\gamma_2}{(\frac{1}{2}\hbar\gamma_2)^2 + (\hbar\Omega_- - \hbar\omega)^2} . \quad (\text{E.25})$$

E.1.6 Complex coupling constant

The excitonic coupling model can be generalised by allowing for the coupling constant to be complex. We write the complex coupling constant κ as

$$\kappa = |\kappa| e^{i\phi} , \quad (\text{E.26})$$

where $|\kappa|$ is the magnitude and ϕ is the phase.

We plug κ into the equations of motion and follow the derivation from Subsection E.1.1 to Subsection E.1.4. For a complex coupling constant, the ratio $\rho = \frac{\Delta k}{|\kappa|}$. Therefore, the complex matrix elements of $\tilde{\mathbf{U}}$ that are not equal to one become

$$\tilde{U}_{12,21} = \mp \frac{1}{2} \frac{\rho}{e^{i\phi}} \pm \frac{\text{sgn}(\rho)}{e^{i\phi}} \sqrt{\frac{1}{4}\rho^2 + 1} . \quad (\text{E.27})$$

We find that the multiplication of the matrix elements of $\tilde{\mathbf{U}}$ that are not equal to one with the oscillating part of the driving force yields a phase shift of the oscillating term:

$$\begin{aligned} \tilde{U}_{12,21} \text{Re}(e^{i\omega t}) &= \left(\mp \frac{1}{2} \rho \pm \text{sgn}(\rho) \sqrt{\frac{1}{4}\rho^2 + 1} \right) \cos(\omega t - \phi) \\ &= U_{12,21} \cos(\omega t - \phi) . \end{aligned} \quad (\text{E.28})$$

After decoupling the equations of motion, the phase ϕ shifts the phase of the response to the driving force by the same phase. More specifically, the phase shift only affects the response term that is multiplied by the non-unity matrix elements of $\tilde{\mathbf{U}}$.

The dissipated power is calculated in the same way as in Equation E.13. We can write the terms depending on the elements of $\tilde{\mathbf{U}}$ and F as

$$(U_{11,22} F_{1,2} \cos(\omega t) + U_{12,21} F_{2,1} \cos(\omega t - \phi))^2 . \quad (\text{E.29})$$

Time-averaging the mixed term of F_1 and F_2 yields

$$\begin{aligned} \langle \cos(\omega t) \cos(\omega t - \phi) \rangle &= \frac{\omega}{2\pi} \int_0^{\frac{2\pi}{\omega}} \cos(\omega t) \cos(\omega t - \phi) dt \\ &= \frac{\cos \phi}{2} . \end{aligned} \quad (\text{E.30})$$

Using these results we can rewrite the absorption strength $I_{1,2}$ of each coupled optical

dipole from Equation E.24 for a complex coupling constant as

$$\begin{bmatrix} I_1 \\ I_2 \end{bmatrix} = \begin{bmatrix} (U_{11}F_1)^2 + (U_{12}F_2)^2 + 2U_{11}U_{12}F_1F_2 \cos \phi \\ (U_{21}F_1)^2 + (U_{22}F_2)^2 + 2U_{21}U_{22}F_1F_2 \cos \phi \end{bmatrix} \text{eV}. \quad (\text{E.31})$$

The mixed terms depend on the cosine of the phase ϕ .

E.1.7 Quadratic Stark shift of the A-exciton

The quadratic shift of the A-exciton is included in the model when fitting the IE-A coupling in the main text. This is carried out by adding the term $-\beta_z F_z^2$ to the uncoupled energy of the optical dipole 1 representing the A-exciton with β_z being the excitonic polarisability. Then, the eigenenergies have an additional term depending on the quadratic energy shift of the optical dipole 1 (A-exciton). The eigenenergies are

$$\hbar\Omega_{\pm} = \hbar\omega_0 - \frac{1}{2}\beta_z F_z^2 \mp \frac{1}{2}\hbar\Delta\omega \mp \frac{1}{2}\sqrt{(\hbar\Delta\omega)^2 + 4\kappa^2 + 2(\beta_z F_z^2)^2 + 2\beta_z F_z^2 \hbar\Delta\omega}. \quad (\text{E.32})$$

The matrix elements of $\tilde{\mathbf{U}}$ that are not equal to one become

$$\tilde{U}_{12,21} = \left(\mp \frac{1}{2} \frac{\beta_z F_z^2}{\kappa} \mp \frac{1}{2} \rho \pm \text{sgn}(\rho) \sqrt{1 + \frac{1}{4}\rho^2 + \frac{1}{4} \left(\frac{\beta_z F_z^2}{\kappa} \right)^2 + \frac{1}{2} \frac{\beta_z F_z^2}{\kappa} \rho} \right) e^{-i\phi}. \quad (\text{E.33})$$

E.1.8 Semi-classical frequency response and absorption of excitons in a semiconductor

In a semi-classical description, the coupling of a dipole to a light field is described by a quantity called the oscillator strength f . The oscillator strength is proportional to the expectation value of the dipole operator squared $|\langle \phi_n | \vec{p} | \phi_0 \rangle|^2$ [CT05, Kli12]. Usually f is a sum over all n resonances of the oscillator. In the following we will only consider the ground state transition from state $|\phi_0\rangle$ to state $|\phi_1\rangle$ with a resonance angular frequency ω_0 . The oscillator strength f is defined as [CT05, Kli12]

$$f = \frac{2m\omega_0}{\hbar} |\langle \phi_1 | \vec{r} | \phi_0 \rangle|^2 = \frac{2m\omega_0}{\hbar e^2} |\langle \phi_1 | \vec{p} | \phi_0 \rangle|^2. \quad (\text{E.34})$$

Then the semi-classical solution for the response of an oscillating dipole with a dephasing rate Γ can be written as [Kar03, Kli12]

$$\vec{r} = \frac{e\vec{E}_0}{m} \frac{f}{\omega_0^2 - \omega^2 - i\Gamma\omega}. \quad (\text{E.35})$$

In the linear optical regime, the optical susceptibility $\chi(\omega)$ relates the probe field \vec{E} to the probe-induced macroscopic polarisation $P(\omega)$ [Kir06]:

$$P(\omega) = \epsilon_0 \chi(\omega) \vec{E} . \quad (\text{E.36})$$

The Coulomb interaction between charges (exciton effects and screening) needs to be considered for a quantum mechanical description of the optical response of semiconductors. These effects are described by the so-called semiconducting Bloch equations (SBEs) [Lin88, Kli12]. The SBEs are a set of coupled equations that include the microscopic polarisation P_k as well as electron and hole distributions [Hau09]. The index k describes the momentum dependence of the charge carriers. The microscopic polarisation is related to the macroscopic polarisation as follows [Koc06]:

$$P(\omega) = |\langle \phi_c | \vec{p} | \phi_v \rangle| \sum_k P_k , \quad (\text{E.37})$$

where the indices c and v stand for valence and conduction band, respectively.

For a classical light field, the optical response of the semiconductor can be calculated by linking the SBEs to Maxwell's wave equation (MSBE) [Kir06]. One can calculate the macroscopic polarisation as [Koc06]

$$P(\omega) = 2 |\langle \phi_c | \vec{p} | \phi_v \rangle|^2 \sum_{\alpha} \frac{|\Psi_{\alpha}(r=0)|^2}{\hbar\omega_{\alpha} - \hbar\omega - i\hbar\gamma_{\alpha}} \vec{E} , \quad (\text{E.38})$$

where Ψ_{α} is the excitonic wavefunction, ω_{α} is the excitonic resonance angular frequency, and γ_{α} is the polarisation dephasing rate. We now consider the excitonic ground state Ψ_0 and rewrite Equation E.38 with the definition of the oscillator strength f in Equation E.34 to:

$$P(\omega) = \frac{e^2 \vec{E}}{m} \frac{f}{\omega_0^2 - \omega^2 - i\gamma\omega} . \quad (\text{E.39})$$

Remarkably, the result for the macroscopic polarisation following the SBEs is the same as the result for the polarisation of an optical dipole driven by an oscillating field, compare Equation E.39 with Equation E.19 and Equation E.35.

M. Kira and S. W. Koch calculate the linear absorption $\alpha(\omega)$ of a quantum well following the MSBEs [Kir06]. Their result for the absorption is the same as the absorption of an array of oscillating dipoles in a two-dimensional plane derived in a classical way shown in Equation E.21 [Kar03].

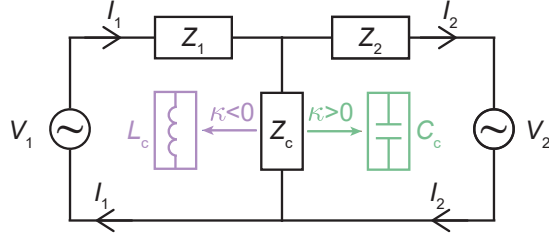


Figure E.2. Sketch of two RLC circuits coupled by a shared impedance Z_c . For a purely capacitive (inductive) coupling the coupling strength κ is positive (negative).

E.1.9 Coupled RLC circuits

Applying the coupling model to the two experimentally observed excitonic couplings yields a positive coupling constant for the IE-B coupling and a negative coupling constant for the IE-A coupling (see discussion in Chapter 6). A negative coupling constant in a mechanical framework is of course counter-intuitive. Therefore, we will look at an alternative, an electrical system consisting of two coupled RLC circuits (see Figure E.2).

First, we derive the equation of motion of a single RLC circuit. The complex impedance of a RLC circuit is given as

$$Z = \frac{1}{i\omega C} + R + i\omega L, \quad (\text{E.40})$$

where C is the capacitance, R is the resistance, and L is the inductance.

The voltage can be related to the current I as

$$V = ZI. \quad (\text{E.41})$$

The current is equal to the change of the charge q on the capacitor in time:

$$I = \frac{dq}{dt}. \quad (\text{E.42})$$

We take the voltage driving the circuit as

$$V = V_0 \text{Re}(e^{i\omega t}) \quad (\text{E.43})$$

and the corresponding charge as

$$q = q_0 \text{Re}(e^{i\omega t}). \quad (\text{E.44})$$

We then calculate the equation of motion of the RLC circuit:

$$\begin{aligned}
 V &= Z \frac{dq}{dt} \\
 V_0 \operatorname{Re}(e^{i\omega t}) &= \left(\frac{1}{i\omega C} + R + i\omega L \right) i\omega q_0 \operatorname{Re}(e^{i\omega t}) \\
 V_0 &= \left(\frac{1}{C} + i\omega R - \omega^2 L \right) q_0 .
 \end{aligned} \tag{E.45}$$

Equation E.45 can be directly compared to the equation of motion of a mechanical oscillator system:

$$F = \left(k + im\omega\gamma - \omega^2 m \right) x . \tag{E.46}$$

The inductance L corresponds to the mass m , the term $\frac{R}{L}$ corresponds to the damping γ , and the inverse of the capacitance $\frac{1}{C}$ corresponds to the spring constant k . Alternatively we can write Equation E.45 as

$$\frac{V}{L} = \frac{d^2 q}{dt^2} + \frac{R}{L} \frac{dq}{dt} + \frac{1}{LC} q . \tag{E.47}$$

Next, we look at two RLC circuits coupled together by a shared impedance Z_c (see Figure E.2). Both circuits are driven by an AC voltage with different magnitude but with the same angular frequency and phase. We consider two distinct cases: Z_c is either a capacitor or an inductor. Let us take $Z_c = \frac{1}{i\omega C_c}$ first. One can then write the equations of motion as:

$$V_1 = L_1 \frac{d^2 q_1}{dt^2} + R_1 \frac{dq_1}{dt} + \frac{1}{C_{1,\text{tot}}} q_1 - \frac{1}{C_c} q_2 , \tag{E.48}$$

$$V_2 = L_2 \frac{d^2 q_2}{dt^2} + R_2 \frac{dq_2}{dt} + \frac{1}{C_{2,\text{tot}}} q_2 - \frac{1}{C_c} q_1 , \tag{E.49}$$

with $C_{1,\text{tot}} = \frac{C_1 C_c}{C_1 + C_c}$ and $C_{2,\text{tot}} = \frac{C_2 C_c}{C_2 + C_c}$ being the series capacitance of $C_{1,2}$ and C_c . The matrix form of this coupling is:

$$\begin{bmatrix} V_1 \\ V_2 \end{bmatrix} = \begin{bmatrix} -\omega^2 L_1 + i\omega R_1 + \frac{1}{C_{1,\text{tot}}} & -\frac{1}{C_c} \\ -\frac{1}{C_c} & -\omega^2 L_2 + i\omega R_2 + \frac{1}{C_{2,\text{tot}}} \end{bmatrix} \begin{bmatrix} q_1 \\ q_2 \end{bmatrix} . \tag{E.50}$$

We define the sign of the electrical coupling in the same way as for the mechanical system shown in Equation E.1. For a capacitive coupling of the two RLC circuits, the coupling

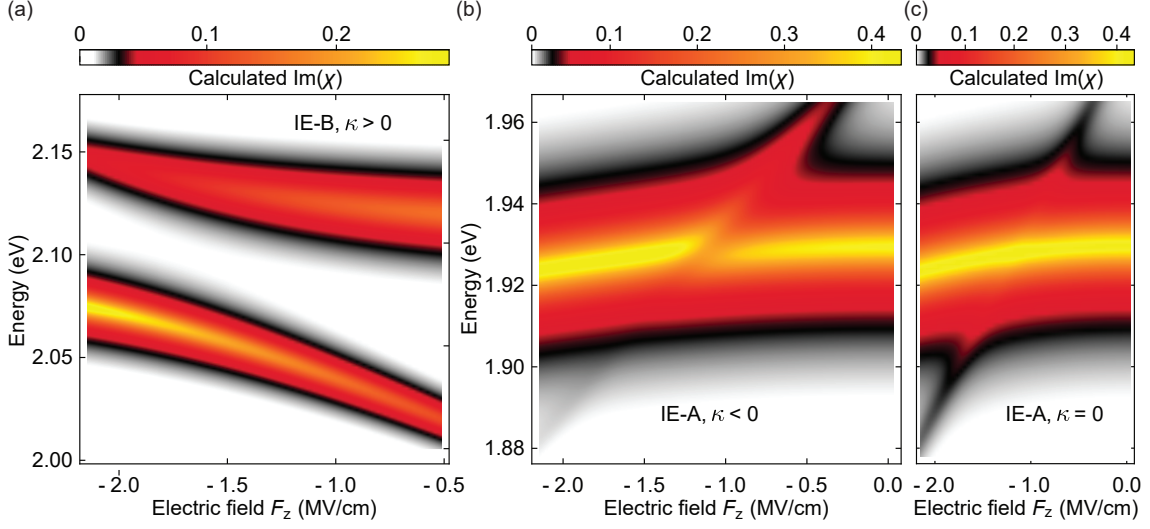


Figure E.3. Colour-maps of the calculated absorption $\text{Im}(\chi)$ of (a) the IE-B and (b) the IE-A coupling as a function of electric field according to Equation E.25. The calculated absorption maps correspond directly to the measurements shown in Figure 6.2a and Figure 6.2b, respectively. (c) Same colour-map as in (b) with the coupling κ set to zero. The used parameters are the same as extracted from fits to the data shown in Figure 6.4. The parameters are summarised in Table 6.1. The three colour-maps are interpolated to first order.

constant is positive. This means the IE-B coupling can be seen as a capacitive coupling.

Next, Z_c is set to $i\omega L_c$. The matrix form of the equations of motion can be written as:

$$\begin{bmatrix} V_1 \\ V_2 \end{bmatrix} = \begin{bmatrix} -\omega^2 (L_1 + L_c) + i\omega R_1 + \frac{1}{C_1} & \omega^2 L_c \\ \omega^2 L_c & -\omega^2 (L_2 + L_c) + i\omega R_2 + \frac{1}{C_2} \end{bmatrix} \begin{bmatrix} q_1 \\ q_2 \end{bmatrix}. \quad (\text{E.51})$$

For an inductive coupling of the two circuits, the coupling constant is negative. The IE-A coupling can be described as an inductive coupling.

E.1.10 Zero coupling case

Figure E.3a and Figure E.3b show the calculated absorption spectra for the IE-B and IE-A coupling corresponding to the measurement regions shown in Fig 6.2. The calculated maps reproduce the experimental data quite well.

Our model also allows us to calculate the absorption spectra for zero coupling. In this case, the off-diagonal elements in the equations of motion in Equation E.1 are zero. Following the analysis, all terms with κ are set to zero. The absorption strength $I_{1,2}$ of each resonance is then only governed by the respective oscillator strength $F_{1,2}$. Figure E.3c shows the calculated absorption spectra for the IE-A coupling for $\kappa = 0$. In the experiment, the

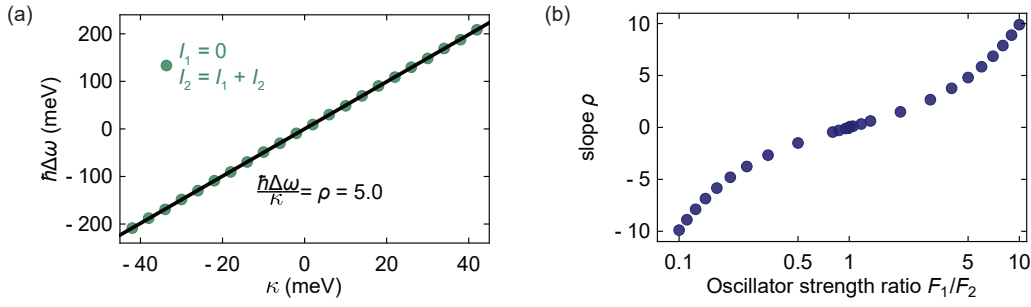


Figure E.4. (a) Plot of the energy detuning $\hbar\Delta\omega$ of the maximum/minimum absorption strength due to constructive/destructive interference in each eigenmode as a function of the coupling strength κ . For the calculation of the absorption strengths according to Equation E.31, the parameters for the IE-A coupling shown in Table 6.1 are used. The electric field offset $F_{z,0}$ and the polarisability β_z are set to zero. The black line is a linear fit to the data and yields a slope of $\rho = 5.0$ for $F_1/F_2 = 5.159$. (b) Plot of the slope ρ as fitted in (a) for varying oscillator strength ratios F_1/F_2 . For a negative dipole moment μ (IE-B), the sign of the slopes is flipped.

IE-resonance is strong on the high-energy side of the A-exciton, while it is weak on the low-energy side. For zero coupling, this interference effect vanishes and the absorption strength of the IE is constant and symmetric with respect to the A-exciton energy. Therefore, the coupling between IE and A is necessary to reproduce the experimentally observed absorption strength.

E.1.11 Experimental observability of interference effects

The effects of the constructive and destructive interference depend strongly on the coupling phase ϕ in the mixed term in Equation E.31. Complete constructive (destructive) interference occurs only for a phase of exactly 0 or π . The more the phase is different from 0 or π , the less apparent is the effect of the interference. This allows us to estimate an error for the fitted phase. The destructive interference of the IE below the A-exciton is best captured for a phase of $\phi = \pi \pm 0.3$. We take the same error for the coupling phase of the IE-B coupling.

Next, we look at the influence of the coupling strength and the oscillator strength ratio on the constructive/destructive interference. Figure E.4a shows the energy detuning $\hbar\Delta\omega$ of the maximum/minimum intensity due to constructive/destructive interference in each eigenmode for various coupling strength values κ . The sign of κ is the same as the sign of the detuning $\hbar\Delta\omega$ needed to reach the extrema. A larger absolute value for κ shifts the absorption strength extrema towards larger detuning. Additionally, the constructively/destructively interfered absorption strengths are spread over a larger detuning range for larger coupling strengths. Let's turn to the large positive coupling strength of the IE-B coupling with $\kappa = 35.8$ meV. The effect of the constructive/destructive interference would only be visible at a high detuning of roughly -175 meV $\cong -5$ MV/cm (see Figure E.4a

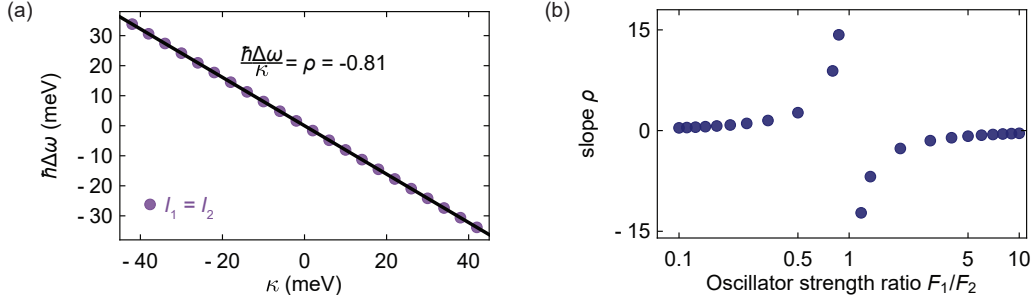


Figure E.5. (a) Plot of the energy detuning $\hbar\Delta\omega$ of the equal absorption strength point, $I_1 = I_2$, as a function of the coupling strength κ . For the calculation of the absorption strengths according to Equation E.31, the parameters for the IE-A coupling shown in Table 6.1 are used. The electric field offset $F_{z,0}$ and the polarisability β_z are set to zero. The black line is a linear fit to the data and yields a slope of $\rho = -0.81$ for $F_1/F_2 = 5.159$. (b) Plot of the slope ρ where $I_1 = I_2$ as a function of the oscillator strength ratio F_1/F_2 . For a negative dipole moment μ (IE-B), the sign of the slopes is flipped.

and Figure E.6 top row). Reaching such high electric fields is experimentally not feasible.

The dependence of the detuning position of the extreme points on κ is fitted with a linear function yielding a slope of $\rho = 5.0$ for $F_1/F_2 = 5.159$. Figure E.4b shows the slope values as a function of the oscillator strength ratio F_1/F_2 . For a large imbalance between F_1 and F_2 , the slopes increase. This means that even for a small κ the detuning needed to reach the extrema is quite large (compare vertical dashed green lines in Figure E.6 top row). Towards $F_1/F_2 = 1$ the slopes approach zero. A smaller imbalance of F_1 and F_2 pushes the extrema towards zero detuning (compare vertical dashed green lines in Figure E.6 top and bottom row). From an experimental point of view, the interplay between coupling strength and oscillator strengths is important for the constructive/destructive interferences to be visible for reasonable experimental parameters (compare Figure E.6).

E.1.12 Equal absorption strength point

According to Equation E.31 we calculate numerically the equal absorption strength point of the two coupled resonances ($I_1 = I_2$). The calculations based on the model predict that the equal absorption strength point is detuned from the crossing point of the uncoupled energy levels. Figure E.5a plots the detuning $\hbar\Delta\omega$ needed to reach the equal intensity point for a certain coupling constant κ : the smaller $|\kappa|$, the lower the detuning of the equal absorption strength point. A linear fit to the calculated data yields a slope of $\rho = -0.81$ for $F_1/F_2 = 5.159$ where the condition $I_1 = I_2$ is fulfilled. The influence of the oscillator strength ratio on the ratio ρ is shown in Figure E.5b. Increasing (decreasing) the oscillator strength imbalance decreases (increases) the ratio ρ . This means that a larger imbalance of the oscillator strengths pushes the equal intensity point towards the uncoupled energy crossing point (compare vertical dashed purple lines in Figure E.6 top and bottom row).

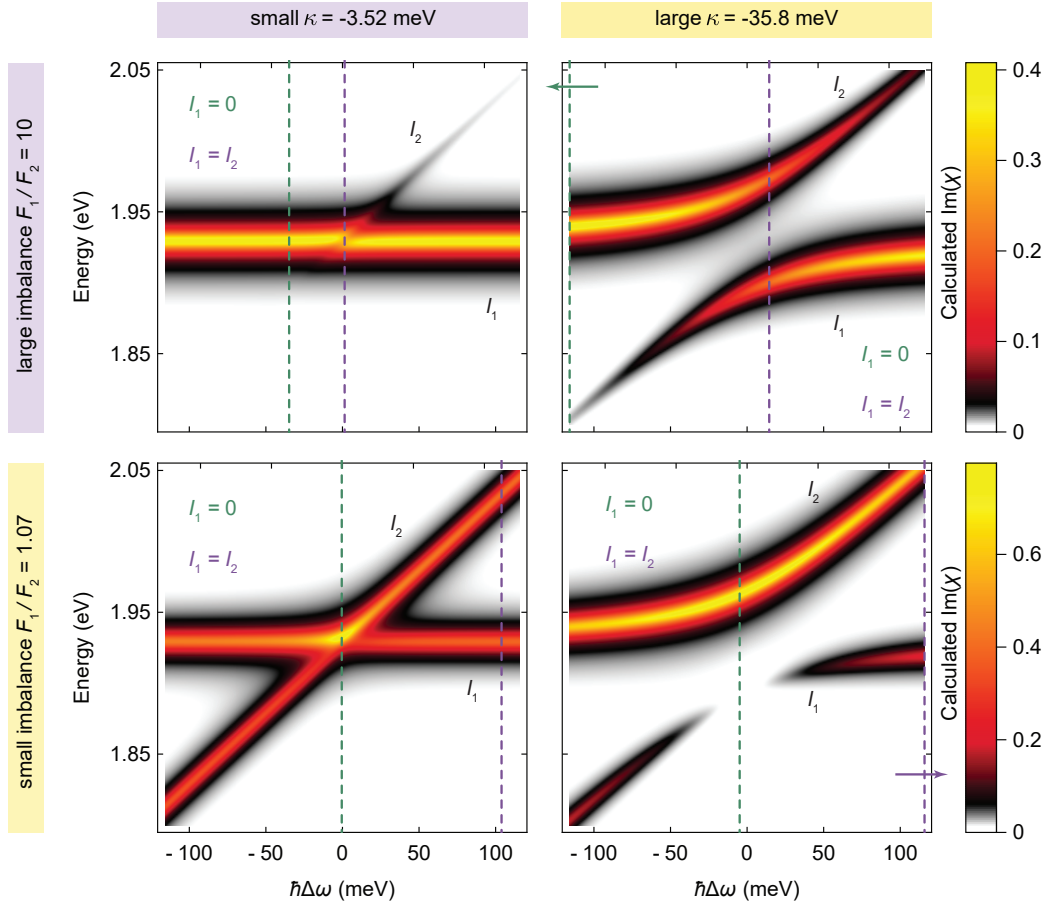


Figure E.6. Colour-map of the calculated absorption $\text{Im}(\chi)$ of an excitonic coupling as a function of energy detuning $\hbar\Delta\omega$ with negative coupling according to Equation E.25. The left (right) column calculation uses a small (large) coupling $\kappa = -3.18$ meV ($\kappa = -35.8$ meV). The top (bottom) row calculation uses a large (small) imbalance of the oscillator strengths $F_1/F_2 = 10$ ($F_1/F_2 = 1.07$). F_1 is set to the A-exciton oscillator strength in table 6.1. The electric field offset $F_{z,0}$ and the polarisability β_z are set to zero. The other parameters used are from the IE-A coupling shown in Table 6.1. The vertical dashed green line indicates the detuning where the absorption strength I_1 vanishes due to the destructive interference in eigenmode 1; the absorption strength I_2 is maximised due to the constructive interference (see Figure E.4). The vertical dashed purple line indicates the detuning where the absorption strengths I_1 and I_2 are identical (see Figure E.5). For a large κ (right column), the extrema (top) and the equal absorption strength point (bottom) lie outside of the depicted detuning range. The extrema (right column, top) are shifted to $\hbar\Delta\omega \ll -1000$ meV; the equal absorption strength point (right column, bottom) is shifted to $\hbar\Delta\omega = 1000$ meV. All colour-maps are interpolated to first order.

E.2 Measurement data processing

An overview for the data processing steps for a typical IE-B spectrum is shown in Figure E.7. The raw reflected signal R and the reference reflectivity spectrum R_0 are used to calculate the differential reflectivity $\Delta R/R_0$ (see Figure E.7a and Figure E.7b). The differential

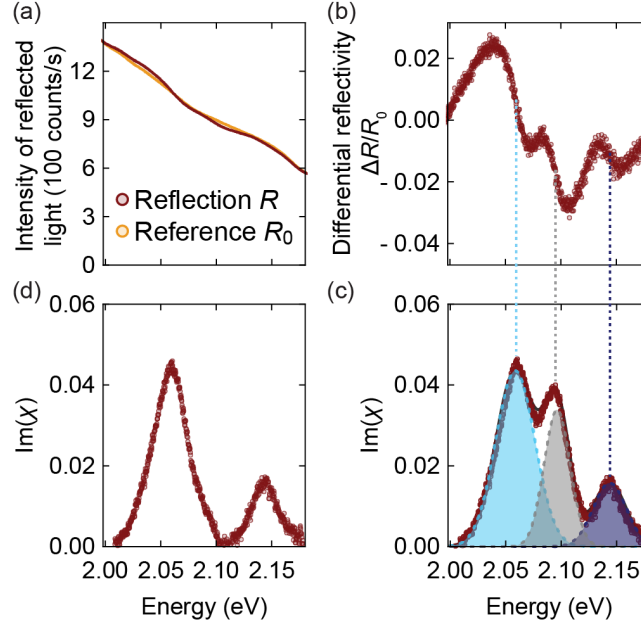


Figure E.7. Data processing overview for a typical IE-B spectrum at $F_z = -2.05$ MV/cm. (a) Raw reflection spectrum R , and reference spectrum R_0 at a large electron density. (b) Differential reflectivity $(R - R_0)/R_0 = \Delta R/R_0$. (c) Imaginary part of the optical susceptibility obtained from the spectrum in (b) using a Kramers-Kronig relationship. The spectrum is fitted by the sum of three Gaussians. The vertical dashed lines highlight the peak position of each excitonic resonance. (d) Subtraction of the uncoupled B_{L1} exciton peak, the grey Gaussian in (c).

reflectivity is then converted into the imaginary part of the optical susceptibility $\text{Im}(\chi)$ which determines the absorption (see Figure E.7c). The conversion is carried out by using a Kramers-Kronig relation that expresses $\text{Im}(\chi)$ as a function of $\Delta R/R_0$ (see Section 3.5.1).

The measured absorption spectra in Main Figure 2a-c are shown without the uncoupled B_{L1} and A_{L2} exciton peaks. The raw data of those three measurements are shown in Figure E.8. Each spectrum is fitted by a sum of three Gaussians. First, the removal procedure of the B_{L1} in Figure E.8a and Figure E.8b is described. The linewidth and amplitude of the subtracted B_{L1} exciton at all electric fields is set to the fitted values at the highest electric field. The energy of the B_{L1} exciton for the scan in Figure E.8a (Figure E.8b) is taken as the fitted values until -0.90 MV/cm (-1.39 MV/cm) and from then on taken as constant. The B_{L1} exciton is then removed with these fitting parameters (see Figure E.7d).

Second, the subtraction of the A_{L2} exciton in Figure E.8b and Figure E.8c is discussed. The linewidth and amplitude of the subtracted A_{L2} exciton at all electric fields is set to the fitted values at zero electric field. The energy is taken to be the fitted zero-field energy modified by the quadratic Stark shift for finite fields. The polarisability is set to the value

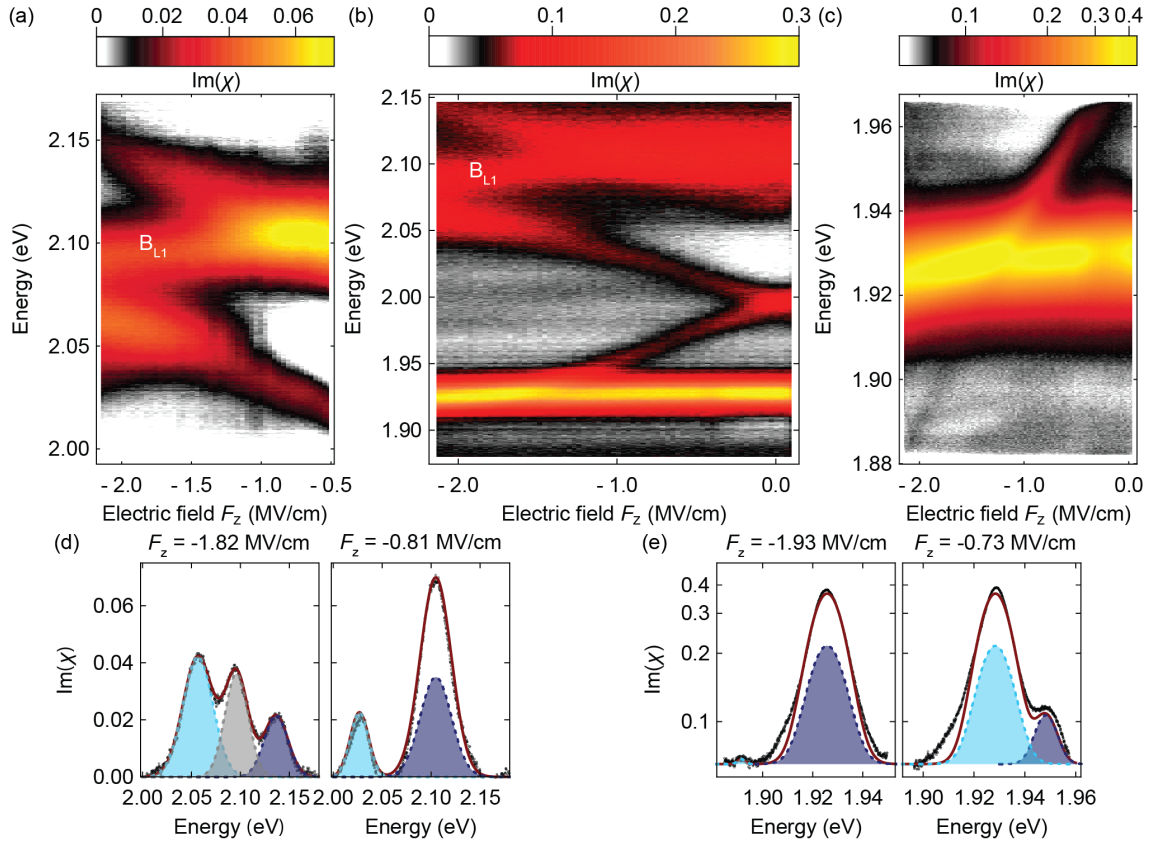


Figure E.8. Measured absorption (σ^+ polarisation) of homobilayer MoS₂ as a function of applied electric field F_z (b) over the whole studied excitonic region, (a) centred around the B-exciton, and (c) centred around the A-exciton. The measurements were carried out at $T = 4.2$ K and $B_z = 9$ T. These are the same measurements as shown in Main Figure 2a-c without the subtraction of the uncoupled B_{L1} and A_{L2} excitons. (d,e) Two example spectra of (d) the IE-B coupling shown in (c) and (e) the IE-A coupling shown in (a). Each spectrum is fitted by a sum of three Gaussians. The grey Gaussian in the left spectrum in (d) corresponds to the uncoupled B_{L1} . The absorption in (c) and (e) is scaled logarithmically.

extracted from the coupled dipole model shown in Table 6.1.

The exciton energies and peak areas shown in Figure 6.2 are extracted from the unmodified measured absorption spectra shown in Figure E.8a and Figure E.8c. The fitting routines yielding the energies and peak areas are described. The IE-A coupling shown in Figure E.8c is fitted as the sum of three Gaussians where the two Gaussians describing the A-excitons in each layer are set to the same energy and intensity (see Figure E.8e). This is a reasonable assumption if the spectra are energetically far away from the energy crossing point compared to the coupling strength. For the IE-B measurement shown in Figure E.8a, spectra at electric fields higher than -0.81 MV/cm are fitted by a sum of three independent Gaussians while for lower electric fields the two B-excitons in each layer are set to the same energy and intensity for reasonable fitting results (see Figure E.8d).

E.3 Computational details of the GW+BSE calculations *

The atomic structures, the quasi-particle band structures, and the optical spectra were obtained using the VASP package [Kre93, Kre96]. Core electrons were treated by the plane-augmented wave scheme [Blo94, Kre99]. A lattice parameter value of 3.22 Å was set for all calculation runs. For all the calculation cells, a grid of $15 \times 15 \times 1$ k-points was used together with a vacuum height of 21.9 Å. Van der Waals interactions between the layers were included by performing the geometry's optimisation process at the PBE-D3 level [Gri10]. All atoms were allowed to relax with a force convergence criterion below 0.005 eV/Å. A Heyd-Scuseria-Ernzerhof (HSE) hybrid functional [Hey04, Hey05, Pai06] was used as an approximation of the exchange-correlation electronic term, including spin-orbit coupling (SOC). It was used to determine the eigenvalues and wave functions as an input for the full-frequency-dependent GW calculations [Shi06] performed at the G_0W_0 level. The electric field was applied at this step, just before GW calculation process. Its application was only a small perturbation to the band structures, considering small/moderate electric field values. For partial occupancies, an energy cutoff of 400 eV and a gaussian smearing of 0.05 eV width were chosen. A tight electronic minimisation tolerance of 10^{-8} eV was set to determine the corresponding derivative of the orbitals with respect to k needed in quasi-particle band structure calculations with a good precision. The direct band gap convergence was carefully checked (smaller than 0.1 eV as a function of k-points sampling). Afterwards, the total number of states included in the GW procedure was set to 1280 together with an energy cutoff of 100 eV for the response function. A Wannier interpolation procedure performed by the WANNIER90 program [Mos08] was used to obtain the band structures. All optical excitonic transitions were calculated by solving the Bethe-Salpeter Equation [Han79, Roh98]. The twelve highest valence bands and the sixteen lowest conduction bands were used to obtain eigenvalues and oscillator strengths on all systems. From these calculations, we use the imaginary part of the complex dielectric function to construct the absorbance with an artificial broadening of 12 meV.

*The calculations were by performed by Iann C. Gerber in Toulouse

Appendix **F**

Supplemental information to Chapter 7: ‘First-order magnetic phase transition of mobile electrons in monolayer MoS₂’

In Chapter 7, we present evidence for a first-order phase transition of itinerant electrons in monolayer MoS₂. In this chapter, we give details on the experimental methods in Section F.1 and show additional experimental data sets in Section F.2. This chapter is partially adapted from the Supplement in Reference [Roc20].

F.1 Experimental details

The measurement setup for all measurements on device 1 is slightly different from the setup described in Section 3.7. The microscope head is the same. However, we cool down the sample in a variable-temperature insert (VTI) within the same helium bath-cryostat. Using a VTI allows the temperature to be controlled which is not possible in the standard inset that we use. With our setup, the sample can reach a temperature as low as $T = 1.6$ K. Additionally, a heater mounted just below the sample allows heating the sample. The VTI’s diameter is smaller than the standard tube so we use a downsized sample cage with smaller piezo positioners. In the smaller cage, the light is focused to a diffraction-limited spot on the sample’s surface using a single aspherical lens ($NA = 0.7$). The PL excitation intensity is kept low, such that no more than 500 nW reaches the sample. The PL microscope head is equipped with full polarisation control such that all four polarisation combinations can be measured. Device 2 is measured at 4.2 T in the setup in Section 3.7.

Upon laser illumination, charges become trapped at defects and at interfaces and screen the electric field across our capacitor [Ju14, Epp18, Wan10]. A direct consequence is that the

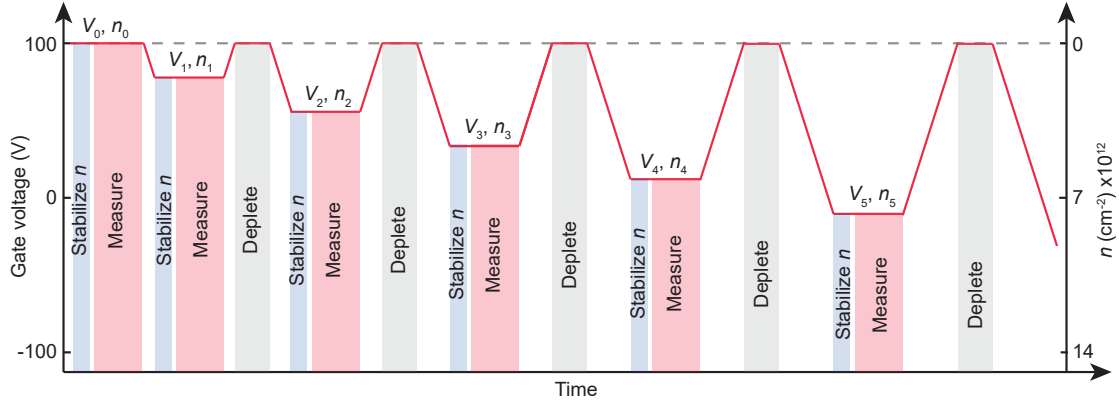


Figure F.1. The gatesweep procedure. In order to circumvent issues stemming from the photo-doping effect, the sample is always depleted before electrons are injected. In this way, a given carrier density n_j is reached at a specific gate voltage V_j . The stabilise, measure and deplete durations were 20 s, 1,200 s, and 10 s, respectively.

electron density under the laser spot decreases with laser exposure time. This effect varies locally as it depends on the exact locations of the defects in the hBN and on the location of imperfections within the van der Waals heterostructure. The carrier density in the MoS₂ monolayer therefore varies locally after a long laser exposure, even within the size of the focused spot. In these experiments, very low laser powers are used. Nevertheless, even at these low powers, changes in the measured optical spectra occur on a slow time-scale of an hour on account of photo-doping. As the acquisition time needed to obtain a full dataset such as Figure 7.2 in Chapter 7 is around ten hours, the problem of the photo-doping must be addressed.

In order to circumvent the problem of photo-doping, we sweep our gate voltage in device 1 in a particular way, as depicted in Figure F.1. The MoS₂ is always depleted after measuring at one density and before measuring at the next. This reinitialisation of the charge state of the monolayer is important as the measurement time at a specific electron density is then shorter than the time scale of the photo-doping effect. For device 2, we found that there is no big photo-doping effect for low powers. Hence, measurements on device 2 were done without the procedure described in Figure F.1.

F.2 Additional photoluminescence data

Here, additional PL data obtained on the monolayer MoS₂ device 1 are presented. We show colour-maps of the PL in the absence of magnetic field, $B_z = 0.00$ T, and at $T = 1.6$ K; and at a magnetic field of $B_z = 9.00$ T and at $T = 30$ K.

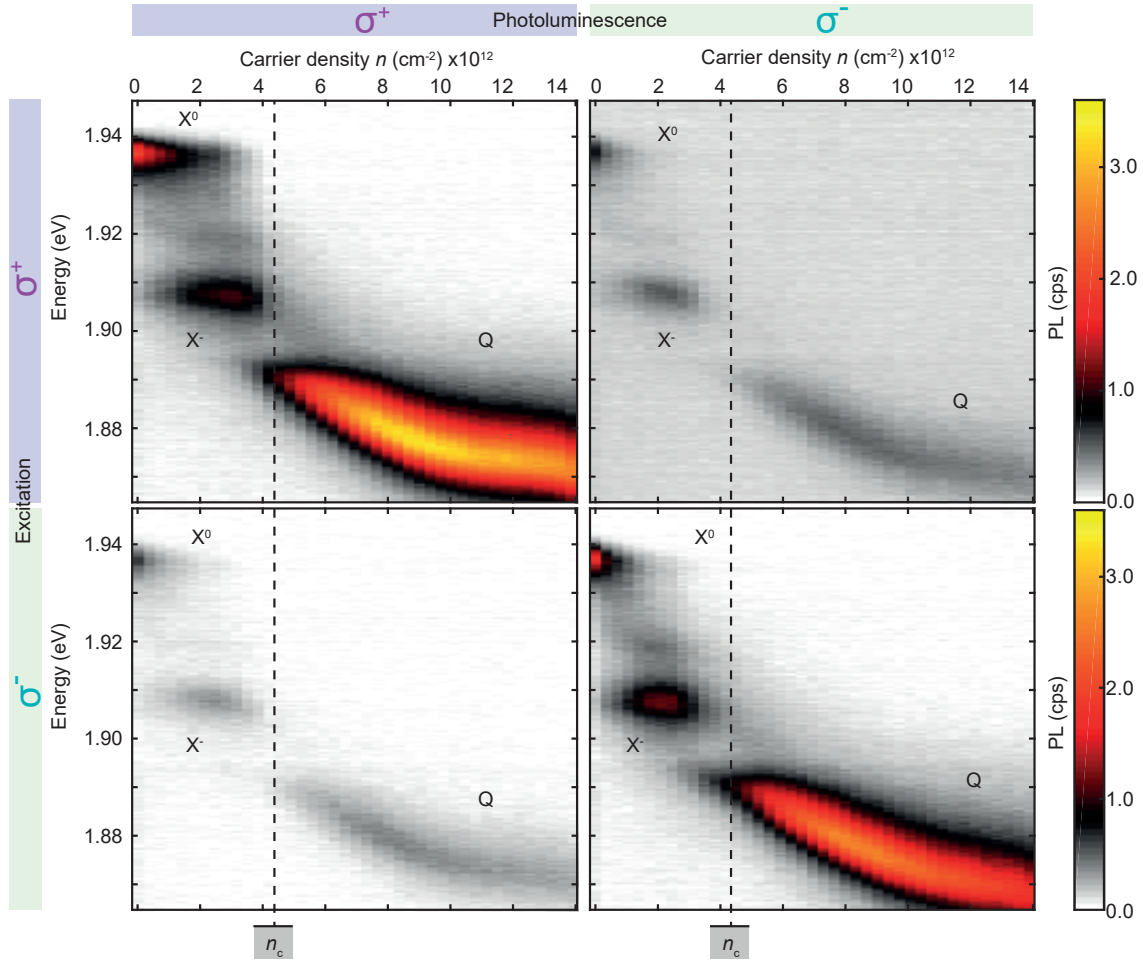


Figure F.2. Photoluminescence of the gated MoS₂ at zero magnetic field and temperature $T = 1.6$ K.

F.2.1 Photoluminescence without an applied magnetic field

Figure 7.2 in Chapter 7 presents colour-maps of the PL as a function of the electron concentration at an external magnetic field of $B_z = 9.00$ T and at a temperature of $T = 1.6$ K. In Figure F.2, we show PL from the same device, but at $B_z = 0.00$ T and $T = 1.6$ K. No hints of a broken-symmetry phase can be detected in the absence of magnetic field, as is also the case in the absorption data [Roc19]. However, even at $B_z = 0.00$ T, the PL energy jumps abruptly by 15 meV at the electron density $n_c = 3.0 \times 10^{12} \text{ cm}^{-2}$, as at $B_z = 9.00$ T. This similarity in the PL at $B_z = 0.00$ T with respect to the PL at $B_z = 9.00$ T can be understood in terms of fluctuations. In the absence of a magnetic field, the spin-up and the spin-down polarised states in the ferromagnetic phase are degenerate. Fluctuations of the sign of the magnetisation on length scales smaller than the focus of our laser spot and on time scales smaller than the integration time of the experiment prevent us from detecting one of these phases. Both spin-up and spin-down phases contribute equally

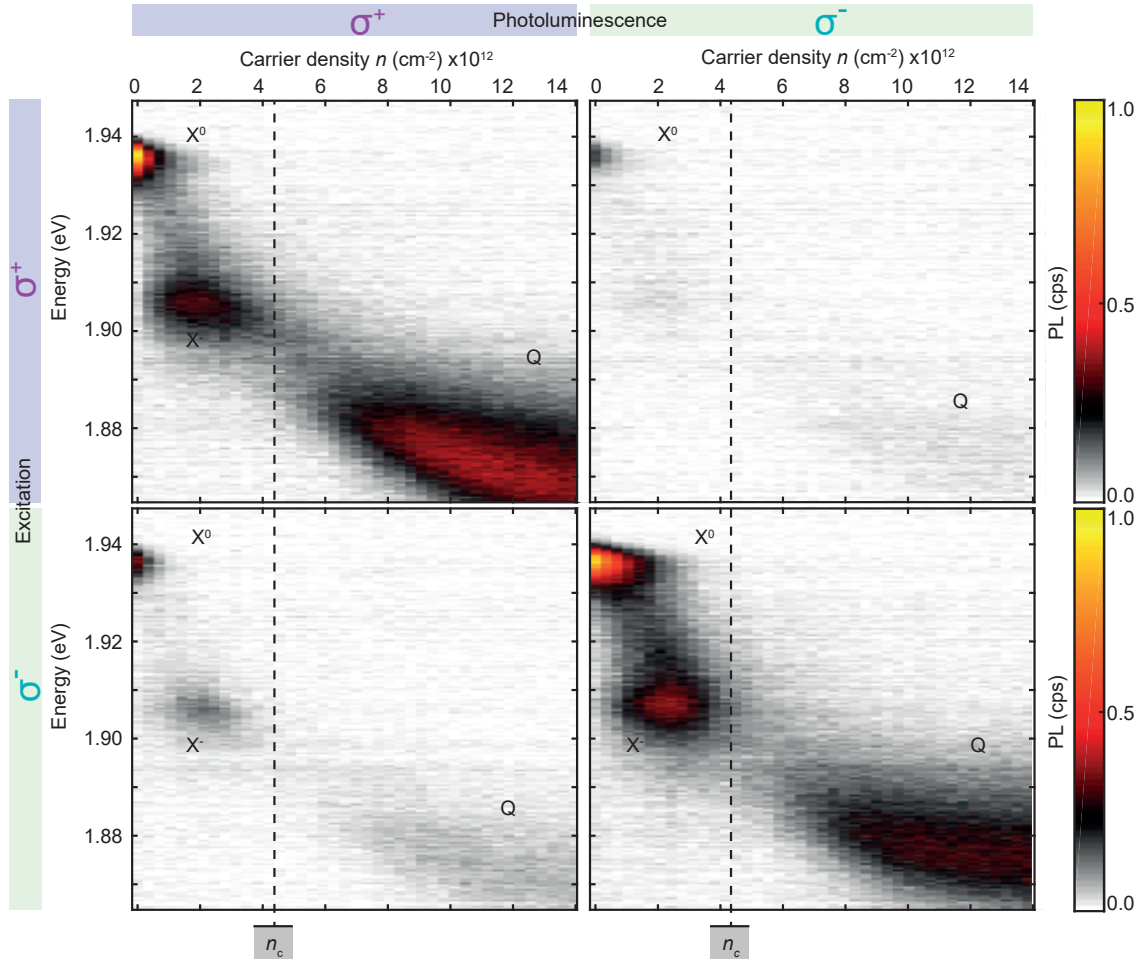


Figure F.3. Photoluminescence of the gated MoS₂ at magnetic field $B_z = 9.00$ T and temperature $T = 30$ K.

to the PL signal. Nevertheless, there is an abrupt change in both E_{PL} and $E_{\text{PL}} - E_{\text{A}}$ at the critical density. This tells us that at $B_z = 0.00$ T and $T = 1.6$ K there is still a change in spin ordering at the critical density, n_c . For $n < n_c$, there are strong correlations between one spin and the next at each moment in time; for $n > n_c$ these correlations disappear.

F.2.2 Photoluminescence at elevated temperature

Figure F.3 shows the PL data from monolayer MoS₂ device 1, at $B_z = 9.00$ T but at an elevated temperature of $T = 30$ K. The contrast between the two collection polarisations is less pronounced than that obtained at lower temperature ($T = 1.6$ K, Figure 7.2 in Chapter 7). The decrease in polarisation contrast was also observed on absorption data in monolayer MoS₂ [Roc19]. However, at $T = 30$ K as at $T = 1.6$ K, a pronounced jump of 15 meV is also observed in the PL on increasing the electron density (Figure F.3). In the light of fluctuations, as discussed in Section F.2.1, the decrease in circular dichroism without

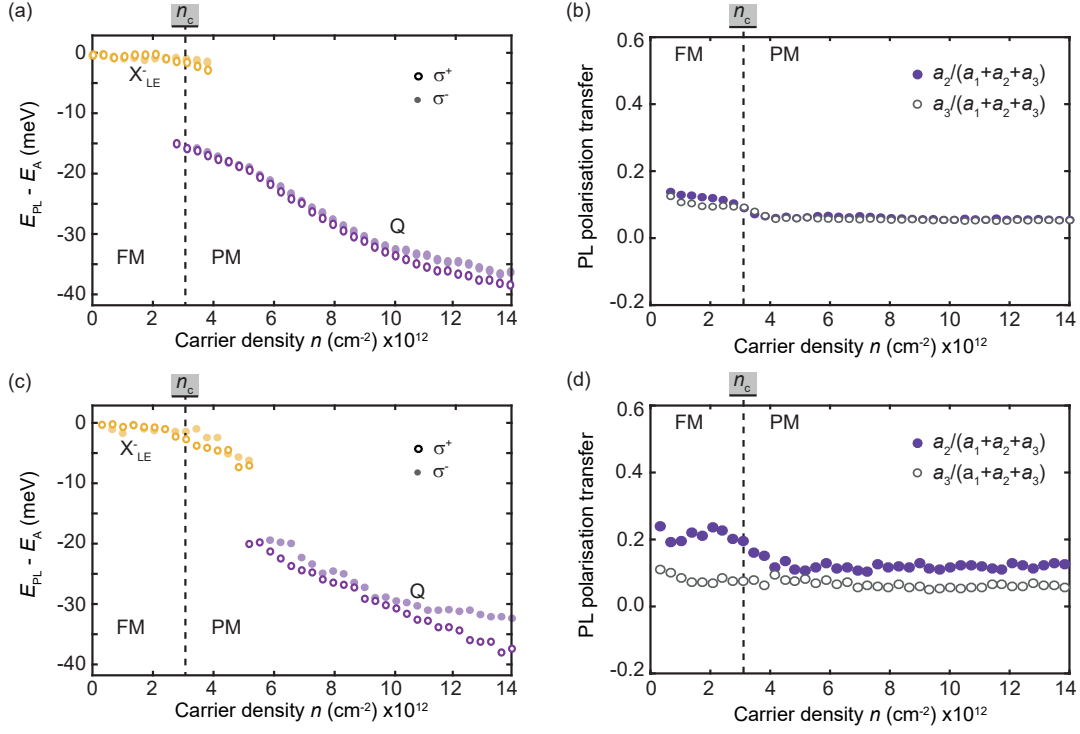


Figure F.4. (a) $E_{\text{PL}} - E_{\text{A}}$, (b) PL polarisation transfer, at $B_z = 0.00$ T and $T = 1.6$ K. (c) $E_{\text{PL}} - E_{\text{A}}$, (d) PL polarisation transfer, at $B_z = 9.00$ T and $T = 30$ K.

a deep change in the optical spectrum is understood in terms of fluctuations. Application of a magnetic field $B_z = 9.00$ T at $T = 1.6$ K stabilises the spin in the ferromagnetic phase: fluctuations from one spin-state to the other become rare. At $B_z = 9.00$ T but at $T = 30$ K, there are thermally driven fluctuations from one spin-state to the other. Nevertheless, the PL spectrum tells us that the phase transition still exists: there are strong local spin-correlations for $n < n_c$; but no spin-correlations for $n > n_c$. We anticipate that application of a larger magnetic field would stabilise the spin in the ferromagnetic phase for $n > n_c$.

Both data-sets ($B_z = 0.00$ T, $T = 1.6$ K; $B_z = 9.00$ T, $T = 30$ K) can be analysed in the same way as the $B_z = 9.00$ T, $T = 1.6$ K data-set, i.e. in terms of $E_{\text{PL}} - E_{\text{A}}$ and the PL polarisation transfer. The results are shown in Figure F.4.

F.2.3 Absorption measurement

The absorption measurements were carried out as in Roch et al. [Roc19]. The differential reflectivity is recorded using extremely weak, broadband illumination. The optical susceptibility is determined from the differential reflectivity. The trion and Q-peak spectral positions were determined by fitting the spectral resonances to a Lorentzian function. This procedure determines the energy of the absorption resonance, E_{A} .

Bibliography

- [Aiv15] G. Aivazian, Z. Gong, A. M. Jones, R.-L. Chu, J. Yan, D. G. Mandrus, C. Zhang, D. Cobden, W. Yao, X. Xu, *Magnetic control of valley pseudospin in monolayer WSe₂*, Nat. Phys. **11**, 148–152 (2015) (Cited on pages [21](#) and [22](#).)
- [Aja17] O. A. Ajayi, J. V. Ardelean, G. D. Shepard, J. Wang, A. Antony, T. Taniguchi, K. Watanabe, T. F. Heniz, S. Strauf, X.-Y. Zhu, C. Hone, James, *Approaching the intrinsic photoluminescence linewidth in transition metal dichalcogenide monolayers*, 2D Mater. **4**, 031011 (2017) (Cited on page [125](#).)
- [Aka15] R. Akashi, M. Ochi, S. Bordács, R. Suzuki, Y. Tokura, Y. Iwasa, R. Arita, *Two-Dimensional Valley Electrons and Excitons in Noncentrosymmetric 3R MoS₂*, Phys. Rev. Applied **4**, 014002 (2015) (Cited on page [159](#).)
- [Ald13] J. S. Alden, A. W. Tsen, P. Y. Huang, R. Hovden, L. Brown, J. Park, D. A. Muller, P. L. McEuen, *Strain solitons and topological defects in bilayer graphene*, PNAS **110**, 11 256–11 260 (2013) (Cited on page [19](#).)
- [Ale90] A. Alexandrou, J. A. Kash, E. E. Mendez, M. Zachau, J. M. Hong, T. Fukuzawa, Y. Hase, *Electric-field effects on exciton lifetimes in symmetric coupled GaAs/Al_{0.3}Ga_{0.7}As double quantum wells*, Phys. Rev. B **42**, 9225–9228 (1990) (Cited on page [21](#).)
- [Ale19] E. M. Alexeev, D. A. Ruiz-Tijerina, M. Danovich, M. J. Hamer, D. J. Terry, P. K. Nayak, S. Ahn, S. Pak, J. Lee, J. I. Sohn, M. R. Molas, M. Koperski, K. Watanabe, T. Taniguchi, K. S. Novoselov, R. V. Gorbachev, H. S. Shin, V. I. Fal’ko, A. I. Tartakovskii, *Resonantly hybridized excitons in moiré superlattices in van der Waals heterostructures*, Nature **567**, 81–86 (2019) (Cited on pages [12](#), [18](#), [104](#), and [121](#).)
- [Ale20] E. M. Alexeev, N. Mullin, P. Ares, H. Nevison-Andrews, O. Skrypka, T. Godde, A. Kozikov, L. Hague, Y. Wang, K. S. Novoselov, L. Fumagalli, J. K. Hobbs, A. I. Tartakovskii, *Emergence of Highly Linearly Polarized Interlayer Exciton Emission in MoSe₂/WSe₂ Heterobilayers with Transfer-Induced Layer Corrugation*, ACS Nano **14**, 11 110–11 119 (2020) (Cited on pages [55](#), [60](#), and [61](#).)
- [And15] P. Andreakou, S. Cronenberger, D. Scalbert, A. Nalitov, N. A. Gippius, A. V. Kavokin, M. Nawrocki, J. R. Leonard, L. V. Butov, K. L. Campman, A. C. Gossard, M. Vladimirova, *Nonlinear optical spectroscopy of indirect excitons in coupled quantum wells*, Phys. Rev. B **91**, 125437 (2015) (Cited on page [104](#).)
- [And21] T. I. Andersen, G. Scuri, A. Sushko, K. De Greve, J. Sung, Y. Zhou, D. S. Wild, R. J. Gelly, H. Heo, D. Bérubé, A. Y. Joe, L. A. Jauregui, K. Watanabe, T. Taniguchi, P. Kim, H. Park, M. D. Lukin, *Excitons in a reconstructed moiré potential in twisted WSe₂/WSe₂ homobilayers*, Nat. Mater. **20**, 480–487 (2021) (Cited on pages [19](#), [20](#), and [54](#).)
- [Aro17] A. Arora, M. Drüppel, R. Schmidt, T. Deilmann, R. Schneider, M. R. Molas, P. Marauhn, S. Michaelis de Vasconcellos, M. Potemski, M. Rohlfing, R. Brats-

- chitsch, *Interlayer excitons in a bulk van der Waals semiconductor*, Nat. Commun. **8**, 639 (2017) (Cited on pages 24, 92, and 93.)
- [Aro18] A. Arora, T. Deilmann, P. Marauhn, M. Drüppel, R. Schneider, M. R. Molas, D. Vaclavkova, S. M. d. Vasconcellos, M. Rohlfing, M. Potemski, R. Bratschitsch, *Valley-contrasting optics of interlayer excitons in Mo- and W-based bulk transition metal dichalcogenides*, Nanoscale **10**, 15 571–15 577 (2018) (Cited on page 92.)
- [Aro21] A. Arora, *Magneto-optics of layered two-dimensional semiconductors and heterostructures: Progress and prospects*, J. Appl. Phys. **129**, 120 902 (2021) (Cited on page 23.)
- [Bac17] P. Back, M. Sidler, O. Cotlet, A. Srivastava, N. Takemura, M. Kroner, A. Imamoğlu, *Giant Paramagnetism-Induced Valley Polarization of Electrons in Charge-Tunable Monolayer MoSe₂*, Phys. Rev. Lett. **118**, 237 404 (2017) (Cited on pages 43, 45, 56, 125, and 127.)
- [Bac18] P. Back, S. Zeytinoglu, A. Ijaz, M. Kroner, A. Imamoğlu, *Realization of an Electrically Tunable Narrow-Bandwidth Atomically Thin Mirror Using Monolayer MoSe₂*, Phys. Rev. Lett. **120**, 037 401 (2018) (Cited on pages 47, 88, and 155.)
- [Bae20] H. Baek, M. Brotons-Gisbert, Z. X. Koong, A. Campbell, M. Rambach, K. Watanabe, T. Taniguchi, B. D. Gerardot, *Highly energy-tunable quantum light from moiré-trapped excitons*, Sci. Adv. **6**, eaba8526 (2020) (Cited on pages 18, 55, 62, and 85.)
- [Bae21] H. Baek, M. Brotons-Gisbert, A. Campbell, V. Vitale, J. Lischner, K. Watanabe, T. Taniguchi, B. D. Gerardot, *Optical read-out of Coulomb staircases in a moiré superlattice via trapped interlayer trions*, Nat. Nanotechnol. **16**, 1237–1243 (2021) (Cited on page 84.)
- [Bai20] Y. Bai, L. Zhou, J. Wang, W. Wu, L. J. McGilly, D. Halbertal, C. F. B. Lo, F. Liu, J. Ardelean, P. Rivera, N. R. Finney, X.-C. Yang, D. N. Basov, W. Yao, X. Xu, J. Hone, A. N. Pasupathy, X.-Y. Zhu, *Excitons in strain-induced one-dimensional moiré potentials at transition metal dichalcogenide heterojunctions*, Nat. Mater. **19**, 1068–1073 (2020) (Cited on pages 55, 61, 62, 67, and 85.)
- [Bar22] E. Barré, O. Karni, E. Liu, A. L. O’Beirne, X. Chen, H. B. Ribeiro, L. Yu, B. Kim, K. Watanabe, T. Taniguchi, K. Barmak, C. H. Lui, S. Refaely-Abramson, F. H. da Jornada, T. F. Heinz, *Optical absorption of interlayer excitons in transition-metal dichalcogenide heterostructures*, Science **376**, 406–410 (2022) (Cited on pages 46, 53, 60, 61, 62, 63, 68, 69, 73, 81, and 84.)
- [Bel99] D. Belitz, T. R. Kirkpatrick, T. Vojta, *First Order Transitions and Multicritical Points in Weak Itinerant Ferromagnets*, Phys. Rev. Lett. **82**, 4707–4710 (1999) (Cited on pages 124 and 129.)
- [Ben21] M. Benelajla, E. Kammann, B. Urbaszek, K. Karrai, *Physical Origins of Extreme Cross-Polarization Extinction in Confocal Microscopy*, Phys. Rev. X **11**, 021 007 (2021) (Cited on page 154.)
- [BG21] M. Brotons-Gisbert, H. Baek, A. Campbell, K. Watanabe, T. Taniguchi, B. D. Gerardot, *Moiré-Trapped Interlayer Trions in a Charge-Tunable WSe₂ / MoSe₂ Heterobilayer*, Phys. Rev. X **11**, 031 033 (2021) (Cited on pages 25 and 84.)
- [Bla94] E. Blackwood, M. J. Snelling, R. T. Harley, S. R. Andrews, C. T. B. Foxon, *Exchange interaction of excitons in GaAs heterostructures*, Phys. Rev. B **50**, 14 246–14 254 (1994) (Cited on page 78.)

- [Blo29] F. Bloch, *Note to the Electron theory of Ferromagnetism and Electrical Conductivity.*, Z. Phys. **57**, 545–555 (1929) (Cited on page 124.)
- [Blo94] P. E. Bloechl, *Projector augmented-wave method*, Phys. Rev. B **50**, 17 953 (1994) (Cited on pages 156 and 179.)
- [Bra16] M. Brando, D. Belitz, F. M. Grosche, T. R. Kirkpatrick, *Metallic quantum ferromagnets*, Rev. Mod. Phys. **88**, 025 006 (2016) (Cited on page 124.)
- [Bra18] J. E. H. Braz, B. Amorim, E. V. Castro, *Valley-polarized magnetic state in hole-doped monolayers of transition-metal dichalcogenides*, Phys. Rev. B **98**, 161 406 (2018) (Cited on page 129.)
- [Bre20a] S. Brem, K.-Q. Lin, R. Gillen, J. M. Bauer, J. Maultzsch, J. M. Lupton, E. Malic, *Hybridized intervalley moiré excitons and flat bands in twisted WSe₂ bilayers*, Nanoscale **12**, 11 088–11 094 (2020) (Cited on pages 16 and 18.)
- [Bre20b] S. Brem, C. Linderälv, P. Erhart, E. Malic, *Tunable Phases of Moiré Excitons in van der Waals Heterostructures*, Nano Lett. **20**, 8534–8540 (2020) (Cited on pages 17, 18, 63, 77, and 83.)
- [But99] L. V. Butov, A. A. Shashkin, V. T. Dolgoplov, K. L. Campman, A. C. Gossard, *Magneto-optics of the spatially separated electron and hole layers in GaAs/Al_xGa_{1-x}As coupled quantum wells*, Phys. Rev. B **60**, 8753–8758 (1999) (Cited on page 66.)
- [Cad17] F. Cadiz, E. Courtade, C. Robert, G. Wang, Y. Shen, H. Cai, T. Taniguchi, K. Watanabe, H. Carrere, D. Lagarde, M. Manca, T. Amand, P. Renucci, S. Tongay, X. Marie, B. Urbaszek, *Excitonic Linewidth Approaching the Homogeneous Limit in MoS₂-Based van der Waals Heterostructures*, Phys. Rev. X **7**, 021 026 (2017) (Cited on pages 30, 125, and 131.)
- [Cal18] E. V. Calman, M. M. Fogler, L. V. Butov, S. Hu, A. Mishchenko, A. K. Geim, *Indirect excitons in van der Waals heterostructures at room temperature*, Nat. Commun. **9**, 1895 (2018) (Cited on page 88.)
- [Cal20] E. V. Calman, L. H. Fowler-Gerace, D. J. Choksy, L. V. Butov, D. E. Nikonov, I. A. Young, S. Hu, A. Mishchenko, A. K. Geim, *Indirect Excitons and Trions in MoSe₂/WSe₂ van der Waals Heterostructures*, Nano Lett. **20**, 1869–1875 (2020) (Cited on pages 55 and 60.)
- [Cao12] T. Cao, G. Wang, W. Han, H. Ye, C. Zhu, J. Shi, Q. Niu, P. Tan, E. Wang, B. Liu, J. Feng, *Valley-selective circular dichroism of monolayer molybdenum disulphide*, Nat. Commun. **3** (2012) (Cited on pages 7, 8, 131, and 133.)
- [Cao18a] Y. Cao, V. Fatemi, A. Demir, S. Fang, S. L. Tomarken, J. Y. Luo, J. D. Sanchez-Yamagishi, K. Watanabe, T. Taniguchi, E. Kaxiras, R. C. Ashoori, P. Jarillo-Herrero, *Correlated insulator behaviour at half-filling in magic-angle graphene superlattices*, Nature **556**, 80–84 (2018) (Cited on page 25.)
- [Cao18b] Y. Cao, V. Fatemi, S. Fang, K. Watanabe, T. Taniguchi, E. Kaxiras, P. Jarillo-Herrero, *Unconventional superconductivity in magic-angle graphene superlattices*, Nature **556**, 43–50 (2018) (Cited on page 25.)
- [Car18] S. Carr, D. Massatt, S. B. Torrisi, P. Cazeaux, M. Luskin, E. Kaxiras, *Relaxation and domain formation in incommensurate two-dimensional heterostructures*, Phys. Rev. B **98**, 224 102 (2018) (Cited on pages 19 and 20.)
- [Car19] F. Carrascoso, D.-Y. Lin, R. Frisenda, A. Castellanos-Gomez, *Biaxial strain*

- tuning of interlayer excitons in bilayer MoS₂*, J. Phys. Mater. **3**, 015 003 (2019) (Cited on pages 12 and 88.)
- [Cas16] L. Casparis, T. Larsen, M. Olsen, F. Kuemmeth, P. Krogstrup, J. Nygård, K. Petersson, C. Marcus, *Gatemon Benchmarking and Two-Qubit Operations*, Phys. Rev. Lett. **116**, 150 505 (2016) (Cited on page 121.)
- [Cav18] L. S. R. Cavalcante, D. R. da Costa, G. A. Farias, D. R. Reichman, A. Chaves, *Stark shift of excitons and trions in two-dimensional materials*, Phys. Rev. B **98**, 245 309 (2018) (Cited on page 21.)
- [Ceb14] F. Ceballos, M. Z. Bellus, H.-Y. Chiu, H. Zhao, *Ultrafast Charge Separation and Indirect Exciton Formation in a MoS₂-MoSe₂ van der Waals Heterostructure*, ACS Nano **8**, 12 717–12 724 (2014) (Cited on pages 12 and 79.)
- [Che12] T. Cheiwchanchamnangij, W. R. L. Lambrecht, *Quasiparticle band structure calculation of monolayer, bilayer, and bulk MoS₂*, Phys. Rev. B **85**, 205 302 (2012) (Cited on page 7.)
- [Che14] A. Chernikov, T. C. Berkelbach, H. M. Hill, A. Rigosi, Y. Li, O. B. Aslan, D. R. Reichman, M. S. Hybertsen, T. F. Heinz, *Exciton Binding Energy and Nonhydrogenic Rydberg Series in Monolayer WS₂*, Phys. Rev. Lett. **113**, 076 802 (2014) (Cited on pages 11, 43, 88, 104, and 127.)
- [Che16] H. Chen, X. Wen, J. Zhang, T. Wu, Y. Gong, X. Zhang, J. Yuan, C. Yi, J. Lou, P. M. Ajayan, W. Zhuang, G. Zhang, J. Zheng, *Ultrafast formation of interlayer hot excitons in atomically thin MoS₂/WS₂ heterostructures*, Nat. Commun. **7**, 12 512 (2016) (Cited on page 12.)
- [Cho20] J. Choi, W.-T. Hsu, L.-S. Lu, L. Sun, H.-Y. Cheng, M.-H. Lee, J. Quan, K. Tran, C.-Y. Wang, M. Staab, K. Jones, T. Taniguchi, K. Watanabe, M.-W. Chu, S. Gwo, S. Kim, C.-K. Shih, X. Li, W.-H. Chang, *Moiré potential impedes interlayer exciton diffusion in van der Waals heterostructures*, Sci. Adv. **6**, eaba8866 (2020) (Cited on pages 17, 21, 54, and 66.)
- [Chu04] A. V. Chubukov, C. Pépin, J. Rech, *Instability of the Quantum-Critical Point of Itinerant Ferromagnets*, Phys. Rev. Lett. **92**, 147 003 (2004) (Cited on pages 124 and 129.)
- [Cia19] A. Ciarrocchi, D. Unuchek, A. Avsar, K. Watanabe, T. Taniguchi, A. Kis, *Polarization switching and electrical control of interlayer excitons in two-dimensional van der Waals heterostructures*, Nat. Photonics **13**, 131 (2019) (Cited on pages 13, 55, 60, 67, 73, and 76.)
- [Ciu98] C. Ciuti, V. Savona, C. Piermarocchi, A. Quattropani, P. Schwendimann, *Role of the exchange of carriers in elastic exciton-exciton scattering in quantum wells*, Phys. Rev. B **58**, 7926–7933 (1998) (Cited on page 104.)
- [Cri12] P. Cristofolini, G. Christmann, S. I. Tsintzos, G. Deligeorgis, G. Konstantinidis, Z. Hatzopoulos, P. G. Savvidis, J. J. Baumberg, *Coupling Quantum Tunneling with Cavity Photons*, Science **336**, 704–707 (2012) (Cited on page 102.)
- [Cro18] E. L. Crowell, M. G. Kuzyk, *Using excited states and degeneracies to enhance the electric polarizability and first hyperpolarizability*, J. Opt. Soc. Am. B **35**, 2412–2422 (2018) (Cited on page 70.)
- [CT05] C. Cohen-Tannoudji, B. Diu, F. Laloë, *Quantum Mechanics. Vol. 2* (Wiley, New York, 2005), ISBN 978-0-471-16435-7 (Cited on page 169.)

- [Dat22] B. Datta, M. Khatoniar, P. Deshmukh, F. Thouin, R. Bushati, S. De Liberato, S. K. Cohen, V. M. Menon, *Highly nonlinear dipolar exciton-polaritons in bilayer MoS₂*, Nat. Commun. **13**, 6341 (2022) (Cited on pages 120 and 140.)
- [Dea10] C. R. Dean, A. F. Young, I. Meric, C. Lee, L. Wang, S. Sorgenfrei, K. Watanabe, T. Taniguchi, P. Kim, K. L. Shepard, J. Hone, *Boron nitride substrates for high-quality graphene electronics*, Nat. Nanotechnol. **5**, 722–726 (2010) (Cited on page 30.)
- [Dei18] T. Deilmann, K. S. Thygesen, *Interlayer Excitons with Large Optical Amplitudes in Layered van der Waals Materials*, Nano Lett. **18**, 2984–2989 (2018) (Cited on pages 12, 88, 89, and 98.)
- [Del19] A. Delteil, T. Fink, A. Schade, S. Höfling, C. Schneider, A. İmamoğlu, *Towards polariton blockade of confined exciton-polaritons*, Nat. Mater. **18**, 219–222 (2019) (Cited on pages 21, 102, 104, 120, and 140.)
- [Die19] S. Dietl, L. Sigl, L. Sponfeldner, G. Gardner, M. Manfra, J. P. Kotthaus, U. Wurstbauer, A. W. Holleitner, *On the parabolicity of dipolar exciton traps and their population of excess charge carriers*, New J. Phys. **21**, 063 028 (2019) (Cited on page 21.)
- [Dru17] M. Drueppel, T. Deilmann, P. Krüger, M. Rohlfing, *Diversity of trion states and substrate effects in the optical properties of an MoS₂ monolayer*, Nat. Commun. **8**, 2117 (2017) (Cited on page 131.)
- [Efi17] D. K. Efimkin, A. H. MacDonald, *Many-body theory of trion absorption features in two-dimensional semiconductors*, Phys. Rev. B **95**, 035 417 (2017) (Cited on pages 11 and 126.)
- [Epp18] A. Epping, L. Banszerus, H. Guttinger, L. Kruckeberg, K. Watanabe, T. Taniguchi, F. Hassler, B. Beschoten, C. Stampfer, *Quantum transport through MoS₂ constrictions defined by photodoping*, J. Phys. Condens. Matter **30**, 205 001 (2018) (Cited on page 181.)
- [Erk21] D. Erkensten, S. Brem, E. Malic, *Exciton-exciton interaction in transition metal dichalcogenide monolayers and van der Waals heterostructures*, Phys. Rev. B **103**, 045 426 (2021) (Cited on page 104.)
- [Fan16] X. Fan, D. J. Singh, W. Zheng, *Valence Band Splitting on Multilayer MoS₂: Mixing of Spin-Orbit Coupling and Interlayer Coupling*, J. Phys. Chem. Lett. **7**, 2175–2181 (2016) (Cited on page 98.)
- [Fan19] H. Fang, B. Han, C. Robert, M. Semina, D. Lagarde, E. Courtade, T. Taniguchi, K. Watanabe, T. Amand, B. Urbaszek, M. Glazov, X. Marie, *Control of the Exciton Radiative Lifetime in van der Waals Heterostructures*, Phys. Rev. Lett. **123**, 067 401 (2019) (Cited on page 49.)
- [Fan21] P. Fan, Z.-G. Zhu, *Magnetic order transition in monolayer MoS₂ induced by strong intervalley correlation*, Phys. Rev. B **104**, 195 417 (2021) (Cited on page 128.)
- [Fer90] R. Ferreira, C. Delalande, H. W. Liu, G. Bastard, B. Etienne, J. F. Palmier, *Resonances in the excitonic transfer in biased double quantum wells*, Phys. Rev. B **42**, 9170–9173 (1990) (Cited on page 104.)
- [Fin95] G. Finkelstein, H. Shtrikman, I. Bar-Joseph, *Optical Spectroscopy of a Two-Dimensional Electron Gas near the Metal-Insulator Transition*, Phys. Rev. Lett. **74**, 976–979 (1995) (Cited on pages 124 and 125.)

- [Fog14] M. M. Fogler, L. V. Butov, K. S. Novoselov, *High-temperature superfluidity with indirect excitons in van der Waals heterostructures*, Nat. Commun. **5**, 4555 (2014) (Cited on page 54.)
- [Fox91] A. M. Fox, D. A. B. Miller, G. Livescu, J. E. Cunningham, W. Y. Jan, *Excitonic effects in coupled quantum wells*, Phys. Rev. B **44**, 6231–6242 (1991) (Cited on page 104.)
- [Fox10] M. Fox, *Optical Properties of Solids* (Oxford University Press, 2010), ISBN 9780199573370 (Cited on pages 10 and 11.)
- [Fre31] J. Frenkel, *On the Transformation of light into Heat in Solids. I*, Phys. Rev. **37**, 17–44 (1931) (Cited on page 9.)
- [Fri14] M. Frimmer, L. Novotny, *The classical Bloch equations*, Am. J. Phys. **82**, 947–954 (2014) (Cited on page 162.)
- [Fö19] M. Förg, L. Colombier, R. K. Patel, J. Lindlau, A. D. Mohite, H. Yamaguchi, M. M. Glazov, D. Hunger, A. Högele, *Cavity-control of interlayer excitons in van der Waals heterostructures*, Nat. Commun. **10**, 3697 (2019) (Cited on pages 13, 46, and 88.)
- [Fö21] M. Förg, A. S. Baimuratov, S. Y. Kruchinin, I. A. Vovk, J. Scherzer, J. Förste, V. Funk, K. Watanabe, T. Taniguchi, A. Högele, *Moiré excitons in MoSe₂-WSe₂ heterobilayers and heterotrilayers*, Nat. Commun. **12**, 1656 (2021) (Cited on pages 13, 24, 55, 60, 76, 80, 81, and 82.)
- [Gei13] A. K. Geim, I. V. Grigorieva, *Van der Waals heterostructures*, Nature **499**, 419–425 (2013) (Cited on page 1.)
- [Ger19] I. C. Gerber, E. Courtade, S. Shree, C. Robert, T. Taniguchi, K. Watanabe, A. Balocchi, P. Renucci, D. Lagarde, X. Marie, B. Urbaszek, *Interlayer excitons in bilayer MoS₂ with strong oscillator strength up to room temperature*, Phys. Rev. B **99**, 035443 (2019) (Cited on pages 12, 13, 88, 89, 90, 98, 104, 111, 113, and 159.)
- [Gil18] R. Gillen, J. Maultzsch, *Interlayer excitons in MoSe₂/WSe₂ heterostructures from first principles*, Phys. Rev. B **97**, 165306 (2018) (Cited on pages 18, 60, and 63.)
- [Gla20] M. M. Glazov, *Optical properties of charged excitons in two-dimensional semiconductors*, J. Chem. Phys. **153**, 034703 (2020) (Cited on page 11.)
- [Gon13] Z. Gong, G.-B. Liu, H. Yu, D. Xiao, X. Cui, X. Xu, W. Yao, *Magnetoelectric effects and valley-controlled spin quantum gates in transition metal dichalcogenide bilayers*, Nat. Commun. **4**, 2053 (2013) (Cited on pages 88, 92, and 159.)
- [Gor11] R. V. Gorbachev, I. Riaz, R. R. Nair, R. Jalil, L. Britnell, B. D. Belle, E. W. Hill, K. S. Novoselov, K. Watanabe, T. Taniguchi, A. K. Geim, P. Blake, *Hunting for Monolayer Boron Nitride: Optical and Raman Signatures*, Small **7**, 465–468 (2011) (Cited on page 28.)
- [Gor19] M. Goryca, J. Li, A. V. Stier, T. Taniguchi, K. Watanabe, E. Courtade, S. Shree, C. Robert, B. Urbaszek, X. Marie, S. A. Crooker, *Revealing exciton masses and dielectric properties of monolayer semiconductors with high magnetic fields*, Nat. Commun. **10**, 4172 (2019) (Cited on pages 9 and 24.)
- [Gri10] S. Grimme, J. Antony, S. Ehrlich, H. Krieg, *A consistent and accurate ab initio parametrization of density functional dispersion correction (DFT-D) for the*

- 94 elements H-Pu*, J. Chem. Phys. **132**, 154104–19 (2010) (Cited on pages 156 and 179.)
- [Gro14] R. Gross, A. Marx, *Festkörperphysik* (De Gruyter Oldenbourg, München, 2014), ISBN 978-3-486-71294-0 (Cited on page 9.)
- [Grz21] M. Grzeszczyk, K. Olkowska-Pucko, K. Nogajewski, K. Watanabe, T. Taniguchi, P. Kossacki, A. Babiński, M. R. Molas, *Exposing the trion's fine structure by controlling the carrier concentration in hBN-encapsulated MoS₂*, Nanoscale **13**, 18 726–18 733 (2021) (Cited on page 11.)
- [Guo19] L. Guo, M. Wu, T. Cao, D. M. Monahan, Y.-H. Lee, S. G. Louie, G. R. Fleming, *Exchange-driven intravalley mixing of excitons in monolayer transition metal dichalcogenides*, Nat. Phys. **15**, 228–232 (2019) (Cited on pages 119 and 120.)
- [Guo20] H. Guo, X. Zhang, G. Lu, *Shedding light on moiré excitons: A first-principles perspective*, Sci. Adv. **6**, eabc5638 (2020) (Cited on pages 17 and 63.)
- [Gus18] M. V. Gustafsson, M. Yankowitz, C. Forsythe, D. Rhodes, K. Watanabe, T. Taniguchi, J. Hone, X. Zhu, C. R. Dean, *Ambipolar Landau levels and strong band-selective carrier interactions in monolayer WSe₂*, Nat. Mater. **17**, 411–415 (2018) (Cited on page 82.)
- [Hal21] D. Halbertal, N. R. Finney, S. S. Sunku, A. Kerelsky, C. Rubio-Verdú, S. Shabani, L. Xian, S. Carr, S. Chen, C. Zhang, L. Wang, D. Gonzalez-Acevedo, A. S. McLeod, D. Rhodes, K. Watanabe, T. Taniguchi, E. Kaxiras, C. R. Dean, J. C. Hone, A. N. Pasupathy, D. M. Kennes, A. Rubio, D. N. Basov, *Moiré metrology of energy landscapes in van der Waals heterostructures*, Nat. Commun. **12**, 242 (2021) (Cited on pages 19 and 54.)
- [Han79] W. Hanke, L. J. Sham, *Many-Particle Effects in the optical Excitations of a semiconductor*, Phys. Rev. Lett. **43**, 387 (1979) (Cited on pages 156 and 179.)
- [Han18] A. T. Hanbicki, H.-J. Chuang, M. R. Rosenberger, C. S. Hellberg, S. V. Sivaram, K. M. McCreary, I. I. Mazin, B. T. Jonker, *Double Indirect Interlayer Exciton in a MoSe₂ /WSe₂ van der Waals Heterostructure*, ACS Nano **12**, 4719–4726 (2018) (Cited on pages 13, 60, 63, and 68.)
- [Hao22] K. Hao, R. Shreiner, A. Kindseth, A. A. High, *Optically controllable magnetism in atomically thin semiconductors*, Sci. Adv. **8**, eabq7650 (2022) (Cited on pages 130, 131, 136, 138, and 141.)
- [Hat15] Y. Hattori, T. Taniguchi, K. Watanabe, K. Nagashio, *Layer-by-Layer Dielectric Breakdown of Hexagonal Boron Nitride*, ACS Nano **9**, 916–921 (2015) (Cited on page 40.)
- [Hau09] H. Haug, S. W. Koch, *Quantum Theory of the Optical and Electronic Properties of Semiconductors* (World Scientific, 2009) (Cited on pages 107 and 170.)
- [Haw91] P. Hawrylak, *Optical properties of a two-dimensional electron gas: Evolution of spectra from excitons to Fermi-edge singularities*, Phys. Rev. B **44**, 3821 (1991) (Cited on pages 125 and 126.)
- [He14] J. He, K. Hummer, C. Franchini, *Stacking effects on the electronic and optical properties of bilayer transition metal dichalcogenides MoS₂, MoSe₂, WS₂, and WSe₂*, Phys. Rev. B **89**, 075 409 (2014) (Cited on pages 68 and 73.)
- [Hey04] J. Heyd, G. E. Scuseria, *Assessment and validation of a screened Coulomb hybrid density functional*, J. Chem. Phys. **120**, 7274 (2004) (Cited on pages 156 and 179.)

- [Hey05] J. Heyd, J. E. Peralta, G. E. Scuseria, R. L. Martin, *Energy band gaps and lattice parameters evaluated with the Heyd-Scuseria-Ernzerhof screened hybrid functional*, J. Chem. Phys. **123**, 174 101 (2005) (Cited on pages 156 and 179.)
- [Hol20] J. Holler, S. Meier, M. Kempf, P. Nagler, K. Watanabe, T. Taniguchi, T. Korn, C. Schüller, *Low-frequency Raman scattering in WSe₂-MoSe₂ heterobilayers: Evidence for atomic reconstruction*, Appl. Phys. Lett. **117**, 013 104 (2020) (Cited on pages 20, 153, and 154.)
- [Hol22] J. Holler, M. Selig, M. Kempf, J. Zipfel, P. Nagler, M. Katzer, F. Katsch, M. V. Ballottin, A. A. Mitioglu, A. Chernikov, P. C. M. Christianen, C. Schüller, A. Knorr, T. Korn, *Interlayer exciton valley polarization dynamics in large magnetic fields*, Phys. Rev. B **105**, 085 303 (2022) (Cited on pages 60, 76, and 79.)
- [Hon14] X. Hong, J. Kim, S.-F. Shi, Y. Zhang, C. Jin, Y. Sun, S. Tongay, J. Wu, Y. Zhang, F. Wang, *Ultrafast charge transfer in atomically thin MoS₂/WS₂ heterostructures*, Nat. Nanotechnol. **9**, 682–686 (2014) (Cited on pages 12 and 79.)
- [Hor18] J. Horng, T. Stroucken, L. Zhang, E. Y. Paik, H. Deng, S. W. Koch, *Observation of interlayer excitons in MoSe₂ single crystals*, Phys. Rev. B **97**, 241 404 (2018) (Cited on page 92.)
- [Hos21] M. S. Hossain, T. Zhao, S. Pu, M. A. Mueed, M. K. Ma, K. A. Villegas Rosales, Y. J. Chung, L. N. Pfeiffer, K. W. West, K. W. Baldwin, J. K. Jain, M. Shayegan, *Bloch ferromagnetism of composite fermions*, Nat. Phys. **17**, 48–52 (2021) (Cited on page 124.)
- [Hsu14] W.-T. Hsu, Z.-A. Zhao, L.-J. Li, C.-H. Chen, M.-H. Chiu, P.-S. Chang, Y.-C. Chou, W.-H. Chang, *Second Harmonic Generation from Artificially Stacked Transition Metal Dichalcogenide Twisted Bilayers*, ACS Nano **8**, 2951–2958 (2014) (Cited on page 38.)
- [Hsu18] W.-T. Hsu, L.-S. Lu, P.-H. Wu, M.-H. Lee, P.-J. Chen, P.-Y. Wu, Y.-C. Chou, H.-T. Jeng, L.-J. Li, M.-W. Chu, W.-H. Chang, *Negative circular polarization emissions from WSe₂/MoSe₂ commensurate heterobilayers*, Nat. Commun. **9**, 1356 (2018) (Cited on pages 13 and 60.)
- [Hsu19] W.-T. Hsu, B.-H. Lin, L.-S. Lu, M.-H. Lee, M.-W. Chu, L.-J. Li, W. Yao, W.-H. Chang, C.-K. Shih, *Tailoring excitonic states of van der Waals bilayers through stacking configuration, band alignment, and valley spin*, Sci. Adv. **5**, eaax7407 (2019) (Cited on page 104.)
- [Hua00] V. Huard, R. T. Cox, K. Saminadayar, A. Arnoult, S. Tatarenko, *Bound States in Optical Absorption of Semiconductor Quantum Wells Containing a Two-Dimensional Electron Gas*, Phys. Rev. Lett. **84**, 187 (2000) (Cited on page 125.)
- [Hua20] Z. Huang, Y. Liu, K. Dini, Q. Tan, Z. Liu, H. Fang, J. Liu, T. Liew, W. Gao, *Robust Room Temperature Valley Hall Effect of Interlayer Excitons*, Nano Lett. **20**, 1345–1351 (2020) (Cited on page 12.)
- [Hua21] X. Huang, T. Wang, S. Miao, C. Wang, Z. Li, Z. Lian, T. Taniguchi, K. Watanabe, S. Okamoto, D. Xiao, S.-F. Shi, Y.-T. Cui, *Correlated insulating states at fractional fillings of the WS₂/WSe₂ moiré lattice*, Nat. Phys. **17**, 715–719 (2021) (Cited on pages 25 and 83.)
- [Hua22] D. Huang, J. Choi, C.-K. Shih, X. Li, *Excitons in semiconductor moiré su-*

- perlattices*, Nat. Nanotechnol. **17**, 227–238 (2022) (Cited on pages 15, 61, and 85.)
- [Ivc05] E. L. Ivchenko, *Optical Spectroscopy of Semiconductor Nanostructures* (Alpha Science, Harrow, UK, 2005), ISBN 1842651501 (Cited on pages 46 and 49.)
- [Jak16] T. Jakubczyk, V. Delmonte, M. Koperski, K. Nogajewski, C. Faugeras, W. Langbein, M. Potemski, J. Kasprzak, *Radiatively Limited Dephasing and Exciton Dynamics in MoSe₂ Monolayers Revealed with Four-Wave Mixing Microscopy*, Nano Lett. **16**, 5333–5339 (2016) (Cited on pages 104 and 140.)
- [Jau19] L. A. Jauregui, A. Y. Joe, K. Pistunova, D. S. Wild, A. A. High, Y. Zhou, G. Scuri, K. D. Greve, A. Sushko, C.-H. Yu, T. Taniguchi, K. Watanabe, D. J. Needleman, M. D. Lukin, H. Park, P. Kim, *Electrical control of interlayer exciton dynamics in atomically thin heterostructures*, Science **366**, 870–875 (2019) (Cited on pages 13, 21, 42, 57, 60, 64, 67, 68, 73, 80, and 84.)
- [Jeo20] T.-Y. Jeong, S. Bae, S.-Y. Lee, S. Jung, Y.-H. Kim, K.-J. Yee, *Valley depolarization in monolayer transition-metal dichalcogenides with zone-corner acoustic phonons*, Nanoscale **12**, 22 487–22 494 (2020) (Cited on page 79.)
- [Jin19a] C. Jin, E. C. Regan, D. Wang, M. Iqbal Bakti Utama, C.-S. Yang, J. Cain, Y. Qin, Y. Shen, Z. Zheng, K. Watanabe, T. Taniguchi, S. Tongay, A. Zettl, F. Wang, *Identification of spin, valley and moiré quasi-angular momentum of interlayer excitons*, Nat. Phys. **15**, 1140–1144 (2019) (Cited on page 12.)
- [Jin19b] C. Jin, E. C. Regan, A. Yan, M. Iqbal Bakti Utama, D. Wang, S. Zhao, Y. Qin, S. Yang, Z. Zheng, S. Shi, K. Watanabe, T. Taniguchi, S. Tongay, A. Zettl, F. Wang, *Observation of moiré excitons in WSe₂/WS₂ heterostructure superlattices*, Nature **567**, 76–80 (2019) (Cited on page 17.)
- [Joe21] A. Y. Joe, L. A. Jauregui, K. Pistunova, A. M. Mier Valdivia, Z. Lu, D. S. Wild, G. Scuri, K. De Greve, R. J. Gelly, Y. Zhou, J. Sung, A. Sushko, T. Taniguchi, K. Watanabe, D. Smirnov, M. D. Lukin, H. Park, P. Kim, *Electrically controlled emission from singlet and triplet exciton species in atomically thin light-emitting diodes*, Phys. Rev. B **103**, L161 411 (2021) (Cited on pages 60, 66, 76, 88, and 91.)
- [Jon14] A. M. Jones, H. Yu, J. S. Ross, P. Klement, N. J. Ghimire, J. Yan, D. G. Mandrus, W. Yao, X. Xu, *Spin-layer locking effects in optical orientation of exciton spin in bilayer WSe₂*, Nat. Phys. **10**, 130–134 (2014) (Cited on page 91.)
- [Ju14] L. Ju, J. J. Velasco, E. Huang, S. Kahn, C. Nosiiglia, H.-Z. Tsai, W. Yang, T. Taniguchi, K. Watanabe, Y. Zhang, *Photoinduced doping in heterostructures of graphene and boron nitride*, Nat. Nanotechnol. **9**, 348 (2014) (Cited on page 181.)
- [Jun23] P. E. F. Junior, J. Fabian, *Signatures of electric field and layer separation effects on the spin-valley physics of MoSe₂/WSe₂ heterobilayers: from energy bands to dipolar excitons*, arXiv:2303.01852 (2023) (Cited on page 68.)
- [Kar03] K. Karrai, R. J. Warburton, *Optical transmission and reflection spectroscopy of single quantum dots*, Superlattices and Microstruct. **33**, 311–337 (2003) (Cited on pages 46, 107, 108, 109, 167, 169, and 170.)
- [Kar19] O. Karni, E. Barré, S. C. Lau, R. Gillen, E. Y. Ma, B. Kim, K. Watanabe, T. Taniguchi, J. Maultzsch, K. Barmak, R. H. Page, T. F. Heinz, *Infrared*

- Interlayer Exciton Emission in MoS₂/WSe₂ Heterostructures*, Phys. Rev. Lett. **123**, 247 402 (2019) (Cited on page 12.)
- [Kar22] O. Karni, E. Barré, V. Pareek, J. D. Georganas, M. K. L. Man, C. Sahoo, D. R. Bacon, X. Zhu, H. B. Ribeiro, A. L. O’Beirne, J. Hu, A. Al-Mahboob, M. M. M. Abdelrasoul, N. S. Chan, A. Karmakar, A. J. Winchester, B. Kim, K. Watanabe, T. Taniguchi, K. Barmak, J. Madéo, F. H. da Jornada, T. F. Heinz, K. M. Dani, *Structure of the moiré exciton captured by imaging its electron and hole*, Nature **603**, 247–252 (2022) (Cited on pages 21 and 63.)
- [Kas06] J. Kasprzak, M. Richard, S. Kundermann, A. Baas, P. Jeambrun, J. M. J. Keeling, F. M. Marchetti, M. H. Szymańska, R. André, J. L. Staehli, V. Savona, P. B. Littlewood, B. Deveaud, L. S. Dang, *Bose–Einstein condensation of exciton polaritons*, Nature **443**, 409–414 (2006) (Cited on pages 104 and 140.)
- [Kat18] J. Katoch, S. Ulstrup, R. J. Koch, S. Moser, K. M. McCreary, S. Singh, J. Xu, B. T. Jonker, R. K. Kawakami, A. Bostwick, E. Rotenberg, C. Jozwiak, *Giant spin-splitting and gap renormalization driven by trions in single-layer WS₂/h-BN heterostructures*, Nat. Phys. **14**, 355–359 (2018) (Cited on page 84.)
- [Kel67] L. V. Keldysh, *Coulomb interaction in thin semiconductor and semimetal films*, JETP Lett. **29**, 716–719 (1967) (Cited on page 11.)
- [Ken21] D. M. Kennes, M. Claassen, L. Xian, A. Georges, A. J. Millis, J. Hone, C. R. Dean, D. N. Basov, A. N. Pasupathy, A. Rubio, *Moiré heterostructures as a condensed-matter quantum simulator*, Nat. Phys. **17**, 155–163 (2021) (Cited on page 25.)
- [Ker19] A. Kerelsky, L. J. McGilly, D. M. Kennes, L. Xian, M. Yankowitz, S. Chen, K. Watanabe, T. Taniguchi, J. Hone, C. Dean, A. Rubio, A. N. Pasupathy, *Maximized electron interactions at the magic angle in twisted bilayer graphene*, Nature **572**, 95–100 (2019) (Cited on page 25.)
- [Kie20] J. Kiemle, F. Sigger, M. Lorke, B. Miller, K. Watanabe, T. Taniguchi, A. Holleitner, U. Wurstbauer, *Control of the orbital character of indirect excitons in MoS₂ / WS₂ heterobilayers*, Phys. Rev. B **101**, 121 404 (2020) (Cited on pages 12 and 121.)
- [Kim15] K. Kim, S. Larentis, B. Fallahazad, K. Lee, J. Xue, D. C. Dillen, C. M. Corbet, E. Tutuc, *Band Alignment in WSe₂–Graphene Heterostructures*, ACS Nano **9**, 4527–4532 (2015) (Cited on pages 42, 66, and 148.)
- [Kir06] M. Kira, S. W. Koch, *Many-body correlations and excitonic effects in semiconductor spectroscopy*, Prog. Quantum Electron. **30**, 155–296 (2006) (Cited on pages 108, 109, 167, and 170.)
- [Kle22] J. Klein, M. Florian, A. Hötger, A. Steinhoff, A. Delhomme, T. Taniguchi, K. Watanabe, F. Jahnke, A. W. Holleitner, M. Potemski, C. Faugeras, A. V. Stier, J. J. Finley, *Trions in MoS₂ are quantum superpositions of intra- and intervalley spin states*, Phys. Rev. B **105**, L041 302 (2022) (Cited on page 11.)
- [Kli12] C. F. Klingshirn, *Semiconductor Optics* (Springer, Berlin, Heidelberg, 2012), ISBN 978-3-642-28361-1 978-3-642-28362-8 (Cited on pages 9, 107, 169, and 170.)
- [Koc06] S. W. Koch, M. Kira, G. Khitrova, H. M. Gibbs, *Semiconductor excitons in new light*, Nat. Mater. **5**, 523–531 (2006) (Cited on pages 107 and 170.)
- [Kor14] A. Kormányos, V. Zólyomi, N. D. Drummond, G. Burkard, *Spin-Orbit Coupling*,

- Quantum Dots, and Qubits in Monolayer Transition Metal Dichalcogenides*, Phys. Rev. X **4**, 011 034 (2014) (Cited on pages 22, 125, and 130.)
- [Kor15] A. Kormányos, G. Burkard, M. Gmitra, J. Fabian, V. Zólyomi, N. D. Drummond, V. Fal'ko, *$\mathbf{k} \cdot \mathbf{p}$ theory for two-dimensional transition metal dichalcogenide semiconductors*, 2D Mater. **2**, 022 001 (2015) (Cited on pages 6, 8, 78, 130, and 159.)
- [Kos13] K. Kosmider, J. W. González, J. Fernández-Rossier, *Large spin splitting in the conduction band of transition metal dichalcogenide monolayers*, Phys. Rev. B **88**, 245 436 (2013) (Cited on page 7.)
- [Kre93] G. Kresse, J. Hafner, *Ab initio molecular dynamics for liquid metals*, Phys. Rev. B **47**, 558–561 (1993) (Cited on pages 156 and 179.)
- [Kre96] G. Kresse, J. Furthmüller, *Efficient iterative schemes for ab initio total-energy calculations using a plane-wave basis set*, Phys. Rev. B **54**, 11 169–11 186 (1996) (Cited on pages 156 and 179.)
- [Kre99] G. Kresse, D. Joubert, *From ultrasoft pseudopotentials to the projector augmented-wave method*, Phys. Rev. B **59**, 1758–1775 (1999) (Cited on pages 156 and 179.)
- [Kuh13] A. V. Kuhlmann, J. Houel, D. Brunner, A. Ludwig, D. Reuter, A. D. Wieck, R. J. Warburton, *A dark-field microscope for background-free detection of resonance fluorescence from single semiconductor quantum dots operating in a set-and-forget mode*, Rev. of Sci. Instrum. **84**, 073 905 (2013) (Cited on page 154.)
- [Kun18] J. Kunstmann, F. Mooshammer, P. Nagler, A. Chaves, F. Stein, N. Paradiso, G. Plechinger, C. Strunk, C. Schüller, G. Seifert, D. R. Reichman, T. Korn, *Momentum-space indirect interlayer excitons in transition-metal dichalcogenide van der Waals heterostructures*, Nat. Phys. **14**, 801–805 (2018) (Cited on page 12.)
- [Kö88] K. Köhler, H.-J. Pollard, L. Schultheis, C. W. Tu, *Photoluminescence of two-dimensional excitons in an electric field: Lifetime enhancement and field ionization in GaAs quantum wells*, Phys. Rev. B **38**, 5496–5503 (1988) (Cited on page 21.)
- [Lai09] B. Laikhtman, R. Rapaport, *Exciton correlations in coupled quantum wells and their luminescence blue shift*, Phys. Rev. B **80**, 195 313 (2009) (Cited on pages 54, 65, and 66.)
- [Lar18] S. Larentis, H. C. P. Movva, B. Fallahazad, K. Kim, A. Behroozi, T. Taniguchi, K. Watanabe, S. K. Banerjee, E. Tutuc, *Large effective mass and interaction-enhanced Zeeman splitting of K-valley electrons in MoSe₂*, Phys. Rev. B **97**, 201 407 (2018) (Cited on page 82.)
- [Lat18] A. Laturia, M. L. V. d. Put, W. G. Vandenberghe, *Dielectric properties of hexagonal boron nitride and transition metal dichalcogenides: from monolayer to bulk*, npj 2D Mater. Appl. **2**, 6 (2018) (Cited on pages 10, 11, 40, 42, and 148.)
- [Lau22] C. N. Lau, M. W. Bockrath, K. F. Mak, F. Zhang, *Reproducibility in the fabrication and physics of moiré materials*, Nature **602**, 41–50 (2022) (Cited on page 31.)
- [Lee10] C. Lee, H. Yan, L. E. Brus, T. F. Heinz, J. Hone, S. Ryu, *Anomalous Lattice Vibrations of Single- and Few-Layer MoS₂*, ACS Nano **4**, 2695–2700 (2010) (Cited on pages 29 and 153.)

- [Lei18] N. Leisgang, J. G. Roch, G. Froehlicher, M. Hamer, D. Terry, R. Gorbachev, R. J. Warburton, *Optical second harmonic generation in encapsulated single-layer InSe*, AIP Adv. **8**, 105 120 (2018) (Cited on pages 37 and 38.)
- [Lei20] N. Leisgang, S. Shree, I. Paradisanos, L. Sponfeldner, C. Robert, D. Lagarde, A. Balocchi, K. Watanabe, T. Taniguchi, X. Marie, R. J. Warburton, I. C. Gerber, B. Urbaszek, *Giant Stark splitting of an exciton in bilayer MoS₂*, Nat. Nanotechnol. **15**, 901–907 (2020) (Cited on pages 40, 104, 116, 117, 149, and 155.)
- [Lei22] N. Leisgang, *Electrical control of excitons in a gated two-dimensional semiconductor*, Ph.D. thesis, University of Basel (2022) (Cited on pages 37, 41, 131, 133, and 134.)
- [Li13] Y. Li, Y. Rao, K. F. Mak, Y. You, S. Wang, C. R. Dean, T. F. Heinz, *Probing Symmetry Properties of Few-Layer MoS₂ and h-BN by Optical Second-Harmonic Generation*, Nano Lett. **13**, 3329–3333 (2013) (Cited on page 37.)
- [Li14] Y. Li, J. Ludwig, T. Low, A. Chernikov, X. Cui, G. Arefe, Y. D. Kim, A. M. van der Zande, A. Rigosi, H. M. Hill, S. H. Kim, J. Hone, Z. Li, D. Smirnov, T. F. Heinz, *Valley Splitting and Polarization by the Zeeman Effect in Monolayer MoSe₂*, Phys. Rev. Lett. **113**, 266 804 (2014) (Cited on page 21.)
- [Li18] Z. Li, T. Wang, Z. Lu, C. Jin, Y. Chen, Y. Meng, Z. Lian, T. Taniguchi, K. Watanabe, S. Zhang, D. Smirnov, S.-F. Shi, *Revealing the biexciton and trion-exciton complexes in BN encapsulated WSe₂*, Nat. Commun. **9**, 3719 (2018) (Cited on page 11.)
- [Li20] W. Li, X. Lu, S. Dubey, L. Devenica, A. Srivastava, *Dipolar interactions between localized interlayer excitons in van der Waals heterostructures*, Nat. Mater. **19**, 624–629 (2020) (Cited on pages 55, 62, and 85.)
- [Li21] H. Li, S. Li, M. H. Naik, J. Xie, X. Li, J. Wang, E. Regan, D. Wang, W. Zhao, S. Zhao, S. Kahn, K. Yumigeta, M. Blei, T. Taniguchi, K. Watanabe, S. Tongay, A. Zettl, S. G. Louie, F. Wang, M. F. Crommie, *Imaging moiré flat bands in three-dimensional reconstructed WSe₂/WS₂ superlattices*, Nat. Mater. pages 945–950 (2021) (Cited on pages 19, 25, 54, and 83.)
- [Lin88] M. Lindberg, S. W. Koch, *Effective Bloch equations for semiconductors*, Phys. Rev. B **38**, 3342–3350 (1988) (Cited on pages 107 and 170.)
- [Lin18] J. Lindlau, M. Selig, A. Neumann, L. Colombier, J. Förste, V. Funk, M. Förg, J. Kim, G. Berghäuser, T. Taniguchi, K. Watanabe, F. Wang, E. Malic, A. Högele, *The role of momentum-dark excitons in the elementary optical response of bilayer WSe₂*, Nat. Commun. **9**, 2586 (2018) (Cited on page 92.)
- [Liu12] Q. Liu, L. Li, Y. Li, Z. Gao, Z. Chen, J. Lu, *Tuning Electronic Structure of Bilayer MoS₂ by Vertical Electric Field: A First-Principles Investigation*, J. Phys. Chem. C **116**, 21 556–21 562 (2012) (Cited on page 98.)
- [Liu13] G.-B. Liu, W.-Y. Shan, Y. Yao, W. Yao, D. Xiao, *Three-band tight-binding model for monolayers of group-VIB transition metal dichalcogenides*, Phys. Rev. B **88**, 085 433 (2013) (Cited on page 7.)
- [Liu15] G.-B. Liu, D. Xiao, Y. Yao, X. Xu, W. Yao, *Electronic structures and theoretical modelling of two-dimensional group-VIB transition metal dichalcogenides*, Chem. Soc. Rev. **44**, 2643–2663 (2015) (Cited on page 7.)

- [Liu21] E. Liu, E. Barré, J. van Baren, M. Wilson, T. Taniguchi, K. Watanabe, Y.-T. Cui, N. M. Gabor, T. F. Heinz, Y.-C. Chang, C. H. Lui, *Signatures of moiré trions in $WSe_2/MoSe_2$ heterobilayers*, Nature **594**, 46–50 (2021) (Cited on pages 25, 84, 85, and 139.)
- [Lor21] E. Lorchat, M. Selig, F. Katsch, K. Yumigeta, S. Tongay, A. Knorr, C. Schneider, S. Höfling, *Excitons in Bilayer MoS_2 Displaying a Colossal Electric Field Splitting and Tunable Magnetic Response*, Phys. Rev. Lett. **126**, 037401 (2021) (Cited on pages 76, 102, and 104.)
- [Los11] D. Loss, F. L. Pedrocchi, A. J. Leggett, *Absence of Spontaneous Magnetic Order of Lattice Spins Coupled to Itinerant Interacting Electrons in One and Two Dimensions*, Phys. Rev. Lett. **107**, 107201 (2011) (Cited on page 124.)
- [Lou22] C. Louca, A. Genco, S. Chiavazzo, T. P. Lyons, S. Randerson, C. Trovatiello, P. Claronino, R. Jayaprakash, K. Watanabe, T. Taniguchi, S. D. Conte, D. G. Lidzey, G. Cerullo, O. Kyriienko, A. I. Tartakovskii, *Nonlinear interactions of dipolar excitons and polaritons in MoS_2 bilayers*, arXiv: 2204.00485 (2022) (Cited on pages 120 and 140.)
- [Lu17] X. Lu, L. Yang, *Stark effect of doped two-dimensional transition metal dichalcogenides*, Appl. Phys. Lett. **111**, 193104 (2017) (Cited on page 157.)
- [Lu19] X. Lu, P. Stepanov, W. Yang, M. Xie, M. A. Aamir, I. Das, C. Urgell, K. Watanabe, T. Taniguchi, G. Zhang, A. Bachtold, A. H. MacDonald, D. K. Efetov, *Superconductors, orbital magnets and correlated states in magic-angle bilayer graphene*, Nature **574**, 653–657 (2019) (Cited on page 25.)
- [Luo20] Y. Luo, R. Engelke, M. Mattheakis, M. Tamagnone, S. Carr, K. Watanabe, T. Taniguchi, E. Kaxiras, P. Kim, W. L. Wilson, *In situ nanoscale imaging of moiré superlattices in twisted van der Waals heterostructures*, Nat. Commun. **11**, 4209 (2020) (Cited on pages 19 and 54.)
- [Lö51] P. Löwdin, *A Note on the Quantum-Mechanical Perturbation Theory*, J. Chem. Phys. **19**, 1396–1401 (1951) (Cited on page 120.)
- [Mac15] D. MacNeill, C. Heikes, K. F. Mak, Z. Anderson, A. Kormányos, V. Zólyomi, J. Park, D. C. Ralph, *Breaking of Valley Degeneracy by Magnetic Field in Monolayer $MoSe_2$* , Phys. Rev. Lett. **114**, 037401 (2015) (Cited on pages 21 and 22.)
- [Mah67] G. D. Mahan, *Excitons in Degenerate Semiconductors*, Phys. Rev. **153**, 882–889 (1967) (Cited on page 126.)
- [Mah22] F. Mahrouche, K. Rezouali, S. Mahtout, F. Zaabar, A. Molina-Sánchez, *Phonons in $WSe_2/MoSe_2$ van der Waals Heterobilayers*, Phys. Status Solidi B **259**, 2100321 (2022) (Cited on pages 62 and 79.)
- [Mai93] M. Z. Maialle, E. A. de Andrada e Silva, L. J. Sham, *Exciton spin dynamics in quantum wells*, Phys. Rev. B **47**, 15776–15788 (1993) (Cited on page 78.)
- [Mak10] K. F. Mak, C. Lee, J. Hone, J. Shan, T. F. Heinz, *Atomically Thin MoS_2 : A New Direct-Gap Semiconductor*, Phys. Rev. Lett. **105**, 136805 (2010) (Cited on pages 2, 5, 7, 8, 104, and 125.)
- [Mak13] K. F. Mak, K. He, C. Lee, G. H. Lee, J. Hone, T. F. Heinz, J. Shan, *Tightly bound trions in monolayer MoS_2* , Nat. Mater. **12**, 207–211 (2013) (Cited on pages 11 and 149.)

- [Man20] S. Manna, H. Huang, S. F. C. da Silva, C. Schimpf, M. B. Rota, B. Lehner, M. Reindl, R. Trotta, A. Rastelli, *Surface passivation and oxide encapsulation to improve optical properties of a single GaAs quantum dot close to the surface*, Appl. Surf. Sci. **532**, 147360 (2020) (Cited on page 1.)
- [Man22] A. J. Mannix, A. Ye, S. H. Sung, A. Ray, F. Mujid, C. Park, M. Lee, J.-H. Kang, R. Shreiner, A. A. High, D. A. Muller, R. Hovden, J. Park, *Robotic four-dimensional pixel assembly of van der Waals solids*, Nat. Nanotechnol. pages 361–366 (2022) (Cited on page 31.)
- [Mar17] K. Marinov, A. Avsar, K. Watanabe, T. Taniguchi, A. Kis, *Resolving the spin splitting in the conduction band of monolayer MoS₂*, Nat. Commun. **8**, 1938 (2017) (Cited on page 125.)
- [Mar22] E. Marchiori, L. Ceccarelli, N. Rossi, L. Lorenzelli, C. L. Degen, M. Poggio, *Nanoscale magnetic field imaging for 2D materials*, Nat. Rev. Phys. **4**, 49–60 (2022) (Cited on pages 137 and 140.)
- [Mas09] D. L. Maslov, A. V. Chubukov, *Nonanalytic paramagnetic response of itinerant fermions away and near a ferromagnetic quantum phase transition*, Phys. Rev. B **79**, 075112 (2009) (Cited on pages 124 and 129.)
- [Mat20] H. Mattiat, N. Rossi, B. Gross, J. Pablo-Navarro, C. Magén, R. Badea, J. Berzovsky, J. M. De Teresa, M. Poggio, *Nanowire Magnetic Force Sensors Fabricated by Focused-Electron-Beam-Induced Deposition*, Phys. Rev. Applied **13**, 044043 (2020) (Cited on pages 137 and 140.)
- [McD21] L. P. McDonnell, J. J. S. Viner, D. A. Ruiz-Tijerina, P. Rivera, X. Xu, V. I. Fal’ko, D. C. Smith, *Superposition of intra- and inter-layer excitons in twistrionic MoSe₂/WSe₂ bilayers probed by resonant Raman scattering*, 2D Mater. **8**, 035009 (2021) (Cited on pages 12, 104, 121, and 154.)
- [McG20] L. J. McGilly, A. Kerelsky, N. R. Finney, K. Shapovalov, E.-M. Shih, A. Ghiotto, Y. Zeng, S. L. Moore, W. Wu, Y. Bai, K. Watanabe, T. Taniguchi, M. Stengel, L. Zhou, J. Hone, X. Zhu, D. N. Basov, C. Dean, C. E. Dreyer, A. N. Pasupathy, *Visualization of moiré superlattices*, Nat. Nanotechnol. **15**, 580–584 (2020) (Cited on page 19.)
- [Men19] L. Mennel, M. Paur, T. Mueller, *Second harmonic generation in strained transition metal dichalcogenide monolayers: MoS₂, MoSe₂, WS₂, and WSe₂*, APL Photonics **4**, 034404 (2019) (Cited on page 38.)
- [Mer66] N. D. Mermin, H. Wagner, *Absence of Ferromagnetism or Antiferromagnetism in One- or Two-Dimensional Isotropic Heisenberg Models*, Phys. Rev. Lett. **17**, 1133 (1966) (Cited on page 124.)
- [Mer20] P. Merkl, F. Mooshammer, S. Brem, A. Girnghuber, K.-Q. Lin, L. Weigl, M. Liebich, C.-K. Yong, R. Gillen, J. Maultzsch, J. M. Lupton, E. Malic, R. Huber, *Twist-tailoring Coulomb correlations in van der Waals homobilayers*, Nat. Commun. **11**, 2167 (2020) (Cited on page 104.)
- [Mil84] D. A. B. Miller, D. S. Chemla, T. C. Damen, A. C. Gossard, W. Wiegmann, T. H. Wood, C. A. Burrus, *Band-Edge Electroabsorption in Quantum Well Structures: The Quantum-Confined Stark Effect*, Phys. Rev. Lett. **53**, 2173–2176 (1984) (Cited on pages 20, 87, and 110.)
- [Mil17] B. Miller, A. Steinhoff, B. Pano, J. Klein, F. Jahnke, A. Holleitner, U. Wurstbauer, *Long-Lived Direct and Indirect Interlayer Excitons in van der Waals*

- Heterostructures*, Nano Lett. **17**, 5229–5237 (2017) (Cited on pages 12, 13, 53, 60, 61, 62, 63, 67, 80, and 84.)
- [Mis19] D. Miserev, J. Klinovaja, D. Loss, *Exchange intervalley scattering and magnetic phase diagram of transition metal dichalcogenide monolayers*, Phys. Rev. B **100**, 014428 (2019) (Cited on page 129.)
- [Mit15] A. A. Mitioglu, P. Plochocka, A. Granados del Aguila, P. C. M. Christianen, G. Deligeorgis, S. Anghel, L. Kulyuk, D. K. Maude, *Optical Investigation of Monolayer and Bulk Tungsten Diselenide (WSe_2) in High Magnetic Fields*, Nano Lett. **15**, 4387–4392 (2015) (Cited on pages 21 and 24.)
- [MM19] G. Muñoz-Matutano, A. Wood, M. Johnsson, X. Vidal, B. Q. Baragiola, A. Reinhard, A. Lemaître, J. Bloch, A. Amo, G. Nogues, B. Besga, M. Richard, T. Volz, *Emergence of quantum correlations from interacting fibre-cavity polaritons*, Nat. Mater. **18**, 213–218 (2019) (Cited on pages 21, 102, 104, 120, and 140.)
- [Mol17] M. R. Molas, C. Faugeras, A. O. Slobodeniuk, K. Nogajewski, M. Bartos, D. M. Basko, M. Potemski, *Brightening of dark excitons in monolayers of semiconducting transition metal dichalcogenides*, 2D Mater. **4**, 021003 (2017) (Cited on page 25.)
- [Mon21] A. R.-P. Montblanch, D. M. Kara, I. Paradisanos, C. M. Purser, M. S. G. Feuer, E. M. Alexeev, L. Stefan, Y. Qin, M. Blei, G. Wang, A. R. Cadore, P. Latawiec, M. Lončar, S. Tongay, A. C. Ferrari, M. Atatüre, *Confinement of long-lived interlayer excitons in WS_2/WSe_2 heterostructures*, Commun. Phys. **4**, 119 (2021) (Cited on page 12.)
- [Mos08] A. A. Mostofi, J. R. Yates, Y.-S. Lee, I. Souza, D. Vanderbilt, N. Marzari, *wannier90: A tool for obtaining maximally-localised Wannier functions*, Comput. Phys. Commun. **178**, 685–699 (2008) (Cited on pages 156 and 179.)
- [Mot38] N. F. Mott, *Conduction in polar crystals. II. The conduction band and ultraviolet absorption of alkali-halide crystals*, Trans. Faraday Soc. **34**, 500–506 (1938) (Cited on page 9.)
- [Nag17a] P. Nagler, M. V. Ballottin, A. A. Mitioglu, F. Mooshammer, N. Paradiso, C. Strunk, R. Huber, A. Chernikov, P. C. M. Christianen, C. Schüller, T. Korn, *Giant magnetic splitting inducing near-unity valley polarization in van der Waals heterostructures*, Nat. Commun. **8**, 1551 (2017) (Cited on pages 24 and 79.)
- [Nag17b] P. Nagler, G. Plechinger, M. V. Ballottin, A. Mitioglu, S. Meier, N. Paradiso, C. Strunk, A. Chernikov, P. C. M. Christianen, C. Sch, T. Korn, *Interlayer exciton dynamics in a dichalcogenide monolayer heterostructure*, 2D Mater. **4**, 025112 (2017) (Cited on pages 13, 24, 65, 66, and 88.)
- [Nag19] P. Nagler, F. Mooshammer, J. Kunstmann, M. V. Ballottin, A. Mitioglu, A. Chernikov, A. Chaves, F. Stein, N. Paradiso, S. Meier, G. Plechinger, C. Strunk, R. Huber, G. Seifert, D. R. Reichman, P. C. M. Christianen, C. Schüller, T. Korn, *Interlayer Excitons in Transition-Metal Dichalcogenide Heterobilayers*, Phys. Status Solidi B **256**, 1900308 (2019) (Cited on pages 91 and 92.)
- [Nai20] M. H. Naik, S. Kundu, I. Maity, M. Jain, *Origin and evolution of ultraflat bands in twisted bilayer transition metal dichalcogenides: Realization of triangular quantum dots*, Phys. Rev. B **102**, 075413 (2020) (Cited on pages 17, 18, and 63.)

- [Naj21] D. Najer, N. Tomm, A. Javadi, A. R. Korsch, B. Petrak, D. Riedel, V. Dolique, S. R. Valentin, R. Schott, A. D. Wieck, A. Ludwig, R. J. Warburton, *Suppression of Surface-Related Loss in a Gated Semiconductor Microcavity*, Phys. Rev. Applied **15**, 044004 (2021) (Cited on page 1.)
- [Nay17] P. K. Nayak, Y. Horbatenko, S. Ahn, G. Kim, J.-U. Lee, K. Y. Ma, A.-R. Jang, H. Lim, D. Kim, S. Ryu, H. Cheong, N. Park, H. S. Shin, *Probing Evolution of Twist-Angle-Dependent Interlayer Excitons in MoSe₂/WSe₂ van der Waals Heterostructures*, ACS Nano **11**, 4041–4050 (2017) (Cited on page 17.)
- [Neg00] V. Negoita, D. W. Snoke, K. Eberl, *Huge density-dependent blueshift of indirect excitons in biased coupled quantum wells*, Phys. Rev. B **61**, 2779–2783 (2000) (Cited on page 65.)
- [Nie19] I. Niehues, A. Blob, T. Stiehm, S. M. d. Vasconcellos, R. Bratschitsch, *Interlayer excitons in bilayer MoS₂ under uniaxial tensile strain*, Nanoscale **11**, 12788–12792 (2019) (Cited on pages 12 and 88.)
- [Nov04] K. S. Novoselov, A. K. Geim, S. V. Morozov, D. Jiang, Y. Zhang, S. V. Dubonos, I. V. Grigorieva, A. A. Firsov, *Electric Field Effect in Atomically Thin Carbon Films*, Science **306**, 666–669 (2004) (Cited on pages 1 and 5.)
- [Nov05a] K. S. Novoselov, A. K. Geim, S. V. Morozov, D. Jiang, M. I. Katsnelson, I. V. Grigorieva, S. V. Dubonos, A. A. Firsov, *Two-dimensional gas of massless Dirac fermions in graphene*, Nature **438**, 197–200 (2005) (Cited on page 5.)
- [Nov05b] K. S. Novoselov, D. Jiang, F. Schedin, T. J. Booth, V. V. Khotkevich, S. V. Morozov, A. K. Geim, *Two-dimensional atomic crystals*, Proc. Natl. Acad. Sci. U.S.A. **102**, 10451–10453 (2005) (Cited on page 149.)
- [Oka18] M. Okada, A. Kutana, Y. Kureishi, Y. Kobayashi, Y. Saito, T. Saito, K. Watanabe, T. Taniguchi, S. Gupta, Y. Miyata, B. I. Yakobson, H. Shinohara, R. Kitaura, *Direct and Indirect Interlayer Excitons in a van der Waals Heterostructure of hBN/WS₂/MoS₂/hBN*, ACS Nano **12**, 2498–2505 (2018) (Cited on page 12.)
- [Orb61] R. Orbach, *Spin-Lattice Relaxation in Rare-Earth Salts*, Proc. R. Soc. London Ser. A **264**, 458–484 (1961) (Cited on page 79.)
- [Pai06] J. Paier, M. Marsman, K. Hummer, G. Kresse, I. C. Gerber, J. G. Ángyán, *Screened hybrid density functionals applied to solids*, J. Chem. Phys. **124**, 154709 (2006) (Cited on pages 156 and 179.)
- [Par21a] I. Paradisanos, G. Wang, E. M. Alexeev, A. R. Cadore, X. Marie, A. C. Ferrari, M. M. Glazov, B. Urbaszek, *Efficient phonon cascades in WSe₂ monolayers*, Nat. Commun. **12**, 538 (2021) (Cited on page 62.)
- [Par21b] P. Parzefall, J. Holler, M. Scheuck, A. Beer, K.-Q. Lin, B. Peng, B. Monserat, P. Nagler, M. Kempf, T. Korn, C. Schüller, *Moiré phonons in twisted MoSe₂-WSe₂ heterobilayers and their correlation with interlayer excitons*, 2D Mater. **8**, 035030 (2021) (Cited on pages 54 and 153.)
- [Par22] S. Park, S. Arscott, T. Taniguchi, K. Watanabe, F. Sirotti, F. Cadiz, *Efficient valley polarization of charged excitons and resident carriers in Molybdenum disulfide monolayers by optical pumping*, Commun. Phys. **5**, 73 (2022) (Cited on page 136.)
- [Ped16] T. G. Pedersen, *Exciton Stark shift and electroabsorption in monolayer transition-metal dichalcogenides*, Phys. Rev. B **94**, 125424 (2016) (Cited on page 111.)

- [Ped17] T. G. Pedersen, *Stark effect in finite-barrier quantum wells, wires, and dots*, New J. Phys. **19**, 043 011 (2017) (Cited on page 70.)
- [Ped19] T. G. Pedersen, *Giant Stark effect in coupled quantum wells: Analytical model*, Phys. Rev. B **100**, 155 410 (2019) (Cited on page 70.)
- [Pei21] N. Peimyoo, T. Deilmann, F. Withers, J. Escolar, D. Nutting, T. Taniguchi, K. Watanabe, A. Taghizadeh, M. F. Craciun, K. S. Thygesen, S. Russo, *Electrical tuning of optically active interlayer excitons in bilayer MoS₂*, Nat. Nanotechnol. **16**, 888–893 (2021) (Cited on pages 102 and 104.)
- [Phi89] C. C. Phillips, R. Eccleston, S. R. Andrews, *Theoretical and experimental picosecond photoluminescence studies of the quantum-confined Stark effect in a strongly coupled double-quantum-well structure*, Phys. Rev. B **40**, 9760–9766 (1989) (Cited on page 21.)
- [Phi19] M. Phillips, C. S. Hellberg, *Commensurate structures in twisted transition metal dichalcogenide heterobilayers*, arXiv:1909.02495 (2019) (Cited on page 68.)
- [Pis18] R. Pisoni, A. Kormányos, M. Brooks, Z. Lei, P. Back, M. Eich, H. Overweg, Y. Lee, P. Rickhaus, K. Watanabe, T. Taniguchi, A. Imamoglu, G. Burkard, T. Ihn, K. Ensslin, *Interactions and Magnetotransport through Spin-Valley Coupled Landau Levels in Monolayer MoS₂*, Phys. Rev. Lett. **121**, 247 701 (2018) (Cited on pages 36, 125, 130, and 150.)
- [Pis19] R. Pisoni, T. Davatz, K. Watanabe, T. Taniguchi, T. Ihn, K. Ensslin, *Absence of Interlayer Tunnel Coupling of K-Valley Electrons in Bilayer MoS₂*, Phys. Rev. Lett. **123**, 117 702 (2019) (Cited on pages 42, 57, 88, and 104.)
- [Pop22] A. Popert, Y. Shimazaki, M. Kroner, K. Watanabe, T. Taniguchi, A. Imamoglu, T. Smoleński, *Optical Sensing of Fractional Quantum Hall Effect in Graphene*, Nano Lett. **22**, 7363–7369 (2022) (Cited on pages 24 and 25.)
- [Pur46] E. M. Purcell, *Spontaneous Emission Probabilities at Radio Frequencies*, Phys. Rev. **69**, 681 (1946) (Cited on page 49.)
- [Pur16] A. A. Puretzky, L. Liang, X. Li, K. Xiao, B. G. Sumpter, V. Meunier, D. B. Geohegan, *Twisted MoSe₂ Bilayers with Variable Local Stacking and Interlayer Coupling Revealed by Low-Frequency Raman Spectroscopy*, ACS Nano **10**, 2736–2744 (2016) (Cited on page 20.)
- [Qiu13] D. Y. Qiu, F. H. da Jornada, S. G. Louie, *Optical Spectrum of MoS₂: Many-Body Effects and Diversity of Exciton States*, Phys. Rev. Lett. **111**, 216 805 (2013) (Cited on pages 7 and 157.)
- [Qua21] J. Quan, L. Linhart, M.-L. Lin, D. Lee, J. Zhu, C.-Y. Wang, W.-T. Hsu, J. Choi, J. Embley, C. Young, T. Taniguchi, K. Watanabe, C.-K. Shih, K. Lai, A. H. MacDonald, P.-H. Tan, F. Libisch, X. Li, *Phonon renormalization in reconstructed MoS₂ moiré superlattices*, Nat. Mater. **20**, 1100–1105 (2021) (Cited on page 19.)
- [Raj17] A. Raja, A. Chaves, J. Yu, G. Arefe, H. M. Hill, A. F. Rigosi, T. C. Berkelbach, P. Nagler, C. Schüller, T. Korn, C. Nuckolls, J. Hone, L. E. Brus, T. F. Heinz, D. R. Reichman, A. Chernikov, *Coulomb engineering of the bandgap and excitons in two-dimensional materials*, Nat. Commun. **8**, 15 251 (2017) (Cited on pages 11 and 24.)
- [Raj19] A. Raja, L. Waldecker, J. Zipfel, Y. Cho, S. Brem, J. D. Ziegler, M. Kulig, T. Taniguchi, K. Watanabe, E. Malic, T. F. Heinz, T. C. Berkelbach,

- A. Chernikov, *Dielectric disorder in two-dimensional materials*, Nat. Nanotechnol. **14**, 832–837 (2019) (Cited on pages 24 and 30.)
- [Ram11] A. Ramasubramaniam, D. Naveh, E. Towe, *Tunable band gaps in bilayer transition-metal dichalcogenides*, Phys. Rev. B **84**, 205325 (2011) (Cited on page 157.)
- [Ras15] F. A. Rasmussen, K. S. Thygesen, *Computational 2D Materials Database: Electronic Structure of Transition-Metal Dichalcogenides and Oxides*, J. Phys. Chem. C **119**, 13169–13183 (2015) (Cited on page 70.)
- [Reg20] E. C. Regan, D. Wang, C. Jin, M. I. Bakti Utama, B. Gao, X. Wei, S. Zhao, W. Zhao, Z. Zhang, K. Yumigeta, M. Blei, J. D. Carlström, K. Watanabe, T. Taniguchi, S. Tongay, M. Crommie, A. Zettl, F. Wang, *Mott and generalized Wigner crystal states in WSe_2/WS_2 moiré superlattices*, Nature **579**, 359–363 (2020) (Cited on pages 25 and 83.)
- [Riv15] P. Rivera, J. R. Schaibley, A. M. Jones, J. S. Ross, S. Wu, G. Aivazian, P. Klement, K. Seyler, G. Clark, N. J. Ghimire, J. Yan, D. G. Mandrus, W. Yao, X. Xu, *Observation of long-lived interlayer excitons in monolayer $MoSe_2-WSe_2$ heterostructures*, Nat. Commun. **6**, 6242 (2015) (Cited on pages 12, 54, 65, 88, and 91.)
- [Riv16] P. Rivera, K. L. Seyler, H. Yu, J. R. Schaibley, J. Yan, D. G. Mandrus, W. Yao, X. Xu, *Valley-polarized exciton dynamics in a 2D semiconductor heterostructure*, Science **351** (2016) (Cited on page 13.)
- [Rob18] C. Robert, M. A. Semina, F. Cadiz, M. Manca, E. Courtade, T. Taniguchi, K. Watanabe, H. Cai, S. Tongay, B. Lassagne, P. Renucci, T. Amand, X. Marie, M. M. Glazov, B. Urbaszek, *Optical spectroscopy of excited exciton states in MoS_2 monolayers in van der Waals heterostructures*, Phys. Rev. Materials **2**, 011001 (2018) (Cited on pages 47 and 156.)
- [Rob20] C. Robert, B. Han, P. Kapuscinski, A. Delhomme, C. Faugeras, T. Amand, M. R. Molas, M. Bartos, K. Watanabe, T. Taniguchi, B. Urbaszek, M. Potemski, X. Marie, *Measurement of the spin-forbidden dark excitons in MoS_2 and $MoSe_2$ monolayers*, Nat. Commun. **11**, 4037 (2020) (Cited on page 25.)
- [Rob21] C. Robert, S. Park, F. Cadiz, L. Lombez, L. Ren, H. Tornatzky, A. Rowe, D. Paget, F. Sirotti, M. Yang, D. Van Tuan, T. Taniguchi, B. Urbaszek, K. Watanabe, T. Amand, H. Dery, X. Marie, *Spin/valley pumping of resident electrons in WSe_2 and WS_2 monolayers*, Nat. Commun. **12**, 5455 (2021) (Cited on page 11.)
- [Roc18] J. G. Roch, N. Leisgang, G. Froehlicher, P. Makk, K. Watanabe, T. Taniguchi, C. Schönenberger, R. J. Warburton, *Quantum-Confined Stark Effect in a MoS_2 Monolayer van der Waals Heterostructure*, Nano Lett. **18**, 1070–1074 (2018) (Cited on pages 21, 69, 87, 91, and 111.)
- [Roc19] J. G. Roch, G. Froehlicher, N. Leisgang, P. Makk, K. Watanabe, T. Taniguchi, R. J. Warburton, *Spin-polarized electrons in monolayer MoS_2* , Nat. Nanotechnol. **14**, 432–436 (2019) (Cited on pages 2, 11, 25, 40, 44, 56, 124, 125, 127, 129, 130, 136, 137, 140, 183, 184, and 185.)
- [Roc20] J. G. Roch, D. Miserev, G. Froehlicher, N. Leisgang, L. Sponfeldner, K. Watanabe, T. Taniguchi, J. Klinovaja, D. Loss, R. J. Warburton, *First-Order Magnetic*

- Phase Transition of Mobile Electrons in Monolayer MoS₂*, Phys. Rev. Lett. **124**, 187 602 (2020) (Cited on page 181.)
- [Roh98] M. Rohlfing, S. G. Louie, *Electron-hole Excitations in Semiconductors and Insulators*, Phys. Rev. Lett. **81**, 2312–2315 (1998) (Cited on pages 156 and 179.)
- [Ros13] J. S. Ross, S. Wu, H. Yu, N. J. Ghimire, A. M. Jones, G. Aivazian, J. Yan, D. G. Mandrus, D. Xiao, W. Yao, X. Xu, *Electrical control of neutral and charged excitons in a monolayer semiconductor*, Nat. Commun. **4**, 1474 (2013) (Cited on pages 11 and 149.)
- [Ros17] J. S. Ross, P. Rivera, J. Schaibley, E. Lee-Wong, H. Yu, T. Taniguchi, K. Watanabe, J. Yan, D. Mandrus, D. Cobden, W. Yao, X. Xu, *Interlayer Exciton Optoelectronics in a 2D Heterostructure p–n Junction*, Nano Lett. **17**, 638–643 (2017) (Cited on page 13.)
- [Ros20] M. R. Rosenberger, H.-J. Chuang, M. Phillips, V. P. Oleshko, K. M. McCreary, S. V. Sivaram, C. S. Hellberg, B. T. Jonker, *Twist Angle-Dependent Atomic Reconstruction and Moiré Patterns in Transition Metal Dichalcogenide Heterostructures*, ACS Nano **14**, 4550–4558 (2020) (Cited on pages 19, 20, 54, and 61.)
- [RP18] R. Ribeiro-Palau, C. Zhang, K. Watanabe, T. Taniguchi, J. Hone, C. R. Dean, *Twistable electronics with dynamically rotatable heterostructures*, Science **361**, 690–693 (2018) (Cited on page 15.)
- [RT19] D. A. Ruiz-Tijerina, V. I. Fal’ko, *Interlayer hybridization and moiré superlattice minibands for electrons and excitons in heterobilayers of transition-metal dichalcogenides*, Phys. Rev. B **99**, 125 424 (2019) (Cited on pages 12, 18, and 121.)
- [Ryt67] N. S. Rytova, *Screened potential of a point charge in a thin film*, Proc. MSU, Phys., Astron. **3**, 30 (1967) (Cited on page 11.)
- [SC13] M. Sup Choi, G.-H. Lee, Y.-J. Yu, D.-Y. Lee, S. Hwan Lee, P. Kim, J. Hone, W. Jong Yoo, *Controlled charge trapping by molybdenum disulphide and graphene in ultrathin heterostructured memory devices*, Nat. Commun. **4**, 1624 (2013) (Cited on page 70.)
- [Sch08] C. Schindler, R. Zimmermann, *Analysis of the exciton-exciton interaction in semiconductor quantum wells*, Phys. Rev. B **78**, 045 313 (2008) (Cited on pages 65 and 66.)
- [Sch11] G. J. Schinner, E. Schubert, M. P. Stallhofer, J. P. Kotthaus, D. Schuh, A. K. Rai, D. Reuter, A. D. Wieck, A. O. Govorov, *Electrostatically trapping indirect excitons in coupled In_xGa_{1-x}As quantum wells*, Phys. Rev. B **83**, 165 308 (2011) (Cited on page 21.)
- [Sch13a] G. J. Schinner, J. Repp, E. Schubert, A. K. Rai, D. Reuter, A. D. Wieck, A. O. Govorov, A. W. Holleitner, J. P. Kotthaus, *Confinement and Interaction of Single Indirect Excitons in a Voltage-Controlled Trap Formed Inside Double InGaAs Quantum Wells*, Phys. Rev. Lett. **110**, 127 403 (2013) (Cited on pages 21, 54, 85, and 140.)
- [Sch13b] G. J. Schinner, J. Repp, E. Schubert, A. K. Rai, D. Reuter, A. D. Wieck, A. O. Govorov, A. W. Holleitner, J. P. Kotthaus, *Many-body correlations of electrostatically trapped dipolar excitons*, Phys. Rev. B **87**, 205 302 (2013) (Cited on page 65.)

- [Sch18] C. Schneider, M. M. Glazov, T. Korn, S. Höfling, B. Urbaszek, *Two-dimensional semiconductors in the regime of strong light-matter coupling*, Nat. Commun. **9**, 2695 (2018) (Cited on page 102.)
- [Sch22] D. Schmitt, J. P. Bange, W. Bennecke, A. AlMutairi, G. Meneghini, K. Watanabe, T. Taniguchi, D. Steil, D. R. Luke, R. T. Weitz, S. Steil, G. S. M. Jansen, S. Brem, E. Malic, S. Hofmann, M. Reutzler, S. Mathias, *Formation of moiré interlayer excitons in space and time*, Nature **608**, 499–503 (2022) (Cited on page 17.)
- [Scu18] G. Scuri, Y. Zhou, A. A. High, D. S. Wild, C. Shu, K. De Greve, L. A. Jauregui, T. Taniguchi, K. Watanabe, P. Kim, M. D. Lukin, H. Park, *Large Excitonic Reflectivity of Monolayer MoSe₂ Encapsulated in Hexagonal Boron Nitride*, Phys. Rev. Lett. **120**, 037402 (2018) (Cited on pages 46 and 88.)
- [Sey19] K. L. Seyler, P. Rivera, H. Yu, N. P. Wilson, E. L. Ray, D. G. Mandrus, J. Yan, W. Yao, X. Xu, *Signatures of moiré-trapped valley excitons in MoSe₂/WSe₂ heterobilayers*, Nature **567**, 66 (2019) (Cited on pages 13, 18, 55, 62, 76, and 85.)
- [Sha17] V. Shahnazaryan, I. Iorsh, I. A. Shelykh, O. Kyriienko, *Exciton-exciton interaction in transition-metal dichalcogenide monolayers*, Phys. Rev. B **96**, 115409 (2017) (Cited on page 104.)
- [Sha19] A. L. Sharpe, E. J. Fox, A. W. Barnard, J. Finney, K. Watanabe, T. Taniguchi, M. A. Kastner, D. Goldhaber-Gordon, *Emergent ferromagnetism near three-quarters filling in twisted bilayer graphene*, Science **365**, 605–608 (2019) (Cited on pages 25 and 124.)
- [Sha21a] S. Shabani, D. Halbertal, W. Wu, M. Chen, S. Liu, J. Hone, W. Yao, D. N. Basov, X. Zhu, A. N. Pasupathy, *Deep moiré potentials in twisted transition metal dichalcogenide bilayers*, Nat. Phys. pages 720–725 (2021) (Cited on pages 19 and 54.)
- [Sha21b] D. N. Shanks, F. MahdikhanySarvejahany, C. Muccianti, A. Alfrey, M. R. Koehler, D. G. Mandrus, T. Taniguchi, K. Watanabe, H. Yu, B. J. LeRoy, J. R. Schaibley, *Nanoscale Trapping of Interlayer Excitons in a 2D Semiconductor Heterostructure*, Nano Lett. **21**, 5641–5647 (2021) (Cited on pages 21, 54, 67, 68, 73, 85, 140, and 146.)
- [Shi06] M. Shishkin, G. Kresse, *Implementation and performance of the frequency-dependent GW method within the PAW framework*, Phys. Rev. B **74**, 035101 (2006) (Cited on pages 156 and 179.)
- [Shi20] Y. Shimazaki, I. Schwartz, K. Watanabe, T. Taniguchi, M. Kroner, A. İmamoğlu, *Strongly correlated electrons and hybrid excitons in a moiré heterostructure*, Nature **580**, 472–477 (2020) (Cited on pages 25, 83, 92, and 104.)
- [Shr19] S. Shree, A. George, T. Lehnert, C. Neumann, M. Benelajla, C. Robert, X. Marie, K. Watanabe, T. Taniguchi, U. Kaiser, B. Urbaszek, A. Turchanin, *High optical quality of MoS₂ monolayers grown by chemical vapor deposition*, 2D Mater. **7**, 015011 (2019) (Cited on page 30.)
- [Shr21] S. Shree, I. Paradisanos, X. Marie, C. Robert, B. Urbaszek, *Guide to optical spectroscopy of layered semiconductors*, Nat. Rev. Phys. **3**, 39–54 (2021) (Cited on pages 43, 46, and 47.)
- [Sid17] M. Sidler, P. Back, O. Cotlet, A. Srivastava, T. Fink, M. Kroner, E. Demler, A. Imamoglu, *Fermi polaron-polaritons in charge-tunable atomically thin semiconductors*, Nat. Phys. **13**, 255–261 (2017) (Cited on pages 11, 125, and 127.)

- [Sig20] L. Sigl, F. Sigger, F. Kronowetter, J. Kiemle, J. Klein, K. Watanabe, T. Taniguchi, J. J. Finley, U. Wurstbauer, A. W. Holleitner, *Signatures of a degenerate many-body state of interlayer excitons in a van der Waals heterostack*, Phys. Rev. Research **2**, 042044 (2020) (Cited on pages 54, 85, and 139.)
- [Sin16] A. Singh, K. Tran, M. Kolarczik, J. Seifert, Y. Wang, K. Hao, D. Pleskot, N. M. Gabor, S. Helmrich, N. Owschimikow, U. Woggon, X. Li, *Long-Lived Valley Polarization of Intravalley Trions in Monolayer WSe₂*, Phys. Rev. Lett. **117**, 257402 (2016) (Cited on page 11.)
- [Siv12] K. Sivalertporn, L. Mouchliadis, A. L. Ivanov, R. Philp, E. A. Muljarov, *Direct and indirect excitons in semiconductor coupled quantum wells in an applied electric field*, Phys. Rev. B **85**, 045207 (2012) (Cited on page 104.)
- [Slo19] A. O. Slobodeniuk, L. Bala, M. Koperski, M. R. Molas, P. Kossacki, K. Nogajewski, M. Bartos, K. Watanabe, T. Taniguchi, C. Faugeras, M. Potemski, *Fine structure of K-excitons in multilayers of transition metal dichalcogenides*, 2D Mater. **6**, 025026 (2019) (Cited on pages 12, 88, 93, and 94.)
- [Smi22] D. S. Smirnov, J. Holler, M. Kempf, J. Zipfel, P. Nagler, M. V. Ballottin, A. A. Mitioglu, A. Chernikov, P. C. M. Christianen, C. Schüller, T. Korn, *Valley-magnetophonon resonance for interlayer excitons*, 2D Mater. **9**, 045016 (2022) (Cited on pages 60, 76, and 79.)
- [Smo19] T. Smoleński, O. Cotlet, A. Popert, P. Back, Y. Shimazaki, P. Knüppel, N. Dietler, T. Taniguchi, K. Watanabe, M. Kroner, A. Imamoglu, *Interaction-Induced Shubnikov–de Haas Oscillations in Optical Conductivity of Monolayer MoSe₂*, Phys. Rev. Lett. **123**, 097403 (2019) (Cited on page 47.)
- [Smo21] T. Smoleński, P. E. Dolgirev, C. Kuhlenskamp, A. Popert, Y. Shimazaki, P. Back, X. Lu, M. Kroner, K. Watanabe, T. Taniguchi, I. Esterlis, E. Demler, A. Imamoglu, *Signatures of Wigner crystal of electrons in a monolayer semiconductor*, Nature **595**, 53–57 (2021) (Cited on pages 2 and 25.)
- [Sno02] D. Snoke, *Spontaneous Bose Coherence of Excitons and Polaritons*, Science **298**, 1368–1372 (2002) (Cited on pages 85 and 139.)
- [Spl10] A. Splendiani, L. Sun, Y. Zhang, T. Li, J. Kim, C.-Y. Chim, G. Galli, F. Wang, *Emerging Photoluminescence in Monolayer MoS₂*, Nano Lett. **10**, 1271–1275 (2010) (Cited on pages 2, 5, 6, 7, 8, and 104.)
- [Spo22] L. Sponfeldner, N. Leisgang, S. Shree, I. Paradisanos, K. Watanabe, T. Taniguchi, C. Robert, D. Lagarde, A. Balocchi, X. Marie, I. C. Gerber, B. Urbaszek, R. J. Warburton, *Capacitively and Inductively Coupled Excitons in Bilayer MoS₂*, Phys. Rev. Lett. **129**, 107401 (2022) (Cited on page 161.)
- [Sri15] A. Srivastava, M. Sidler, A. V. Allain, D. S. Lembke, A. Kis, A. Imamoglu, *Valley Zeeman effect in elementary optical excitations of monolayer WSe₂*, Nat. Phys **11**, 141–147 (2015) (Cited on page 21.)
- [Ste14] A. Steinhoff, M. Rösner, F. Jahnke, T. O. Wehling, C. Gies, *Influence of Excited Carriers on the Optical and Electronic Properties of MoS₂*, Nano Lett. **14**, 3743–3748 (2014) (Cited on page 84.)
- [Sti16a] A. V. Stier, K. M. McCreary, B. T. Jonker, J. Kono, S. A. Crooker, *Exciton diamagnetic shifts and valley Zeeman effects in monolayer WS₂ and MoS₂ to 65 Tesla*, Nat. Commun. **7**, 10643 (2016) (Cited on pages 23 and 24.)

- [Sti16b] A. V. Stier, N. P. Wilson, G. Clark, X. Xu, S. A. Crooker, *Probing the Influence of Dielectric Environment on Excitons in Monolayer WSe₂: Insight from High Magnetic Fields*, Nano Lett. **16**, 7054–7060 (2016) (Cited on page 11.)
- [Sto38] E. C. Stoner, *Collective electron ferromagnetism*, Proc. Royal Soc. Lond. A **165**, 0372–0414 (1938) (Cited on page 124.)
- [Sun20] J. Sung, Y. Zhou, G. Scuri, V. Zólyomi, T. I. Andersen, H. Yoo, D. S. Wild, A. Y. Joe, R. J. Gelly, H. Heo, S. J. Magorrian, D. Bérubé, A. M. M. Valdivia, T. Taniguchi, K. Watanabe, M. D. Lukin, P. Kim, V. I. Fal’ko, H. Park, *Broken mirror symmetry in excitonic response of reconstructed domains in twisted MoSe₂/MoSe₂ bilayers*, Nat. Nanotechnol. **15**, 750–754 (2020) (Cited on pages 12, 19, 54, 92, 104, and 121.)
- [Sur01] R. Suris, V. Kochereshko, G. Astakhov, D. Yakovlev, W. Ossau, J. Nürnberger, W. Faschinger, G. Landwehr, T. Wojtowicz, G. Karczewski, J. Kossut, *Excitons and Trions Modified by Interaction with a Two-Dimensional Electron Gas*, Phys. Status Solidi (b) **227**, 343–352 (2001) (Cited on pages 11, 126, and 130.)
- [Sur18] A. Surrente, L. Klopotoski, N. Zhang, M. Baranowski, A. A. Mitioğlu, M. V. Ballottin, P. C. M. Christianen, D. Dumcenco, Y.-C. Kung, D. K. Maude, A. Kis, P. Plochocka, *Intervalley Scattering of Interlayer Excitons in a MoS₂/MoSe₂/MoS₂ Heterostructure in High Magnetic Field*, Nano Lett. **18**, 3994–4000 (2018) (Cited on page 79.)
- [Sus19] A. Sushko, K. De Greve, T. I. Andersen, G. Scuri, Y. Zhou, J. Sung, K. Watanabe, T. Taniguchi, P. Kim, H. Park, M. D. Lukin, *High resolution imaging of reconstructed domains and moire patterns in functional van der Waals heterostructure devices*, arXiv:1912.07446 (2019) (Cited on pages 19, 54, and 61.)
- [Tan07] T. Taniguchi, K. Watanabe, *Synthesis of high-purity boron nitride single crystals under high pressure by using Ba–BN solvent*, J. Cryst. Growth **303**, 525–529 (2007) (Cited on page 28.)
- [Tan20a] L. B. Tan, O. Cotlet, A. Bergschneider, R. Schmidt, P. Back, Y. Shimazaki, M. Kroner, A. İmamoğlu, *Interacting Polaron-Polaritons*, Phys. Rev. X **10**, 021011 (2020) (Cited on page 120.)
- [Tan20b] Y. Tang, L. Li, T. Li, Y. Xu, S. Liu, K. Barmak, K. Watanabe, T. Taniguchi, A. H. MacDonald, J. Shan, K. F. Mak, *Simulation of Hubbard model physics in WSe₂/WS₂ moiré superlattices*, Nature **579**, 353–358 (2020) (Cited on pages 25 and 83.)
- [Tan21] Y. Tang, J. Gu, S. Liu, K. Watanabe, T. Taniguchi, J. Hone, K. F. Mak, J. Shan, *Tuning layer-hybridized moiré excitons by the quantum-confined Stark effect*, Nat. Nanotechnol. **16**, 52–57 (2021) (Cited on pages 12, 104, and 121.)
- [Thu22] D. Thureja, A. Imamoglu, T. Smoleński, I. Amelio, A. Popert, T. Chervy, X. Lu, S. Liu, K. Barmak, K. Watanabe, T. Taniguchi, D. J. Norris, M. Kroner, P. A. Murthy, *Electrically tunable quantum confinement of neutral excitons*, Nature page 298–304 (2022) (Cited on page 21.)
- [Tra96] N. Traynor, M. Snelling, R. Harley, R. Warburton, M. Hopkinson, *Investigation of g-factors Zeeman splittings, exchange interactions and field-dependent spin relaxation in III–V quantum wells*, Surf. Sci. **361–362**, 435–438 (1996) (Cited on page 78.)

- [Tra19] K. Tran, G. Moody, F. Wu, X. Lu, J. Choi, K. Kim, A. Rai, D. A. Sanchez, J. Quan, A. Singh, J. Embley, A. Zepeda, M. Campbell, T. Autry, T. Taniguchi, K. Watanabe, N. Lu, S. K. Banerjee, K. L. Silverman, S. Kim, E. Tutuc, L. Yang, A. H. MacDonald, X. Li, *Evidence for moiré excitons in van der Waals heterostructures*, *Nature* **567**, 71 (2019) (Cited on pages 13, 16, 17, 55, and 60.)
- [Tra20] K. Tran, J. Choi, A. Singh, *Moiré and beyond in transition metal dichalcogenide twisted bilayers*, *2D Mater.* **8**, 022002 (2020) (Cited on pages 14, 15, 17, and 20.)
- [Uen90] T. Uenoyama, L. J. Sham, *Effect of finite hole mass on edge singularities in optical spectra*, *Phys. Rev. Lett.* **65**, 1048–1051 (1990) (Cited on pages 125 and 126.)
- [Unu18] D. Unuchek, A. Ciarrocchi, A. Avsar, K. Watanabe, T. Taniguchi, A. Kis, *Room-temperature electrical control of exciton flux in a van der Waals heterostructure*, *Nature* **560**, 340–344 (2018) (Cited on pages 12, 21, and 54.)
- [Unu19] D. Unuchek, A. Ciarrocchi, A. Avsar, Z. Sun, K. Watanabe, T. Taniguchi, A. Kis, *Valley-polarized exciton currents in a van der Waals heterostructure*, *Nat. Nanotechnol.* **14**, 1104–1109 (2019) (Cited on pages 21, 54, 88, and 91.)
- [Vak04] K. Vakili, Y. P. Shkolnikov, E. Tutuc, E. P. De Poortere, M. Shayegan, *Spin Susceptibility of Two-Dimensional Electrons in Narrow AlAs Quantum Wells*, *Phys. Rev. Lett.* **92**, 226401 (2004) (Cited on page 124.)
- [VdD18] M. Van der Donck, F. M. Peeters, *Rich many-body phase diagram of electrons and holes in doped monolayer transition metal dichalcogenides*, *Phys. Rev. B* **98**, 115432 (2018) (Cited on page 129.)
- [Ver19] I. Verzhbitskiy, D. Vella, K. Watanabe, T. Taniguchi, G. Eda, *Suppressed Out-of-Plane Polarizability of Free Excitons in Monolayer WSe₂*, *ACS Nano* **13**, 3218–3224 (2019) (Cited on pages 87 and 91.)
- [Via19] F. Vialla, M. Danovich, D. A. Ruiz-Tijerina, M. Massicotte, P. Schmidt, T. Taniguchi, K. Watanabe, R. J. Hunt, M. Szyniszewski, N. D. Drummond, T. G. Pedersen, V. I. Fal’ko, F. H. L. Koppens, *Tuning of impurity-bound inter-layer complexes in a van der Waals heterobilayer*, *2D Mater.* **6**, 035032 (2019) (Cited on pages 13, 60, and 149.)
- [Wal98] S. N. Walck, T. L. Reinecke, *Exciton diamagnetic shift in semiconductor nanostructures*, *Phys. Rev. B* **57**, 9088–9096 (1998) (Cited on page 24.)
- [Wan37] G. H. Wannier, *The Structure of Electronic Excitation Levels in Insulating Crystals*, *Phys. Rev.* **52**, 191–197 (1937) (Cited on page 9.)
- [Wan10] H. Wang, Y. Wu, C. Cong, J. Shang, T. Yu, *Hysteresis of electronic transport in graphene transistors*, *ACS Nano* **4**, 7221 (2010) (Cited on page 181.)
- [Wan12] Y. Y. Wang, R. X. Gao, Z. H. Ni, H. He, S. P. Guo, H. P. Yang, C. X. Cong, T. Yu, *Thickness identification of two-dimensional materials by optical imaging*, *Nanotechnology* **23**, 495713 (2012) (Cited on page 28.)
- [Wan15a] G. Wang, L. Bouet, M. M. Glazov, T. Amand, E. L. Ivchenko, E. Palleau, X. Marie, B. Urbaszek, *Magneto-optics in transition metal diselenide monolayers*, *2D Mater.* **2**, 034002 (2015) (Cited on pages 21, 24, and 79.)
- [Wan15b] G. Wang, X. Marie, I. Gerber, T. Amand, D. Lagarde, L. Bouet, M. Vidal, A. Balocchi, B. Urbaszek, *Giant Enhancement of the Optical Second-Harmonic Emission of WSe₂ Monolayers by Laser Excitation at Exciton Resonances*, *Phys. Rev. Lett.* **114**, 097403 (2015) (Cited on pages 104 and 140.)

- [Wan16] K. Wang, B. Huang, M. Tian, F. Ceballos, M.-W. Lin, M. Mahjouri-Samani, A. Boulesbaa, A. A. Puretzy, C. M. Rouleau, M. Yoon, H. Zhao, K. Xiao, G. Duscher, D. B. Geohegan, *Interlayer Coupling in Twisted WSe_2/WS_2 Bilayer Heterostructures Revealed by Optical Spectroscopy*, ACS Nano **10**, 6612–6622 (2016) (Cited on page 12.)
- [Wan17a] G. Wang, C. Robert, M. Glazov, F. Cadiz, E. Courtade, T. Amand, D. Lagarde, T. Taniguchi, K. Watanabe, B. Urbaszek, X. Marie, *In-Plane Propagation of Light in Transition Metal Dichalcogenide Monolayers: Optical Selection Rules*, Phys. Rev. Lett. **119**, 047401 (2017) (Cited on pages 24 and 25.)
- [Wan17b] L. Wang, Z. Wang, H.-Y. Wang, G. Grinblat, Y.-L. Huang, D. Wang, X.-H. Ye, X.-B. Li, Q. Bao, A.-S. Wee, S. A. Maier, Q.-D. Chen, M.-L. Zhong, C.-W. Qiu, H.-B. Sun, *Slow cooling and efficient extraction of C-exciton hot carriers in MoS_2 monolayer*, Nat. Commun. **8**, 13906 (2017) (Cited on page 7.)
- [Wan17c] Y. Wang, Z. Wang, W. Yao, G.-B. Liu, H. Yu, *Interlayer coupling in commensurate and incommensurate bilayer structures of transition-metal dichalcogenides*, Phys. Rev. B **95**, 115429 (2017) (Cited on pages 17 and 120.)
- [Wan18a] G. Wang, A. Chernikov, M. M. Glazov, T. F. Heinz, X. Marie, T. Amand, B. Urbaszek, *Colloquium: Excitons in atomically thin transition metal dichalcogenides*, Rev. Mod. Phys. **90**, 021001 (2018) (Cited on pages 9, 10, and 88.)
- [Wan18b] Z. Wang, Y.-H. Chiu, K. Honz, K. F. Mak, J. Shan, *Electrical Tuning of Interlayer Exciton Gases in WSe_2 Bilayers*, Nano Lett. **18**, 137–143 (2018) (Cited on page 92.)
- [Wan19] Z. Wang, D. A. Rhodes, K. Watanabe, T. Taniguchi, J. C. Hone, J. Shan, K. F. Mak, *Evidence of high-temperature exciton condensation in two-dimensional atomic double layers*, Nature **574**, 76–80 (2019) (Cited on page 54.)
- [Wan20a] L. Wang, E.-M. Shih, A. Ghiotto, L. Xian, D. A. Rhodes, C. Tan, M. Claassen, D. M. Kennes, Y. Bai, B. Kim, K. Watanabe, T. Taniguchi, X. Zhu, J. Hone, A. Rubio, A. N. Pasupathy, C. R. Dean, *Correlated electronic phases in twisted bilayer transition metal dichalcogenides*, Nat. Mater. **19**, 861–866 (2020) (Cited on pages 25 and 83.)
- [Wan20b] T. Wang, Z. Li, Y. Li, Z. Lu, S. Miao, Z. Lian, Y. Meng, M. Blei, T. Taniguchi, K. Watanabe, S. Tongay, D. Smirnov, C. Zhang, S.-F. Shi, *Giant Valley-Polarized Rydberg Excitons in Monolayer WSe_2 Revealed by Magneto-photocurrent Spectroscopy*, Nano Lett. **20**, 7635–7641 (2020) (Cited on page 24.)
- [Wan20c] T. Wang, S. Miao, Z. Li, Y. Meng, Z. Lu, Z. Lian, M. Blei, T. Taniguchi, K. Watanabe, S. Tongay, D. Smirnov, S.-F. Shi, *Giant Valley-Zeeman Splitting from Spin-Singlet and Spin-Triplet Interlayer Excitons in $WSe_2/MoSe_2$ Heterostructure*, Nano Lett. **20**, 694–700 (2020) (Cited on pages 55 and 60.)
- [Wan21a] J. Wang, Q. Shi, E.-M. Shih, L. Zhou, W. Wu, Y. Bai, D. Rhodes, K. Barmak, J. Hone, C. Dean, X.-Y. Zhu, *Diffusivity Reveals Three Distinct Phases of Interlayer Excitons in $MoSe_2 / WSe_2$ Heterobilayers*, Phys. Rev. Lett. **126**, 106804 (2021) (Cited on pages 17, 21, 54, and 85.)
- [Wan21b] X. Wang, J. Zhu, K. L. Seyler, P. Rivera, H. Zheng, Y. Wang, M. He, T. Taniguchi, K. Watanabe, J. Yan, D. G. Mandrus, D. R. Gamelin, W. Yao, X. Xu, *Moiré trions in $MoSe_2/WSe_2$ heterobilayers*, Nat. Nanotechnol. **16**, 1208–1213 (2021) (Cited on pages 25 and 84.)

- [Wan22] X. Wang, C. Xiao, H. Park, J. Zhu, C. Wang, T. Taniguchi, K. Watanabe, J. Yan, D. Xiao, D. R. Gamelin, W. Yao, X. Xu, *Light-induced ferromagnetism in moiré superlattices*, Nature **604**, 468–473 (2022) (Cited on pages 124 and 130.)
- [Wes20] A. Weston, Y. Zou, V. Enaldiev, A. Summerfield, N. Clark, V. Zólyomi, A. Graham, C. Yelgel, S. Magorrian, M. Zhou, J. Zultak, D. Hopkinson, A. Barinov, T. H. Bointon, A. Kretinin, N. R. Wilson, P. H. Beton, V. I. Fal’ko, S. J. Haigh, R. Gorbachev, *Atomic reconstruction in twisted bilayers of transition metal dichalcogenides*, Nat. Nanotechnol. **15**, 592–597 (2020) (Cited on pages 19, 54, and 61.)
- [Wij15] M. M. v. Wijk, A. Schuring, M. I. Katsnelson, A. Fasolino, *Relaxation of moiré patterns for slightly misaligned identical lattices: graphene on graphite*, 2D Mater. **2**, 034010 (2015) (Cited on page 19.)
- [Wil17] N. R. Wilson, P. V. Nguyen, K. Seyler, P. Rivera, A. J. Marsden, Z. P. L. Laker, G. C. Constantinescu, V. Kandyba, A. Barinov, N. D. M. Hine, X. Xu, D. H. Cobden, *Determination of band offsets, hybridization, and exciton binding in 2D semiconductor heterostructures*, Sci. Adv. **3**, e1601832 (2017) (Cited on page 12.)
- [Wor96] R. E. Worsley, N. J. Traynor, T. Grevatt, R. T. Harley, *Transient Linear Birefringence in GaAs Quantum Wells: Magnetic Field Dependence of Coherent Exciton Spin Dynamics*, Phys. Rev. Lett. **76** (1996) (Cited on page 78.)
- [Woz20] T. Wozniak, P. E. Faria Junior, G. Seifert, A. Chaves, J. Kunstmann, *Exciton g factors of van der Waals heterostructures from first-principles calculations*, Phys. Rev. B **101**, 235408 (2020) (Cited on pages 20, 23, 24, 54, 60, 76, 81, and 82.)
- [Wu13] S. Wu, J. S. Ross, G.-B. Liu, G. Aivazian, A. Jones, Z. Fei, W. Zhu, D. Xiao, W. Yao, D. Cobden, X. Xu, *Electrical tuning of valley magnetic moment through symmetry control in bilayer MoS₂*, Nat. Phys. **9**, 149–153 (2013) (Cited on page 91.)
- [Wu18] F. Wu, T. Lovorn, A. H. MacDonald, *Theory of optical absorption by interlayer excitons in transition metal dichalcogenide heterobilayers*, Phys. Rev. B **97**, 035306 (2018) (Cited on pages 16, 17, 25, 54, 63, and 77.)
- [Xia12] D. Xiao, G.-B. Liu, W. Feng, X. Xu, W. Yao, *Coupled Spin and Valley Physics in Monolayers of MoS₂ and Other Group-VI Dichalcogenides*, Phys. Rev. Lett. **108**, 196802 (2012) (Cited on pages 7, 8, and 125.)
- [Xia14] J. Xiao, M. Long, X. Li, Q. Zhang, H. Xu, K. S. Chan, *Effects of van der Waals interaction and electric field on the electronic structure of bilayer MoS₂*, J. Phys.: Condens. Matter **26**, 405302 (2014) (Cited on page 157.)
- [Xu20] Y. Xu, S. Liu, D. A. Rhodes, K. Watanabe, T. Taniguchi, J. Hone, V. Elser, K. F. Mak, J. Shan, *Correlated insulating states at fractional fillings of moiré superlattices*, Nature **587**, 214–218 (2020) (Cited on pages 24, 25, and 83.)
- [Yao08] W. Yao, D. Xiao, Q. Niu, *Valley-dependent optoelectronics from inversion symmetry breaking*, Phys. Rev. B **77**, 235406 (2008) (Cited on pages 7 and 8.)
- [Yil19] D. Yildiz, M. Kisiel, U. Gysin, O. Gürlü, E. Meyer, *Mechanical dissipation via image potential states on a topological insulator surface*, Nat. Mater. **18**, 1201–1206 (2019) (Cited on pages 137 and 140.)
- [Yoo19] H. Yoo, R. Engelke, S. Carr, S. Fang, K. Zhang, P. Cazeaux, S. H. Sung, R. Hovden, A. W. Tsen, T. Taniguchi, K. Watanabe, G.-C. Yi, M. Kim, M. Luskun,

- E. B. Tadmor, E. Kaxiras, P. Kim, *Atomic and electronic reconstruction at the van der Waals interface in twisted bilayer graphene*, Nat. Mater. **18**, 448–453 (2019) (Cited on page 19.)
- [Yu15] H. Yu, Y. Wang, Q. Tong, X. Xu, W. Yao, *Anomalous Light Cones and Valley Optical Selection Rules of Interlayer Excitons in Twisted Heterobilayers*, Phys. Rev. Lett. **115**, 187002 (2015) (Cited on pages 16 and 54.)
- [Yu17] H. Yu, G.-B. Liu, J. Tang, X. Xu, W. Yao, *Moiré excitons: From programmable quantum emitter arrays to spin-orbit-coupled artificial lattices*, Sci. Adv. **3** (2017) (Cited on pages 15, 16, 17, 18, 54, 60, and 76.)
- [Yu18] H. Yu, G.-B. Liu, W. Yao, *Brightened spin-triplet interlayer excitons and optical selection rules in van der Waals heterobilayers*, 2D Mater. **5**, 035021 (2018) (Cited on pages 15 and 16.)
- [Yua20] L. Yuan, B. Zheng, J. Kunstmann, T. Brumme, A. B. Kuc, C. Ma, S. Deng, D. Blach, A. Pan, L. Huang, *Twist-angle-dependent interlayer exciton diffusion in WS_2 - WSe_2 heterobilayers*, Nat. Mater. **19**, 617–623 (2020) (Cited on page 17.)
- [Yun12] W. S. Yun, S. W. Han, S. C. Hong, I. G. Kim, J. D. Lee, *Thickness and strain effects on electronic structures of transition metal dichalcogenides: $2H$ - MX_2 semiconductors ($M = Mo, W$; $X = S, Se, Te$)*, Phys. Rev. B **85**, 033305 (2012) (Cited on page 6.)
- [Yus00] G. Yusa, H. Shtrikman, I. Bar-Joseph, *Onset of exciton absorption in modulation-doped $GaAs$ quantum wells*, Phys. Rev. B **62**, 15390–15393 (2000) (Cited on pages 124 and 125.)
- [Zen12] H. Zeng, J. Dai, W. Yao, D. Xiao, X. Cui, *Valley polarization in MoS_2 monolayers by optical pumping*, Nat. Nanotech. **7**, 490–493 (2012) (Cited on pages 131 and 133.)
- [Zha05] Y. Zhang, Y.-W. Tan, H. L. Stormer, P. Kim, *Experimental observation of the quantum Hall effect and Berry’s phase in graphene*, Nature **438**, 201–204 (2005) (Cited on page 5.)
- [Zha13] W. Zhao, R. M. Ribeiro, M. Toh, A. Carvalho, C. Kloc, A. H. Castro Neto, G. Eda, *Origin of Indirect Optical Transitions in Few-Layer MoS_2 , WS_2 , and WSe_2* , Nano Lett. **13**, 5627–5634 (2013) (Cited on page 6.)
- [Zha15] X. Zhang, X.-F. Qiao, W. Shi, J.-B. Wu, D.-S. Jiang, P.-H. Tan, *Phonon and Raman scattering of two-dimensional transition metal dichalcogenides from monolayer, multilayer to bulk material*, Chem. Soc. Rev. **44**, 2757–2785 (2015) (Cited on pages 29 and 153.)
- [Zha17a] C. Zhang, C.-P. Chuu, X. Ren, M.-Y. Li, L.-J. Li, C. Jin, M.-Y. Chou, C.-K. Shih, *Interlayer couplings, Moiré patterns, and 2D electronic superlattices in MoS_2/WSe_2 hetero-bilayers*, Sci. Adv. **3**, e1601459 (2017) (Cited on page 16.)
- [Zha17b] X.-X. Zhang, T. Cao, Z. Lu, Y.-C. Lin, F. Zhang, Y. Wang, Z. Li, J. C. Hone, J. A. Robinson, D. Smirnov, S. G. Louie, T. F. Heinz, *Magnetic brightening and control of dark excitons in monolayer WSe_2* , Nat. Nanotechol. **12**, 883–888 (2017) (Cited on page 25.)
- [Zha18] N. Zhang, A. Surrente, M. Baranowski, D. K. Maude, P. Gant, A. Castellanos-Gomez, P. Plochocka, *Moiré Intralayer Excitons in a $MoSe_2/MoS_2$ Heterostructure*, Nano Lett. **18**, 7651–7657 (2018) (Cited on page 17.)

- [Zha19] L. Zhang, R. Gogna, G. W. Burg, J. Horng, E. Paik, Y.-H. Chou, K. Kim, E. Tutuc, H. Deng, *Highly valley-polarized singlet and triplet interlayer excitons in van der Waals heterostructure*, Phys. Rev. B **100**, 041 402 (2019) (Cited on page 60.)
- [Zha20] L. Zhang, Z. Zhang, F. Wu, D. Wang, R. Gogna, S. Hou, K. Watanabe, T. Taniguchi, K. Kulkarni, T. Kuo, S. R. Forrest, H. Deng, *Twist-angle dependence of moiré excitons in $WS_2/MoSe_2$ heterobilayers*, Nat. Commun. **11**, 5888 (2020) (Cited on page 104.)
- [Zha21] L. Zhang, F. Wu, S. Hou, Z. Zhang, Y.-H. Chou, K. Watanabe, T. Taniguchi, S. R. Forrest, H. Deng, *Van der Waals heterostructure polaritons with moiré-induced nonlinearity*, Nature **591**, 61–65 (2021) (Cited on page 102.)
- [Zho21] Y. Zhou, J. Sung, E. Brutschea, I. Esterlis, Y. Wang, G. Scuri, R. J. Gelly, H. Heo, T. Taniguchi, K. Watanabe, G. Zaránd, M. D. Lukin, P. Kim, E. Demler, H. Park, *Bilayer Wigner crystals in a transition metal dichalcogenide heterostructure*, Nature **595**, 48–52 (2021) (Cited on pages 25, 83, and 84.)
- [Zhu03] J. Zhu, H. L. Stormer, L. N. Pfeiffer, K. W. Baldwin, K. W. West, *Spin Susceptibility of an Ultra-Low-Density Two-Dimensional Electron System*, Phys. Rev. Lett. **90**, 056 805 (2003) (Cited on page 124.)
- [Zhu11] Z. Y. Zhu, Y. C. Cheng, U. Schwingenschlögl, *Giant spin-orbit-induced spin splitting in two-dimensional transition-metal dichalcogenide semiconductors*, Phys. Rev. B **84**, 153 402 (2011) (Cited on pages 6 and 7.)
- [Zhu20] Y. V. Zhumagulov, A. Vagov, D. R. Gulevich, P. E. Faria Junior, V. Perebeinos, *Trion induced photoluminescence of a doped MoS_2 monolayer*, J. Chem. Phys. **153**, 044 132 (2020) (Cited on pages 11, 131, and 132.)
- [Zip18] J. Zipfel, J. Holler, A. A. Mitioglu, M. V. Ballottin, P. Nagler, A. V. Stier, T. Taniguchi, K. Watanabe, S. A. Crooker, P. C. M. Christianen, T. Korn, A. Chernikov, *Spatial extent of the excited exciton states in WS_2 monolayers from diamagnetic shifts*, Phys. Rev. B **98**, 075 438 (2018) (Cited on page 24.)
- [Zom14] P. J. Zomer, M. H. D. Guimarães, J. C. Brant, N. Tombros, B. J. van Wees, *Fast pick up technique for high quality heterostructures of bilayer graphene and hexagonal boron nitride*, Appl. Phys. Lett. **105**, 013 101 (2014) (Cited on pages 30 and 31.)

Acknowledgements

My PhD has been a long and arduous journey, and, as such, it can not be completed alone. This chapter is dedicated to all the people that helped me grow scientifically, and those who also touched me on a personal level.

First and foremost, I would like to thank my PhD advisor Richard Warburton for hosting me in his group and for giving me the great opportunity to perform independent research in a world-class lab environment. Discussions with Richard were always very stimulating and I benefited greatly from his vast knowledge of semiconductor physics and optics. I would also like to thank my second advisor Ilaria Zardo for her mentoring and support and for taking the time to read my thesis. Next, I would like to thank Alexander Tartakovskii from the University of Sheffield for taking up the role of my external examiner and for his interest in my thesis.

In my time as a PhD student, I benefited immensely from the expertise of my research group and from other people at (outside) the University of Basel. I owe a lot to Jonas Roch, who supervised and supported me at the beginning of my PhD. Thank you very much for introducing me to exfoliating and stacking and showing me how our experimental setup works. We had a lot of fun together in the lab and in the fabrication facilities. I would also like to thank my colleague Nadine Leisgang with whom I spent many days fabricating samples, measuring them, and discussing the results. Then, I would like to thank Dima Miserev for helping us understand the emission spectra of MoS₂. My thanks go out to all the people roaming the cleanroom and stacking facilities in Basel for discussing and helping with various fabrication processes and for sharing the latest tips and tricks.

The results on homobilayer MoS₂ arose from a great collaboration with Bernhard Urbaszek and his research team from Toulouse. I want to thank Bernhard for initiating this project, his guidance, and his enthusiasm to discuss new physical phenomena. It has been my pleasure working together with Shivangi Shree and Ioannis Paradisanos on this project – thank you both for your support and for the countless stimulating discussions that we had. On the same line, I want to thank Iann Gerber, who helped us understand our experimental results a lot with his theoretical calculations.

Also, I want to thank Arne Ludwig and Timo Kruck from the Ruhr-Universität Bochum for their great collaboration in the project of trying to improve the optical quality of near-surface InAs quantum dots using surface passivation. I am not only very grateful

for the quantum dot wafer they grew in Bochum, but also for the interesting and helpful discussions and the great support during this project. A big thanks also goes to Alisa Javadi, Nam Ngyuen, Clemens Spinnler, and Liang Zhai for helping a 2D guy measure and understand 0D.

The biggest and most heartfelt thanks goes out to the whole Nano-Photonics group past and present: Nadia Antoniadis, Andrea Corazza, Marcel Erbe, Sigurd Flågan, Yannik Fontana, Simon Geyer, Marie Gruet, Mark Hogg, Tomek Jakubczyk, Alisa Javadi, Nadine Leisgang, Sebu Leni, Matthias Löbl, Daniel Najer, Nam Nguyen, Ben Petrak, Daniel Riedel, Jonas Roch, Carolin Schrader, Clemens Spinnler, Willy Stehl, Natasha Tomm, Viktoria Yurgens, and Liang Zhai.

You were always willing to help in the lab or give advice when I needed it. Lunch and tea break discussions and after work beers have certainly contributed to this thesis. We had a lot of fun during the (online) game evenings, the countless BBQs, the bar evenings, Fasnacht, and the beer brewing sessions. I really enjoyed all the activities and trips of all kinds with you guys, especially trips to the mountains, be it hiking, skiing, or doing a via ferrata. You guys rock! (Or should I say Schlager?)

A big thanks go to Nadia Antoniadis, Sigurd Flågan, Simon Geyer, Nadine Leisgang, Nam Nguyen, Clemens Spinnler, and Liang Zhai for proofreading and correcting this thesis. Your feedback significantly improved the quality of this manuscript.

I highly appreciate the excellent environment provided by the Department of Physics at the University of Basel. The cleanroom facilities allowed me to build complete samples from scratch and the steady supply of liquid helium made sure that experiments could run continuously. The exceptional work from the mechanical workshop, the electronic workshop, and the administrative team made my life as a PhD student much easier – thank you all for your help over the last few years.

My doctoral study was part of the Swiss Nanoscience Institute (SNI) PhD school. I want to thank the SNI for the generous funding. Also, I want to thank the administrative team of the SNI for organising various meetings and events that helped me broaden my scientific horizon beyond 2D materials. The amazing environment and the discussions and drinks with the other SNI PhD students made all these get-togethers quite memorable.

Finally, I want to thank my family and friends for their great support over all these years.

Ich möchte meiner Familie für die stetige Unterstützung während meiner Promotion danken. Ihr hattet immer ein offenes Ohr für mich und habt mir oft bei schweren Entscheidungen geholfen. Eure Liebe, Zuneigung und Inspiration hat mich stets vorangetrieben und motiviert. Dafür kann ich euch allen nicht genug danken!

Curriculum vitae

Lukas Sponfeldner

Personal information

Email address: lukas.sponfeldner7@gmail.com
Date of birth: 7th September 1993
Place of birth: Cham, Germany
Citizenship: German

Education

2018 – 2022 **PhD in Experimental Physics**
University of Basel, Switzerland
Thesis: *Controlling the excitonic response and the electronic ground state in two-dimensional semiconductors*
Advisor: Prof. Dr. Richard J. Warburton

2015 – 2018 **Master in Applied and Engineering Physics**
Technical University of Munich, Germany
Thesis: *On the parabolicity of dipolar exciton traps*
Advisor: Prof. Dr. Alexander W. Holleitner

2016 (6 months) **Exchange studies**
Hong Kong University of Science and Technology

2012 – 2015 **Bachelor in Engineering Science**
Technical University of Munich, Germany
Thesis: *Deposition of Carbon Nanotubes by Dielectrophoresis*
Advisor: Prof. Dr. Alexander W. Holleitner

2004 – 2012 **High school**
Joseph-von-Fraunhofer Gymnasium, Cham

List of Publications

1. L. Sponfeldner, N. Leisgang, S. Shree, I. Paradisanos, K. Watanabe, T. Taniguchi, C. Robert, D. Lagarde, A. Balocchi, X. Marie, I. C. Gerber, B. Urbaszek, and R. J. Warburton, *Capacitively and inductively coupled excitons in bilayer MoS₂*, *Physical Review Letters* **129**, 107401 (2022)
2. N. Leisgang*, S. Shree*, I. Paradisanos*, L. Sponfeldner*, C. Robert, D. Lagarde, A. Balocchi, K. Watanabe, T. Taniguchi, X. Marie, R. J. Warburton, I. C. Gerber, and B. Urbaszek, *Giant Stark splitting of an exciton in bilayer MoS₂*, *Nature Nanotechnology* **15**, 901-907 (2020)
*These authors contributed equally.
3. J. G. Roch, D. Miserev, G. Froehlicher, N. Leisgang, L. Sponfeldner, K. Watanabe, T. Taniguchi, J. Klinovaja, D. Loss, and R. J. Warburton, *First-order magnetic phase transition of mobile electrons in monolayer MoS₂*, *Physical Review Letters* **124**, 187602 (2020)
4. S. Dietl, L. Sigl, L. Sponfeldner, G. Gardner, M. Manfra, J. P. Kotthaus, U. Wurstbauer, and A. W. Holleitner, *On the parabolicity of dipolar exciton traps and their population of excess charge carriers*, *New Journal of Physics* **21**, 063028 (2019)
5. C. Karnetzky, L. Sponfeldner, M. Engl, and A. W. Holleitner, *Ballistic and resonant negative photocurrents in semiconducting carbon nanotubes*, *Physical Review B* **95**, 161405(R) (2017)